



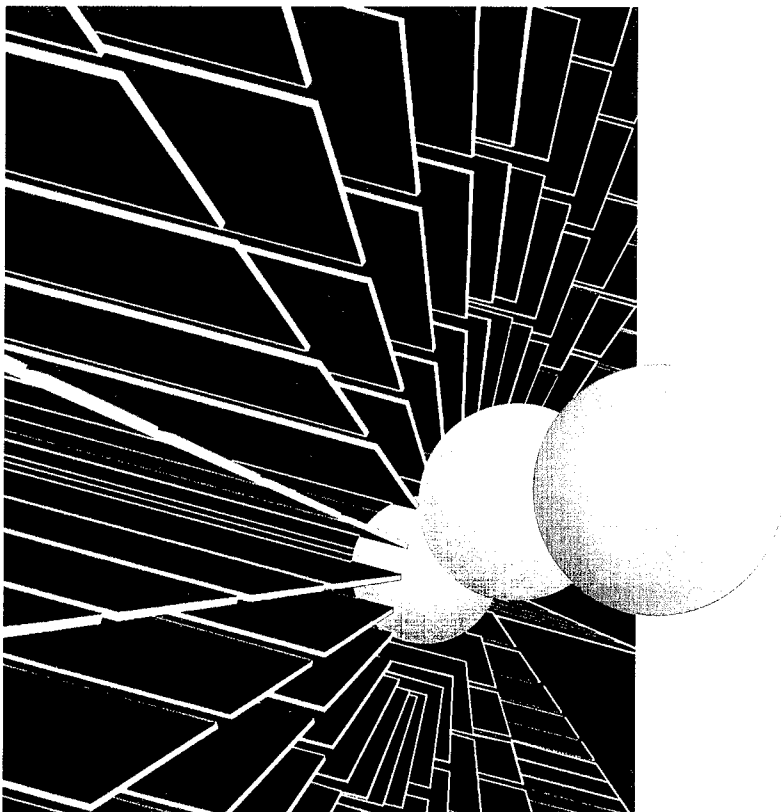
Research, Development and Technology

University of Missouri-Rolla

RDT 01-005

Metallic Dampers for Seismic Design and Retrofit of Bridges

RI 97-009



May, 2001

TECHNICAL REPORT DOCUMENTATION PAGE

1. Report No. RDT 01-005	2. Government Accession No.	3. Recipient's Catalog No.	
4. Title and Subtitle METALLIC DAMPERS FOR SEISMIC DESIGN AND RETROFIT OF BRIDGES		5. Report Date May, 2001	
		6. Performing Organization Code University of Missouri-Rolla	
7. Author(s) Genda Chen, Huimin Mu and Eric R. Bothe		8. Performing Organization Report No. RDT 01-005/RI 97-009	
9. Performing Organization Name and Address University of Missouri-Rolla 111 Butler-Carlton Civil Engineering Hall 1870 Miner Circle, Rolla, MO 65409-0030		10. Work Unit No.	
		11. Contract or Grant No.	
12. Sponsoring Agency Name and Address Missouri Department of Transportation Research, Development and Technology P. O. Box 270-Jefferson City, MO 65102		13. Type of Report and Period Covered Final Report	
		14. Sponsoring Agency Code MoDOT	
15. Supplementary Notes The investigation was conducted in cooperation with the U. S. Department of Transportation, Federal Highway Administration.			
16. Abstract A practical bearing scheme is proposed in this study, consisting of expansion rocker bearings and steel rods (metallic dampers). It can accommodate seismic effects while it allows for free thermal expansion. Tests of metallic dampers have shown that dampers of straight rods can contribute over 10% damping at the small-to-medium displacement range. Extensive tests on a 1/10-scale bridge model indicated that metallic dampers can also significantly reduce the dynamic responses of the bridge by isolating vibration propagating from the substructure to the superstructure. High rocker bearings provided considerable damping to the bridge-damper system by dissipating energy along the friction surface between pin and web of the bearings. They remain stable even at the peak ground acceleration of 0.54g at resonance. To account for pounding effect at the expansion joints of bridges, design equations for determining the equivalent viscous damping corresponding to various sizes of bridge joints were developed. Integrating the equivalent damping into the response spectrum analysis procedure allows engineers to analyze the bridges with pounding effect in a linear fashion.			
17. Key Words Metallic Damper, Stiffness Degradation, Energy Dissipation, Vibration Isolation, Dynamic Stability, Pounding Effect, Equivalent Viscous Damping, Seismic Performance, Design Equation, Infrequent Earthquake Events.		18. Distribution Statement No restrictions. This document is available to the public through National Technical Information Center, Springfield, Virginia 22161	
19. Security Classification (of this report) Unclassified	20. Security Classification (of this page) Unclassified	21. No. of Pages 131	22. Price

Final Report

RDT 01-005

METALLIC DAMPERS FOR SEISMIC DESIGN AND RETROFIT OF BRIDGES

MISSOURI DEPARTMENT OF TRANSPORTATION
RESEARCH, DEVELOPMENT AND TECHNOLOGY

BY: Genda Chen, Ph.D., P.E.
Huimin Mu, Ph. D. Candidate
Eric R. Bothe, EIT

Acknowledgment to:

University Transportation Center at the University of Missouri-Rolla

JEFFERSON CITY, MISSOURI
DATE SUBMITTED: May, 2001

The opinions, findings, and conclusions expressed in this publication are those of the principal investigators and the Missouri Department of Transportation. They are not necessarily those of the U.S. Department of Transportation, Federal Highway Administration. This report does not constitute a standard, specification or regulation.

EXECUTIVE SUMMARY

The purpose of this study was to develop an economic solution for the design and retrofit of continuous steel girder bridges in low occurrence seismic zones such as the Central and Eastern United States. Prior to 1975, the construction of such bridges exclusively used high rocker bearings and included two expansion joints at the ends of bridge decks for thermal expansion and contraction. They were designed with no seismic considerations. In this report, metallic dampers (steel rods) are introduced between the substructure and superstructure to improve the seismic performance of the bridges. Metallic dampers are used to provide restraint to the longitudinal movement of the bridges' superstructure under non-seismic loads and yield as fuse-like elements during a strong earthquake event. The scope of work included optimization of metallic dampers, experimental study of the cyclic behavior of full-scale dampers, experimental study of the dynamic behavior of high rocker bearings and dampers installed in a small-scale bridge system, and analytical development of a simplified procedure to account for pounding effect in the response spectrum analysis of highway bridges.

A total of four full-scale dampers, three with straight steel rods and one with linearly tapered rods, and an approximately 1/10-scale steel-girder bridge with various combinations of weight on the deck and different configurations of a small-scale metallic damper were tested in laboratory. Pounding effects on bridge responses were extensively studied with a simplified bridge model from which an equivalent damping concept has been developed based on the maximum deck displacement and mechanical energy criteria, respectively. The concept was validated with a number of linear and nonlinear analyses of a three-span bridge, A-237R in Southeast Missouri. The following conclusions can be drawn from the analytical and experimental investigations:

1. No material stiffness degradation of dampers was observed in the test range and the hysteresis loop in the load-displacement plane was steadily developed. Metallic dampers can dissipate an appreciable amount of energy even at a low level of loading. For straight-rod dampers, it was recommended that 10% equivalent viscous damping be used in bridge design. The equivalent damping of the tapered-rod dampers rapidly increased with the applied load after the initiation of yielding.
2. The performance of the dampers was consistent with respect to load and displacement. Under the same load, the tapered rods deformed considerably more than straight rods and revealed more uniform strain distribution along the steel rods, resulting in more energy dissipation.
3. Metallic dampers were also effective as isolation units. Their engagement in the small-scale steel-girder bridge significantly reduced the strain on the bridge columns and the acceleration of the steel girders. These results ensure that, in the event of a destructive earthquake, damage will be localized to the dampers while the columns retain their structural integrity.
4. Overturning of rocker bearings was not observed throughout the test program. Rocker bearings remained stable even when the bridge was subjected to a harmonic excitation of 0.54g at resonance.
5. Pounding reduces the maximum deck displacements of highway bridges during a strong earthquake event. It is similar to damping effect. The equivalent damping, structural damping plus pounding effect, is strongly dependent upon the gap width of

expansion joints and the dominant frequency of earthquake excitations. There is no conclusive functional relation between the equivalent damping and the frequency bandwidth of excitations.

6. The equivalent damping based on the displacement criterion is significantly more accurate than that from the energy criterion. It can be used in the linear analysis (time history or response spectrum procedure) of highway bridges so long as the gap width of expansion joints is greater than 60% the deck displacement when pounding is ignored.
7. Displacement-based design equations of equivalent damping are sufficiently accurate in representing pounding effect on the seismic responses of highway bridges with seat-type abutments. They are recommended for practical applications. Use of the equivalent damping concept simplifies the dynamic analysis of a geometrically nonlinear bridge system due to presence of expansion joints into that of an associated linear system.

**PROTECTED UNDER INTERNATIONAL COPYRIGHT
ALL RIGHTS RESERVED
NATIONAL TECHNICAL INFORMATION SERVICE
U.S. DEPARTMENT OF COMMERCE**

Reproduced from
best available copy.



TABLE OF CONTENTS

	Page
LIST OF FIGURES.....	viii
LIST OF TABLES	xii
LIST OF SYMBOLS	xiii
1. INTRODUCTION	1
1.1. Objectives.....	1
1.2. Present Conditions.....	2
2. TECHNICAL APPROACH AND EVALUATION OF FULL-SCALE DAMPERS FOR BRIDGE APPLICATIONS	5
2.1 Optimization of Metallic Dampers.....	5
2.2 Design of Full-Scale Dampers	6
2.3 Testing of Full-Scale Dampers.....	12
2.4 Results and Discussion of Full-Scale Damper Tests.....	16
2.5 Summary	23
3. TECHNICAL APPROACH AND EVALUATION OF A SMALL-SCALE BRIDGE	24
3.1 Recommended Procedure for Design of Metallic Dampers.....	24
3.2 Design and Fabrication of a Small-Scale Bridge and Dampers	25
3.3 Testing of a Small-Scale Bridge.....	29
3.4 Results and Discussion of Small-Scale Bridge Tests.....	37
3.5 Summary	48
4. POUNDING EFFECT ON BRIDGE BEHAVIOR	50
4.1 Theory of Pounding Action.....	51
4.1.1 Equation of Motion.....	51
4.1.2 Energy Equation	55
4.2 Earthquake Characteristics.....	57
4.3 Discussion on the Nonlinear Gap Element	65
4.4. Practical Procedure to Account for Pounding Effect	70
4.4.1 Equivalent Damping Concept.....	70
4.4.2 Displacement Method.....	70
4.4.3 Energy Method	77
4.5. Summary	83
5. APPLICATION OF THE EQUIVALENT DAMPING PROCEDURE TO BRIDGE A-237R	84
5.1 FEM Modeling	85
5.1.1 Foundation	85
5.1.1.1 Soil Property Estimation	85
5.1.1.2 Foundation Stiffness.....	88
5.1.1.3 Foundation Damping.....	92
5.1.2 Superstructure and Substructure.....	92
5.2 Dynamic Responses	94
5.2.1 Ground Motion	94
5.2.2 Bridge Analysis Procedures in Five Cases	98
5.3.3 Bridge Responses.....	100
5.3 Summary	104

6. CONCLUSIONS AND RECOMMENDATIONS	105
7. BIBLIOGRAPHY	108
8. APPENDIX	109
A. Additional Experimental Data of Full-Scale Dampers.....	109
B. Additional Experimental Data of Small-Scale Bridge	113
C. Tensile Test Data	126
D. Single Mode Response Spectrum Analysis Procedure.....	130

LIST OF FIGURES

	Page
Figure 1.1. Standard Bearing Arrangement	3
Figure 1.2. Proposed Damper Location on Bridge.....	4
Figure 2.1. Cantilevered Steel Rod	5
Figure 2.2. Schematic of Full-Scale Damper	7
Figure 2.3. Arrangement of Steel Rods.....	7
Figure 2.4. Determination of Equivalent Stiffness.....	8
Figure 2.5. Damper Rods of Full-Scale Damper: Straight and Tapered	9
Figure 2.6. Side View of Full-Scale Damper	9
Figure 2.7. Base Plate 1 of Full-Scale Damper	10
Figure 2.8. Base Plate 2 of Full-Scale Damper	10
Figure 2.9. Bottom Plate of Full-Scale Damper	11
Figure 2.10. Top Plate of Full-Scale Damper	11
Figure 2.11. HP VXI Unit Used to Generate Input Data	12
Figure 2.12. Data Acquisition System for Full-Scale Dampers	13
Figure 2.13. Full-Scale Damper 2 before Testing.....	13
Figure 2.14. Rod Location for Test 1	14
Figure 2.15. Rod Location for Tests 2 through 5	14
Figure 2.16. LVDT Location on Top Plate of Full-Scale Damper for Tests 1-3	15
Figure 2.17. LVDT Location on Top Plate of Full-Scale Damper for Tests 4 and 5.....	15
Figure 2.18. Strain Gauge Location on Full-Scale Damper	16
Figure 2.19. Input Data Generated by HP VXI Unit for Full-Scale Damper Tests	16
Figure 2.20. Load vs. Longitudinal Displacement of Damper 1	17
Figure 2.21. Stress-Strain Curve of Steel Rods.....	17
Figure 2.22. Load vs. Strain, Side Gauge of Damper 1	18
Figure 2.23. Load vs. Strain, Upper Gauge of Damper 1	19
Figure 2.24. Load vs. Strain, Middle Gauge of Damper 1	20
Figure 2.25. Load vs. Strain, Lower Gauge of Damper 1	20
Figure 2.26. Height of Bar vs. Total Strain of Dampers 1 and 4	21
Figure 2.27. Load-Longitudinal Loop Area vs. Load, Full-Scale Damper	21
Figure 2.28. Damping Ratio vs. Displacement	22
Figure 3.1. Side View, Small-Scale Bridge	25
Figure 3.2. Front View, Small-Scale Bridge	26
Figure 3.3. Connection Details, Small-Scale Bridge	26
Figure 3.4. Connection Details, Small-Scale Bridge (Cont'd).....	27
Figure 3.5. Web Portion of Columns	27
Figure 3.6. Front and Side Views, Small-Scale Bridge	30
Figure 3.7. Front View, Small-Scale Bridge	30
Figure 3.8. Side View, Small-Scale Bridge	31
Figure 3.9. Small-Scale Damper with Strain Gauge and LVDT's	31
Figure 3.10. Accelerometers Attached to Girders.....	32
Figure 3.11. Data Acquisition Unit for Small-Scale Bridge	32
Figure 3.12. HP VXI Unit	33
Figure 3.13. Strain Gauge Location on Small-Scale Damper	34

Figure 3.14. Strain Gauge Location on Column Base of Small-Scale Bridge	34
Figure 3.15. Accelerometer Location on Small-Scale Bridge	35
Figure 3.16. LVDT Location on Small Scale Bridge.....	35
Figure 3.17. 1952 Taft Earthquake Input (Modified).....	36
Figure 3.18. 1940 El Centro Earthquake Input (Modified).....	36
Figure 3.19. Harmonic Input	37
Figure 3.20. Acceleration Amplification Factor of Bridge without Damper	38
Figure 3.21. Acceleration Amplification Factor of Bridge with Damper 2	39
Figure 3.22. Acceleration Amplification Factor of Bridge with Damper 3	39
Figure 3.23. Acceleration Amplification Factor of Bridge with Damper 4	40
Figure 3.24. Load on Bar 1 of the Damper	41
Figure 3.25. Load vs. Relative Displacement, Damper 1, Small-Scale Bridge	41
Figure 3.26. Load vs. Relative Displacement, Damper 2, Small-Scale Bridge	42
Figure 3.27. Load vs. Relative Displacement, Damper 3, Small-Scale Bridge	42
Figure 3.28. Load vs. Relative Displacement, Damper 4, Small-Scale Bridge	43
Figure 3.29. Acceleration vs. Input, Taft Earthquake, Damper 3	44
Figure 3.30. Displacement vs. Input, Taft Earthquake, Damper 3.....	45
Figure 3.31. Acceleration vs. Input, El Centro Earthquake, Damper 3	45
Figure 3.32. Displacement vs. Input, El Centro Earthquake, Damper 3	46
Figure 3.33. Acceleration vs. Input, Harmonic Input, Damper 3.....	46
Figure 3.34. Displacement vs. Input, Harmonic Input, Damper 3	47
Figure 3.35. Strain vs. Input, Harmonic Input, Damper 3.....	47
Figure 3.36. Acceleration vs. Input, Re-Test of Damper 3	48
Figure 4.1. Actual Expansion Joint between Superstructure and Abutment.....	50
Figure 4.2. SDOF Pounding Model	51
Figure 4.3. Displacement at Bridge Deck under Harmonic Excitation.....	54
Figure 4.4. Velocity at Bridge Deck under Harmonic Excitation.....	54
Figure 4.5. Acceleration at Bridge Deck under Harmonic Excitation	54
Figure 4.6. Pounding Force under Harmonic Excitation	55
Figure 4.7. Input Energy under Harmonic Excitation.....	56
Figure 4.8. Kinetic Energy under Harmonic Excitation.....	56
Figure 4.9. Potential Energy under Harmonic Excitation	57
Figure 4.10. Acceleration Time Histories of Twelve Earthquake Records	59
Figure 4.11. Original and Smoothed FFT Spectra of Twelve Earthquake Records.....	61
Figure 4.12. Frequency Bandwidth Definition.....	65
Figure 4.13. Non-link Gap Element.....	65
Figure 4.14. Maximum Response vs. Stiffness Ratio	67
Figure 4.15. Maximum Energy vs. Stiffness Ratio	68
Figure 4.16. Pounding Force vs. Stiffness Ratio.....	69
Figure 4.17. Damping Energy vs. Stiffness Ratio.....	69
Figure 4.18. Equivalent Damping Concept.....	70
Figure 4.19. Equivalent Damping Ratio vs. Normalized Gap Width	72
Figure 4.20. Equivalent Damping Ratio vs. Frequency Ratio	72
Figure 4.21. Equivalent Damping Ratio vs. Structural Damping Ratio.....	73
Figure 4.22. Comparison of Displacement Time Histories.....	74
Figure 4.23. Displacement-Based Equivalent Damping Ratio for $\beta = 1$	75

Figure 4.24. Displacement-Based Equivalent Damping Ratio for $\beta = 0.5$	75
Figure 4.25. Displacement-Based Equivalent Damping Ratio for $\beta = 2$	76
Figure 4.26. Displacement-Based Design Equation for $\beta = 1$	76
Figure 4.27. Displacement-Based Design Equation for $\beta = 0.5$	77
Figure 4.28. Displacement-Based Design Equation for $\beta = 2$	77
Figure 4.29. Mechanical Energy Difference vs. Damping Ratio of Linear System	78
Figure 4.30. Mechanical Energy under the Miyagiken Earthquake.....	79
Figure 4.31. Energy-Based Equivalent Damping Ratio for $\beta = 1$	79
Figure 4.32. Energy-Based Equivalent Damping Ratio for $\beta = 0.5$	80
Figure 4.33. Energy-Based Equivalent Damping Ratio for $\beta = 2$	80
Figure 4.34. Mechanical Energy under Miyagew Earthquake.....	81
Figure 4.35. Energy-Based Design Equation for $\beta = 1$	82
Figure 4.36. Energy-Based Design Equation for $\beta = 0.5$	82
Figure 4.37. Energy-Based Design Equation for $\beta = 2$	83
Figure 5.1. General Elevation of Bridge A-237R	84
Figure 5.2. Standard Penetration Test (SPT) Blow-Count Values.....	86
Figure 5.3. Pile Bearing Capacity From in-Situ Test.....	87
Figure 5.4. Variation of Shear Modulus With Shear Strain Amplitude.....	88
Figure 5.5. Vertical Load-Displacement Relation	90
Figure 5.6. Lateral Load-Displacement Relation	90
Figure 5.7. 3-D FEM Model of Bridge A-237R	93
Figure 5.8. Gap Element	93
Figure 5.9. Synthetic Ground Motion (SF100103) at Pile Cap Base.....	95
Figure 5.10. Synthetic Ground Motion (SF100203) at Pile Cap Base.....	95
Figure 5.11. Acceleration Response Spectra for SF100103.....	96
Figure 5.12. Acceleration Response Spectra for SF100203.....	97
Figure 5.13. FFT for SF100103 Ground Motion	98
Figure 5.14. FFT for SF100203 Ground Motion	98
Figure 5.15. Deformed Shape under Horizontal Earthquake	99
Figure A.1. Load vs. Longitudinal Displacement, LVDT 3, Damper 2.....	109
Figure A.2. Load vs. Longitudinal Displacement, Lower Gauge of Bar 2, Damper 2 ..	109
Figure A.3. Load vs. Strain, Middle Gauge of Bar 1, Damper 2	110
Figure A.4. Load vs. Longitudinal Displacement, LVDT 3, Damper 3.....	110
Figure A.5. Load vs. Longitudinal Displacement, LVDT 2, Damper 4.....	111
Figure A.6. Load vs. Strain, Lower Gauge of Bar 2, Damper 4	111
Figure A.7. Load vs. Strain, Middle Gauge of Bar 1, Damper 4	112
Figure A.8. Load vs. Strain, Upper Gauge of Bar 2, Damper 4.....	112
Figure B.1. Acceleration vs. Input, Taft Earthquake, Without Damper	113
Figure B.2. Acceleration vs. Input, El Centro Earthquake, Without Damper.....	113
Figure B.3. Acceleration vs. Input, Harmonic Input, Without Damper.....	114
Figure B.4. Strain vs. Input, Harmonic Input, Without Damper.....	114
Figure B.5. Acceleration vs. Input, Taft Earthquake, Damper 1.....	115
Figure B.6. Displacement vs. Input, Taft Earthquake, Damper 1	115
Figure B.7. Acceleration vs. Input, El Centro Earthquake, Damper 1	116
Figure B.8. Displacement vs. Input, El Centro Earthquake, Damper 1	116

Figure B.9. Acceleration vs. Input, Harmonic Input, Damper 1	117
Figure B.10. Displacement vs. Input, Harmonic Input, Damper 1	117
Figure B.11. Strain vs. Input, Harmonic Input, Damper 1	118
Figure B.12. Acceleration vs. Input, Taft Earthquake, Damper 2.....	118
Figure B.13. Displacement vs. Input, Taft Earthquake, Damper 2	119
Figure B.14. Acceleration vs. Input, El Centro Earthquake, Damper 2.....	119
Figure B.15. Displacement vs. Input, El Centro Earthquake, Damper 2	120
Figure B.16. Acceleration vs. Input, Harmonic Input, Damper 2	120
Figure B.17. Displacement vs. Input, Harmonic Input, Damper 2	121
Figure B.18. Strain vs. Input, Harmonic Input, Damper 2.....	121
Figure B.19. Acceleration vs. Input, Taft Earthquake, Damper 4.....	122
Figure B.20. Displacement vs. Input, Taft Earthquake, Damper 4	122
Figure B.21. Acceleration vs. Input, El Centro Earthquake, Damper 4.....	123
Figure B.22. Displacement vs. Input, El Centro Earthquake, Damper 4	123
Figure B.23. Acceleration vs. Input, Harmonic Input, Damper 4	124
Figure B.24. Displacement vs. Input, Harmonic Input, Damper 4	124
Figure B.25. Strain vs. Input, Harmonic Input, Damper 4.....	125
Figure C.1. Tensile Rod Detail.....	126
Figure C.2. Tensile Rod Setup and Data Acquisition	126
Figure C.3. Rod after Failure	127
Figure C.4. Fracture Surface, Test 1	127
Figure C.5. Fracture Surface, Tests 2 and 3	127
Figure C.6. Load vs. Axial Displacement, Test 1	128
Figure C.7. Load vs. Axial Displacement, Tests 2 and 3, Respectively	128
Figure D.1. Bridge A-237R Subjected to an Assumed Longitudinal Loading	130
Figure D.2. Bridge Deck Subjected to Equivalent Longitudinal Seismic Loading	131

LIST OF TABLES

	Page
Table 2.1. Summary of Results for the Full-Scale Dampers.....	23
Table 3.1. Small-Scale Bridge Test Cases	37
Table 4.1. Input Ground Motion Characteristics.....	58
Table 4.2. Structural Model Damping Energy and Pounding Force vs. Stiffness Ratio..	66
Table 5.1. Computer Model and Analysis Procedure	85
Table 5.2. Estimated Soil Properties	87
Table 5.3. Theoretical vs. Experimental Bearing Capacity.....	88
Table 5.4. Characteristics of Input Ground Motions.....	98
Table 5.5. Input Earthquake and Structure Characteristics	101
Table 5.6. Bridge Responses under the SF100103a Earthquake (Displacement Method)	101
Table 5.7. Bridge Responses under the SF100103b Earthquake (Displacement Method)	102
Table 5.8. Bridge Responses under the SF100203a Earthquake (Displacement Method)	102
Table 5.9. Bridge Responses under the SF100203b Earthquake (Displacement Method)	102
Table 5.10. Equivalent Damping Ratios under Various Earthquake Excitations: Case 3 (Energy Method)	103
Table 5.11. Equivalent Damping Ratios under Various Earthquake Excitations: Case 3 (Displacement Method).....	103
Table C.1. Summary of Tensile Test Results.....	129

LIST OF SYMBOLS

The following symbols have been used in this report.

A = acceleration coefficient

A_{\max} = maximum displacement of the system

A_{ξ} = damping modification factor

a = acceleration of the input ground motion

B = damping effect factor

B_f = frequency bandwidth

B_w = width of the wall

b = width of column web

C_s = seismic coefficient

c = system damping coefficient

d_{\max} = maximum displacement

$d(x)$ = diameter of steel rods

E = modulus of elasticity

E_s = Young's modulus of the soil

E_k = relative kinetic energy of the mass

E_D = total energy dissipated by the structural damping and pounding

E_{Ds} = structural damping energy

E_{Dp} = structural pounding energy

E_p = relative potential energy due to the elastic strain

E_{PE} = passive force of the backfill soil

E_I = input energy imposed on the structure by an seismic event

$E_{m_{pd}}$ = mechanical energy of the system with pounding

$E_{m_{nopd}}$ = mechanical energy of the system without pounding

EQ = earthquake load

f = unit friction mobilized along a pile segment

f_{\max} = maximum unit friction

f_y = yielding stress of steel

G_{\max} = maximum shear modulus

g = gravitational acceleration

H = length of steel rods

H_s = height of soil face

h = height of column web

$h(u)$ = unit impulsive response function associated with the linear system without pounding

$I(x)$ = moment of inertia

i = backfill slope angle

K = spring constant in the gap element

K_{PE} = passive pressure coefficient of the backfill soil

k = system stiffness

k_{eq} = weighted average stiffness

k_r = elastic stiffness of steel rods or rotational stiffness

k_s = longitudinal stiffness
 L = height of a fixed pier
 M = difference of the mechanical energy
 M_{\min} = minimum value of the difference of the mechanical energy
 M_1, M_2 = bending moment
 M_p, M_p' = plastic moment
 $M(x)$ = bending moment at x distance
 m = mass
 m_n = number of dampers
 N = SPT value
 n = number of rods
 P = concentrated load
 $P_{y\max}$ = maximum yielding force
 $p(t)$ = pounding force
 Q_{\max} = maximum longitudinal force
 q = tip resistance of the pile
 q_{\max} = maximum tip resistance of the pile
 R = response modification factor
 R_f = reduction factor
 S = site coefficient
 S_a = spectral acceleration
 S_p, S_p' = plastic section modulus
 T = natural period
 t = time
 t^- = time instant immediately before time t
 t^+ = time instant immediately after time t
 Δt = short period
 V = shear force
 W = gravity load
 W_c = concrete weight
 W_d = energy dissipated in steel rods
 W_m = weight of miscellaneous items
 W_T = total weight
 W_w = weight of girder
 W_s = elastic energy stored in steel rods
 x = distance measured from a fixed support
 $x(t)$ = lateral displacement of the system
 $\ddot{x}_g(t)$ = ground acceleration
 z = vertical displacement of the pile
 z_{c1}, z_{c2} = critical vertical displacement of the pile
 α = overstrength factor
 β = frequency ratio between excitation and natural frequency
 β_s = non-seismic load factor
 γ = unit weight of the backfill soil
 δ = gap width
 η = relative weight of secant and elastic stiffness

ϕ = angle of friction among soil particles

φ = angle of friction among soil and abutment

μ_D = ductility demand

μ_C = ductility capacity

ξ = structural damping ratio

ξ', ξ_s = equivalent viscous damping ratio

$\sigma_m(x)$ = maximum stress

ω = natural frequency

ω_0 = natural frequency of the undamped bridge model without pounding

ω_D = natural frequency of the damped bridge model without pounding

ℓ = length of steel rods

ℓ_1, ℓ_2 = moment arm

1. INTRODUCTION

The American Association of State Highway and Transportation Officials (AASHTO) published the first version of seismic criteria in 1975. This same organization approved the Seismic Design Guidelines for Highway Bridges published by the Federal Highway Administration (FHWA) in 1981 as the standard specification for all fifty states. Nearly all bridges (other than on the West Coast) built prior to 1975 had little if any seismic design consideration.

Damage to bridge structures can be catastrophic in the event of a strong earthquake. Closure of the damaged bridge, if in a critical transportation network, will block emergency services to people in a heavily damaged area immediately after an earthquake. Later, the fallen bridge often slows reconstruction of structures in the area as well as the reconstruction of people's lives. There exists a need to retrofit these bridges in order to upgrade their seismic capacity to prevent loss of life or severe disruption in a society in the case of a strong earthquake.

High rocker bearings were used extensively in highway bridge constructions. They were generally considered deficient under service loads due to corrosion-related variability in performance, loss of articulation, and anchorage failure. Their performance under cyclic loading was recently studied by Mander *et al* (1996). How they respond to earthquake excitations at the bridge system level has not been studied yet. Since many bridges in the state of Missouri are subjected to seismic hazard from New Madrid Faults in Southern Missouri, the dynamic stability of rocker bearings is of great concern to engineers. On the other hand, considering the low seismicity in Mid West, engineers from this region often seek an economic solution such that bridges behave in a conventional way under non-seismic load and they will be protected from catastrophic damage in the event of a strong earthquake. A good example to show such effort was the use of lockup devices in the Cape Girardeau cable-stayed bridge. To further this effort, the Missouri Department of Transportation explored the potential use of metallic dampers in seismic design and retrofit of highway bridges in the current study. As part of this investigation, the seismic behavior of rocker bearings is demonstrated with shake table tests for a small-scale highway bridge. In addition, pounding effects on the seismic responses of steel-girder bridges with expansion joints are studied.

1.1. Objectives

The objective of this study was to develop a practical bearing arrangement scheme for continuous steel girder highway bridges in infrequent seismic zones such as the Central and Eastern United States. The bearing arrangement should be suitable to accommodate seismic forces while it allows for free thermal expansion.

The bearing scheme under development consists of laterally restrained expansion bearings under every steel girder at pier supports and several metallic dampers on one pier. The dampers serve as fixed supports of the bridge superstructure along the traffic direction. In case of a strong earthquake, the dampers yield before the formation of plastic hinges at the column bases of bridge pier so that the dampers dissipate energy and the bridges are protected from catastrophic damage. The scope of the project included:

1) to optimally shape the metallic damper with experimental verification so that it is deformed with a uniform curvature and thus dissipates maximum energy during earthquakes, 2) to experimentally study the cyclic behavior of full scale metallic dampers, 3) to investigate the dynamic behavior of high rocker bearings and the seismic effectiveness of dampers by testing a small scale bridge with a shake table, and 4) to analytically develop a simplified procedure to account for the pounding effect in seismic design of highway bridges.

1.2. Present Conditions

With the advent of new materials and construction technologies, civil engineers are pushing their limits further than ever before. Buildings are being built taller despite strong wind loads and bridges are crossing wider distances with larger bridge spans and more spans per continuous span bridge.

Use of continuous spans reduces the risk of the potential leak of water around expansion joints and consequent deterioration of a bridge's substructure. It can also reduce the probability of dropping of the spans from their supporting piers during an earthquake. The continuous spans generally add redundancy into the bridges for improved seismic performance. For these same reasons, many simply-supported existing bridges were recently retrofitted by eliminating as many existing expansion joints as possible to improve the overall integrity of the bridge. Many old bridges built 30~40 years ago have fixed bearings at one intermediate bent and expansion bearings at other bents. A bearing scheme of this kind transfers the seismic load from the superstructure to the substructure through one fixed pier only. Consequently, construction of continuous spans and increases in span length introduce a substantial amount of bending moment at the fixed pier in the traffic direction. This necessitates the need for more than one pier engaged to carry the inertial force within the conventional design methodology. Therefore, seismic load and thermal stress are in conflict with each other in the design of continuous span bridges.

Thermal stresses are considerably important in bridges located in infrequent seismic zones yet with a wide range of seasonal temperature changes. Fluctuations in thermal stresses occur daily, year round. Cosmetic cracks in the concrete substructures are not the only problem, they can lead to structural cracks affecting the life of the bridge. The Central and Eastern United States are in such locations. An optimal bearing arrangement can be used to solve the conflict between seismic loads and thermal stresses. The desired bearing arrangement would be the standard arrangement for free thermal expansion but with special mechanical units, called dampers, to reduce the seismic load for bridge design.

Since bridge foundations are often covered with soil, their post-earthquake inspection is costly. Repairing them is even more expensive and generally not recommended if an alternative is available. Seismic design of a bridge should at least consider excluding the possibility for any potential damage in the foundations. This goal can be achieved by installing isolators between the superstructure and the substructure of the bridge, which will prevent seismic vibration from propagating between them and thus reduce the inertial force on the bridge structure and foundations significantly. There are several systems in use that belong to this category, including the Lead-Rubber

Elastomeric Bearing System and the Friction-Pendulum system. These systems are both economical and effective in suppressing excessive responses when used in areas of high seismic activity where moderate earthquakes occur every few years and considerably outweigh the design of bridges due to other loads such as thermal stresses. In addition, they also perform well based on laboratory tests and scattered field observations on buildings.

However, in the Mid West, earthquakes occur infrequently. An isolation bearing installed on bridges may not be subjected to real earthquakes in the life span of the bridges. Economy therefore is a driving force in the selection of the type of bearings. Since high rocker bearings were used extensively in bridge construction, continuing use of the bearings is likely one of the most economic solutions for seismic retrofit projects. As an alternative to isolation bearings systems, steel rods (metallic dampers) are introduced to upgrade the seismic performance of highway bridges.

The proposed system consists of metallic dampers installed between the substructure and superstructure of one pier with laterally restrained expansion rocker bearings on top of all piers. For existing bridges, the fixed bearings need to be converted into expansion bearings. The pier with the metallic dampers functions as a fixed support to carry longitudinal forces induced by all loads (live, vertical braking force or wind load, etc) except for the earthquake load. Under the design earthquake, the metallic dampers will yield before a plastic hinge can develop at the base of the supporting pier. Together with the expansion bearings, they subsequently constitute a flexible link between the superstructure and substructure of the bridge and thus isolate the superstructure from the vibration energy at the foundation level. The excessive seismic response in the bridge is suppressed through damping of the metallic dampers, and more importantly, through softening of the bridge system after the dampers start yielding. Figure 1.1 shows the old standard bearing arrangement used in the bridges built 30~40 years ago, in which only the third bent provides the restraint to the longitudinal movement of superstructure. Figure 1.2 shows the proposed location of a metallic damper in bridge applications. After the damper is installed, the fixed bearings at the third bent as shown in Figure 1.1 are required to be modified into expansion bearings to make the damper effective.

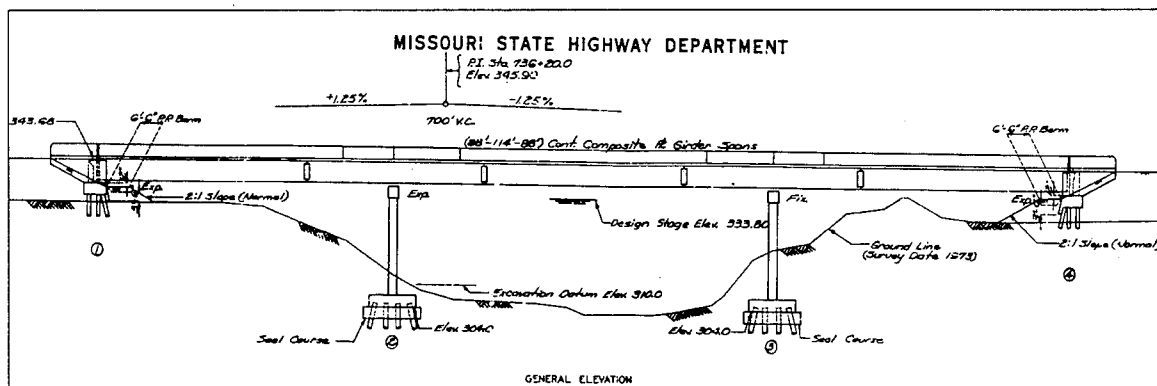


Figure 1.1. Standard Bearing Arrangement

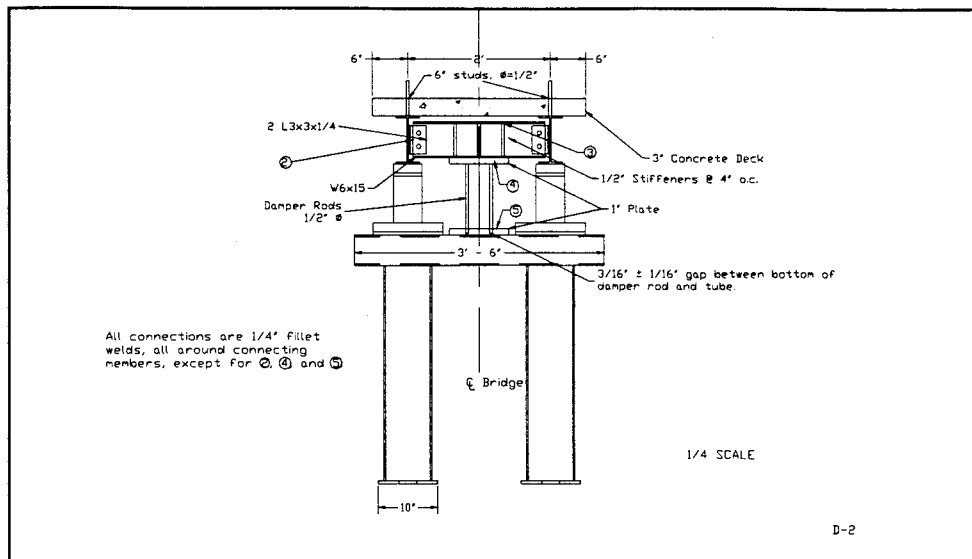


Figure 1.2. Proposed Damper Location on Bridge

Without further study, the advantages of the proposed system over the current available isolation systems are obvious. Engineers can easily apply this system in their seismic retrofit practice. With regards to thermal expansion, the system performs well in exactly the same way as any conventional bearing scheme. The damper is composed of several metallic bars made of low carbon steel. They are inexpensive and the damper can be easily replaced immediately after an earthquake in which they are subjected to a substantial amount of inelastic deformation. Since, during an earthquake, they are designed to yield before a plastic hinge forms at the bottom of the bridge piers, bridge damage is localized. This fuse-like ductile failure can avoid the catastrophic damage to the bridge substructures (Buckle, 1995).

During the past three decades, metallic plate dampers have received increasing attention from the earthquake engineering community and their implementations in building design were cited in several references (Ciampi, 1991; Fiero *et al.*, 1993; etc.). The state-of-the-art and state-of-practice development of metallic plate dampers was reported by Hanson *et al.* (1993). Over the years, many types of dampers made of mild steel were developed to fit in different applications. Several geometric configurations such as triangular and hourglass shapes have been employed in the design of these dampers so that the yielding spreads almost uniformly throughout the material. The result of these efforts has led to devices that are able to endure repeated inelastic deformations in a stable manner, avoiding concentrations of yielding and premature failure. Extensive experimental studies have been conducted to investigate the cyclic behavior of the individual damper and its effectiveness to suppress seismic responses of a building structure (Whittaker *et al.*, 1991; Tsai *et al.*, 1993). Dargush and Soong (1995) also conducted analytical work on the behavior of the metallic dampers.

All previous work basically focused on the development of metallic plate dampers for building applications. Further research on the optimal shape of metallic dampers for bridge applications is of practical significance. The hysteretic behavior under the exposed condition needs to be studied to ensure the dampers yield with sufficient ductility during a severe earthquake.

2. TECHNICAL APPROACH AND EVALUATION OF FULL-SCALE DAMPERS FOR BRIDGE APPLICATIONS

In building applications, metallic plate dampers are installed and restrained to deform in the plane of a frame between the floor beam and brace. Hourglass plates and triangular plates provide maximum energy dissipation when subjected to double-curvature and single-curvature bending, respectively. In the bridge application proposed here, the metallic dampers are installed between the superstructure and substructure. The dampers can deform in virtually any plane, depending on the configuration of the bridge's deck and the piers' orientation with respect to the deck. Neither hourglass plates nor triangular plates will be deformed with uniform curvature under these circumstances.

2.1 Optimization of Metallic Dampers

In bridge applications, dampers are installed between the deck and capbeam. They are subjected to lateral seismic forces from virtually any direction. It is therefore appropriate to design dampers with structural components of a symmetric cross section. Circular rods were used in this study. Assume a steel rod of varying diameter is cantilevered as shown in Figure 2.1. When a concentrated load, P , is applied at the cantilevered tip, the rod is subjected to a linear moment distribution. That is,

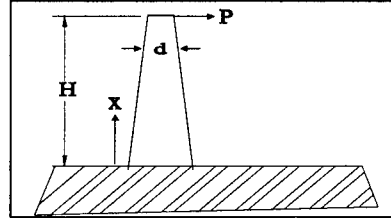


Figure 2.1. Cantilevered Steel Rod

$$M(x) = P(H-x) \quad (2.1)$$

in which H is the rod length and x measures the distance of a cross section from the fixed support. The moment of inertia of a circular section is,

$$I(x) = \pi d^4(x)/64 \quad (2.2)$$

and the maximum stress at the cross section can then be expressed into,

$$\sigma_m(x) = [M(x)d/2]/I(x) = 32P(H-x)/\pi d^3(x) \quad (2.3)$$

where $d(x)$ is the diameter of the rod. To force the entire rod to yield simultaneously under the point load, $\sigma_m(x) = f_y$. Here, f_y is the yielding strength of the steel rod. Therefore,

$$d(x) = [32P(H-x)/\pi f_y]^{1/3} \quad (2.4)$$

Obviously, the optimal shape of the steel rod is a tapered round bar with the diameter decreasing with the bar's height to the one-third power (Buckle and King, 1980).

To evenly distribute the concentrated load from any direction to steel rods, a symmetric configuration is preferred. The best scheme would be to place steel rods in a circular pattern. While this is the optimal bar shape and configuration, at this time, it is not economical to fabricate. Because of this, two different shaped rods, straight and linearly tapered, arranged in a square and triangle pattern will be tested. A schematic of the damper with tapered rods is shown in Figure 2.2 and Figure 2.3.

2.2 Design of Full-Scale Dampers

The full-scale dampers in this study were designed based on a typical bridge in the New Madrid Region. Consider a 220-foot, four-span continuous steel-girder bridge in Cape Girardeau County, Missouri with seven girders supporting two lanes of traffic. The middle two spans are 60 ft in length while the outside spans are 50 ft. The steel girders are fixed in the direction of traffic at the center pier and free to move at the other piers and abutments. The seismic load on the bridge was estimated according to the 1996 AASHTO Specifications.

The peak ground acceleration at the bridge site is $A=0.15g$. Considered as an essential structure, the bridge was classified as Seismic Performance Category B. The soil condition at the bridge site was assumed to be classified as Soil Profile Type II with a soil coefficient of $S=1.2$. In recognition of the ductile behavior of steel rods of dampers, a higher value of the response modification factor, $R=10\sim12$, was used (ICBO, 1994).

Earthquake Load. Considering a dead load of 1 k/ft on each girder, the total gravity load from deck and girder, W , is equal to 1540 kips. The earthquake load on each damper is determined by,

$$EQ \text{ (earthquake load per damper)} = C_S W \quad (2.5)$$

in which C_S is the seismic coefficient. According to the AASHTO Specifications (1996), the coefficient can be expressed as,

$$C_S = 1.2AS/(RT^{2/3}m_n) \quad (2.6)$$

where m_n is equal to the number of dampers and the resulting quantity must be less than $2.5A/m_n$.

Average Stiffness. With the elastic stiffness of the damper,

$$k_r = 3EI/H^3 \quad (2.7)$$

and the secant stiffness of the yielding damper, k/R . The weighted average stiffness during earthquake load can be estimated by,

$$k_{eq} = k_r[(1+\eta/R)/(1+\eta)] \quad (2.8)$$

in which η denotes the relative weight of the secant stiffness versus the elastic stiffness as shown in Figure 2.4. The natural period of the corresponding linear system, T , can then be determined by,

$$T = 2\pi(W/k_{eq}g)^{1/2} \quad (2.9)$$

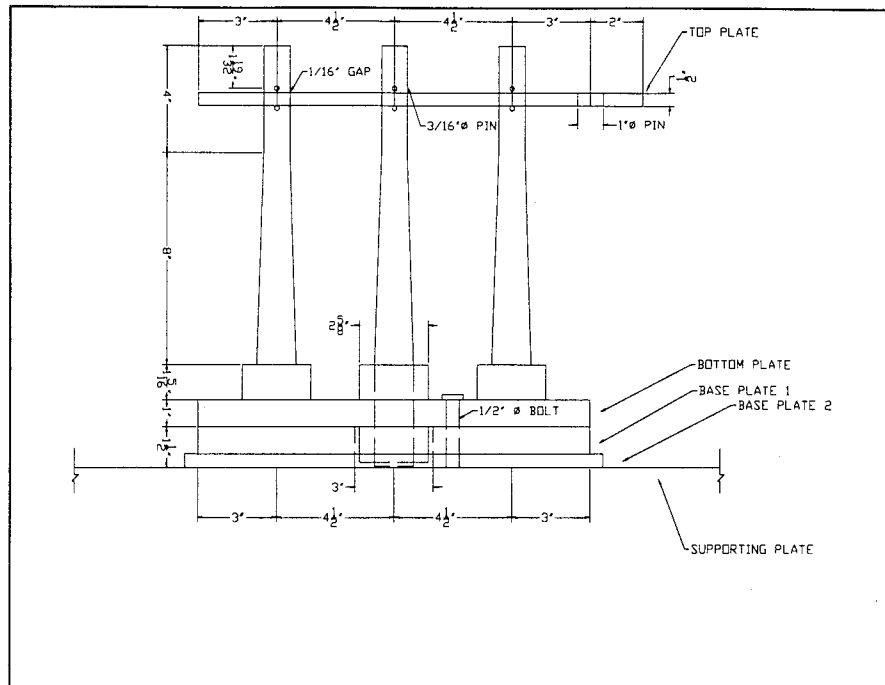


Figure 2.2. Schematic of Full-Scale Damper

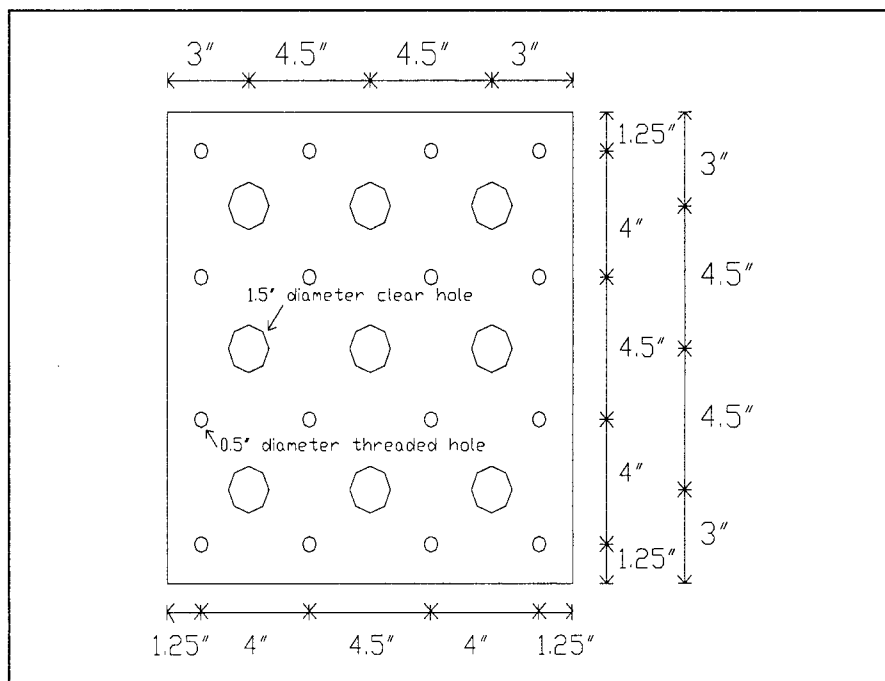


Figure 2.3. Arrangement of Steel Rods

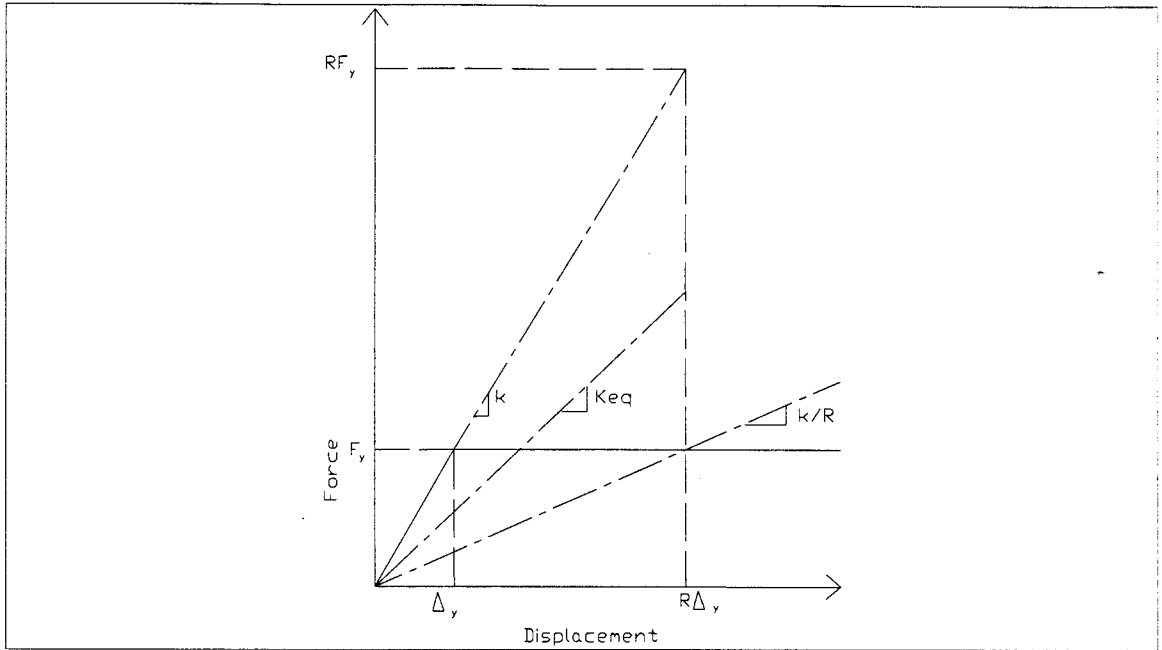


Figure 2.4. Determination of Equivalent Stiffness

Damper Rod Diameter. The load on each rod is,

$$P = EQ/n \quad (2.10)$$

where n is the number of rods. With a yielding stress, $f_y = 36$ ksi, d can be calculated from Eq. (2.4) to be between 1.28 and 1.59 in when $H = 10$ in, $g = 386$ in/sec², $nm = 35$ and $\eta = 1 \sim 3$. A diameter of 1½ in is used in this investigation. The expected yielding displacement at the cantilever end of such a steel rod is 0.055 in. Figures 2.5 through 2.10 show the final design of the full-scale damper. In Figure 2.10, plate A refers to the top plate used with the straight bars and plate B refers to the top plate used with the tapered rods.

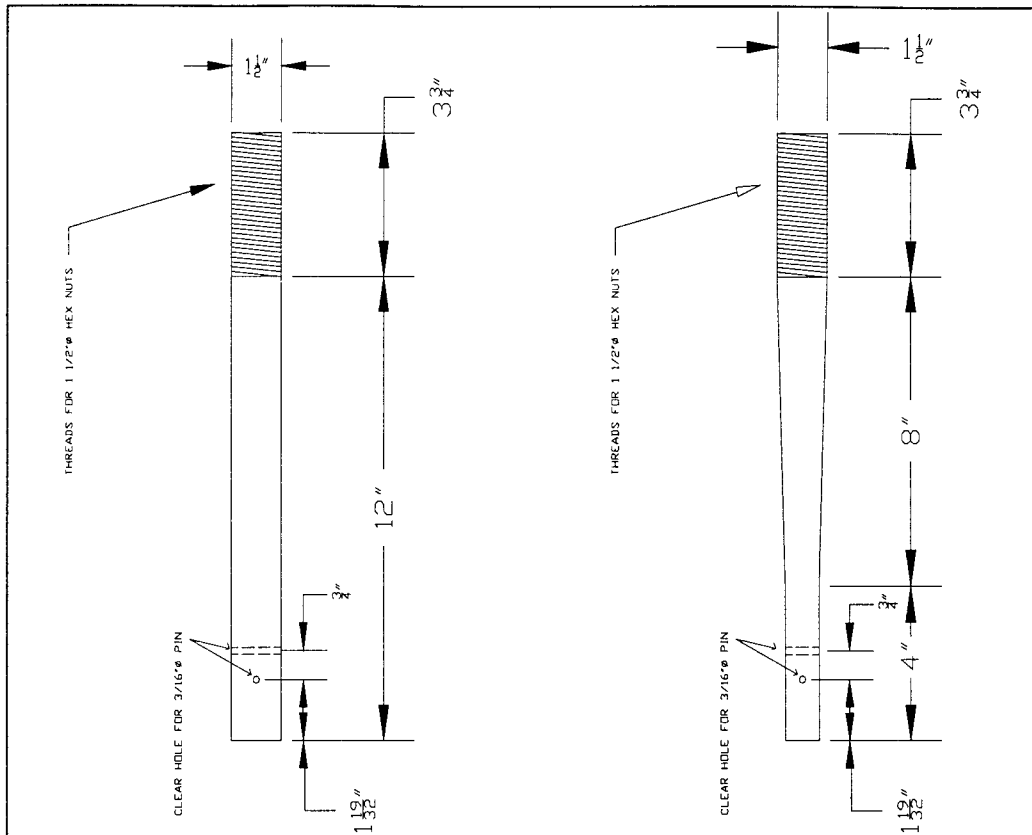


Figure 2.5. Damper Rods of Full-Scale Damper: Straight and Tapered

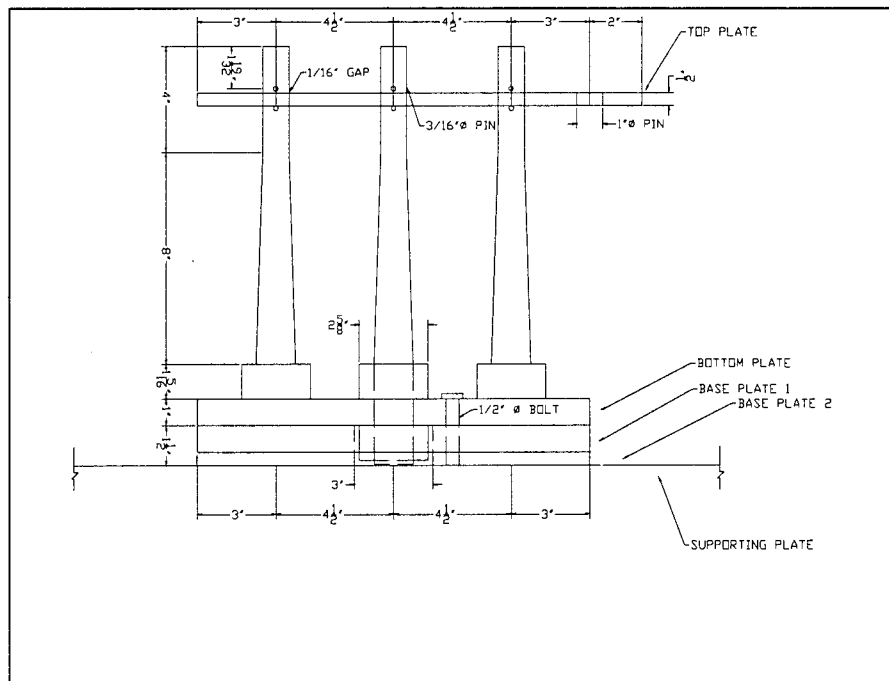


Figure 2.6. Side View of Full-Scale Damper

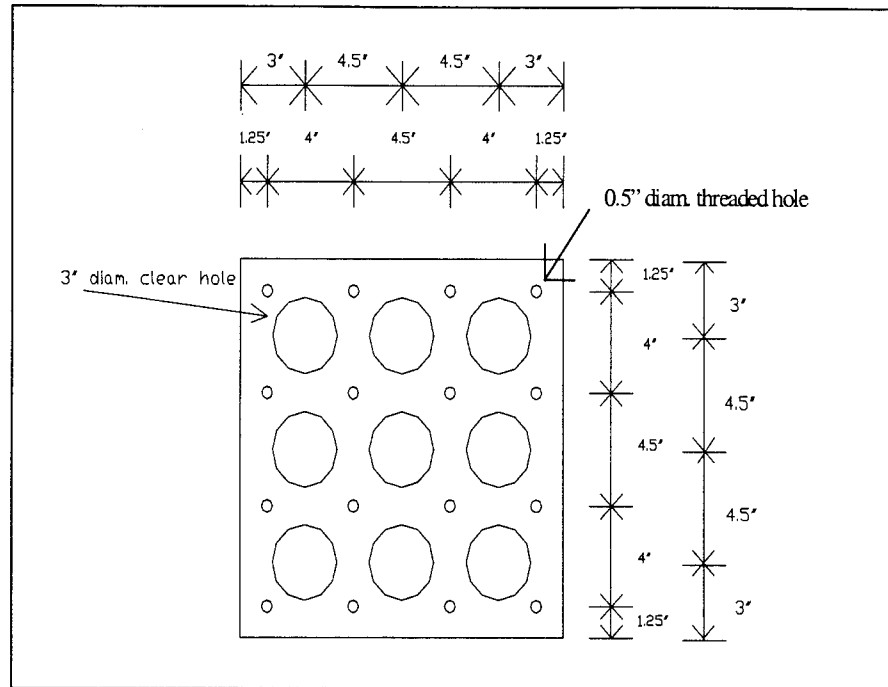


Figure 2.7. Base Plate 1 of Full-Scale Damper

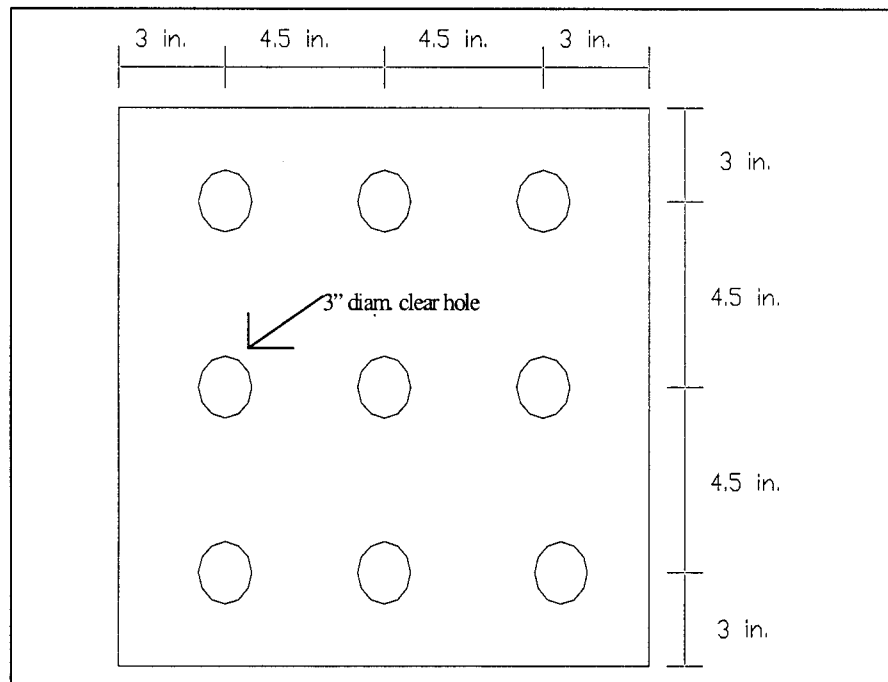


Figure 2.8. Base Plate 2 of Full-Scale Damper

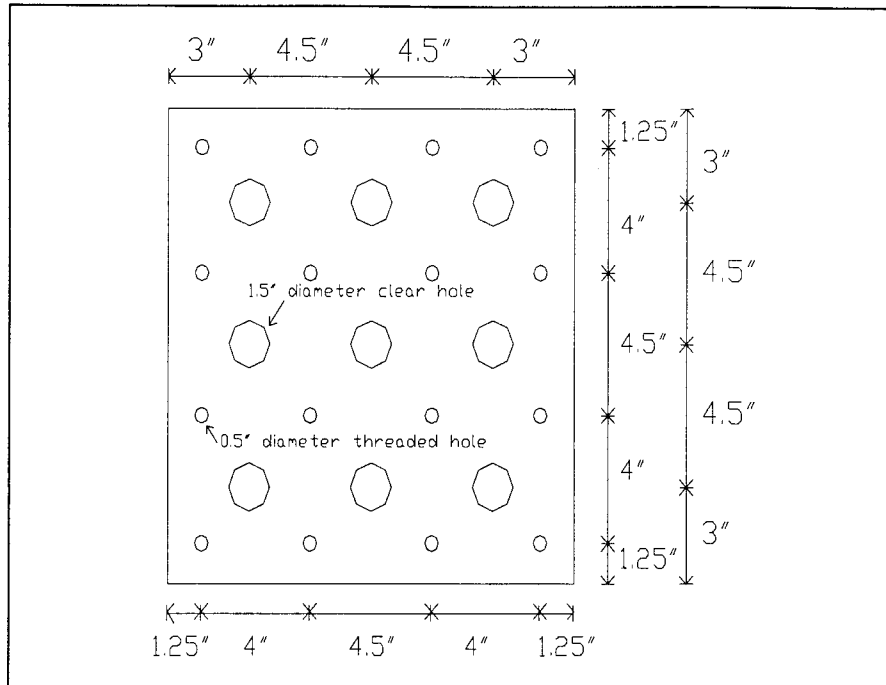


Figure 2.9. Bottom Plate of Full-Scale Damper

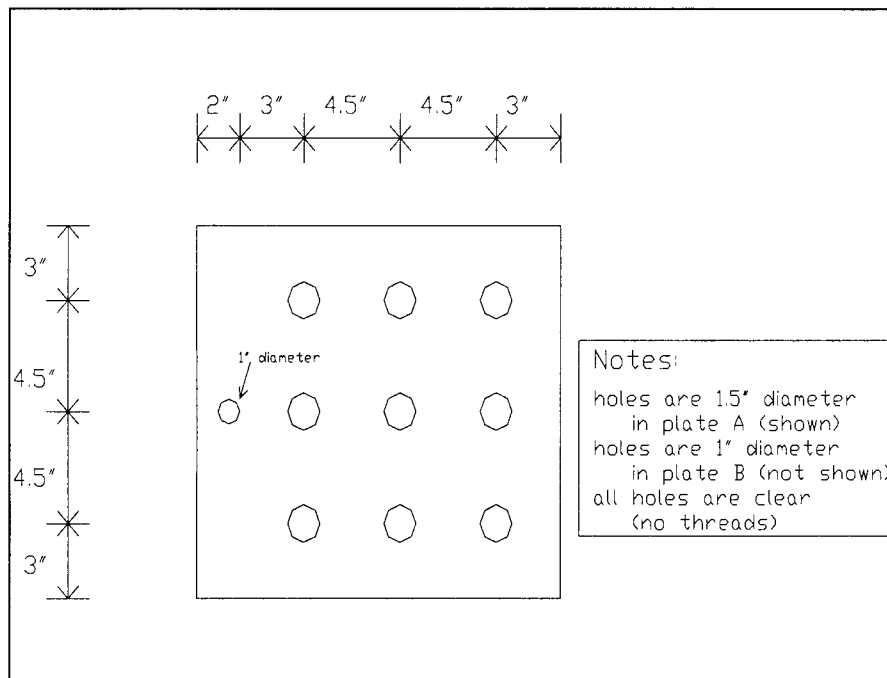


Figure 2.10. Top Plate of Full-Scale Damper

2.3 Testing of Full-Scale Dampers

Test Setup. Four full-scale dampers were tested in the Engineering Research Laboratory located at the University of Missouri - Rolla. Each damper was bolted to the strong floor and load was applied using the available 22 kip MTS hydraulic actuator. The tests were set up as illustrated in Figures 2.11-2.15. The HP VXI machine shown in Figure 2.11 was used to generate the input for the full-scale damper tests. The data acquisition system shown in Figure 2.12 was used to acquire strain, load and deflection data. The full-scale damper was fabricated at a local machine shop and assembled as shown in Figure 2.13. The steel rods were configured for each test as shown in Figures 2.14 and 2.15.

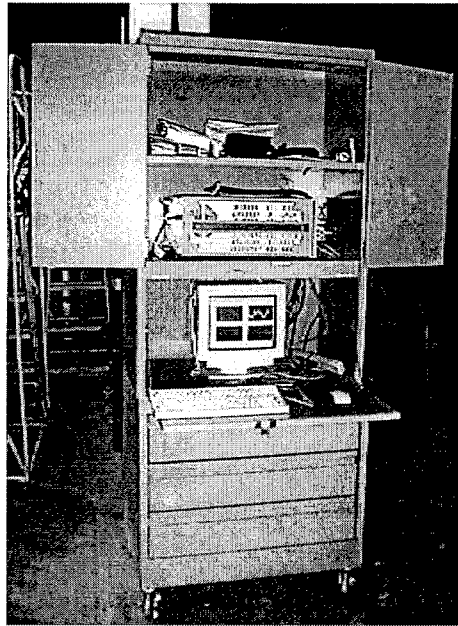


Figure 2.11. HP VXI Unit Used to Generate Input Data

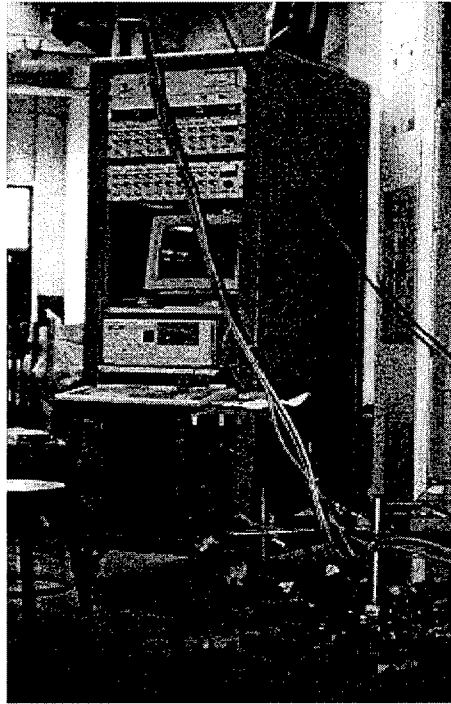


Figure 2.12. Data Acquisition System for Full-Scale Dampers

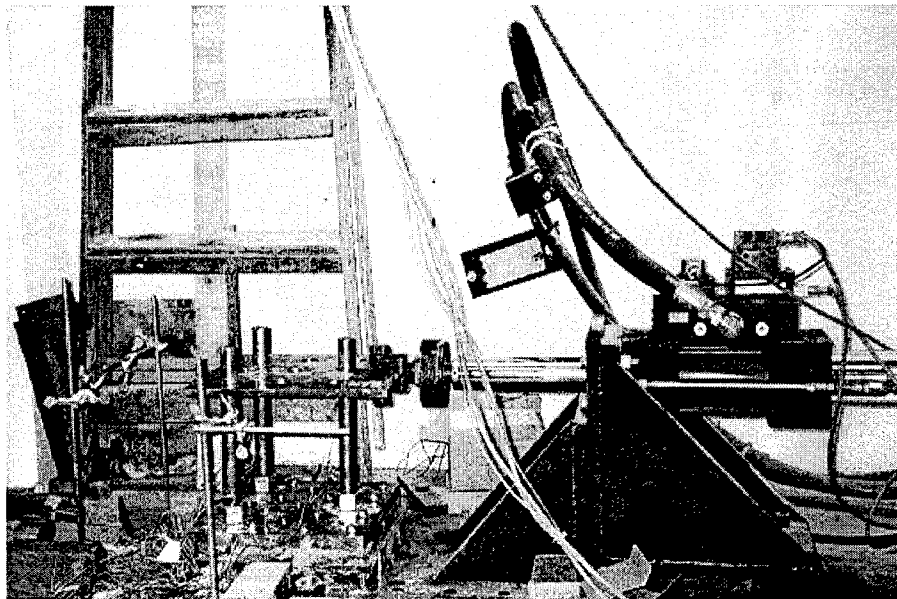


Figure 2.13. Full-Scale Damper 2 before Testing.

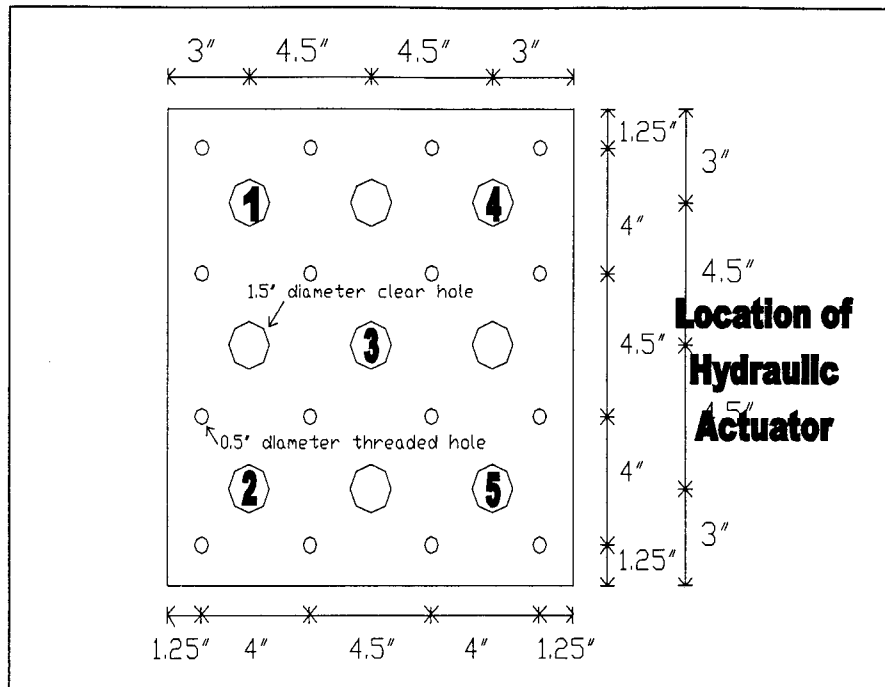


Figure 2.14. Rod Location for Test 1

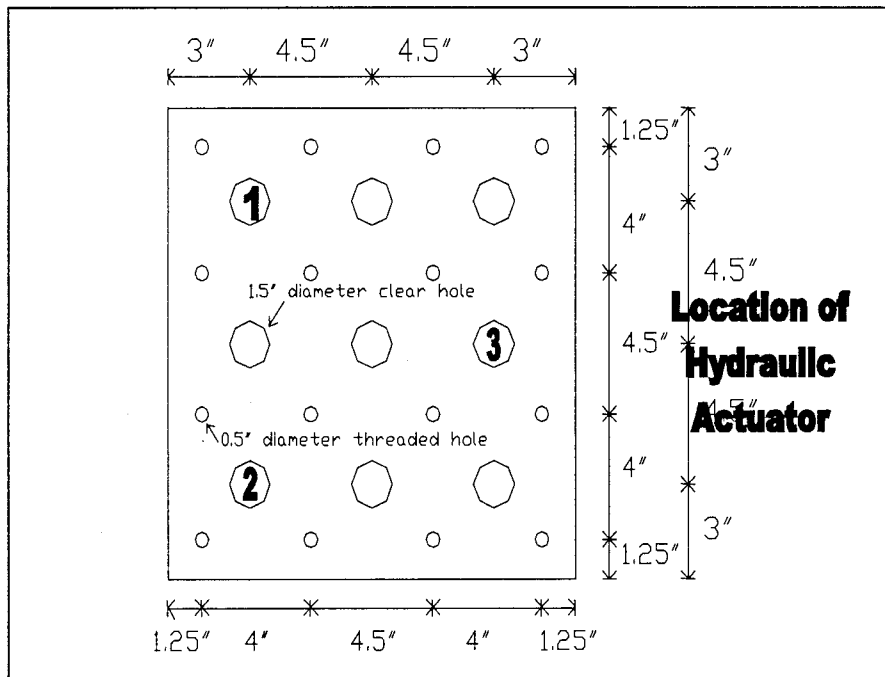


Figure 2.15. Rod Location for Tests 2 through 5

Instrumentation and Applied Load. Several linear variable differential transducers (LVDTs) and strain gauges were deployed on steel rods as indicated in Figures 2.16 through 2.18. The LVDTs were used to measure longitudinal displacement of the damper at the top plate, which is in the same plane of motion as the hydraulic arm. The strain gauges were utilized to measure the longitudinal and transverse strain. The HP

VXI Unit, depicted in Figure 2.11, was used to generate the progressive displacement as shown in Figure 2.19 to control the movement of the hydraulic actuator.

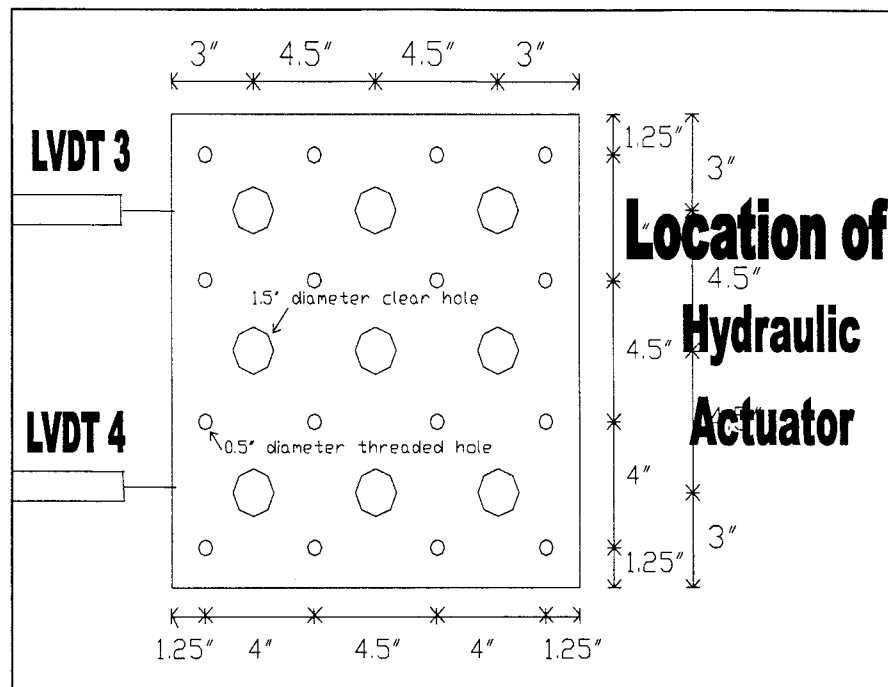


Figure 2.16. LVDT Location on Top Plate of Full-Scale Damper for Tests 1-3

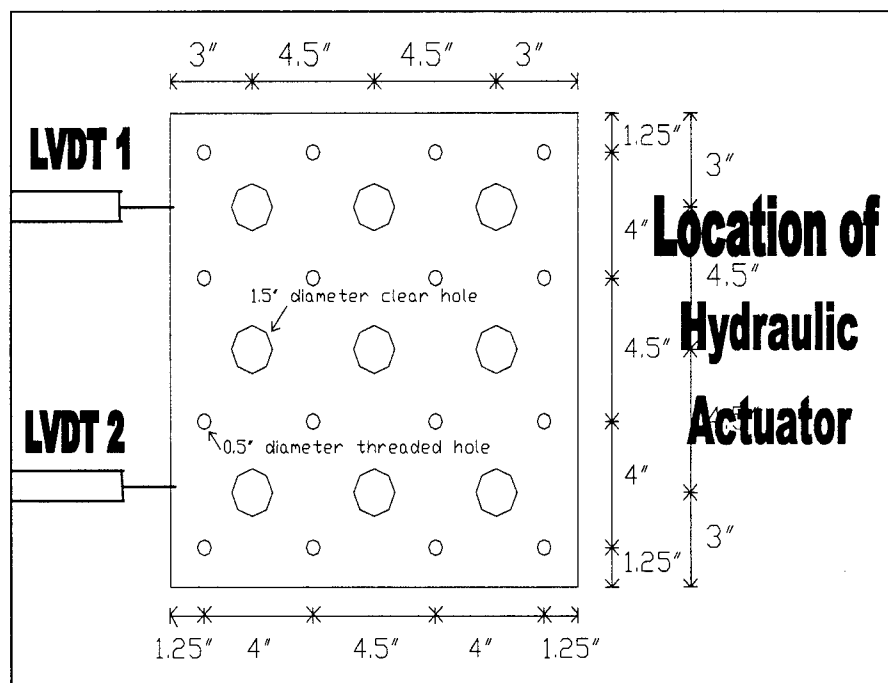


Figure 2.17. LVDT Location on Top Plate of Full-Scale Damper for Tests 4 and 5

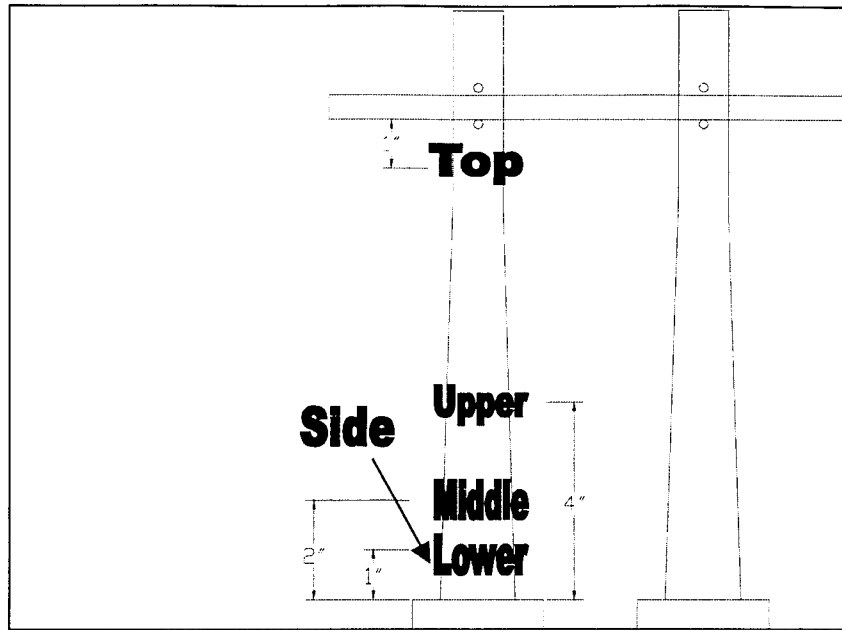


Figure 2.18. Strain Gauge Location on Full-Scale Damper

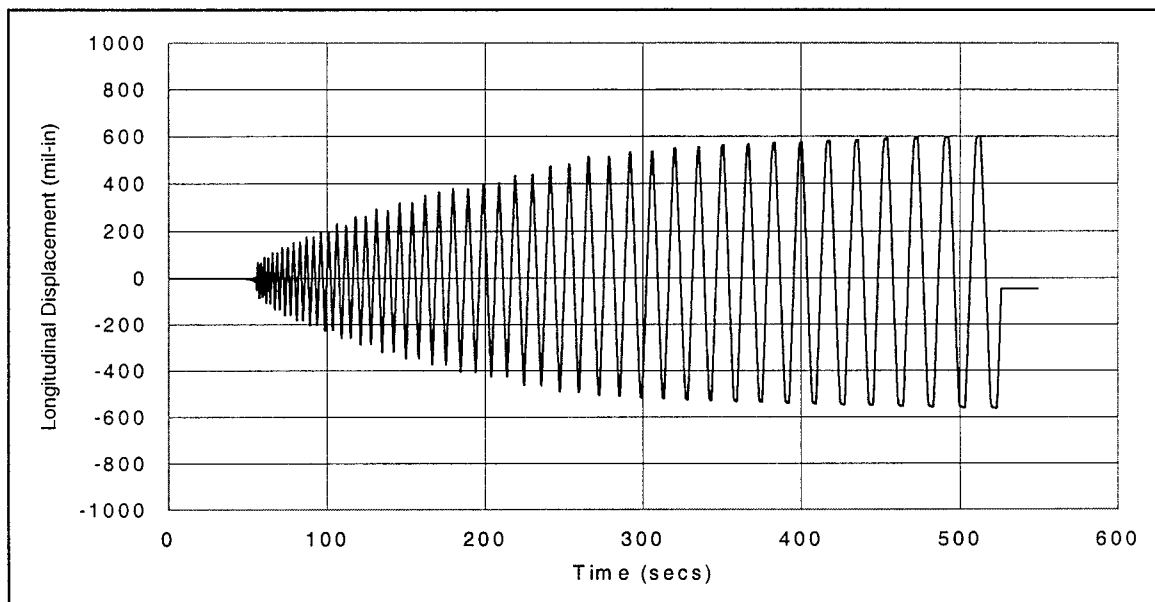


Figure 2.19. Input Data Generated by HP VXI Unit for Full-Scale Damper Tests

2.4 Results and Discussion of Full-Scale Damper Tests

This section mainly summarizes in detail the results from the test of full-scale Damper 1. They are representative of the other tests. Test results of the other dampers are included in Appendix A. The load-longitudinal displacement loop is presented in Figure 2.20 for Test 1. It can be observed that the hysteresis curve is almost symmetric about the origin. The area enclosed by the hysteresis loop represents the energy

dissipation of the tested damper. Although tested up to a ± 0.6 inch longitudinal deflection of the top plate, the damper did not yield significantly and thus the hysteresis loop was not as fat as expected. There are two reasons for this discrepancy. First, the slack in the connections of the test fixture absorbed about 0.35 in without applying any load on the steel rods. Secondly, after the test, it was found by tensile tests that the steel material used for Damper 1 had a yield stress of about 86 ksi as indicated in Figure 2.21. As a result, the damper did not yield substantially. Nevertheless, the test results show the steady development of the hysteresis loop, in Figure 2.20, as the input displacement increases.

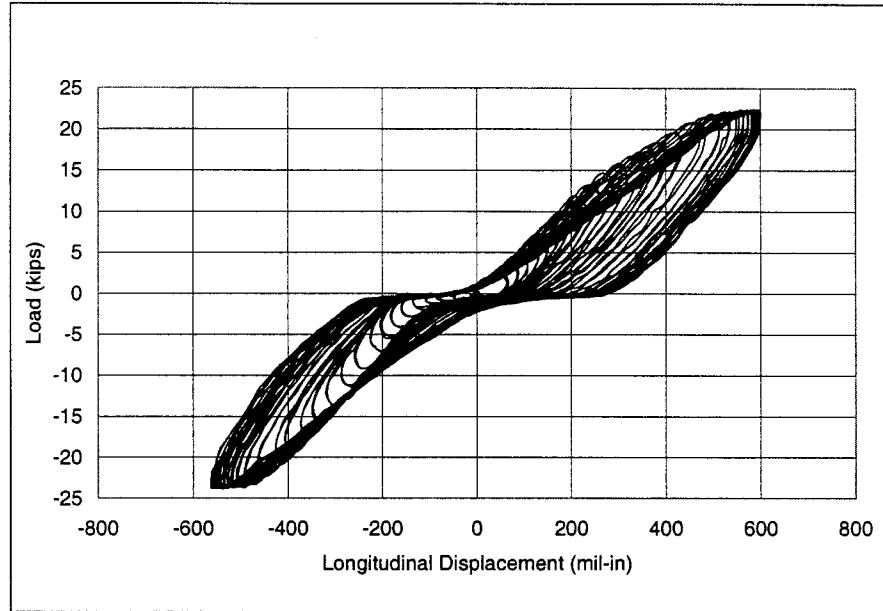


Figure 2.20. Load vs. Longitudinal Displacement of Damper 1

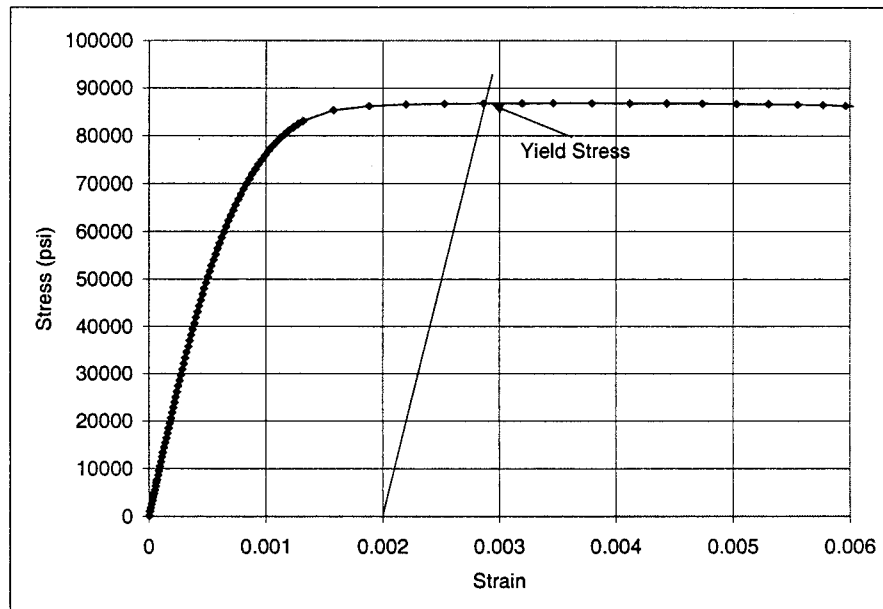


Figure 2.21. Stress-Strain Curve of Steel Rods

It is noted that the curve is "pinched" at the middle. This is due to the fact that there is slack in the connection between the hydraulic actuator arm and the damper so that there is movement around zero loading as discussed earlier,. There may also have been some slack at the connection between the rods and the base plate. It was noticed that the bolts connecting the bars to the base plate were loose during removal of the damper. It was this slack that caused a slight stiffness reduction as can be inferred from Figure 2.20. However, no material degradation occurred since the stiffness of the unloading portion of the load-displacement curve remained constant. All the factors contributing to the slack of the test setup can be removed in real applications by casting the steel rods and the bottom plate at one time and tightly bolting the top plate to a bridge member.

Due to the looseness in the connection of the test fixture, it may be more interesting to examine the load-strain curves. Figure 2.22 depicts the strain level at the bottom and side surface of bar 2. Figures 2.23-2.25, respectively, show the load-strain relation of the front surface of Bar 2 at the upper, middle and lower strain gauges.

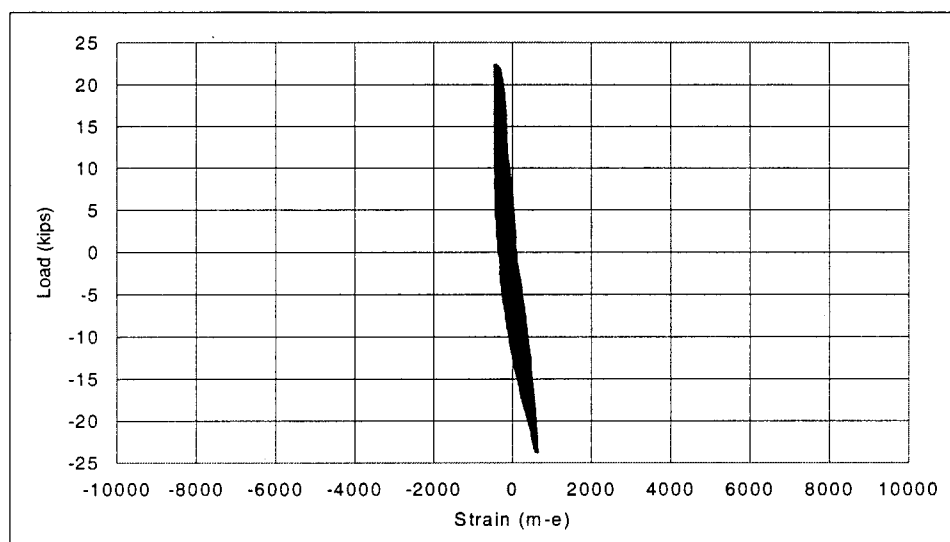


Figure 2.22. Load vs. Strain, Side Gauge of Damper 1

By inspection of Figure 2.22, one can see that the maximum transverse strain encountered from the test of Damper 1 is significantly less than 1000 micro-strain. This is 5 to 8 times smaller than the strain measured on the front of the bar as seen in Figure 2.25. This result indicates that the transverse movement of the damper assembly is negligible as the damper is only subjected to longitudinal load. As one can see from Figures 2.23-2.25, the strain level increases rapidly as the point of interest moves down the steel rods. The fat loop shown in Figure 2.25 indicates much larger energy dissipation at the bottom of the steel rods. To have a better understanding about the range where yielding has occurred, the maximum strain of the cross sections is presented in Figure 2.26 as a function of bar height for Damper 1 and Damper 4. The yielding strain (approximately equal to 2800 micro-strain) observed from the test data is also shown in the figure. For Damper 1, one can see that only the bottom 2.3 in. of bar experiences yielding at the test loading level. For Damper 4, about 5.0 in of the bar has

yielded at the same level of applied displacement, indicating an improved energy dissipation capacity. This result agrees with the theoretical analysis in Section 2.1. It is noted that, for the tapered rods, the strain level is higher for the middle gauge than for the lower gauge. This is because a linearly tapered bar shown in Figure 2.5, has a smaller diameter at the location of the middle gauge than the optimal diameter given by Eq. (2.4). It is worth noting that the strain levels at the top of the steel rods were also monitored and indicates a negligible strain at this location. This result confirms the pin condition in the test setup.

To quantify the energy dissipation capability of the dampers, the area of each hysteresis loop from the test results is presented as a function of the applied displacement in Figure 2.27. It can be clearly observed that the hysteresis loop area (dissipated energy) increased nonlinearly with the level of applied displacement. At the same displacement, the five-bar damper (Damper 1) dissipated more energy than the other straight-bar dampers (Dampers 2 and 3). However, it dissipated less energy than the three-tapered-bar damper (Damper 4) as the displacement increased.

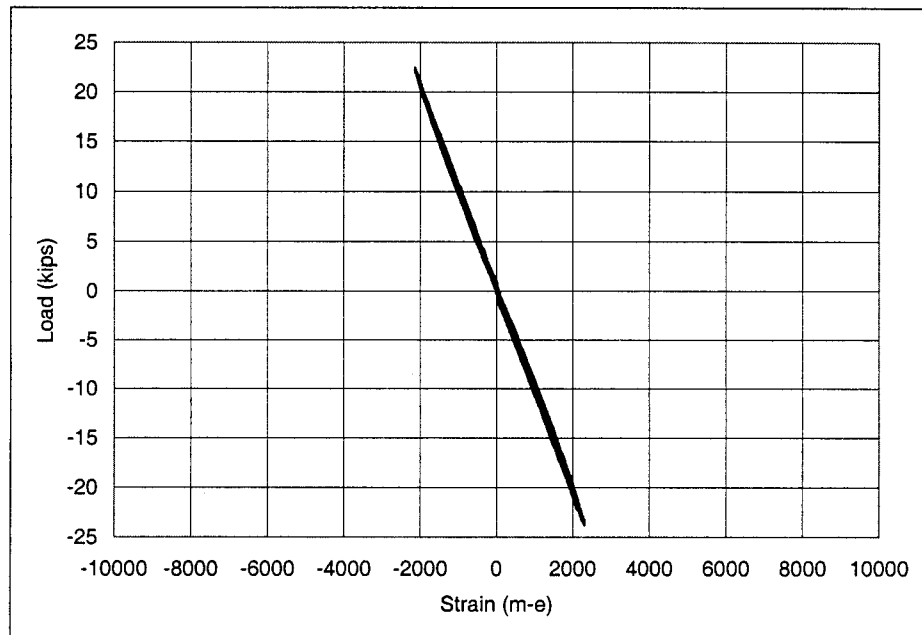


Figure 2.23. Load vs. Strain, Upper Gauge of Damper 1

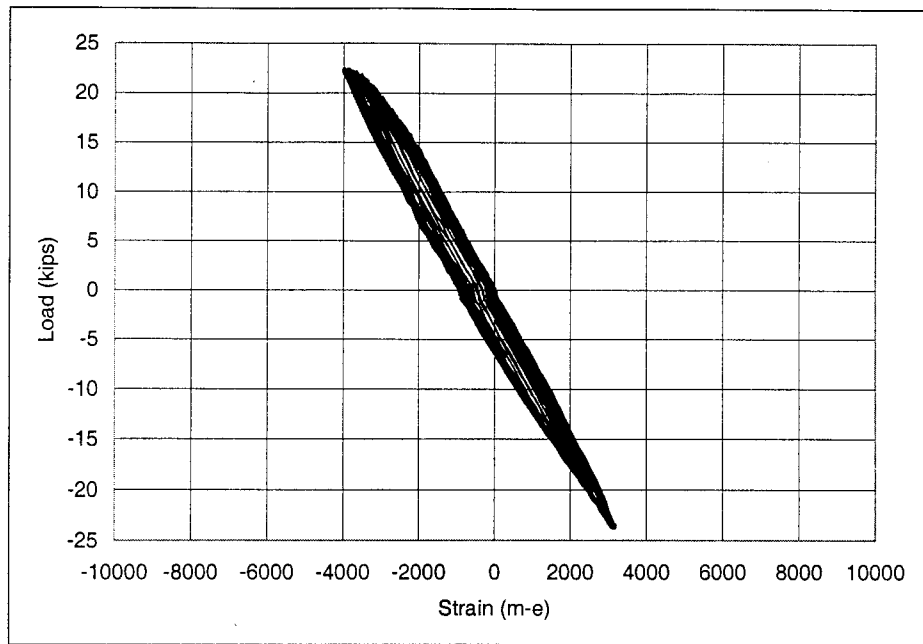


Figure 2.24. Load vs. Strain, Middle Gauge of Damper 1

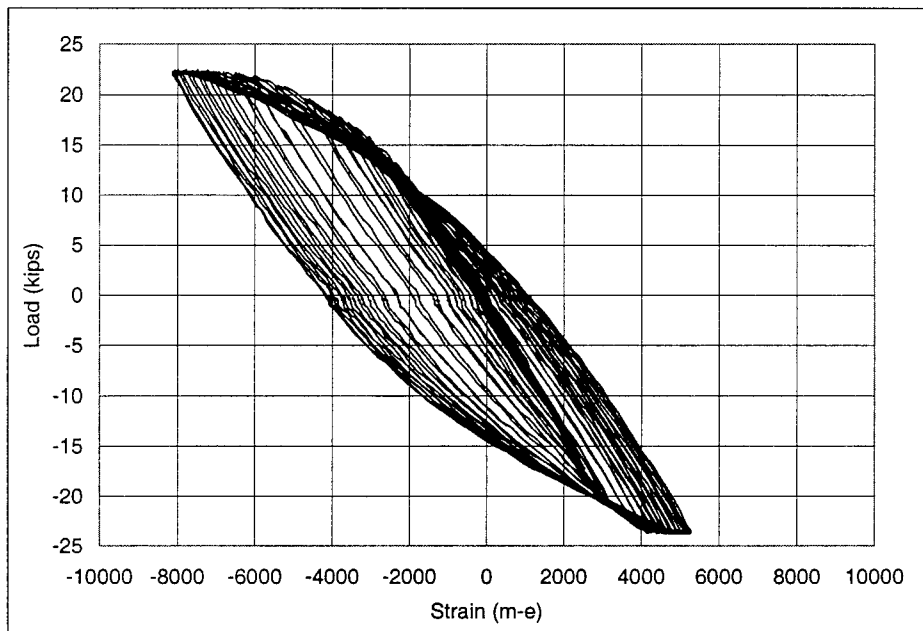


Figure 2.25. Load vs. Strain, Lower Gauge of Damper 1

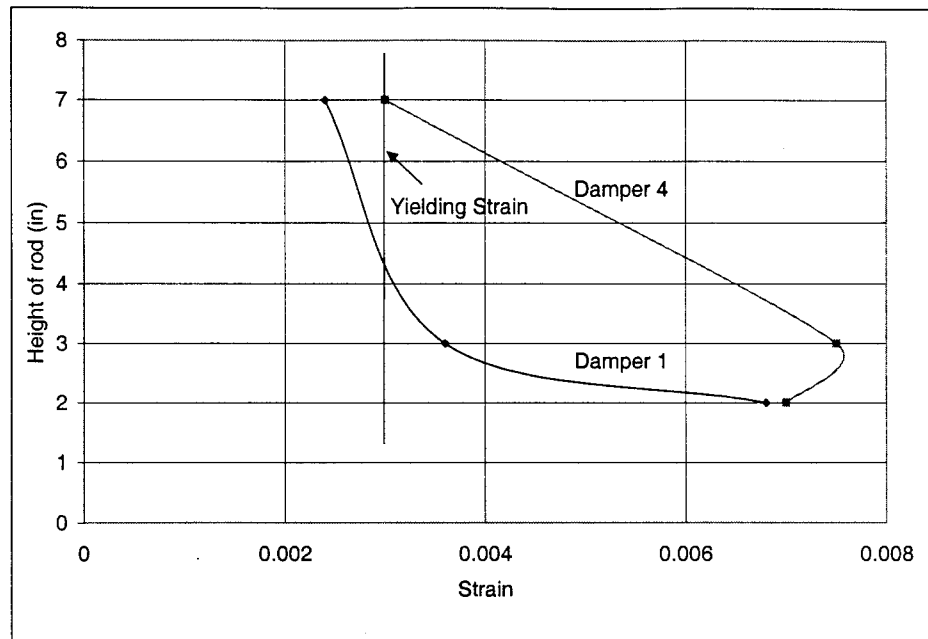


Figure 2.26. Height of Bar vs. Total Strain of Dampers 1 and 4

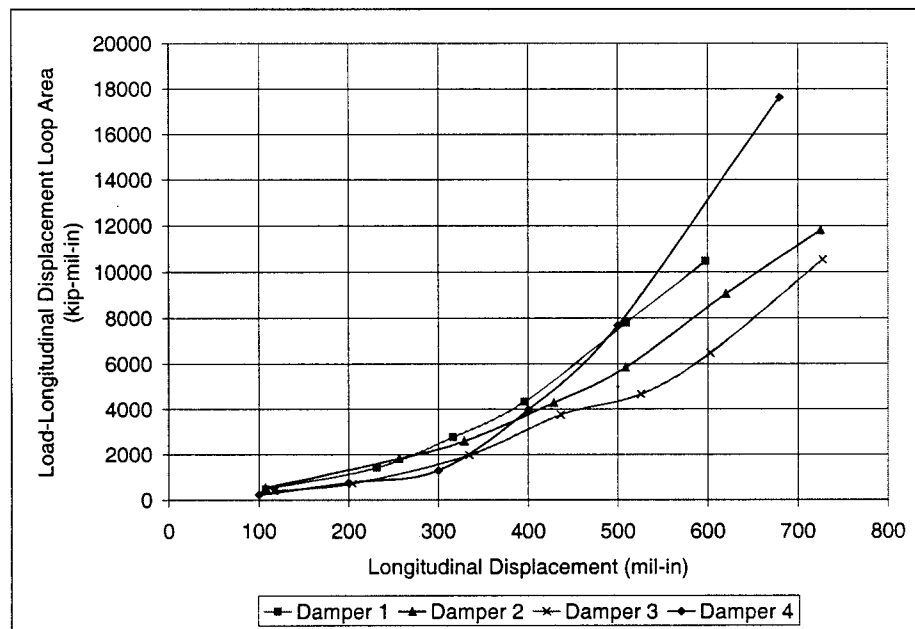


Figure 2.27. Load-Longitudinal Loop Area vs. Load, Full-Scale Damper

In structural dynamics, it is more relevant to see the change of damping ratio instead of the dissipated energy. Therefore, Figure 2.27 is reproduced in Figure 2.28 as a damping ratio between the dissipated energy and the elastic energy stored in the damper. The formal definition of the equivalent viscous damping ratio is,

$$\xi_S = W_D / 4\pi W_S \quad (2.11)$$

where W_D and W_S denote the energy dissipated per cycle and the elastic energy stored in the damper, respectively.

It can be seen from Figure 2.28 that for Dampers 1 through 3, the damping ratio decreased under small displacement and then increased slowly with the applied displacement. The initial decrease in damping ratio is mainly due to the small elastic energy at small displacement. However, the overall variation of the damping ratio is not significant, especially for large displacement. Therefore, for practical applications, it can be considered as a constant. As a conservative estimation, $\xi_S = 0.1$ is recommended for straight-bar dampers in bridge applications. It can also be seen that the damping ratio for Damper 4 increases significantly for larger displacements. This can be expected for tapered rods, as they are capable of dissipating more energy than straight rods.

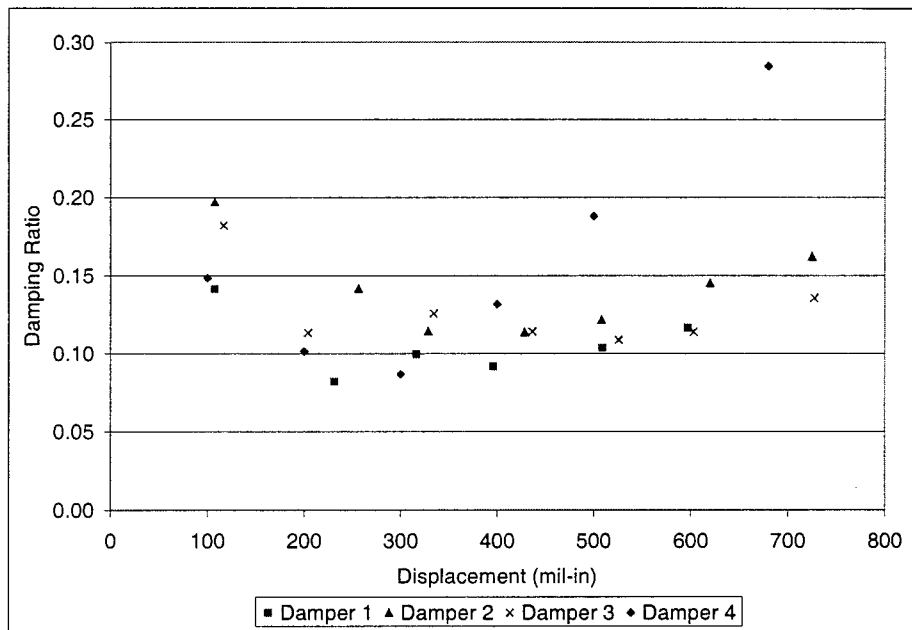


Figure 2.28. Damping Ratio vs. Displacement

To see the consistency of the test results, the load and displacement at the top of the dampers corresponding to 0.0028 strain at the bottom of the bars are compared in Table 2.1 for four dampers. It can be seen that the first damper of five straight rods and the second damper of three straight rods experienced similar displacement and their loads are proportional to the number of bars. Compared with Damper 2, the fourth damper of three tapered rods experienced a larger displacement. This results from the additional flexibility due to tapering of the bars. The strain readings for Damper 3 seem unusual due to the attachment and wiring of the strain gauges, and thus they are not included in Table 2.1.

Table 2.1. Summary of Results for the Full-Scale Dampers

Test	Number of Bars	Load at Initial Yielding (kips)	Disp. at 0.0028 Strain Level (in)
1*	5	20	0.40
2*	3	12	0.38
3*	3	---	---
4**	3	10	0.41

*Straight Rods

**Tapered Rods

---Data Not Available

2.5 Summary

Based on a series of tests on four full-scale dampers, the following observations can be made:

1. No significant stiffness degradation was observed in the test range and the hysteresis loop of the metallic dampers was steadily developed. A reasonable energy dissipation capability of the dampers was observed even at a small loading level. Although metallic dampers dissipate energy by yielding, their equivalent viscous damping ratio slowly changed with the applied load for straight-bar dampers. For practical applications, the damping ratio can be considered as a constant. Test results have indicated that for straight rods a 10 percent damping with respect to the damper stiffness can be used for pinned-fixed steel rods in bridge design. More tests on tapered rods may be necessary to establish a conclusive relation between the equivalent damping ratio and applied displacement for practical design.
2. Performance of the dampers was consistent with respect to load and displacement. As expected, the load each damper carried at the same lateral displacement is proportional to the number of rods. At the same applied load, the damper with tapered rods experienced more displacement. The tapered rods thus dissipated more energy than the straight rods. This difference in energy dissipation would most likely increase with the applied displacement.

3. TECHNICAL APPROACH AND EVALUATION OF A SMALL-SCALE BRIDGE

3.1 Recommended Procedure for Design of Metallic Dampers

The test results presented in Section 2 have indicated that the metallic dampers are promising in dissipating energy and thus reducing the seismic responses of bridges. The following ultimate strength design method is proposed to design such dampers for applications to steel girder highway bridges.

Step 1. Determine/evaluate the plastic moment, M_p , at the bottom of the new/existing fixed pier.

Step 2. Determine the maximum yielding force, $P_{y\max}$, of the damper and select the rod size. To ensure the damper yielding prior to the formation of a plastic hinge at the bottom of the fixed pier, the maximum yielding force of the damper unit can be computed by,

$$P_{y\max} = M_p / \alpha L \quad (3.1)$$

with the assumption that earthquake loads are only transferred through the damper. Here, L is the height of the fixed pier; α is the steel overstrength factor and usually assigned to be 1.3 for design purposes. The size of the damper unit is determined based on the force $P_{y\max}$.

Step 3. Check for longitudinal forces due to non-seismic loads.

$$\beta_s Q_{\max} < P_{y\max} \quad (3.2)$$

where Q_{\max} is the maximum longitudinal force of all load combinations in AASHTO (1996) due to non-seismic loads, β_s (>1.0) is the factor on the non-seismic loads to ensure the damper will behave elastically under these loads.

Step 4. Evaluate the maximum displacement of the superstructure under a design earthquake. Use the equivalent viscous damping ratio determined by Eq. (2.11) and then calculate the reduction factor, R_f , of the seismic displacement at the bridge deck from the design response spectrum corresponding to 5% damping ratio. The maximum displacement of the bridge deck without pounding action at expansion joints under the design earthquake is determined to be,

$$d_{\max} = (T^2 / 4\pi^2) (S_a / R_f) \quad (3.3)$$

$$R_f = [\xi(1 - e^{-0.05B}) / (0.05(1 - e^{-\xi B}))]^{0.5} \quad (3.4)$$

where S_a is the spectral acceleration at the effective bridge period, T , with inelastic behaviors of the damper unit considered; $B = 18$ for the upper bound and 65 for the lower bound (Hanson et al, 1993) and ξ is the equivalent damping ratio due to the damper unit.

Step 5. Design for ductility. The ductility demand is determined by,

$$\mu_D = d_{\max} / d_y \quad (3.5)$$

where d_y is the yielding displacement of the damper. The final check for a sound design of a damper is to ensure sufficient ductility as follows,

$$FS \cdot \mu_D < \mu_C \quad (3.6)$$

in which μ_C is the ductility capacity of the designed damper and FS is the factor of safety for ductility design. Both parameters must be determined in consultation with the owner of the bridges, the Missouri Department of Transportation for this study.

3.2 Design and Fabrication of a Small-Scale Bridge and Dampers

Based on the discussion with engineers at the Missouri Department of Transportation, the small-scale bridge was designed to simulate the three-span continuous bridge A-237 in New Madrid County, Missouri. Since the bridge deck was designed for gravity loads and it was substantially stiffer than a bridge column, the bridge model was simplified into a single span with cantilevers at both ends to fit into the test facility. The concrete bridge deck is 7 feet long, 3 feet wide, and 3½ inches thick. Both width and height of the model is approximately 1/10 those dimensions of Bridge A-237, respectively. The bridge model is therefore referred to as a 1/10-scaled model.

Design of Bridge Members. The design of the bridge members was based on a 1.6 k-ft moment at the column base that was estimated from the seismic load on the bridge superstructure (AASHTO, 1996). A 6"×10"×½" base plate was used to connect the bridge columns to the shake table with ¾" diameter A325-N bolts. The substructure was composed of W8x15 columns and T5x5x½ beams. The concrete bridge deck rested on two W8x15 girders. Two W5x16 crossbeams were connected to the W8x15 girders with 2L3x3x¼ and ¾" diameter A325-N bolts. A 5"×10"×1" plate was used to attach a metallic damper to the W5x16 crossbeam with ½" diameter A325-N bolts. Figures 3.1-3.4 show the final design of the small-scale bridge.

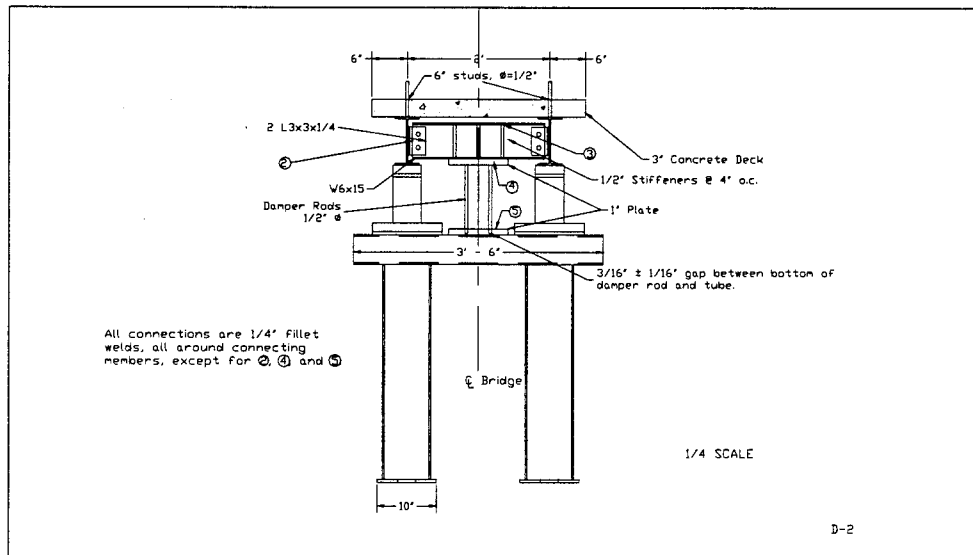


Figure 3.1. Side View, Small-Scale Bridge

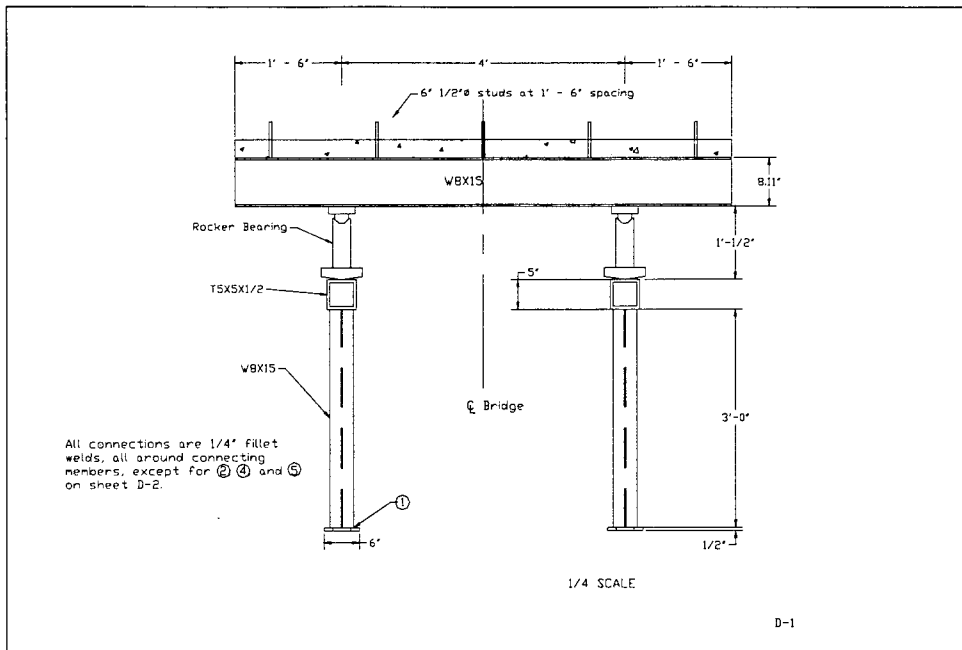


Figure 3.2. Front View, Small-Scale Bridge

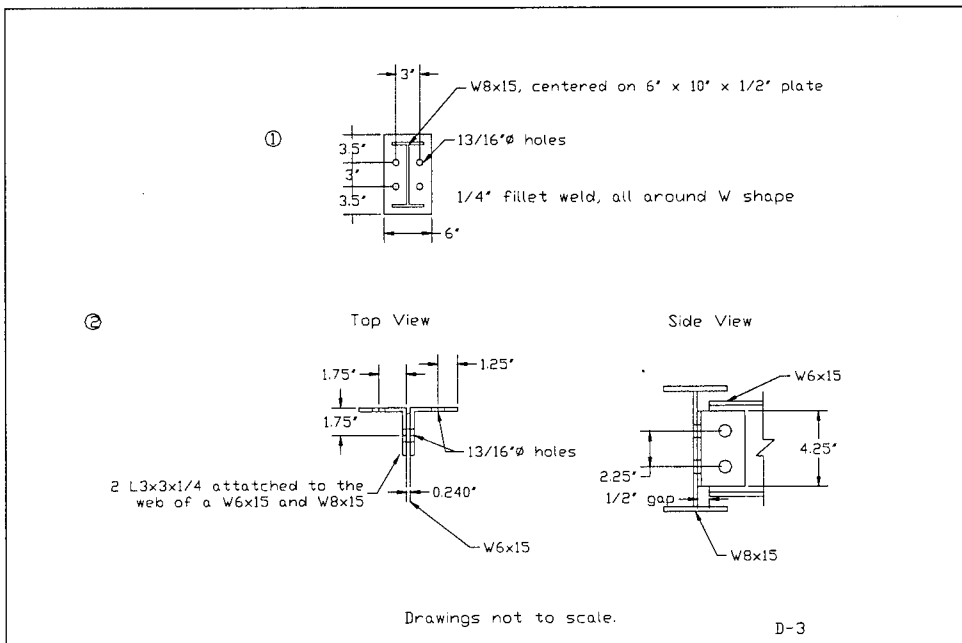


Figure 3.3. Connection Details, Small-Scale Bridge

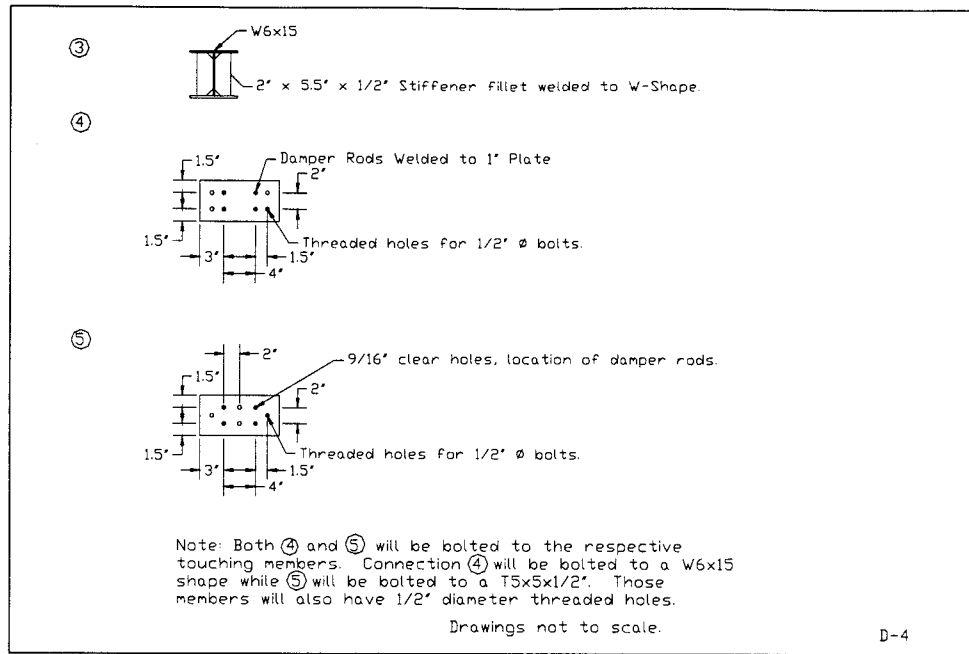


Figure 3.4. Connection Details, Small-Scale Bridge (Cont'd)

Design of a Small-Scale Damper. A small-scale damper unit was designed using the proposed procedure in Section 3.1. The superstructure consisted of a concrete deck and two steel girders as shown in Figure 3.1. The bridge deck measured 7'x3'x3½" with a unit weight of 150 pcf. The weight of the concrete, W_C , was 920 lbs. The weight of the two W8x15 Girders, W_{W8x15} , was 210 lbs. Also, a miscellaneous weight, $W_M = 10$ lbs, was included to account for the shear studs and the top damper plate. The total weight was,

$$W_T = W_C + W_{W8x15} + W_M = 1140 \text{ lbs} \quad (3.7)$$

1) Determine the plastic moment at the column base. Only the web portion of the column, shown in Figure 3.5, was considered in the calculation of plastic moment for better representation of the reinforced concrete column in the prototype bridge, A-237 in New Madrid County. The dimensions of the column web were $b = 8.11$ in and $h = 0.245$ in. The plastic section modulus of the web can be calculated by,

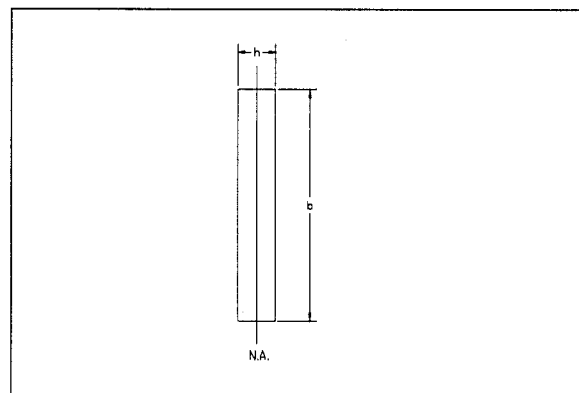


Figure 3.5. Web Portion of Columns

$$S_p = (b)(h/2)(h/2) = 70.43 \times 10^{-6} \text{ ft}^3 \quad (3.8)$$

Therefore the plastic moment of the web section can be determined by,

$$M_p = S_p f_y \quad (3.9)$$

The yielding stress of the column, f_y , was assumed to be 100 ksi. Eq. (3.9) therefore gave rise to $M_p = 1014 \text{ ft-lbs}$

2) Determine the maximum yielding force of the damper rods. Consider the steel overstrength factor, α , to be 1.3 and the height of the substructure, L , equal to 41 in as shown in Figure 3.2. Using Eq (3.1), for two columns,

$$P_{y\max} = 2M_p/\alpha L = 457 \text{ lbs} \quad (3.10)$$

Steel rods were considered as fixed-pinned members with ℓ equal to 11 inches as illustrated in the scale bridge details, Figure 3.1 through Figure 3.4. By following the derivation of Eq. (3.8), the plastic section modulus of a circular rod can be expressed into,

$$S_p' = (\pi d^2/8)(4d/3\pi) = d^3/6 \quad (3.11)$$

From Eq (3.9), the plastic moment for 2 rods is,

$$M_p' = 2(d^3/6)f_y \quad (3.12)$$

where $M_p' \leq P_{y\max}\ell$ or $d \leq 0.532 \text{ in.}$ Use $d = 0.5 \text{ in.}$

3) Check for longitudinal forces due to non-seismic loads. This step is not applicable to this test because the bridge model was tested under ground motions only.

4) Evaluate the maximum displacement of the superstructure under a design earthquake. The moment of inertia for a circular section was calculated using Eq. (2.2) as $I = 3.07 \times 10^{-3} \text{ in}^4$. With the modulus of elasticity $E = 29,000 \text{ ksi}$, the yielding displacement of the pinned-fixed rods can be computed by,

$$d_y = 2f_y\ell^2/3Ed = 0.556 \text{ in.} \quad (3.13)$$

To determine the maximum elastic displacement of the damper, the bridge column was assumed rigid. The stiffness of bridge along the traffic direction, contributed by two rods, can be determined by

$$k_r = 2(3EI)/\ell^3 = 401 \text{ lb/in} \quad (3.14)$$

The natural frequency and period of the bridge can then be calculated respectively by

$$\omega = (kg/W_T)^{0.5} = 11.6 \text{ rad/sec} \quad (3.15)$$

$$T = 2\pi/\omega = 0.54 \text{ sec} \quad (3.16)$$

in which g is the gravitational acceleration, equal to 386 in/sec^2 . With the maximum spectral acceleration corresponding to 5% damping, S_a , under the 1940 El Centro Earthquake equal to 350 in/sec^2 , the maximum displacement was calculated by,

$$d_{\max} = S_a/\omega^2 = 2.579 \text{ in.} \quad (3.17)$$

or $d_{\max}/3 = 0.86$ in., which is greater than $d_y (=0.556$ in.). Therefore, two rods are likely yielding under the 1/3 scale El Centro Earthquake.

Since the steel rods were inserted into slightly oversized holes on the bottom plate as noted in Figure 3.4, they were actually subject to partial rotation restraint. To understand whether the steel rods actually yield during the 1/3 El Centro Earthquake, the designed damper was checked by assuming the rods being fully restrained in rotation at both ends. In this case, the yielding displacement of the rods was,

$$d_y = f_y \ell^2 / 3Ed = 0.278 \text{ in} \quad (3.18)$$

From Eq. (3.14), the stiffness was calculated to be,

$$k_r = 2(12EI)/\ell^3 = 1604 \text{ lb/in} \quad (3.19)$$

Using Eqs. (3.15) and (3.16), the vibration period became,

$$T = 2\pi/\omega = 0.27 \text{ sec} \quad (3.20)$$

Eq. (3.17) then gave rise to, $d_{\max} = S_a/\omega^2 = 0.645$ in. under the El Centro Earthquake or $d_{\max}/3 = 0.215$ in., which is less than $d_y (=0.278$ in.). It is unlikely that the damper will yield under this circumstance. Overall, the designed damper seems to experience a limited deformation and thus may or may not be yielding under the 1/3 El Centro earthquake. Since the 11-inch long steel rods of 1/2" in diameter are already slender, further reduction in diameter may not make the rods significantly dissipate energy even though they could possibly be yielded theoretically.

It should be noted that the original plan was to construct the damper rods out of low strength steel with $f_y=36$ ksi. It was found difficult to secure such a material in the project period in today's market. After several months of search, decision was made to use the so-called A36 steel rods from a steel factory. To determine the yield strength of the steel material, two tensile tests were conducted on specimens. The load-displacement curves were presented in Appendix C, indicating a yield strength of slightly over 100 ksi determined with the 0.2% Offset Method.

3.3 Testing of a Small-Scale Bridge

Test Setup. Experimental testing of the small-scale bridge was performed in the Engineering Research Laboratory at the University of Missouri - Rolla. The bridge model was fabricated at General Machine Shop in Rolla and assembled on the MTS shake table as illustrated in Figures 3.6 through 3.8. A four-rod damper was installed between cross beam and capbeam of the bridge pier as shown in Figure 3.9. Two accelerometers were attached to the girders as shown in Figure 3.10. Two data acquisition systems were used for these tests. The data acquisition shown in Figure 3.11 was used to measure strains on the damper and bridge columns. The HP VXI machine, shown in Figure 3.12, was used for acquiring acceleration and deflection values. The VXI machine was also used to generate the 1940 El Centro and 1952 Taft Earthquake for the small-scale bridge tests.

The shake table used for the tests is 4 ft \times 7 ft in size and can support a maximum payload of 20 tons. It is effective in the frequency range of 0.01 to 10 Hz with a

maximum stroke of ± 1 inch. The MTS 406 controller for the shake table can generate sine waves for harmonic tests.

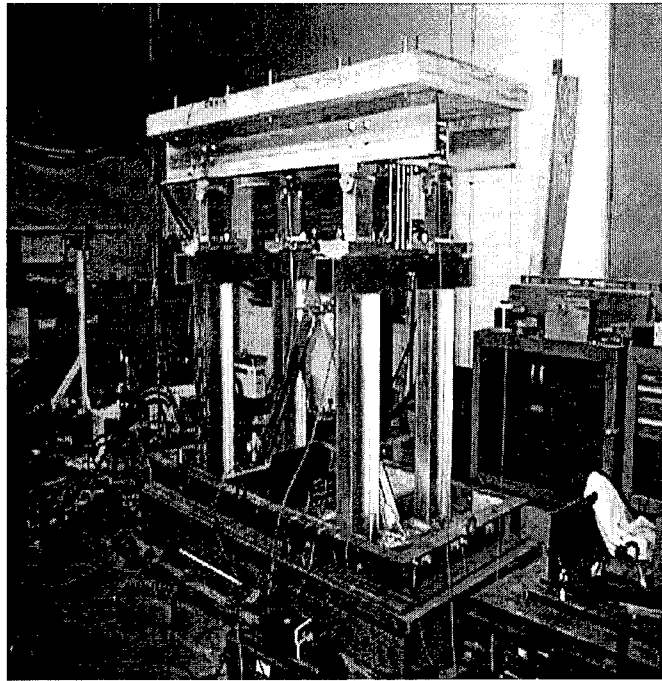


Figure 3.6. Front and Side Views, Small-Scale Bridge

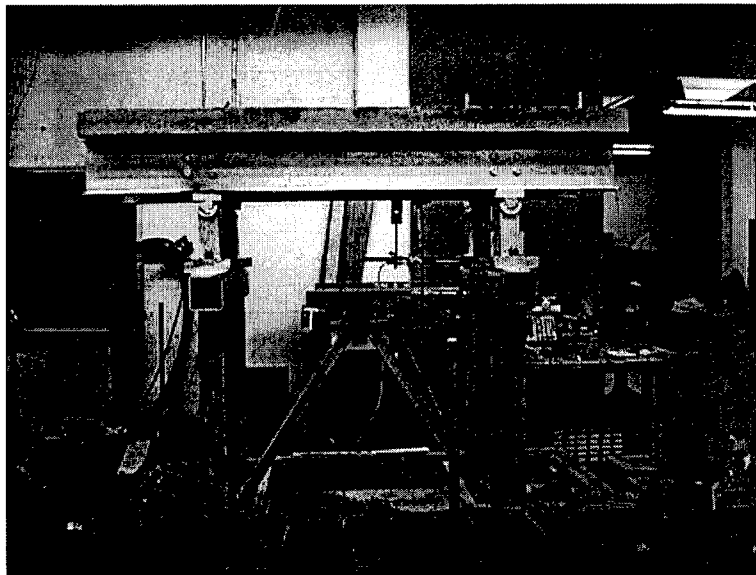


Figure 3.7. Front View, Small-Scale Bridge



Figure 3.8. Side View, Small-Scale Bridge

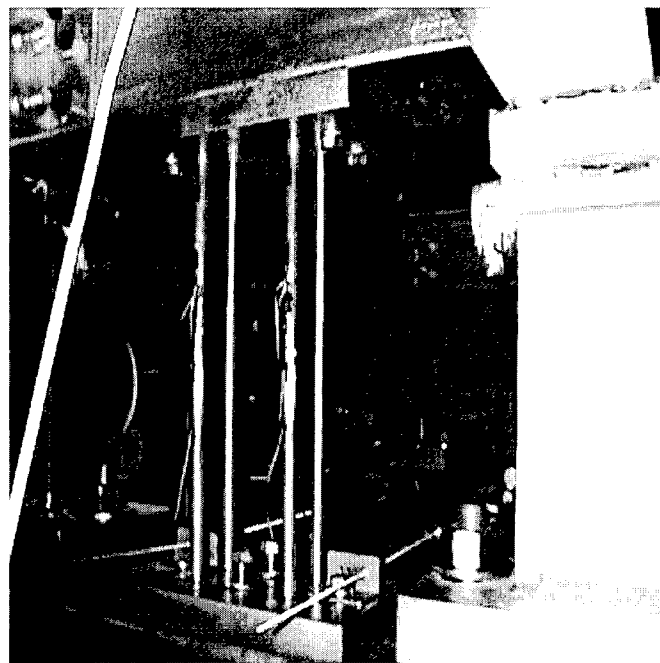


Figure 3.9. Small-Scale Damper with Strain Gauge and LVDT's

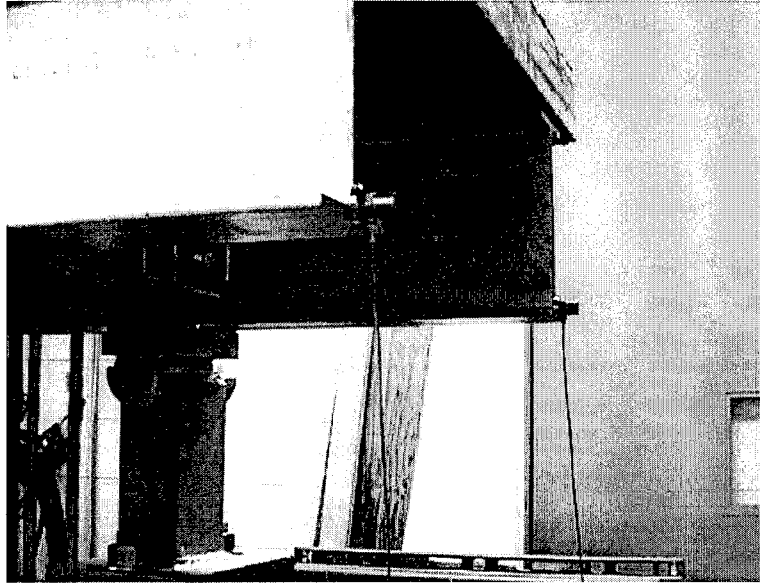


Figure 3.10. Accelerometers Attached to Girders



Figure 3.11. Data Acquisition Unit for Small-Scale Bridge

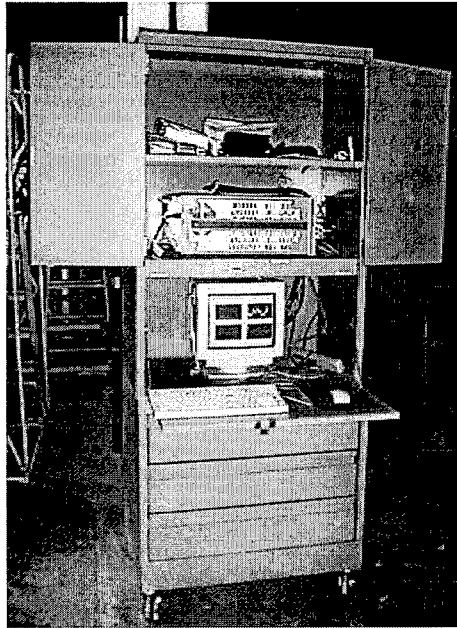


Figure 3.12. HP VXI Unit

LVDT, Strain Gauge and Accelerometer Location. Four strain gauges were attached to the steel rods of the small-scale damper as illustrated in Figure 3.13. Strain gauges 1 and 3 were six inches from the bottom of the upper damper plate. Strain gauges 2 and 4 were located one inch from the bottom of the upper damper plate. Strain gauges 5 through 10 were located near the column bases. Specifically, strain gauges 5, 6, 7 and 10 were attached two inches from the base plate on the column web and gauges 8 and 9 two inches from the base plate on the column flange as shown in Figure 3.14. Four accelerometers were deployed on the bridge model as illustrated in Figure 3.15. Accelerometer 0 was on the shake table, accelerometers 1 and 3 were located on the girders, and accelerometer 2 was located on the 5x5x1/2 structural tube. Relative distance between substructure and superstructure was measured with LVDTs 1 and 2 as shown in Figure 3.16.

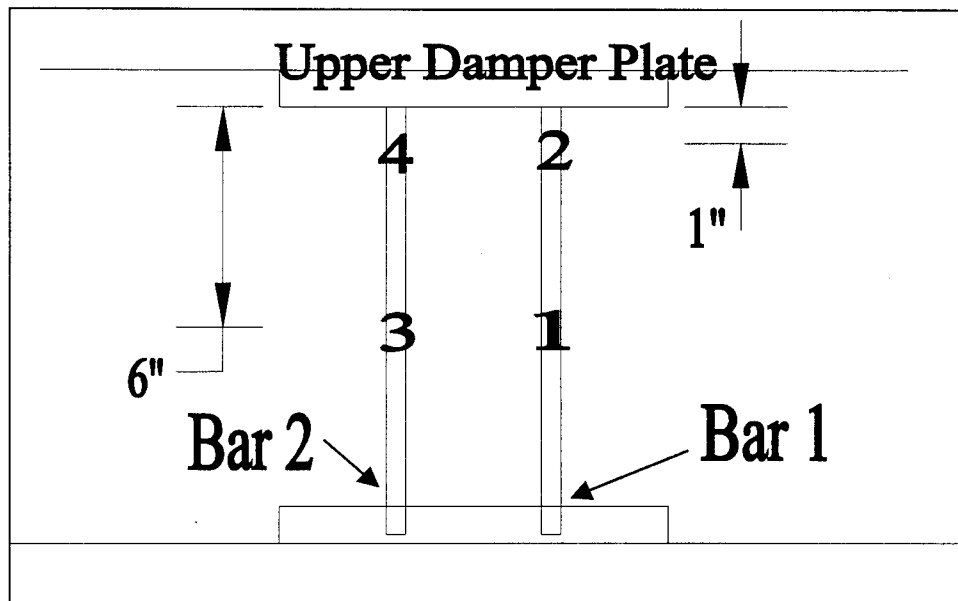


Figure 3.13. Strain Gauge Location on Small-Scale Damper

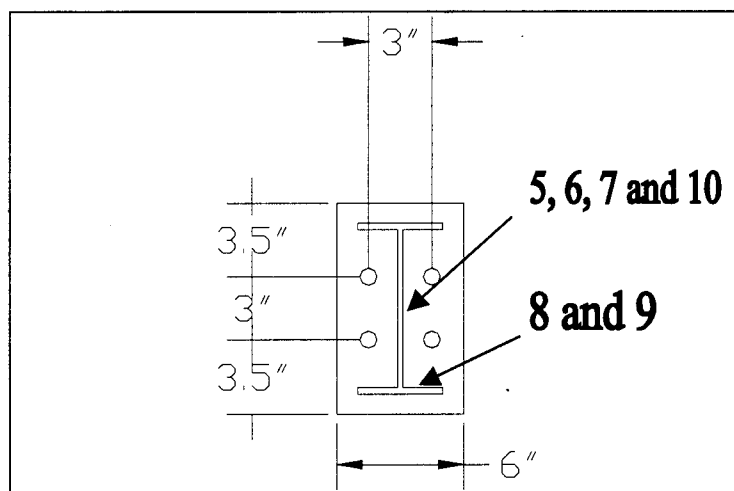


Figure 3.14. Strain Gauge Location on Column Base of Small-Scale Bridge

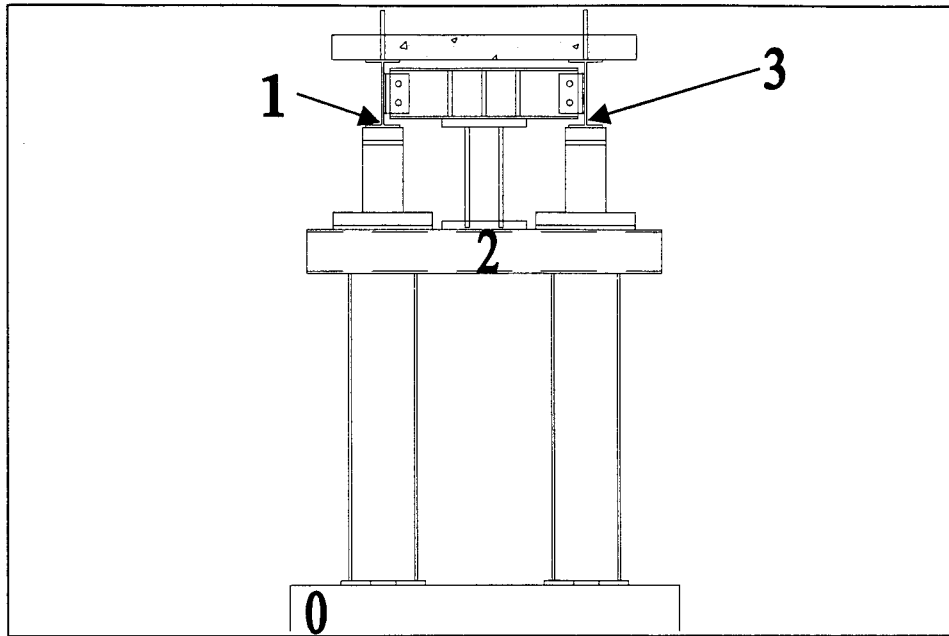


Figure 3.15. Accelerometer Location on Small-Scale Bridge

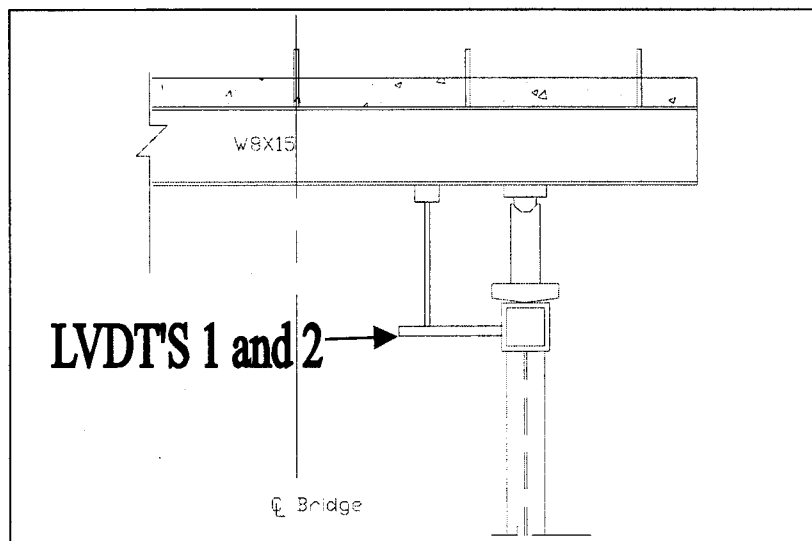


Figure 3.16. LVDT Location on Small Scale Bridge

Input Data. The bridge was subjected to three input types: the 1952 Taft Earthquake input, the 1940 El Centro Earthquake input and harmonic input. The Taft and El Centro earthquake records were scaled to a peak acceleration of 0.218g and 0.194g, respectively. These factors were determined by the maximum stroke (± 1 in.) of the shake table since the table is displacement controlled. Their time scale was compressed to approximately 1/2 and 2/5, respectively, to have their dominant frequency close to the natural frequency of the small-scale bridge model with the four-rod damper installed. The actual input to the bridge model was measured with accelerometer 0, located on the shake

table. These types of modified earthquake ground motions and harmonic excitation are presented in Figures 3.17-3.19.

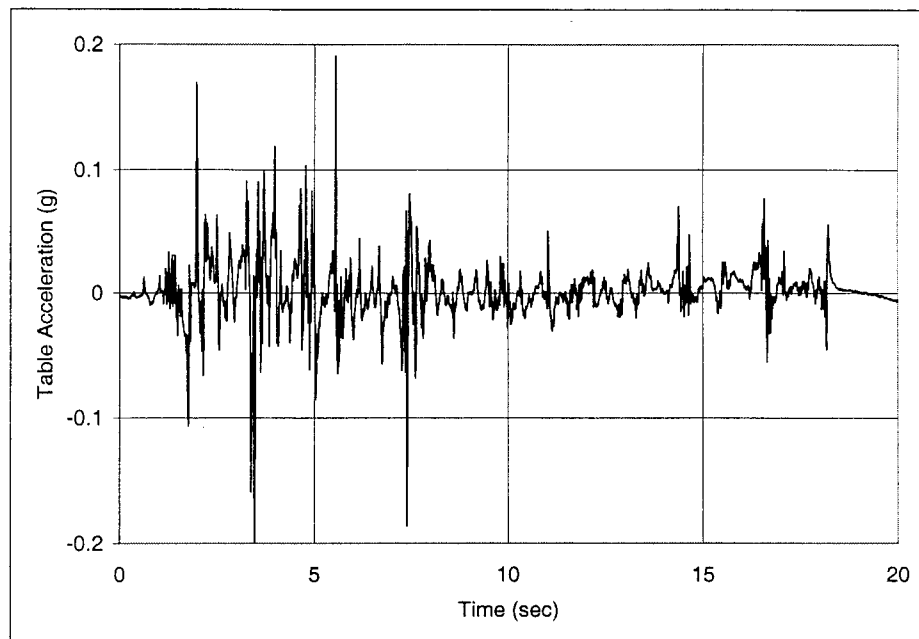


Figure 3.17. 1952 Taft Earthquake Input (Modified)

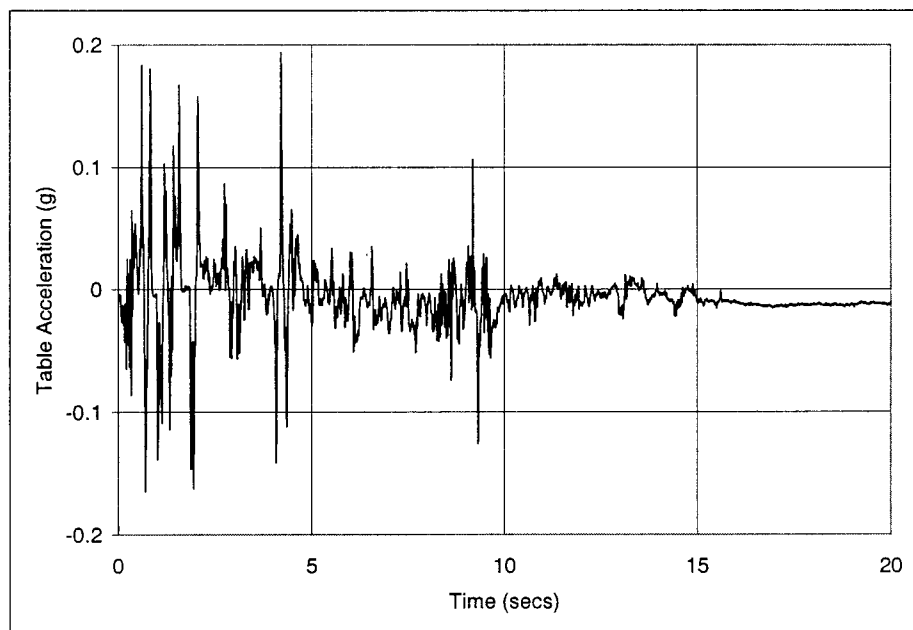


Figure 3.18. 1940 El Centro Earthquake Input (Modified)

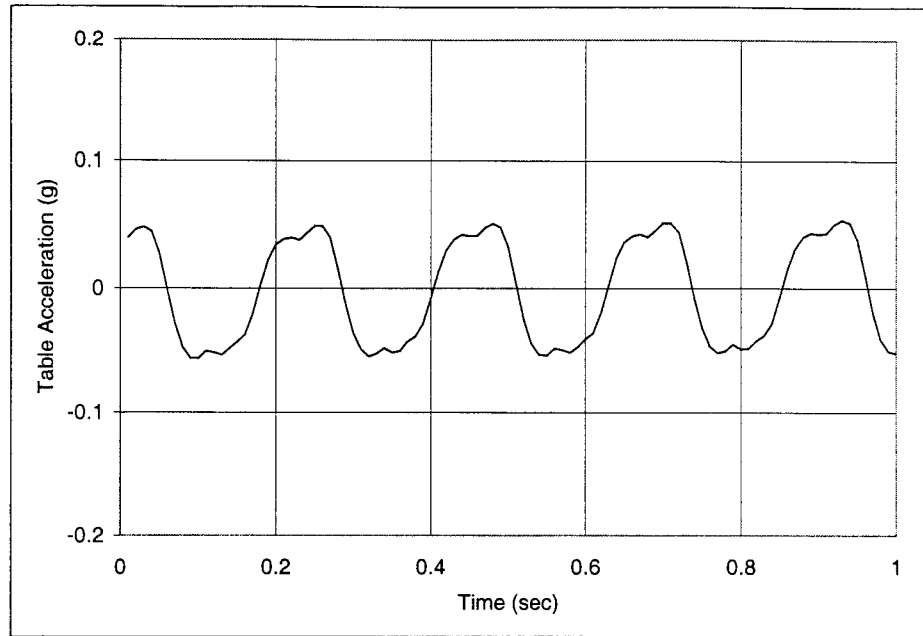


Figure 3.19. Harmonic Input

Test Procedure. The natural frequencies of the bridge model varied when different dampers were installed. The fundamental frequency of the bridge model was identified, first, by conducting a series of harmonic tests. The bridge model was then tested under the excitation of the modified Taft and El Centro earthquakes. Finally, a series of resonant tests were performed at different amplitudes of harmonic input with the intent of increasing the strain in steel rods.

3.4 Results and Discussion of Small-Scale Bridge Tests

A total of four small-scale dampers were tested in the Engineering Research Laboratory. Including the case without the damper on the bridge model, five test cases were planned in this study. The number of steel rods and their idealized support condition of various test cases are summarized in Table 3.1.

Table 3.1. Small-Scale Bridge Test Cases

Test	Number of Rods	Support Condition
Without Damper	N/A	N/A
Damper 1	4	fixed-pinned
Damper 2	2	fixed-pinned
Damper 3	2	fixed-fixed
Damper 4*	2	fixed-fixed

*1600 lbs of weight added to superstructure.

Dynamic Amplification Factor. The acceleration amplifications from the shake table to the girder of bridge with or without damper are referred to as acceleration amplification factors. They are respectively presented in Figures 3.20 through 3.23 for the bridge without damper, with Dampers 2, 3 and 4. It can be observed that the fundamental frequency of various test cases ranges from 3.5 to 4.25 Hz under a low level of excitation (± 0.1 " stroke at the shake table). In reference to Damper 3, Damper 2 is more flexible due to the pinned-fixed support condition. The bridge model with Damper 4 is also more flexible because of additional weight on the bridge deck. The measured fundamental frequencies confirm these intuitive relations. However, as the level of excitation increases, their frequency relation becomes more complicated since the friction of rocker bearings plays a more significant role in the vibration of the bridge system. The stronger the external disturbance, the more likely the bearings undergo sliding between pin and web, resulting in more energy dissipation by friction. At the same time, the superstructure is less restrained in horizontal direction by the web of bearings during the bridge vibration. Consequently, the peak acceleration amplification and its corresponding frequency decrease as can be clearly seen from Figures 3.21 -3.23. It is also observed that the acceleration amplification curve becomes flatter when the bridge receives stronger excitation, e.g. ± 0.3 " stroke at the shake table. This trend indicates the increase of damping effect due to the friction in rocker bearings. Indeed, it is speculated that the damping effect is so significant that the bridge system vibrates in a nonlinear fashion. The exception to the above trend is the acceleration amplification effect of the bridge model with bearings on the damper side pier fixed by tightening the rocker plate into the capbeam of the pier. The amplification factor is not decreasing when the external excitation becomes stronger though the frequency corresponding to the peak response is still reduced. This is mainly because the bridge system may not vibrate appreciably under this condition so that damping effect is almost the same at different levels of excitation as observed from Figure 3.20.

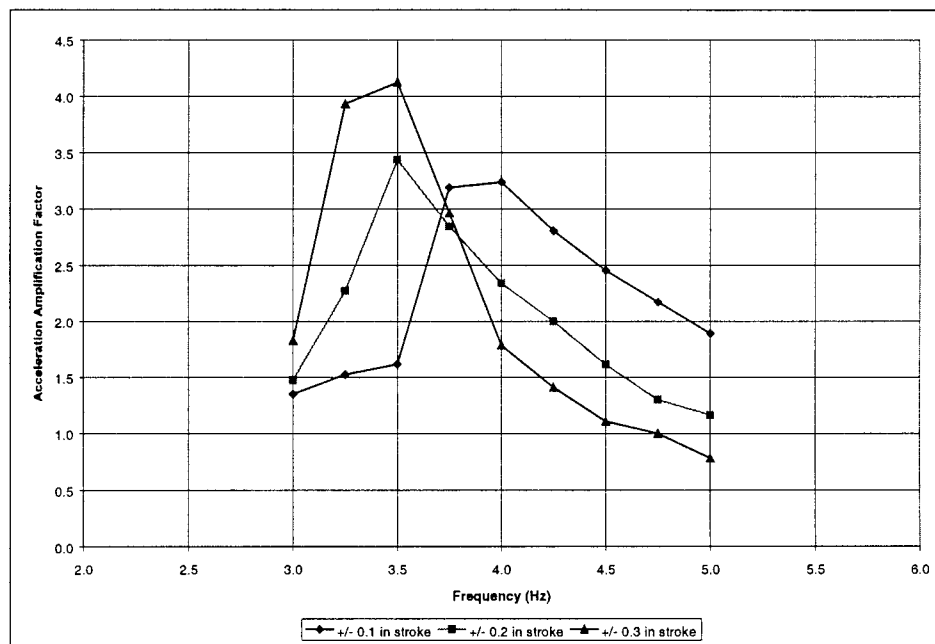


Figure 3.20. Acceleration Amplification Factor of Bridge without Damper

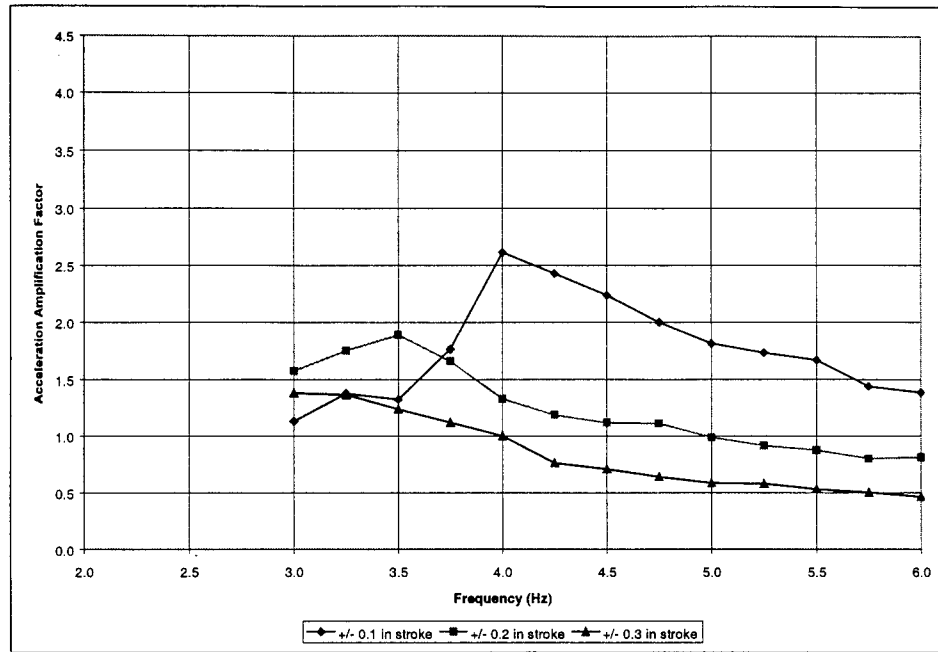


Figure 3.21. Acceleration Amplification Factor of Bridge with Damper 2

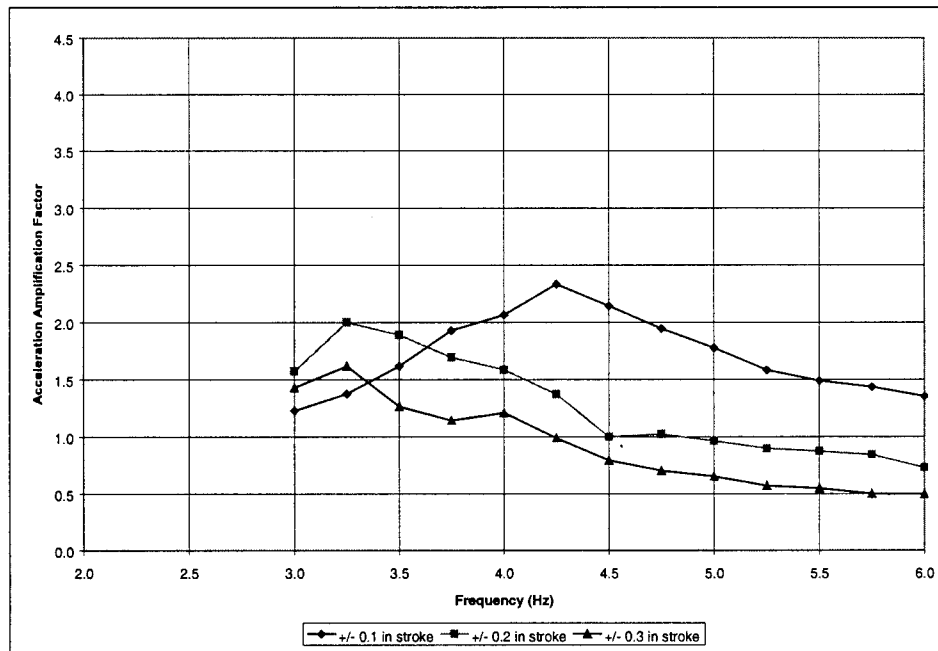


Figure 3.22. Acceleration Amplification Factor of Bridge with Damper 3

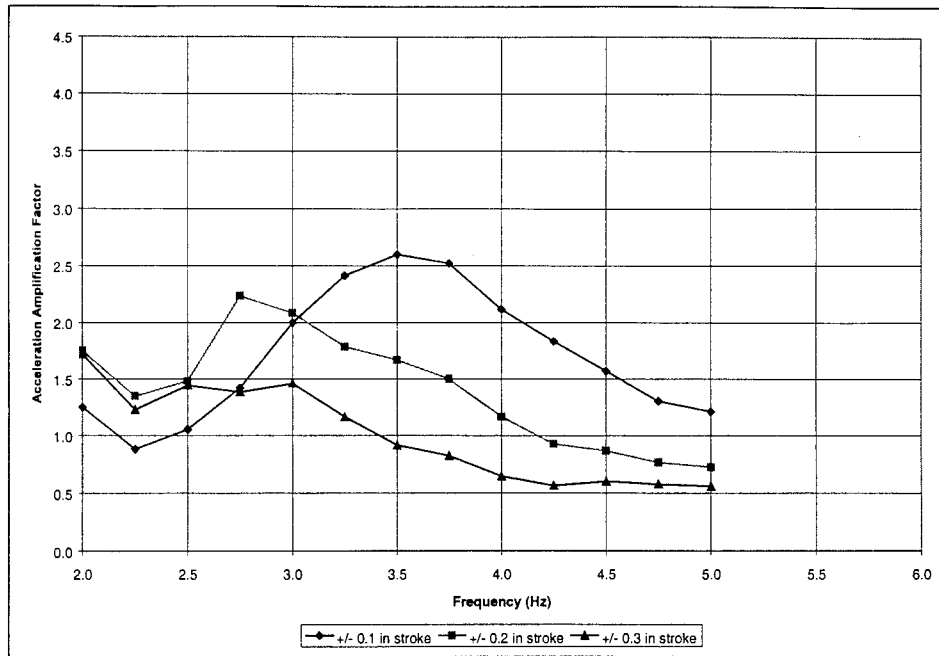


Figure 3.23. Acceleration Amplification Factor of Bridge with Damper 4

Load-Displacement Relation. To establish the load-relative displacement relationship, the seismic load on the damper was determined from the measured strains in the following way. Consider Bar 1 of the Damper with strain gauges 1 and 2 as shown in Figure 3.13. A free body diagram of Bar 1 between the top of the bar and the cross section at strain gauge 1 is illustrated in Figure 3.24 with l_1 being the member length. The moment, M_1 , at the gauge can be determined by summing the moment about the cut cross section. That is,

$$M_1 = M - V l_1 \quad (3.21)$$

Similarly, the moment at strain gauge 2 can be calculated by,

$$M_2 = M - V l_2 \quad (3.22)$$

where M_1 and M_2 are the moments at strain gauges 1 and 2, respectively. They are the resultants of the stress distribution on the cut section determined by multiplying the measured strain by a modulus of elasticity. M is the moment at the top of the bar. V is the shear force at the top, which is considered as the load on the rod. Subtracting out M and solving for V yields,

$$V = (M_1 - M_2)/(l_2 - l_1) \quad (3.23)$$

Figures 3.25 through 3.28 depict the relationship between the load (V) on the damper and relative displacement (d) of the superstructure and substructure for each damper under harmonic loading. The equation to best fit the test data of two rods is also given in the figures for each test case. It is observed that the load on the damper increases linearly with the relative displacement, indicating that all dampers behave elastically. Indeed, the maximum displacement of Dampers 1 and 2 is approximately 0.17 in and 0.07 in, respectively, as shown in Figures 3.25 and 3.26. Both are significantly less than the

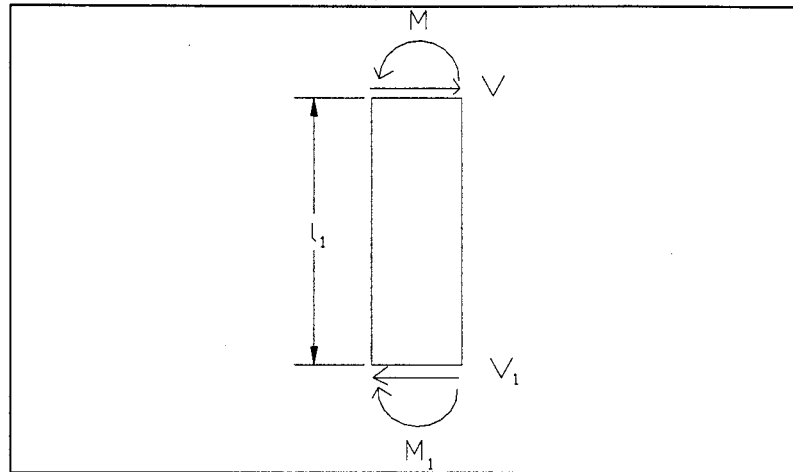


Figure 3.24. Load on Bar 1 of the Damper

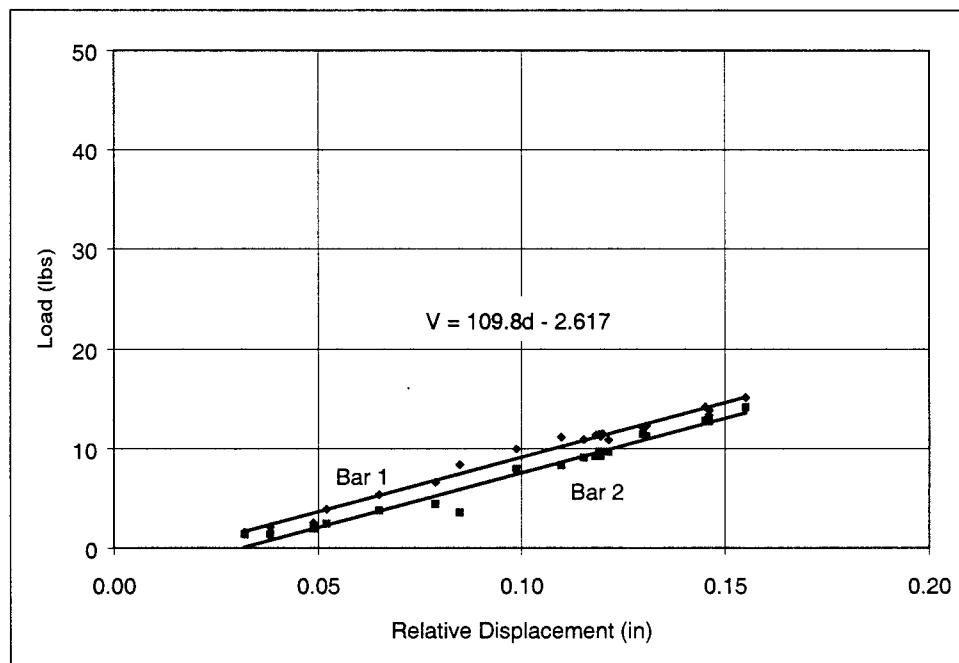


Figure 3.25. Load vs. Relative Displacement, Damper 1, Small-Scale Bridge

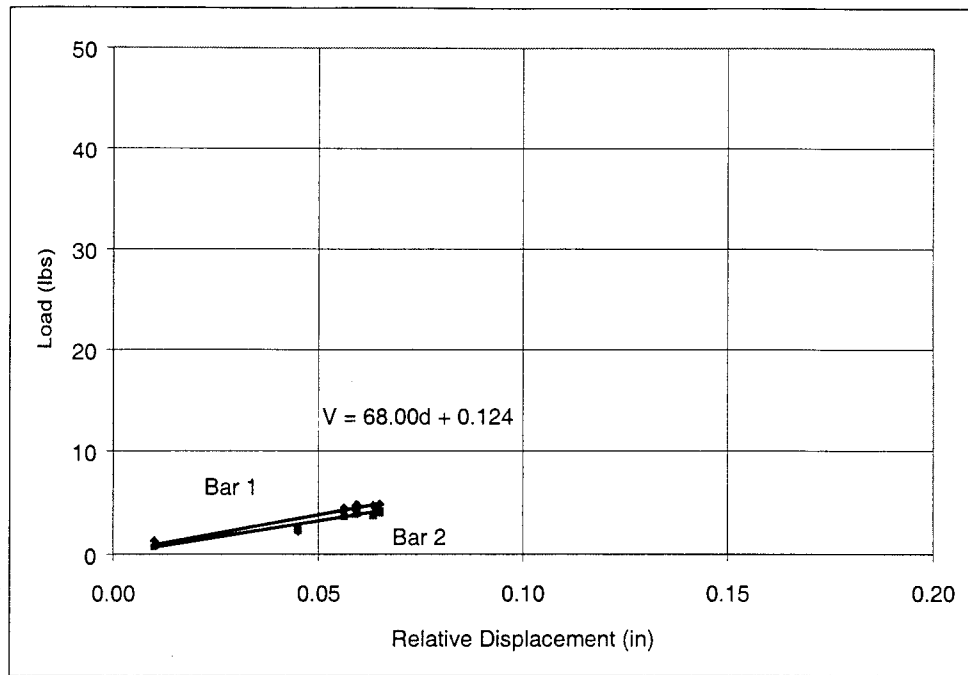


Figure 3.26. Load vs. Relative Displacement, Damper 2, Small-Scale Bridge

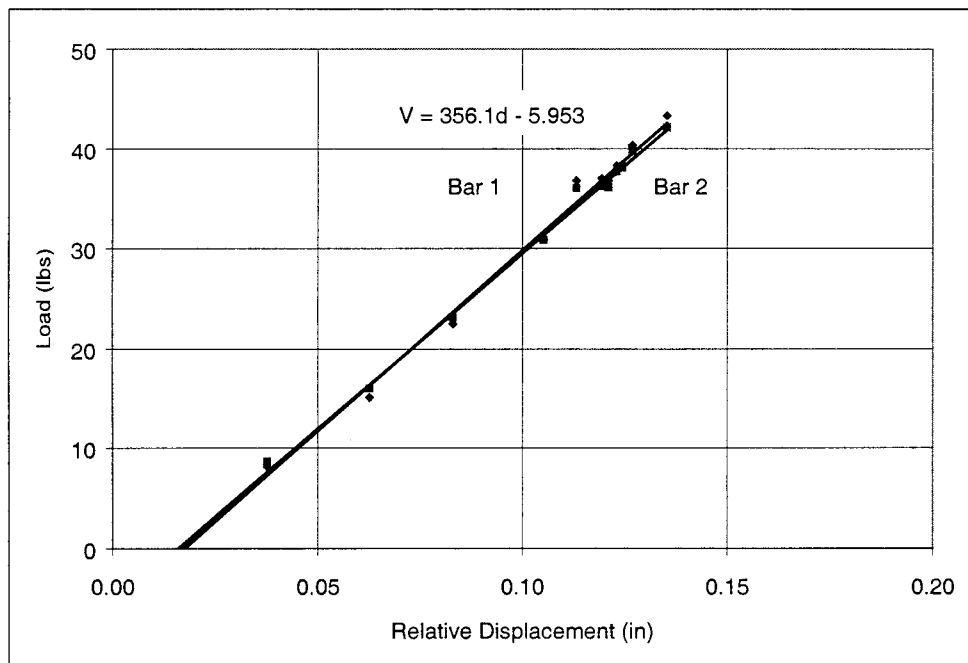


Figure 3.27. Load vs. Relative Displacement, Damper 3, Small-Scale Bridge

yielding displacement (0.556 in.) of the pinned-fixed steel rods as estimated from Eq. (3.13). It is believed that, in addition to the oversized holes for steel rods, these results are mainly due to the shift in natural frequency and increase in damping as a result of significant friction effect. Both load and displacement of Damper 2 are 50% smaller than those of Damper 1. This is apparently due to a decrease in input acceleration for Damper 2 than Damper 1, which can be confirmed from Figures B.5 through B.18. It can also be observed that the average stiffness coefficient or the average slope of load-displacement curves of two rods for Damper 1 (4 steel rods) is 61 % higher than that of Damper 2 (2 steel rods). This discrepancy results from possible variation of the end conditions of two dampers. Figures 3.25 and 3.26 also indicate that the rods in the front row of each damper are subjected to approximately the same displacement. It can thus be concluded that no torsional motion occurs in the bridge deck.

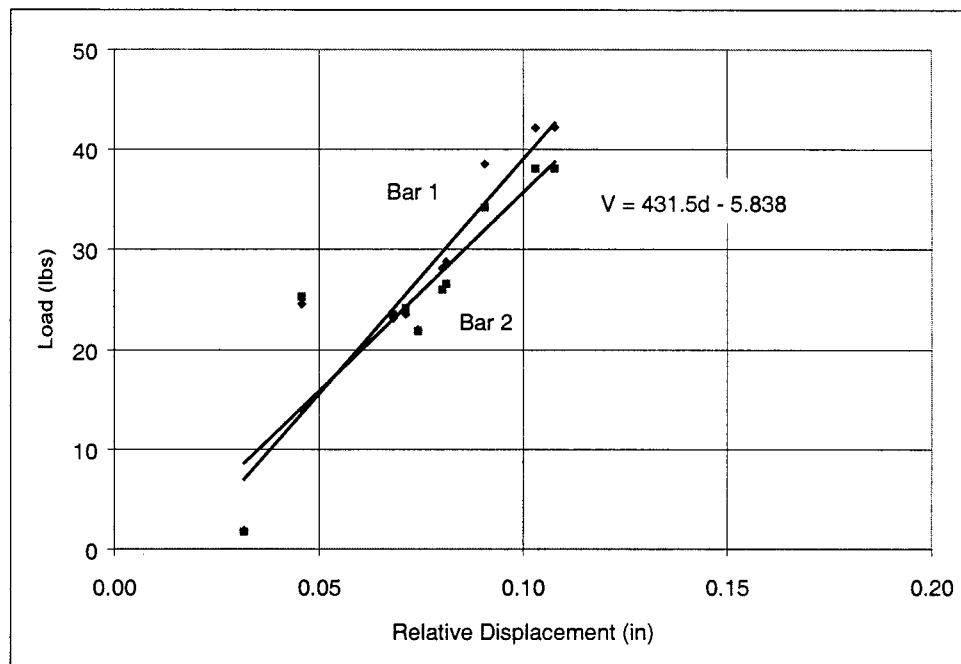


Figure 3.28. Load vs. Relative Displacement, Damper 4, Small-Scale Bridge

Figures 3.27 and 3.28 respectively show the load-displacement relationships of two-rod dampers 3 and 4 with both ends of the steel rods fixed. Damper 4 is the same as Damper 3 except for an added weight of 1600 lbs on the superstructure. It was previously thought that the added weight on the superstructure would generate a larger relative displacement between the superstructure and substructure. It can be concluded, from a comparison of Figures 3.27 and 3.28, that this was not the case. The added weight only slightly increases the strain of the steel rods in the test range.

Dampers 3 and 4 are identical in design. Experimental data, however, indicates that the average stiffness of the steel rods of Damper 4 is 21% higher than that of Damper 3. This percentage of change is significantly lower than that for pinned-fixed rods (61%), mainly representing less uncertainty in the end restraint condition.

Test Results of Damper 3. Figures 3.29-3.35 present the maximum acceleration, maximum displacement, and maximum strain as a function of input level under various

types of excitations when Damper 3 is installed on the bridge model. These results are similar for the other small-scale damper tests, which can be found in Appendix B. Careful examination on the maximum acceleration of the two girders, shown in Figure 3.33, implies there is no significant torsional motion in the bridge deck.

It is clearly seen from Figures 3.29 and 3.31 that the maximum acceleration at the bridge capbeam is larger due to the El Centro earthquake than the Taft earthquake even though the latter has a slightly larger peak ground motion. This is mainly because the El Centro earthquake includes a wider spectrum of frequency components. Compared to the harmonic excitation, as given in Figure 3.33, both earthquake-induced accelerations at the bridge girders are 50% to 75% less within the capacity of the testing facility. Nevertheless, all figures show the isolation effect of the metallic damper. The maximum acceleration at the bridge girders and deck are smaller than that of the capbeam as the excitation to the bridge increases. This effect is especially obvious under harmonic excitation. This reduction in response at the bridge deck is definitely due to the presence of the metallic damper since the deck's response is always larger than that of the capbeam without dampers as illustrated in Figures B.1 through B.4. The maximum displacement of Damper 3 is almost identical when measured at different points. This result indicates that there is little non-uniform stressing between the two rods. All measurements suggest that the maximum displacement, acceleration and strain linearly increase at low excitation and remain almost constant at high excitation. It is likely that the increase in friction from the high rocker bearings is responsible for the insensitive bridge responses to high disturbances. Because of this increasing damping effect, the high rocker bearings are always stable even though the bridge with Damper 1 was resonant at the excitation of 0.54g.

From a comparison of Figures 3.35 and B.4, one can see that when the damper is engaged, strain values increase on the damper while the values decrease on the column base. This validates the premise that metallic dampers are effective as an isolation unit, ensuring that in the event of a destructive earthquake, damage will be localized to the damper while the column retains its structural integrity.

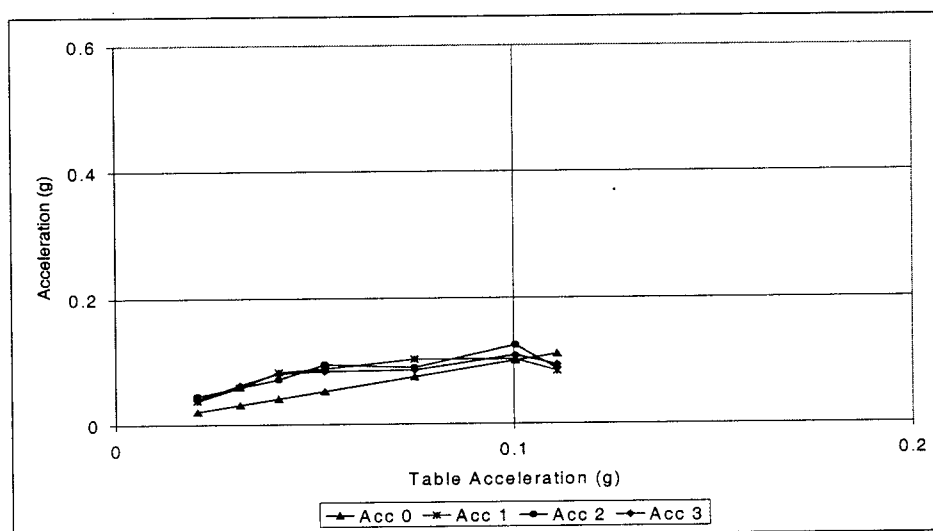


Figure 3.29. Acceleration vs. Input, Taft Earthquake, Damper 3

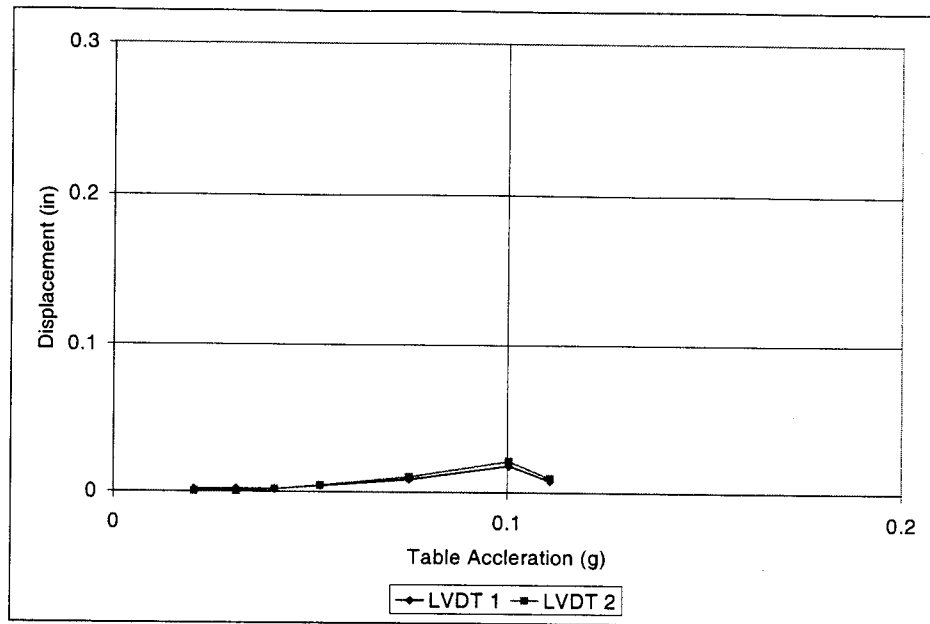


Figure 3.30. Displacement vs. Input, Taft Earthquake, Damper 3

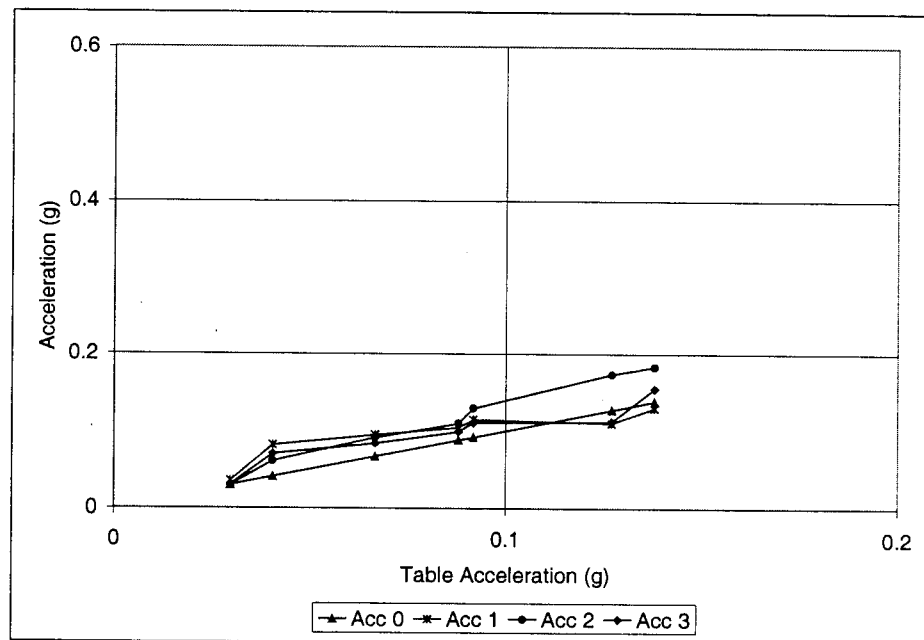


Figure 3.31. Acceleration vs. Input, El Centro Earthquake, Damper 3

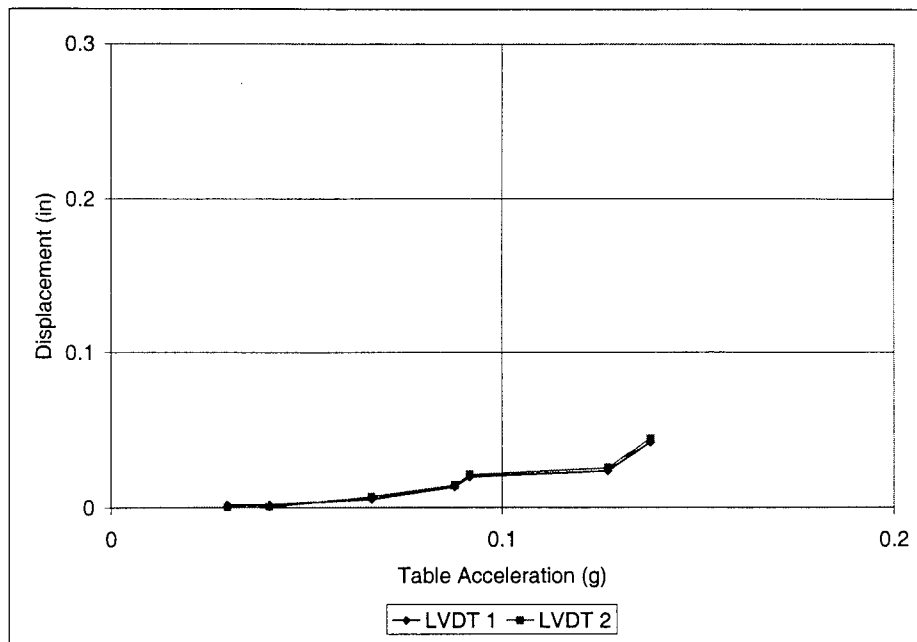


Figure 3.32. Displacement vs. Input, El Centro Earthquake, Damper 3

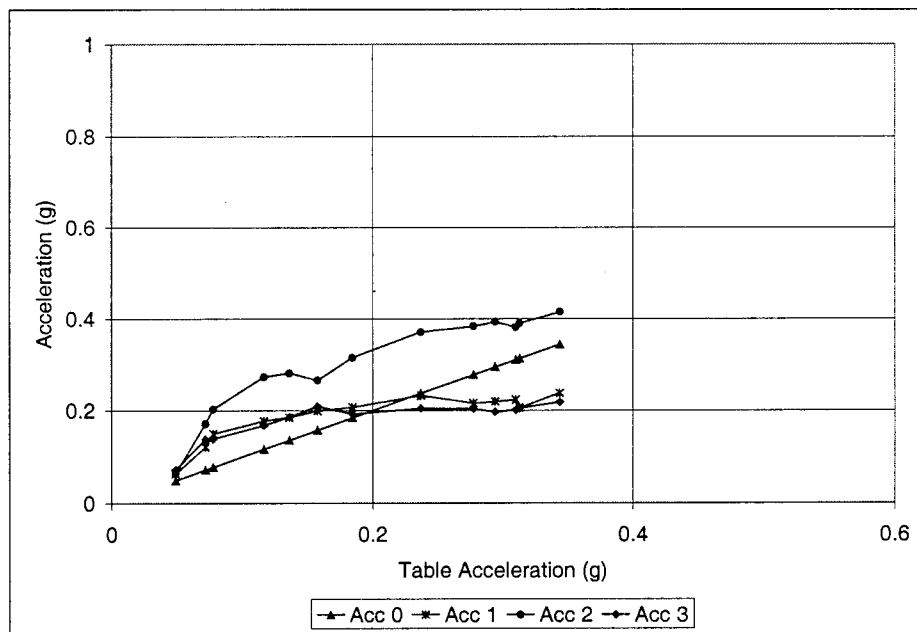


Figure 3.33. Acceleration vs. Input, Harmonic Input, Damper 3

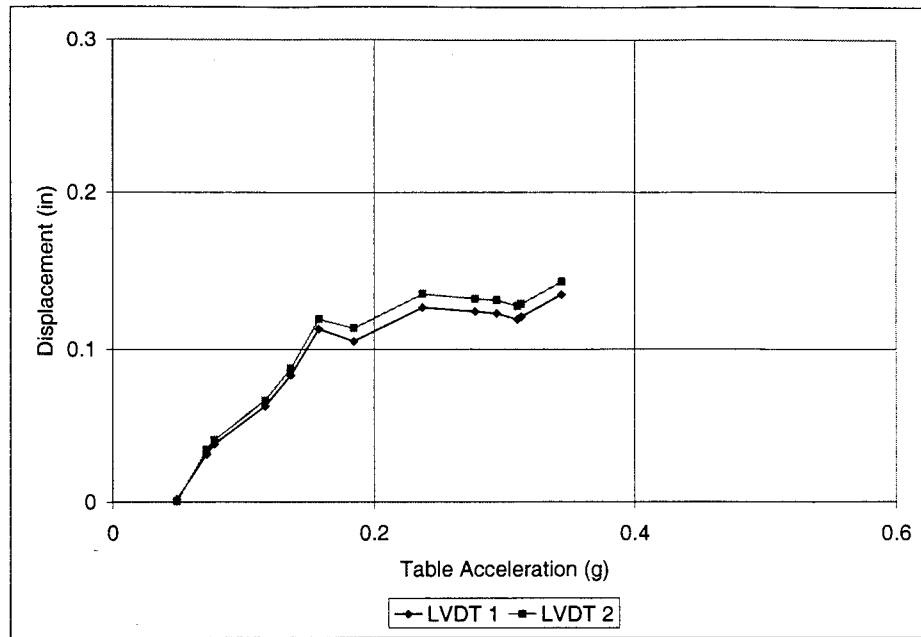


Figure 3.34. Displacement vs. Input, Harmonic Input, Damper 3

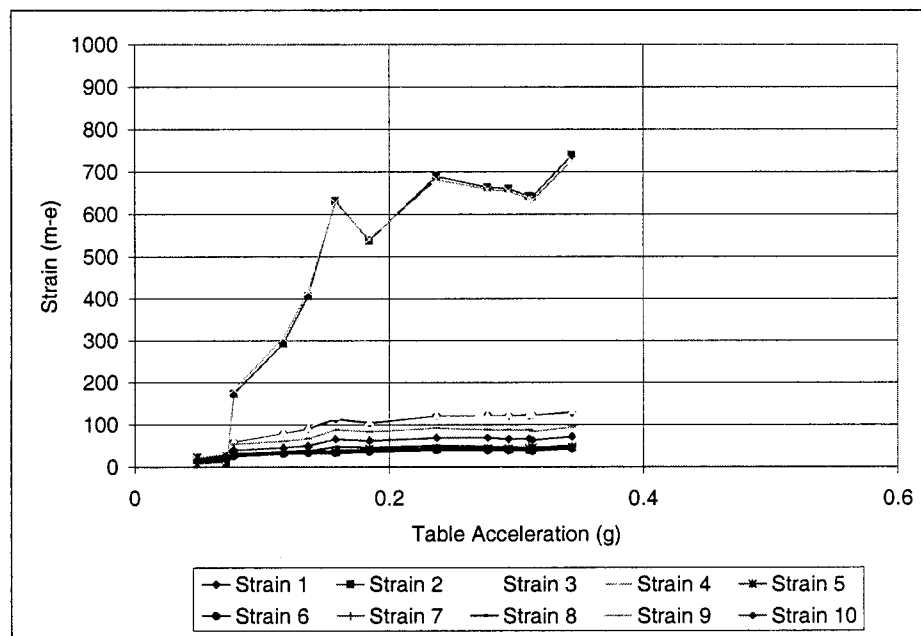


Figure 3.35. Strain vs. Input, Harmonic Input, Damper 3

To show the repeatability of the test results, the small-scale bridge model with Damper 3 was re-tested after a dozen other tests. Figure 3.36 presents the acceleration at various elevations of the bridge under harmonic loading. By comparing Figure 3.36 with Figure 3.33, it can be concluded that test results are generally repeatable. In both tests, the bridge model behaved in the same way.

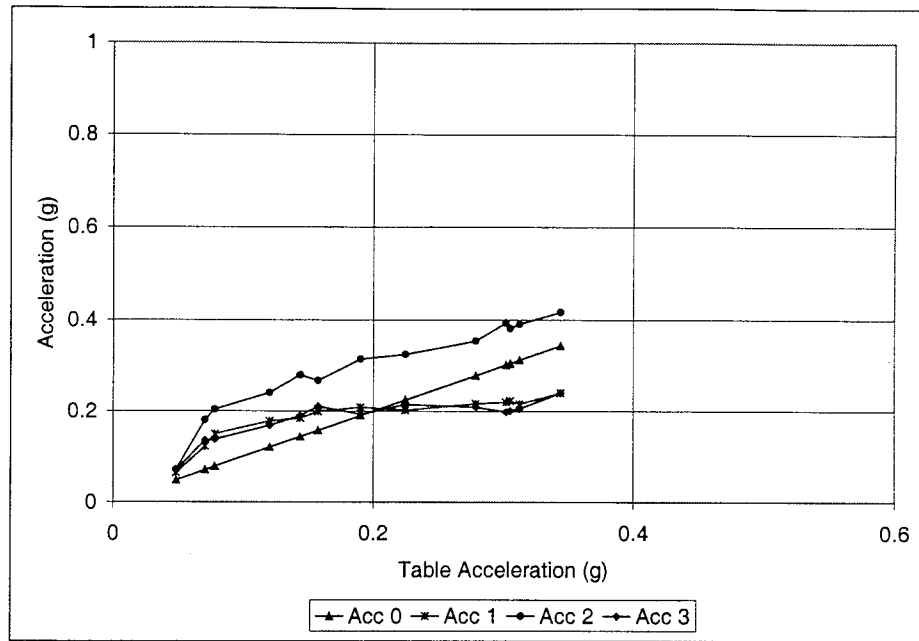


Figure 3.36. Acceleration vs. Input, Re-Test of Damper 3

3.5 Summary

Based on a series of tests on four small-scale dampers, the following observations can be made:

1. Metallic dampers were effective as isolation units. When a damper was engaged, stress increased on the damper and decreased on the column base. The acceleration at the bridge deck and girders dropped below that of the substructure. This ensures that in the event of a destructive earthquake, damage will be localized to the dampers while the columns retain their structural integrity.
2. Overturning of rocker bearings did not occur throughout the test programs. Rocker bearings were stable even when the bridge was subjected to an excitation of 0.54g at resonance.
3. Tests on the small-scale dampers were repeatable even though the friction effect made the bridge-damper system become highly nonlinear. However, the friction surface condition on the rocker bearings may change over the sufficient time period. The friction effect on the seismic performance of bridge with metallic dampers is a very complex issue and may be difficult to characterize. Future study should be directed to the continuing monitoring of friction features of rocker bearings to better understand the friction contribution to the attenuation of dynamic responses of bridges.
4. The small-scale metallic dampers tested in this study were not subjected to yielding yet. It was mainly due to the significant damping effect from the rocker bearings.
5. A practical procedure was recommended and used to design the small-scale metallic dampers for the 1/10-scale bridge model. Test results of the bridge model suggested that the procedure has led to a sound design that the dampers were subjected to

substantially larger stress than that of the bridge columns. The dampers were expected to yield before a plastic hinge is formed at the columns.

4. POUNDING EFFECT ON BRIDGE BEHAVIOR

Steel-girder bridges consist of a superstructure, bearings, a substructure and a foundation. Typically, the superstructure includes several deck segments separated by expansion joints to accommodate the effect of thermal expansion. During a strong earthquake, two sides of an expansion joint move in and out of phase and they may pound each other as the intensity of the earthquake increases. For instance, many elevated structures or bridges were found to have experienced minor damages at the ends of deck segments around expansion joints during the 1995 Kobe earthquake (Buckle, 1995). The level of damage is repairable and often will not impede the immediate access of emergency vehicles for the post-earthquake recovery of affected areas. How pounding affects the seismic behavior of bridges is a subject of this section. A simple procedure to account for the pounding effect in practical applications is developed.

The seismic response of bridges is a function of ground motion, superstructure and substructure type, bearing behavior, pounding effect and soil-foundation-structure interaction. During earthquakes, expansion joints open and close and two adjacent deck segments at a joint may pound each other resulting in additional longitudinal force to the bridge structures. Due to the open and close nature of expansion joints and the nonlinear soil behavior, the seismic analysis of bridges is often a process involving the modeling of several nonlinear components. As a typical expansion joint of steel-girder bridges in the Central and Eastern United States, the steel girder is supported on a seat-type abutment as shown in Figure 4.1. A pair of pounding forces is generated when the bridge deck and the abutment move against each other. The force acting on the abutment is transmitted to the back fill behind the abutment or the abutment foundation. The pounding force on the bridge deck changes the seismic input energy to the bridge and the bridge response. The pounding force varies with the ground motion, gap width, structural characteristics, abutment and foundation properties.

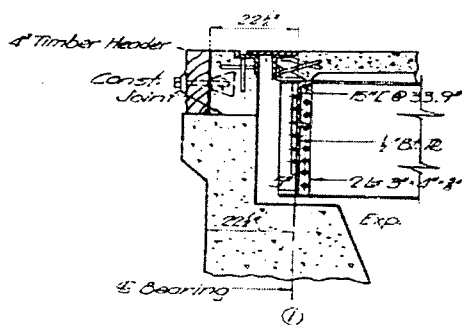


Figure 4.1. Actual Expansion Joint between Superstructure and Abutment

4.1 Theory of Pounding Action

4.1.1 Equation of Motion

To understand the pounding effect on the seismic behavior of bridges, it is important to illustrate the pounding process. Considering a simple bridge model of a single degree of freedom (SDOF) as shown in Figure 4.2, the lateral motion of the model is restrained when the bridge displacement equals the gap width δ . The model consists of a mass (m), two elastic columns of stiffness k and a viscous damper with damping coefficient of c . The gap width of the expansion joint between the superstructure and abutment in Figure 4.1 is represented by δ and both the superstructure and abutment are assumed rigid for simplicity. Therefore, no plastic deformation and energy loss will occur in the process of pounding. The bridge model including the representation of the abutment is subjected to the ground acceleration $\ddot{x}_g(t)$.

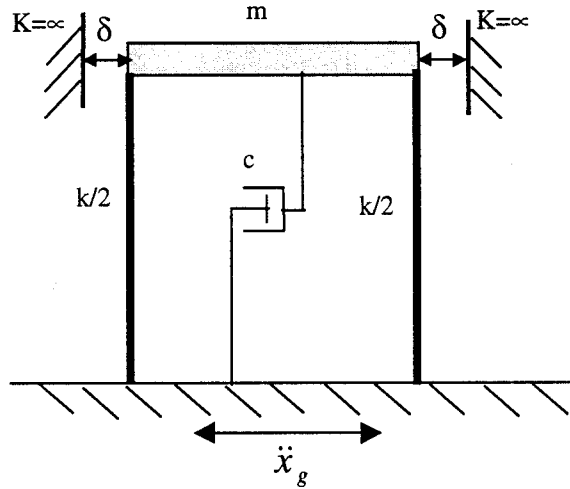


Figure 4.2. SDOF Pounding Model

An action and a reaction force are induced between the superstructure and abutment when the displacement of the superstructure exceeds the gap width. They are considered as a pair of internal pounding forces since the bridge model includes the abutment and foundation system. The equation of motion of the SDOF system can be written as

$$m\ddot{x}(t) + c\dot{x}(t) + p(t) + kx(t) = -m\ddot{x}_g(t) \quad (4.1)$$

in which $x(t)$ is the lateral displacement of the model with respect to the ground and $p(t)$ represents the pounding force.

The pounding force $p(t)$ can be determined from the velocity change of the superstructure according to the impulse-momentum theory. It can be expressed as

$$p(t) = \begin{cases} 0 & |x(t)| < \delta \\ \frac{m[\dot{x}(t^+) - \dot{x}(t^-)]}{t^+ - t^-}, & t^- \leq t \leq t^+ \text{ and } |x(t)| = \delta \end{cases} \quad (4.2)$$

in which t^- and t^+ denote the time instants immediately before and after the time t . Since the plastic deformation and energy loss within the short period from t^- to t^+ is neglected, the velocities immediately before and after the pounding must be equal in magnitude and opposite in direction. That is,

$$\dot{x}(t^+) = -\dot{x}(t^-). \quad (4.3)$$

The pounding force defined in Eq. (4.2) is generated at select time instants when $x(t) = \pm\delta$. Combining Eqs. (4.1-4.3) thus results in a geometric nonlinear problem even though all materials of the bridge model are assumed elastic. Consequently, an iterative method in the time domain must be used to solve the equations. In general, the displacement and velocity of the bridge model can be determined by the following Duhamel's integration:

$$x(t) = \int_0^t [-m\ddot{x}_g(\tau) - p(\tau)]h(t-\tau)d\tau, \quad (4.4)$$

$$\dot{x}(t) = \int_0^t [-m\ddot{x}_g(\tau) - p(\tau)]\frac{dh(t-\tau)}{dt}d\tau \quad (4.5)$$

provided the initial displacement and velocity are zero at the time instant $t = 0$. In Eqs. (4.4) and (4.5), $h(u)$ is the unit impulsive response function associated with the linear system without pounding. It is defined by

$$h(u) = \frac{e^{-\xi u \omega_0}}{m\omega_D} \cdot \sin(\omega_D u) \quad (4.6)$$

where ω_0 and $\omega_D (\omega_0 \sqrt{1-\xi^2})$ are respectively the natural frequency of the undamped and damped bridge model without pounding, and ξ is the corresponding damping ratio ($c/2m\omega_0$). Let $t = t^-$ and $t^+ - t^- = \Delta t$. Here Δt is a small time increment. The pounding force can be approximately determined from Eqs. (4.2) and (4.3) as

$$p(\tau) = \begin{cases} 0, & |x(t)| < \delta \\ -\frac{2m\dot{x}(t)}{\Delta t}, & |x(t)| = \delta \end{cases} \quad (t \leq \tau \leq t + \Delta t) \quad (4.7)$$

which is constant over the short period Δt . In addition, the ground motion can be assumed to linearly vary with time between time instant t and $t + \Delta t$:

$$\ddot{x}(\tau) = \ddot{x}_g(t) + \frac{\ddot{x}_g(t + \Delta t) - \ddot{x}_g(t)}{\Delta t}(\tau - t), \quad t \leq \tau \leq t + \Delta t. \quad (4.8)$$

After a tedious derivation, the displacement and velocity of the bridge model at the time $t + \Delta t$ can be calculated using the following iterative formula:

$$x(t + \Delta t) = x(t) + \dot{x}(t)\Delta t - \left[m\ddot{x}_g(t + \Delta t) + p(t) \right] \int_0^{\Delta t} h(u)du + \frac{\ddot{x}_g(t + \Delta t) - \ddot{x}_g(t)}{\Delta t} \int_0^{\Delta t} uh(u)du, \quad (4.9)$$

$$\dot{x}(t + \Delta t) = -\omega_0^2 \Delta t x(t) + (1 - 2\xi\omega_0\Delta t)\dot{x}(t) - \left[m\ddot{x}_g(t) + p(t) \right] h(\Delta t) + \frac{\ddot{x}_g(t + \Delta t) - \ddot{x}_g(t)}{\Delta t} \int_0^{\Delta t} h(u)du. \quad (4.10)$$

It is noted that $p(t)$ in Eqs. (4.9) and (4.10) is equal to either zero or $-2m\dot{x}(t)/\Delta t$, depending on the displacement $x(t)$. In this study, the solution algorithms described by Eqs. (4.9) and (4.10) are implemented in the SAP2000 computer code with the finite element method (FEM). The pounding action is introduced in the code by using a nonlinear gap element. A non-linear time history analysis was used to calculate the bridge's response and pounding force.

When the bridge model is subjected to a harmonic excitation of 1.5 kips, the superstructure's relative displacement, relative velocity and absolute acceleration with and without the pounding effect were calculated for a set of parameters ($m = 1.5$ slugs, $k = 60$ kips/in, $\xi = 0.05$, $\beta = 0.5$ and $\delta = 0.025$ in.) and are shown in Figures 4.3-4.5. The new parameter β represents the ratio between the excitation frequency and the natural frequency ω_0 . It can be observed from these figures that both the shape and the magnitude of the response time histories are quite different between the bridge model with and without pounding effect. Due to pounding action, the response time histories reveal additional pulses. The maximum displacement is reduced and equal to the gap width while both the maximum velocity and acceleration increase. Therefore, pounding is restraining the maximum displacement.

The pounding force was also calculated and it is illustrated in Figure 4.6. It is clearly seen that pounding occurs at discrete time instants. The pounding force varies with time but approaches a constant value as the response of the bridge model reaches the steady-state motion. Since no plastic deformation and energy loss is considered in this study, the displacement peaks of the associated linear system become their mirror images about the gap width due to the pounding effect.

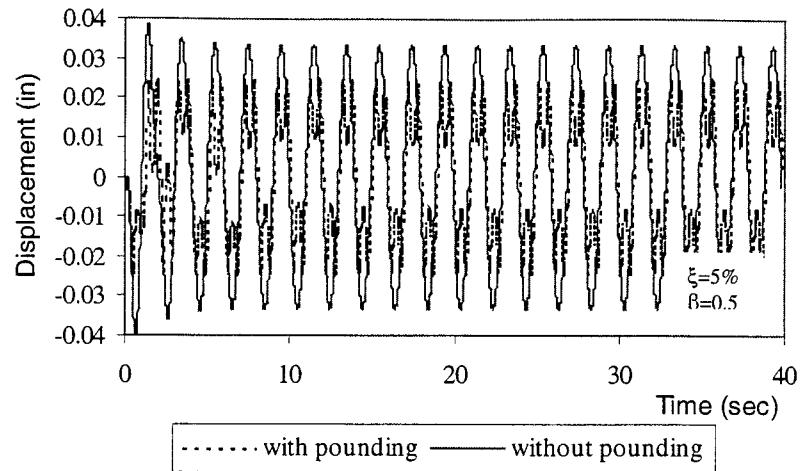


Figure 4.3. Displacement at Bridge Deck under Harmonic Excitation

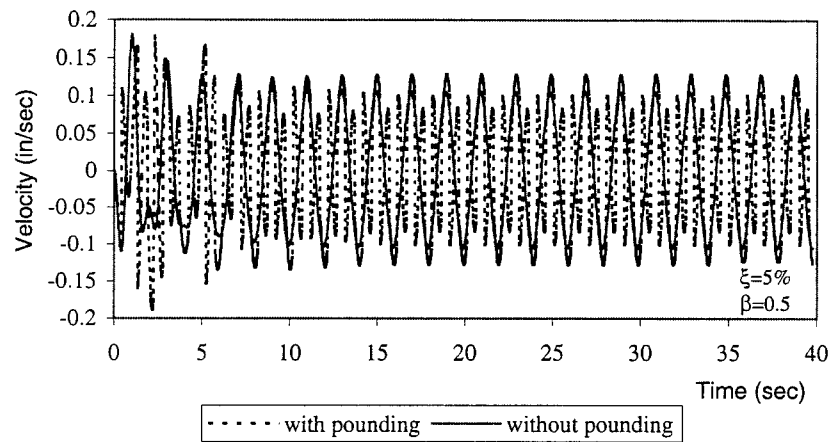


Figure 4.4. Velocity at Bridge Deck under Harmonic Excitation

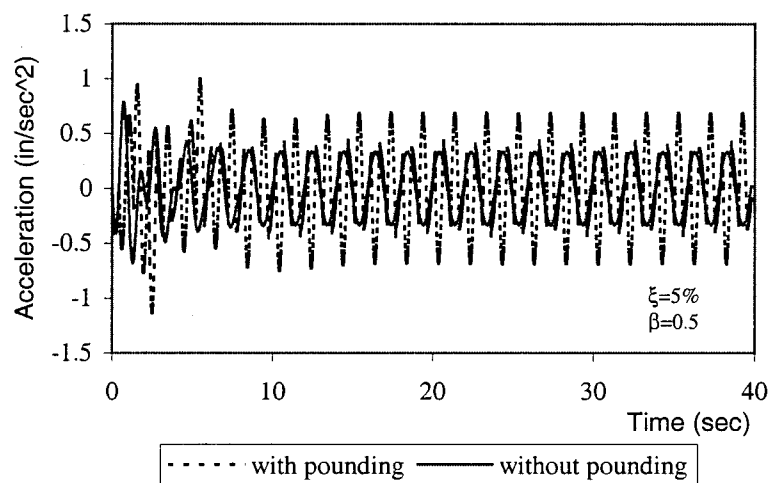


Figure 4.5. Acceleration at Bridge Deck under Harmonic Excitation

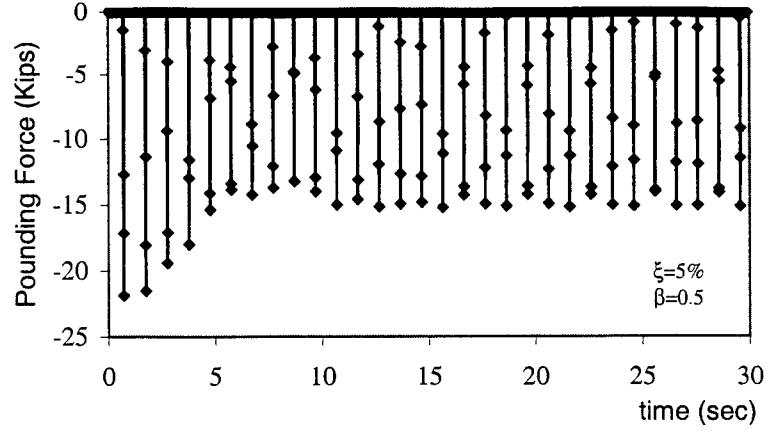


Figure 4.6. Pounding Force under Harmonic Excitation

4.1.2 Energy Equation

Another way to study pounding effects is to observe the energy balance of the system. The bridge system involves the total energy imposed to the structure, the energy dissipated by the viscous damper and pounding action, and the kinetic and potential energy stored in the structure. Under earthquake loads, introduction of the energy concept can also reflect the duration effect of the seismic excitation on the bridge response. The energy equation can be formulated by multiplying the individual term in Eq. (4.1) by the incremental displacement and integrating it over a certain time period (0, t). The resulting equation can be expressed as

$$E_K + E_D + E_P = E_I \quad (4.11)$$

in which E_K is the relative kinetic energy of the mass; E_D is the total energy dissipated by the structural damping E_{D_s} and pounding E_{D_p} ; E_P is the relative potential energy due to the elastic strain; and E_I is the input energy imposed on the structure by the seismic event. These energy quantities can further be expressed into

$$\left. \begin{aligned} E_K &= \int_0^t m \dot{x}(t) dx(t) = \frac{m \dot{x}^2(t)}{2} \\ E_D &= E_{D_s} + E_{D_p} \\ E_{D_s} &= \int_0^t c \dot{x}(t) dx(t) = \int_0^t c \dot{x}^2(t) dt \\ E_{D_p} &= \int_0^t p(t) dx(t) \\ E_P &= \int_0^t kx(t) dx(t) = \frac{kx^2(t)}{2} \\ E_I &= -\int_0^t m \ddot{x}_g(t) dx(t). \end{aligned} \right\} \quad (4.12)$$

They are balanced at any time instant throughout the duration of the loading. From an energy perspective, the system's responses under the harmonic excitation, with and without the pounding effect, are illustrated in Figures 4.7-4.9. Both the input energy and kinetic energy increase due to the pounding effect while the potential energy is reduced corresponding to the change of displacement. For instance, the potential energy is periodic and its maximum value is proportional to the square of the gap width. As indicated in Eq. (4.11), the difference between the input energy and the mechanic energy (potential + kinetic) is equal to the total energy absorbed by the structural damping and pounding. Since the displacement and velocity together represents a state of the bridge movement, the mechanic energy may be an important parameter to describe the seismic demand on the bridge in addition to reflecting the damping and pounding effect indirectly.

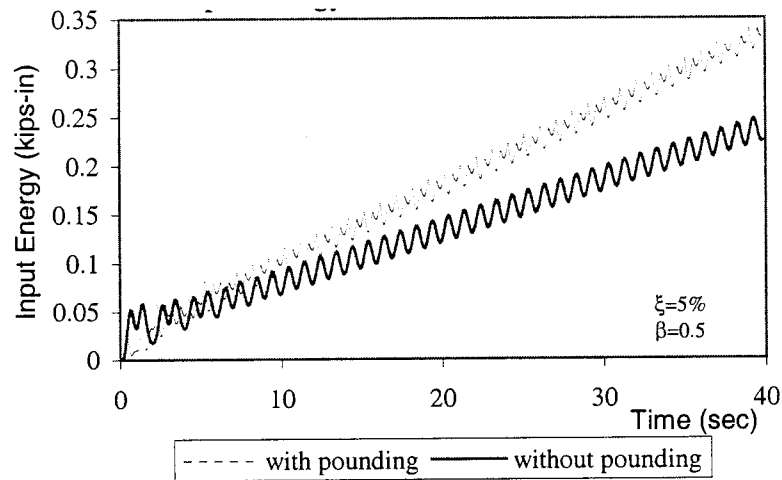


Figure 4.7. Input Energy under Harmonic Excitation

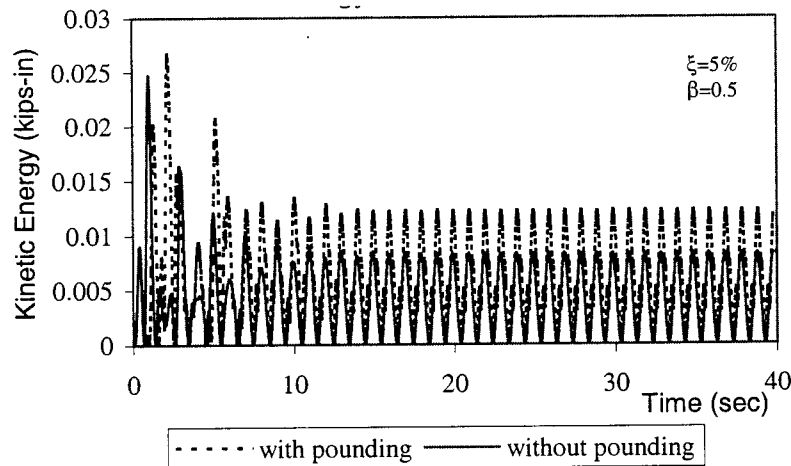


Figure 4.8. Kinetic Energy under Harmonic Excitation

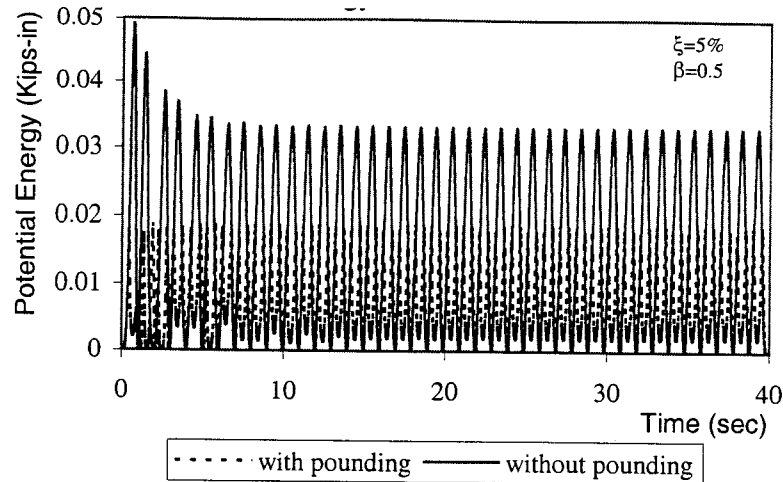


Figure 4.9. Potential Energy under Harmonic Excitation

4.2 Earthquake Characteristics

The bridge analysis under harmonic loads is only intended to study the general effect of pounding on the displacement, velocity, acceleration and energy. How pounding affects the seismic responses of bridges is of main concern in this study. Due to the complexity of the pounding process under random ground motions, a statistical approach is used to investigate the pounding effect. Therefore, a suite of twelve ground motions recorded during six earthquakes are included in this study as listed in the first two columns of Table 4.1. The acceleration time histories of the twelve records are presented in Figure 4.10. These ground motions represent a wide spectrum of earthquake excitations.

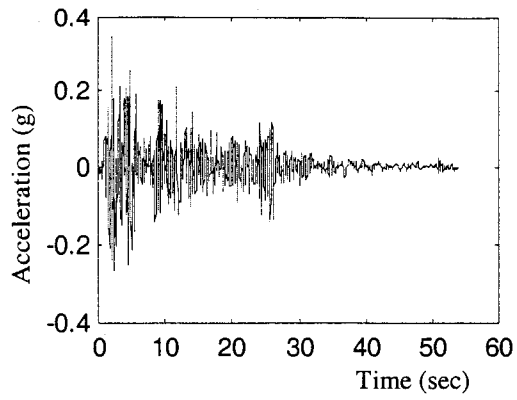
It is expected that pounding effects depend on structural properties, gap width and the earthquake characteristics such as amplitude, dominant frequency and frequency components. The amplitude can be represented by the peak ground acceleration listed in the third column of Table 4.1. The dominant frequency of each ground motion is identified from its Fourier Amplitude Spectrum (Fast Fourier Transform or FFT). Due to the random nature of earthquake loads, the Fourier spectrum of the ground motion changes irregularly. Therefore, the spectrum is smoothed to facilitate the determination of the dominant frequency. Figure 4.11 compares the original and the smoothed Fourier spectrum of the twelve earthquake records. The dominant frequency is defined as the frequency corresponding to the peak of the smoothed Fourier spectrum. The multi-frequency components of an earthquake excitation can impose a significant amount of seismic energy into the bridge structure even though its dominant frequency is not in resonance with the bridge. To characterize the frequency component effects, a parameter called frequency bandwidth is introduced in this report. It is defined as the difference in frequency corresponding to the $1/\sqrt{2}$ times peak value of the smoothed Fourier Amplitude Spectrum, which follows the half-power method for the identification of structural model damping. Considering a smoothed Fourier spectrum sketched in Figure 4.12, the frequency bandwidth can mathematically be written as

$$B_f = f_2 - f_1 \quad (4.13)$$

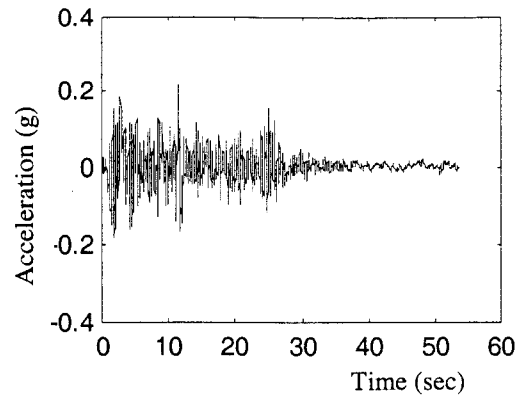
in which f_1 and f_2 correspond to the magnitude of the Fourier Amplitude Spectrum $A/\sqrt{2}$ and A is the peak value of the spectrum at the dominant frequency f_{\max} . As one can see, the frequency bandwidth measures how seismic energy distributes over the frequency spectrum. The wider the bandwidth (B_f), the more evenly distributed the seismic energy. The harmonic excitation can be viewed as a special case of the earthquake input with a zero bandwidth. Both the dominant frequency and the frequency bandwidth of the twelve earthquakes are listed in Table 4.1.

Table 4.1. Input Ground Motion Characteristics

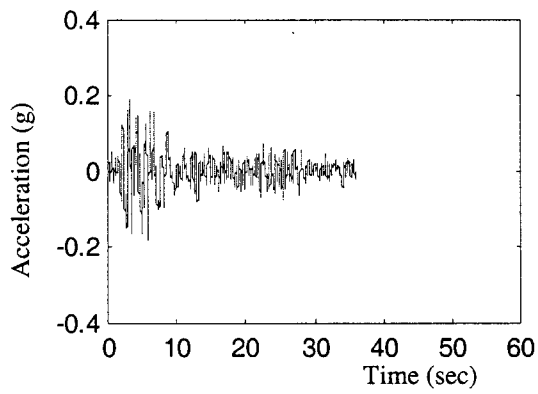
Record	Earthquake Component	Peak Acceleration (g)	Dominant Frequency (Hz)	Bandwidth (Hz)
Elcs00e	1940 El Centro, S00E	0.3484	1.75	1.7645
Elcs90w	1940 El Centro, S90W	0.2142	1.88	2.5019
Hachew	1968 Hachinohe, EW	0.1866	1.04	1.4718
Hachns	1968 Hachinohe, NS	0.2296	0.94	3.1658
Mexn90w	1985 Mexico City, N90W	0.1713	0.49	0.1887
Mexs00e	1985 Mexico City, S00E	0.1000	0.47	0.1887
Miyagew	1978 Miyagiken Oki, EW	0.1645	2.71	4.4647
Miyagns	1978 Miyagiken Oki, NS	0.1404	1.98	2.4974
Pacs16e	1971 Pacoima, S16E	1.1707	2.49	4.3592
Pacs74w	1971 Pacoima, S174W	1.0757	2.34	1.195
Taftn21e	1952 Taft, N21E	0.1557	1.39	2.2226
Tafts69e	1952 Taft, S69E	0.1794	2.28	2.5716



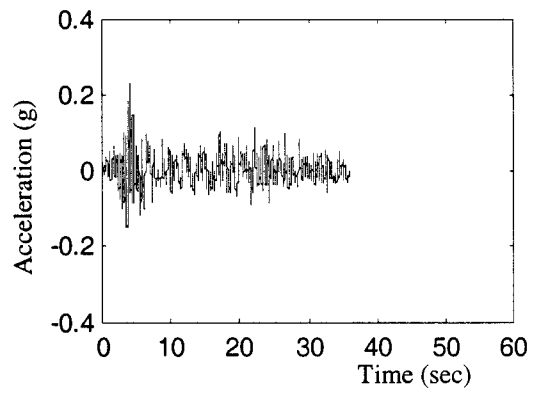
(a) Elcs00e



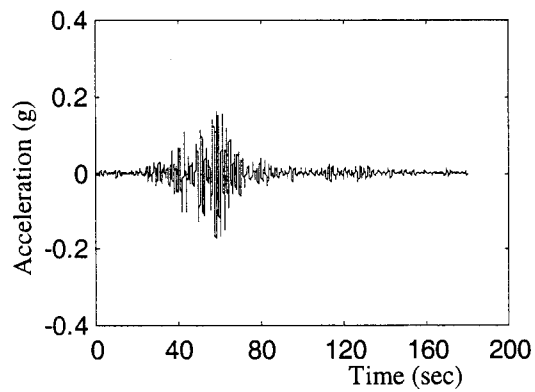
(b) Elcs90w



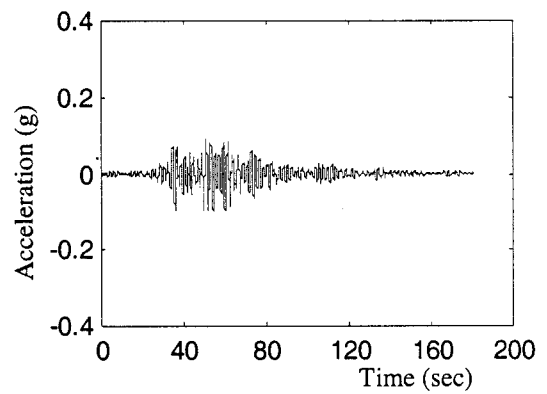
(c) Hachew



(d) Hachns



(e) Mexn90w



(f) Mexs00e

Figure 4.10. Acceleration Time Histories of Twelve Earthquake Records

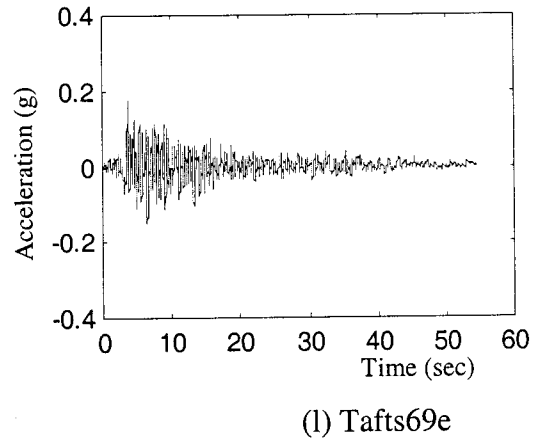
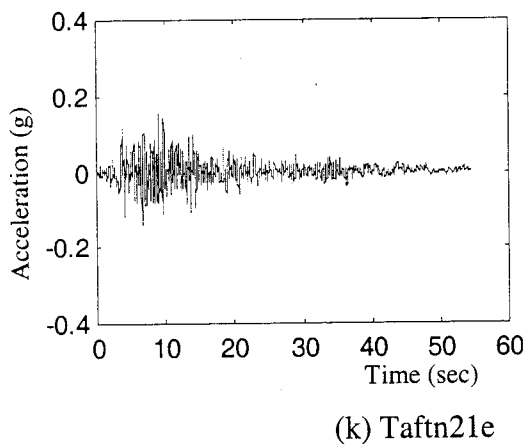
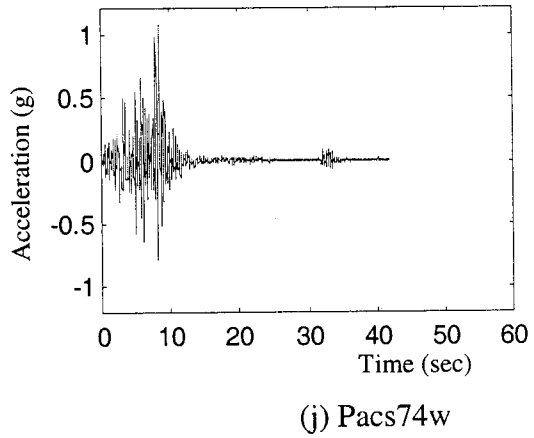
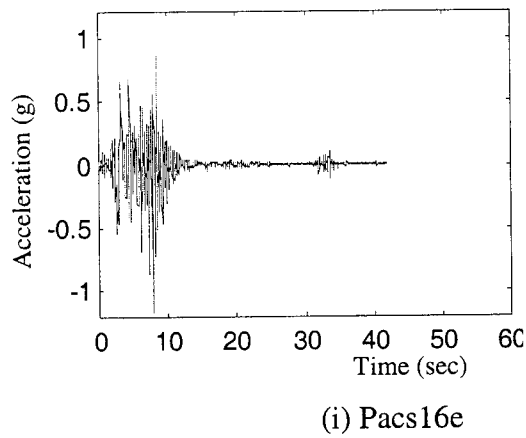
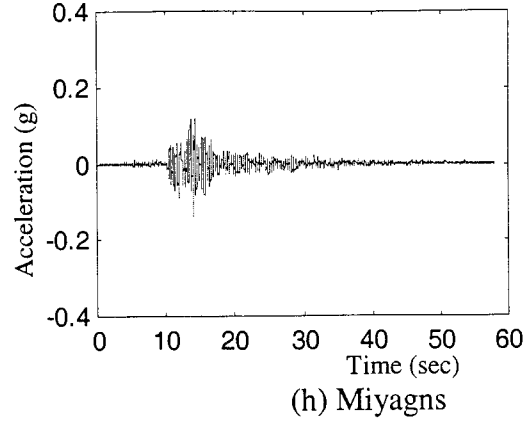
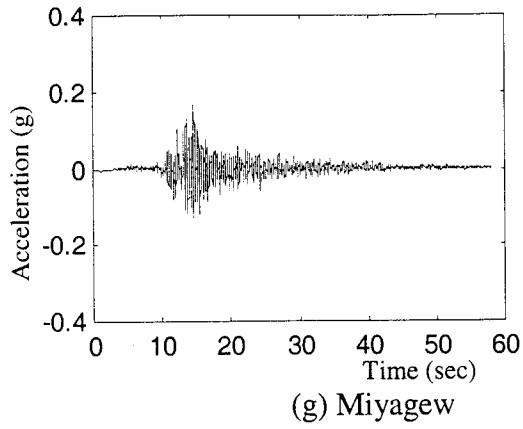
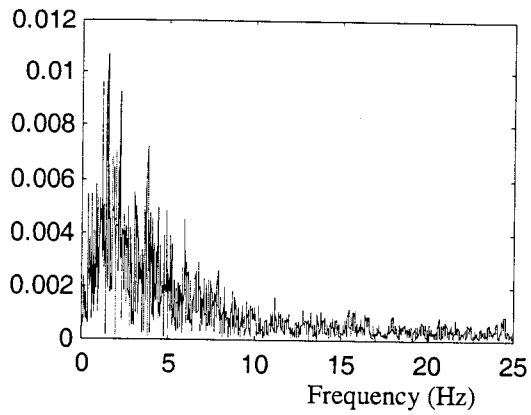
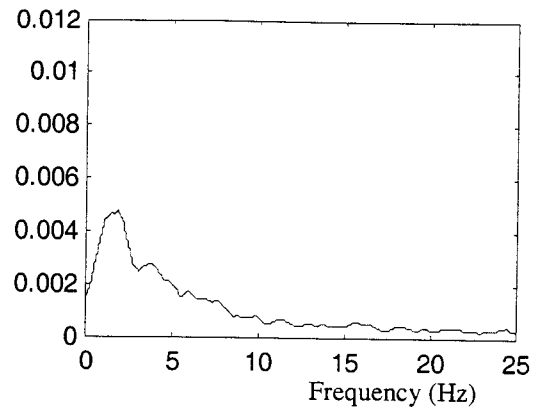


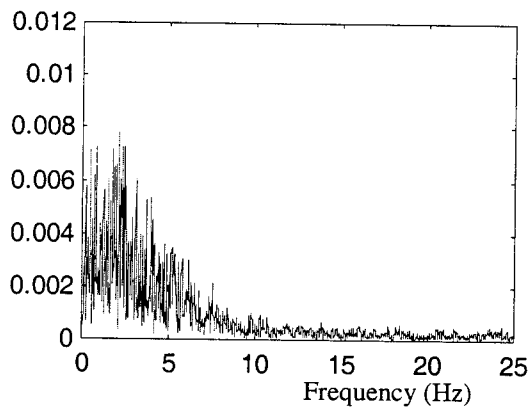
Figure 4.10. Acceleration Time Histories of Twelve Earthquake Records (cont'd)



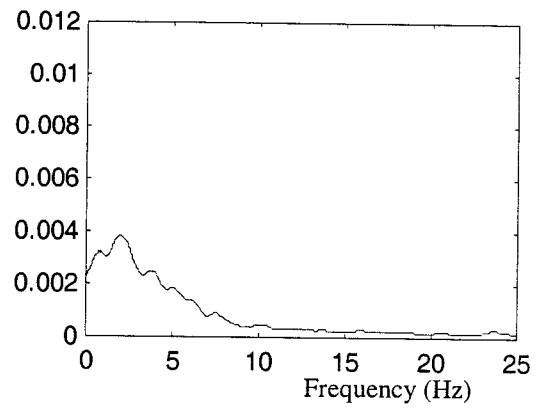
(aA) FFT for Elcs00e



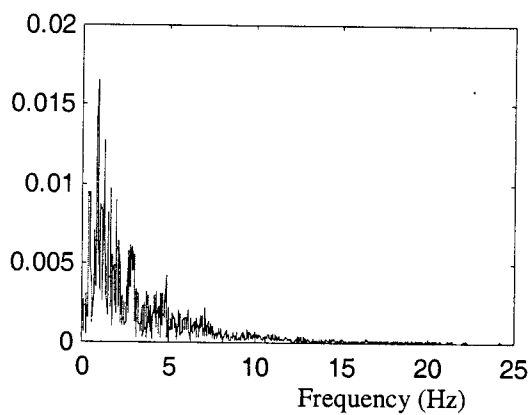
(aB) Smoothed FFT for Elcs00e



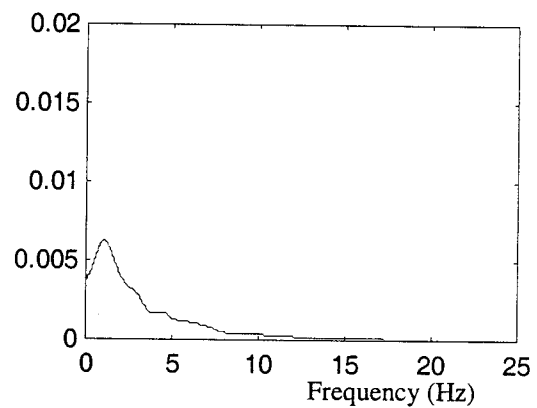
(bA) FFT for Elcs90w



(bB) Smoothed FFT for Elcs90w

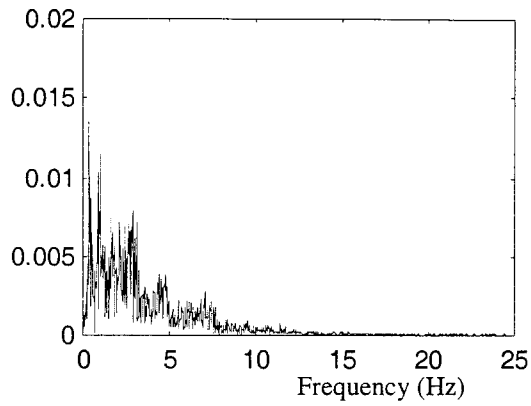


(cA) FFT for Hachew

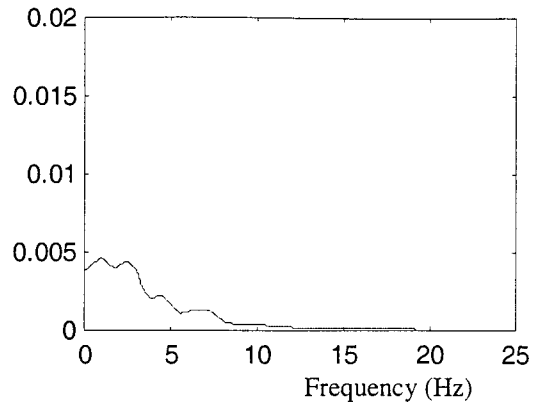


(cB) Smoothed FFT for Hachew

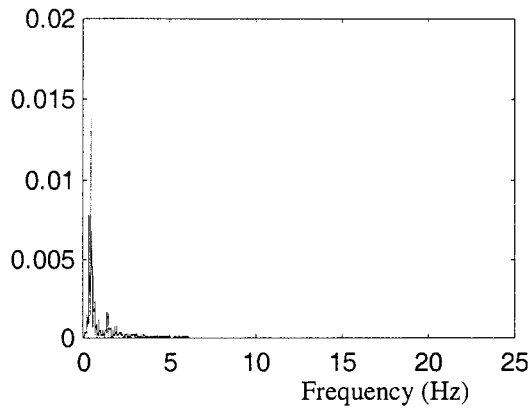
Figure 4.11. Original and Smoothed FFT Spectra of Twelve Earthquake Records



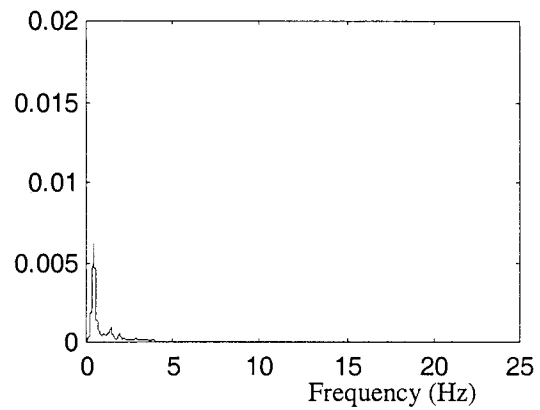
(dA) FFT for Hachns



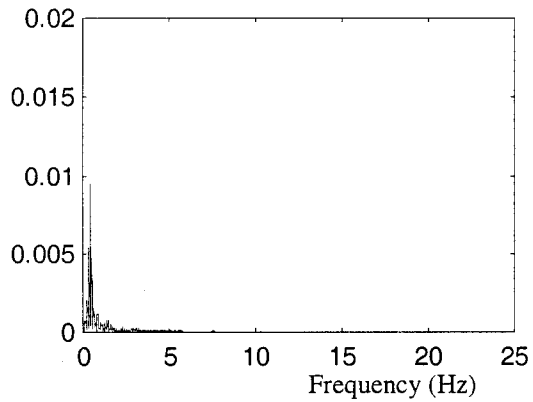
(dB) Smoothed FFT for Hachns



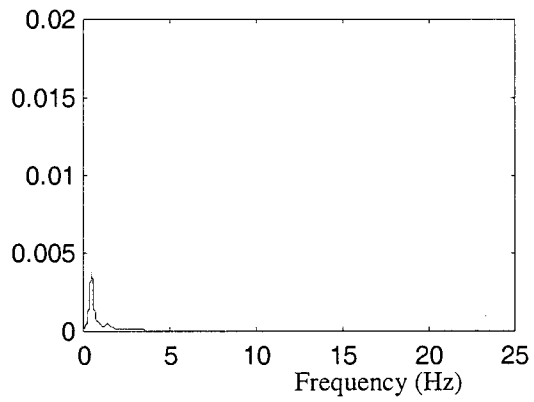
(eA) FFT for Mexn90w



(eB) Smoothed FFT for Mexn90w

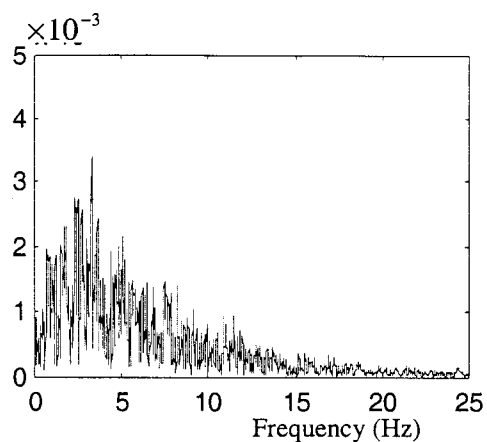


(fA) FFT for Mexs00e

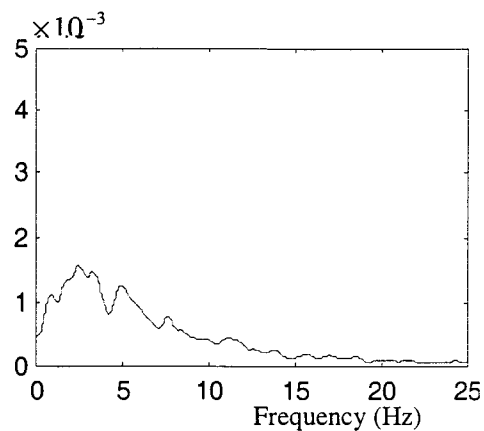


(fB) Smoothed FFT for Mexs00e

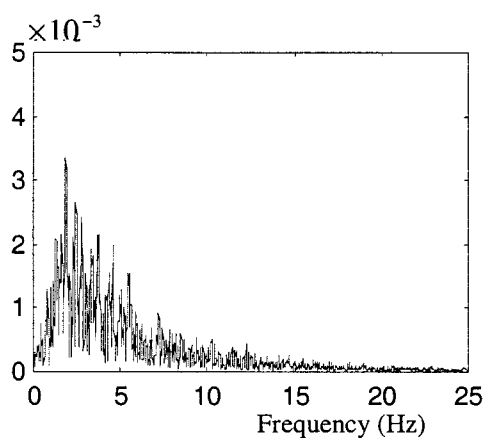
Figure 4.11. Original and Smoothed FFT Spectra of Twelve Earthquake Records (cont'd)



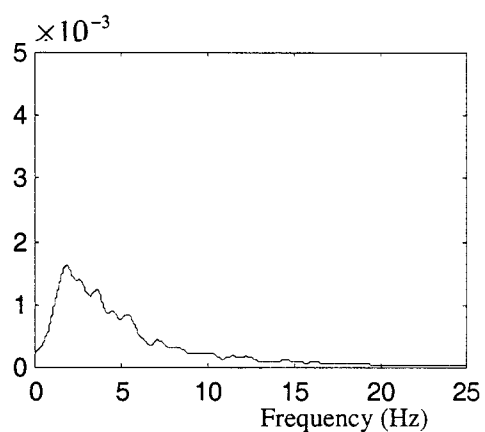
(gA) FFT for Miyagew



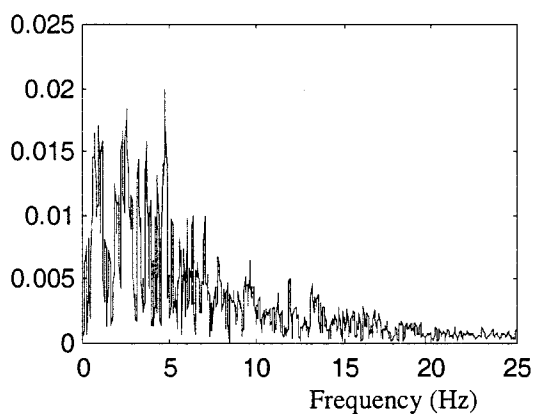
(gB) Smoothed FFT for Miyagew



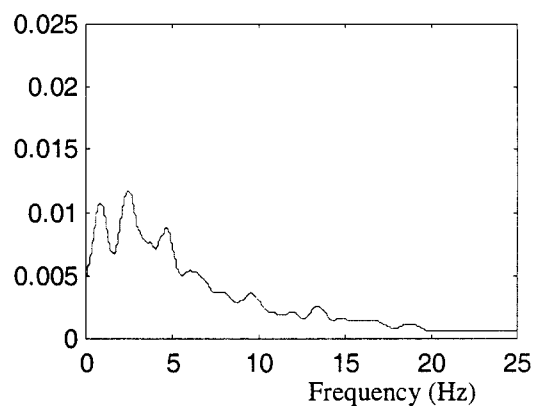
(hA) FFT for Miyagws



(hB) Smoothed FFT for Miyagws

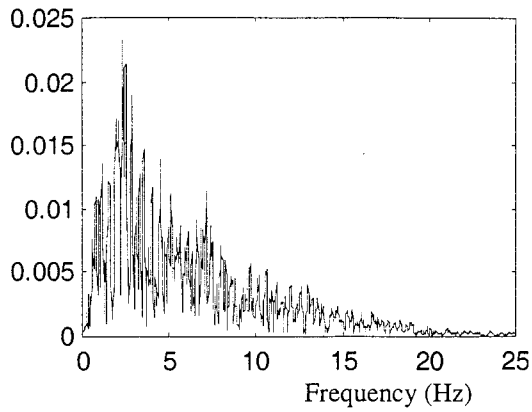


(iA) FFT for Pacs16e

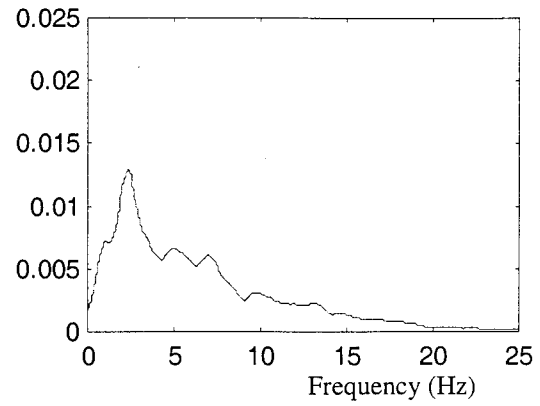


(iB) Smoothed FFT for Pacs16e

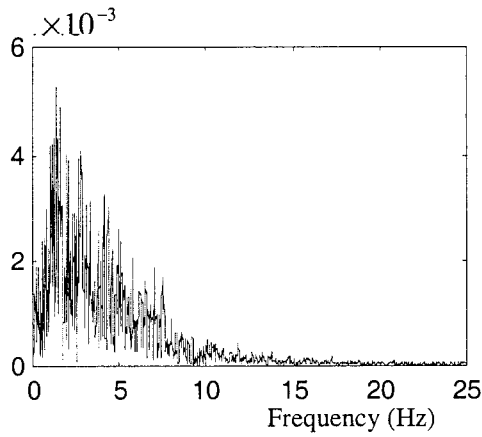
Figure 4.11. Original and Smoothed FFT Spectra of Twelve Earthquake Records (cont'd)



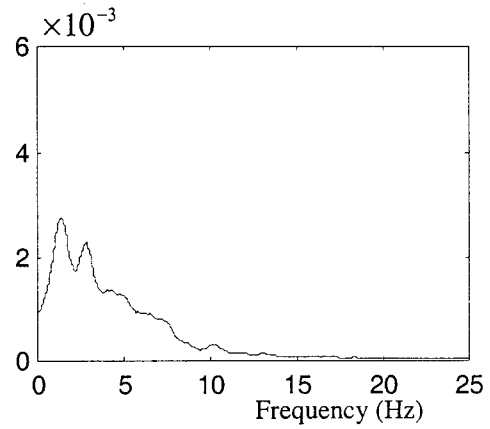
(jA) FFT for Pacs74w



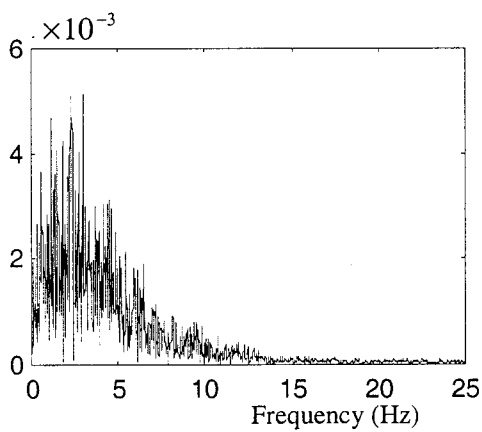
(jB) Smoothed FFT for Pacs74w



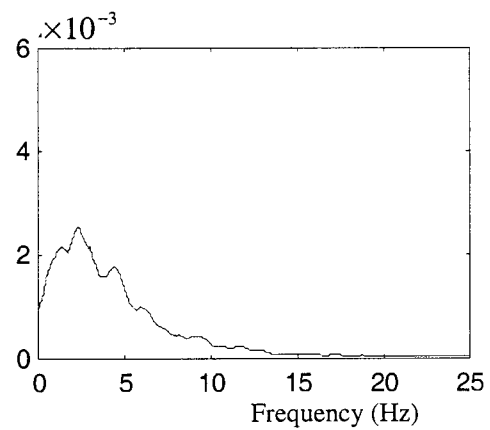
(kA) FFT for Taftn21e



(kB) Smoothed FFT for Taftn21e



(lA) FFT for Tafts69e



(lB) Smoothed FFT for Tafts69e

Figure 4.11. Original and Smoothed FFT Spectra of Twelve Earthquake Records (cont'd)

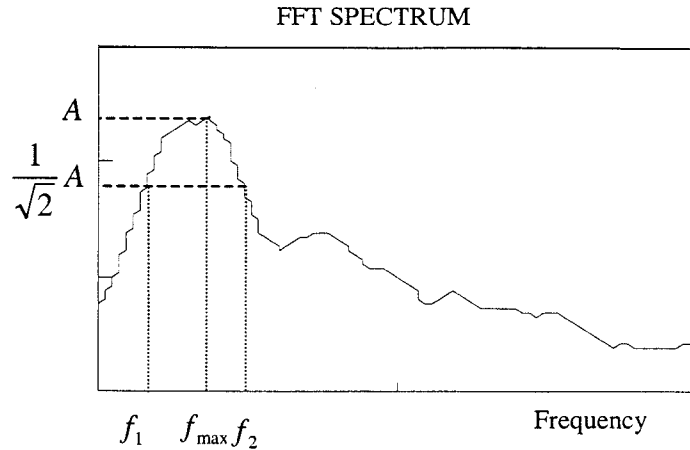


Figure 4.12. Frequency Bandwidth Definition

It can be observed from the table that the bandwidth for Mexn90w and Mexs00e is pretty small and their effects on bridge behaviors are expected to be similar to harmonic loading. The bandwidths for other earthquakes range from 1.2 to 4.5 Hz.

4.3 Discussion on the Nonlinear Gap Element

A nonlinear gap element called the non-link element in SAP2000 computer code was used to simulate the pounding action. It is schematically shown in Figure 4.13. The element has two parameters: open distance and spring constant (K). The open distance denotes the gap width between the superstructure and abutment of the bridge model and the spring constant (K) represents the stiffness of the abutment and its surrounding soil medium. The joints i and j mean the location of the abutment and the superstructure of the bridge model.

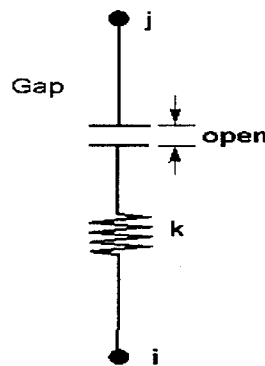


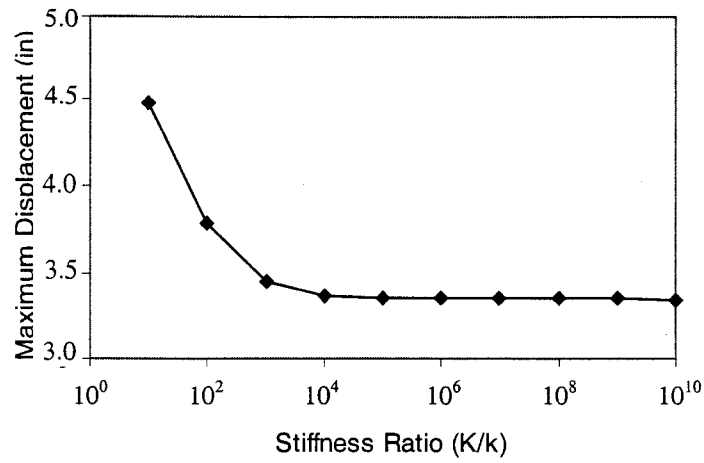
Figure 4.13. Non-link Gap Element

The abutment is assumed rigid in this study. The spring constant K is thus equal to infinity. However, it is claimed in the SAP2000 Analysis Reference Volume I that a K value significantly greater than 10^4 times as large as the corresponding stiffness in any connected elements may cause numerical difficulties during the search for a solution. To

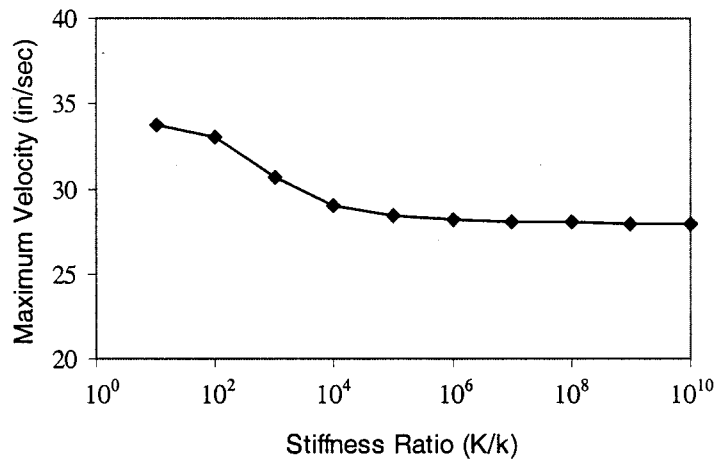
determine a reasonable spring constant, the following sensitivity analysis was conducted under the Elcs00e earthquake. The maximum responses and energy are plotted in Figures 4.14 and 4.15 as a function of the stiffness ratio K/k (k is the column stiffness of the bridge model). These figures show that both the responses and the energy remain nearly constant as the stiffness ratio increases from 10^5 to 10^{10} . When the stiffness ratio is larger than 10^{10} , the SAP2000 software will show a numerical error message since the K value is too large. The pounding force and the total damping energy due to the structural damping and pounding are given in Table 4.2 for various stiffness ratios. For a stiffness ratio from 10 to 10^4 , the pounding force can be retrieved from the computer analysis but its magnitude and shape change significantly as illustrated in Figure 4.16. For a stiffness ratio larger than 10^6 , the pounding force becomes unavailable and the damping energy is reasonable. When the stiffness ratio exceeds 10^7 , the damping energy changes suddenly as indicated in Figure 4.17 and it is converging to an asymptotic value.

Table 4.2. Structural Model Damping Energy and Pounding Force vs. Stiffness Ratio

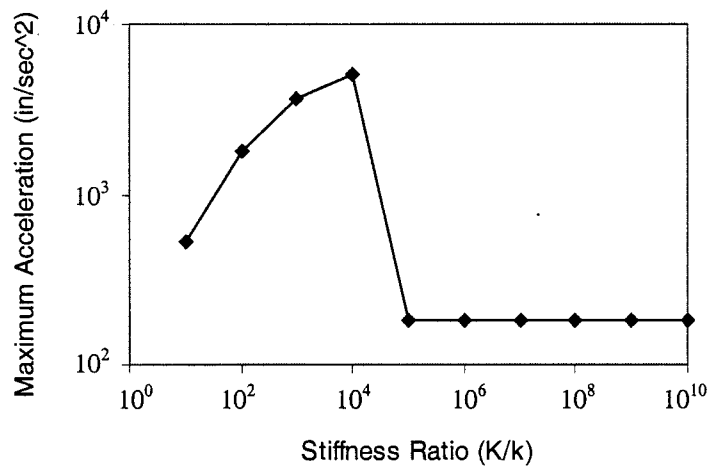
Stiffness Ratio	Structural Model Damping Energy (kips-in)	Pounding Force (kips)
10	4303	553
10^2	3552	2545
10^3	3397	5424
10^4	3472	7460
10^5	3461	0
10^6	3441	0
10^7	3944	0
10^8	1.29×10^4	0
10^9	-3.39×10^5	0
10^{10}	-1.06×10^7	0
10^{11}	Fail due to numerical error	



(a) Displacement

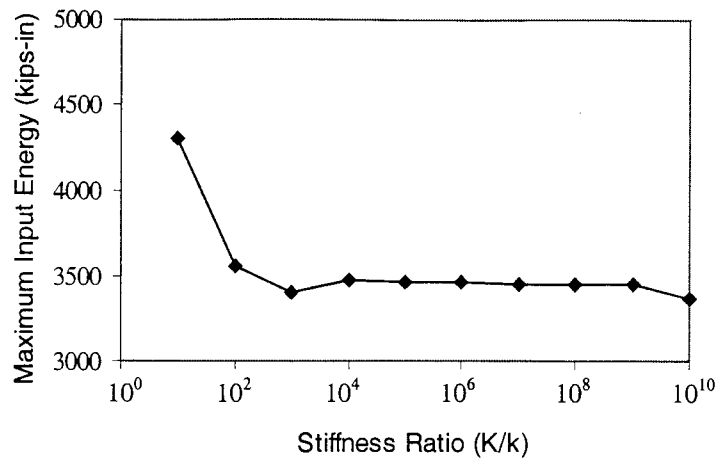


(b) Velocity

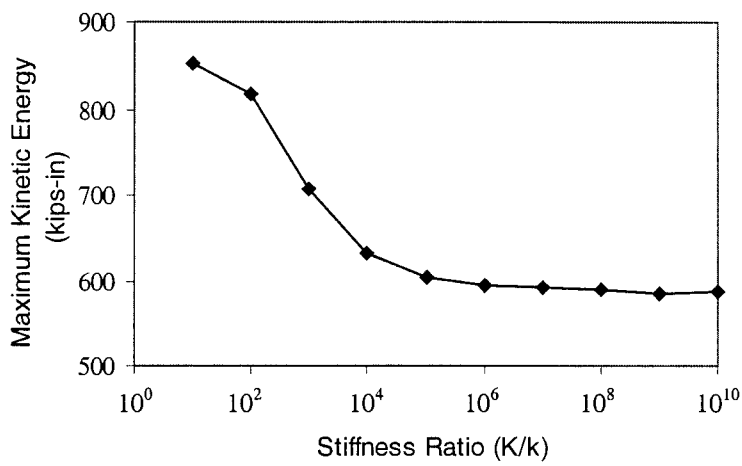


(c) Acceleration

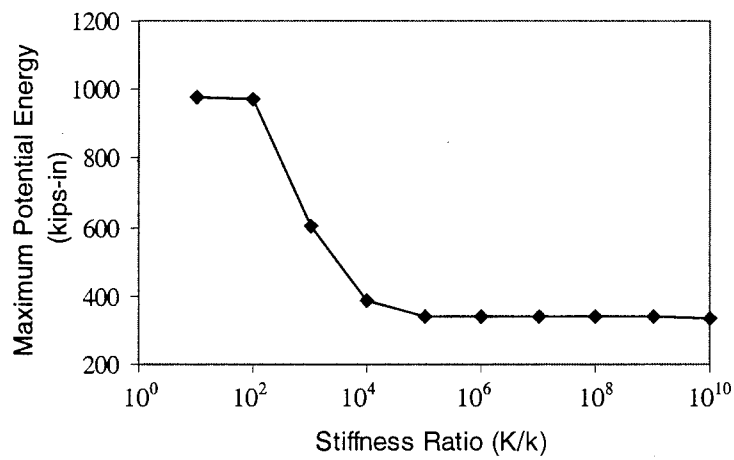
Figure 4.14. Maximum Response vs. Stiffness Ratio



(a) Input Energy

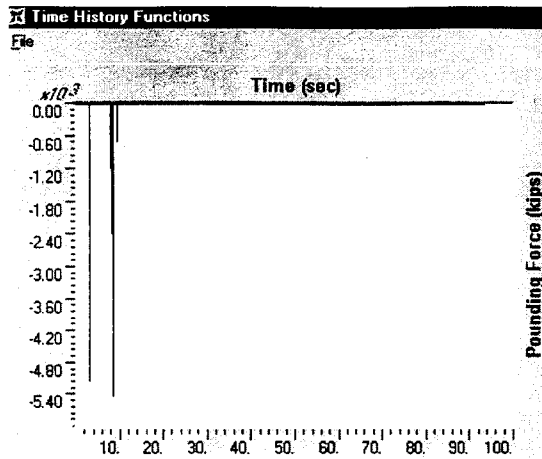


(b) Kinetic Energy

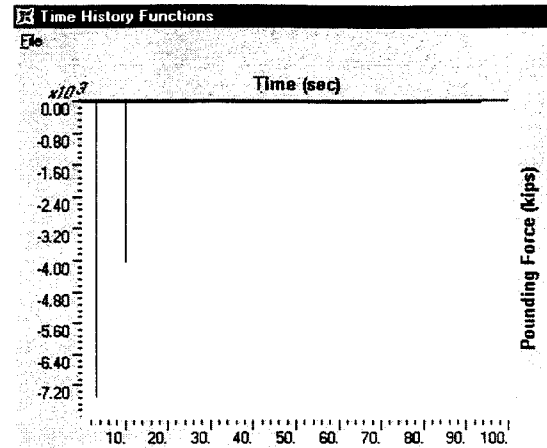


(c) Potential Energy

Figure 4.15. Maximum Energy vs. Stiffness Ratio

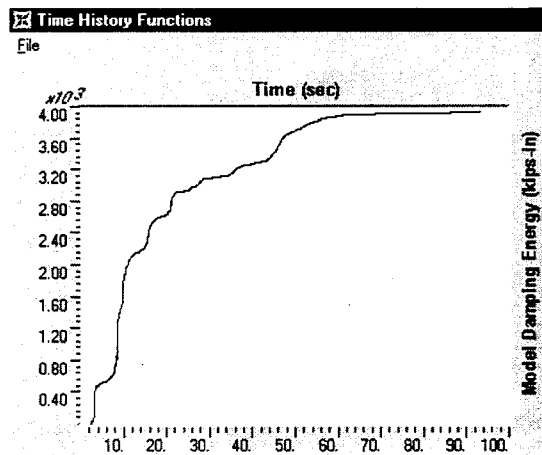


Stiffness Ratio ($K/k=10^3$)

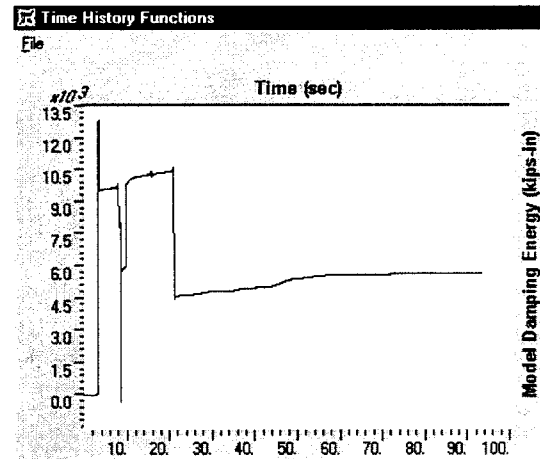


Stiffness Ratio ($K/k=10^4$)

Figure 4.16. Pounding Force vs. Stiffness Ratio



Stiffness Ratio ($K/k=10^7$)



Stiffness Ratio ($K/k=10^8$)

Figure 4.17. Damping Energy vs. Stiffness Ratio

Based on the above analysis, the following observations are made:

1. The pounding force from the nonlinear gap element is sensitive to stiffness K and it becomes unavailable when K/k exceeds 10^4 .
2. The damping energy directly retrieved from the SAP2000 program is unstable when K/k is larger than 10^7 . However, the total damping energy can be obtained by subtracting the mechanic energy from the input energy as described by Eq. (4.11)
3. Since pounding occurs in an extremely short time, it is difficult to characterize the force generated during the pounding process for practical applications. On the contrary, the seismic responses such as displacement and acceleration include the pounding effects and they can be easily converted into earthquake forces for design purposes. Therefore, a stiffness ratio of 10^9 is recommended to represent the rigid abutment.

4.4. Practical Procedure to Account for Pounding Effect

4.4.1 Equivalent Damping Concept

For a specific structure, the SAP2000 computer code can be used to analyze the structure with pounding effect. However, this approach may not be acceptable for routine design in practice since it is time consuming and requires expertise to do the job. In most cases, engineers are used to analyzing linear structures with the response spectrum method. A simple linear analysis procedure is therefore being developed in this report to take into account the nonlinear behavior of pounding. To this endeavor, the equivalent damping concept is proposed. Considering two SDOF systems of equal mass and stiffness as illustrated in Figure 4.18, one system is horizontally restrained with pounding effect and the other is a linear system and free to move laterally. A design parameter such as the maximum displacement of the linear system in Figure 4.18(b) can be made equal to that of the non-linear system defined in Figure 4.18(a) by selecting its viscous damping coefficient. This coefficient of the linear system is referred to as equivalent damping including the structural damping and pounding effect. Two methods are being developed to determine the equivalent damping. One is based on the equal maximum displacement of the two systems and is referred to as the Displacement Method. The other is based on the minimum difference in the mechanical energy time history of the two systems over the duration of ground motion and is referred to as the Energy Method. Apparently, the Displacement Method captures the instantaneous maximum response of the system, while the Energy Method is focused on the average response of the system.

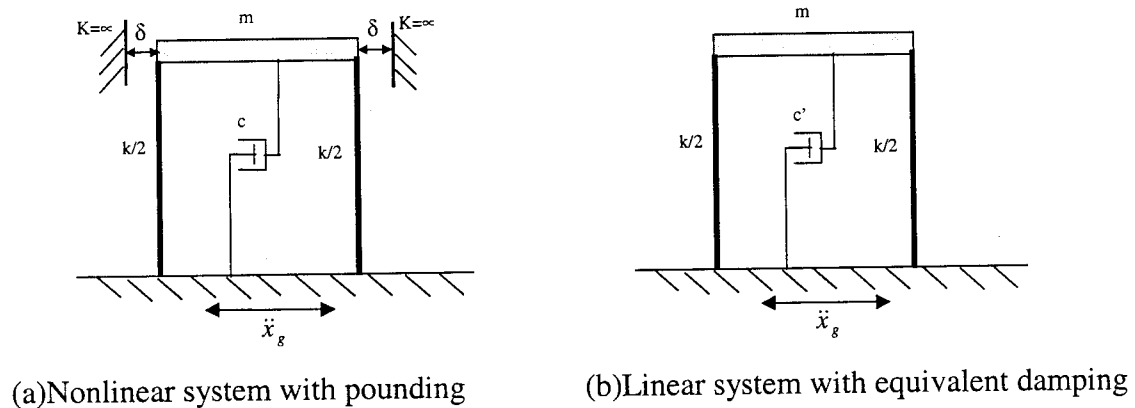


Figure 4.18. Equivalent Damping Concept

4.4.2 Displacement Method

For the linear system in Figure 4.18(b), the maximum displacement under a harmonic excitation can be determined by

$$x_{\max} = \frac{ma}{k} \cdot \left[(1 - \beta^2)^2 + (2\xi'\beta)^2 \right]^{\frac{1}{2}} \quad (4.14)$$

in which ma represents the amplitude of the harmonic excitation and ξ' denotes the damping ratio of the linear system. According to the equivalent damping concept, the maximum displacement (x_{\max}) must be equal to the gap width (δ). From this relation, the equivalent damping ratio (ξ') can be written as a function of the gap width:

$$\xi' = \frac{\left\{ \left(\frac{k\delta}{ma} \right)^{-2} - (1 - \beta^2)^2 \right\}^{\frac{1}{2}}}{2 \cdot \beta} \quad (4.15)$$

Since it is straightforward to determine the maximum displacement (A_{\max}) of the system defined in Figure 4.18(a) when pounding effect is not considered, the gap width in Eq. (4.15) is normalized by A_{\max} . Eq. (4.15) then becomes:

$$\xi' = \frac{\left\{ \left(\frac{\delta}{A_{\max}} \right)^{-2} \cdot \left[(1 - \beta^2)^2 + (2\xi\beta)^2 \right] - (1 - \beta^2)^2 \right\}^{\frac{1}{2}}}{2 \cdot \beta} \quad (4.16)$$

Eq. (4.16) indicates that, under harmonic excitations, the equivalent damping ratio changes nonlinearly with the normalized gap width (δ/A_{\max}), frequency ratio (β) and structural damping ratio (ξ). Their relations are depicted in Figures 4.19-4.21. It is observed from Figure 4.19 that the equivalent damping ratio decreases as the gap widens and eventually approaches the structural damping ratio when pounding does not occur. The equivalent damping curves are exactly the same for frequency ratios $\beta = 0.5$ and $\beta = 2$ under the harmonic excitation, which can easily be verified by checking Eq. (4.16). Figure 4.20 shows that the equivalent damping ratio is the smallest at resonance since the response is amplified significantly under this condition. The equivalent damping changes with the frequency ratio more rapidly when $\beta < 1$ than when $\beta > 1$. As indicated in Figure 4.21, the effect of the structural damping on the equivalent damping is negligible unless the bridge system is at resonance.

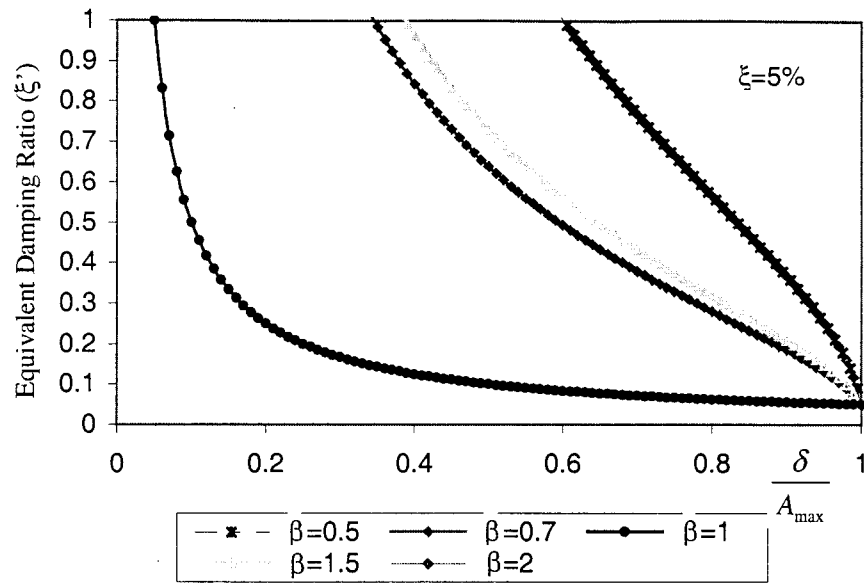


Figure 4.19. Equivalent Damping Ratio vs. Normalized Gap Width

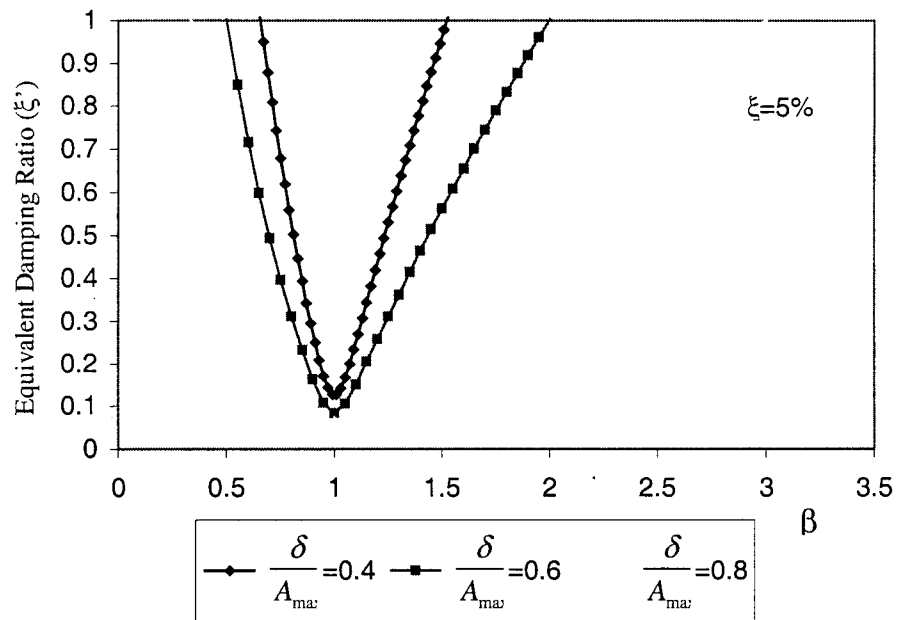


Figure 4.20. Equivalent Damping Ratio vs. Frequency Ratio

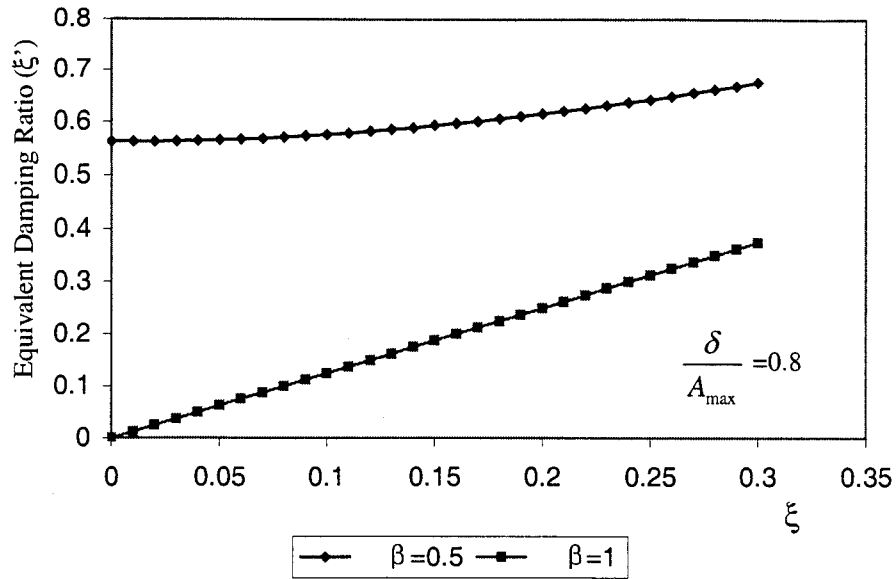
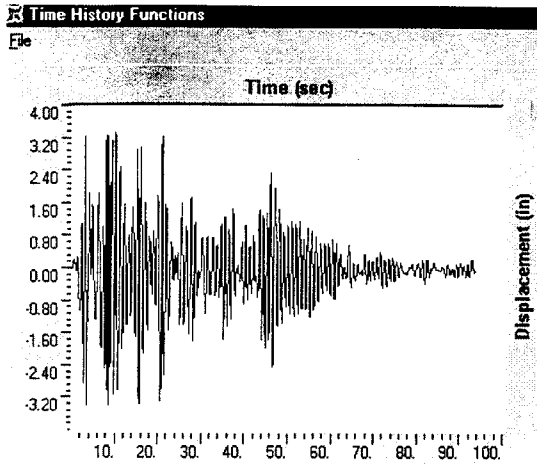


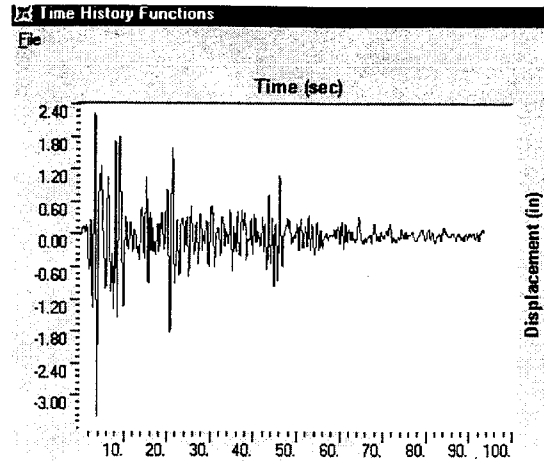
Figure 4.21. Equivalent Damping Ratio vs. Structural Damping Ratio

The above discussion under harmonic loads gives one a general concept of how the equivalent damping changes with such key factors as gap width, frequency ratio, and structural damping. Under earthquake loading, the frequency ratio is interpreted as the ratio between the dominant frequency of the earthquake excitation and the natural frequency of the structure. The maximum displacement of the structure without consideration of pounding effect (A_{\max}) is again used to normalize the gap width. In what follows, the equivalent damping ratio of a general SDOF system shown in Figure 4.18 is determined under the twelve earthquake records listed in Table 4.1. As an example, the displacement time history of the system with pounding effect and the corresponding linear system of the equivalent damping are illustrated in Figure 4.22 under the S00E Component of the El Centro Earthquake record (Elcs00e). It is observed that these two systems have the same maximum displacement even though they respond to the earthquake quite differently. The former system has experienced the maximum displacement many times while the latter system has once. This result reflects the essence of the Displacement Method.



Max Displacement = 3.36 in

a) Structure with pounding, $\xi = 0.05$



Max Displacement = 3.36 in

b) Structure without pounding, $\xi' = 0.385$

Figure 4.22. Comparison of Displacement Time Histories

Since structures are subjected to the maximum displacement at resonance, the following study is focused on the development of design equations for $\beta = 0.5$, 1.0 and 2.0 . The equivalent damping ratio of the SDOF system is plotted in Figures 4.23-4.25 as a function of the normalized gap width when the system is excited by the twelve earthquake records. It can be clearly observed from the figures that under earthquake loading the equivalent damping is larger for $\beta = 1$ and smaller for $\beta = 0.5$ or $\beta = 2.0$ than that due to harmonic loads. This is because earthquakes involve many frequency components. Although their dominant frequency is equal to the natural frequency of the SDOF system for the case of $\beta = 1$, other components do not cause resonance of the system. As a result, the equivalent damping must be larger. For the case of $\beta = 0.5$ or $\beta = 2$, there may be some frequency components close to the natural frequency of the system and, therefore, the equivalent damping is smaller. It is also seen from Figures 4.23-4.25 that the equivalent damping associated with the Mexico Earthquake records (Mexs00e and Mexn90w) is significantly closer to that under harmonic loading since these records have a narrow frequency band as indicated in Table 4.1. To reflect the random nature of general earthquakes, the Mexico Earthquake is excluded in the following development of design equations. The average curves and regression curves of the equivalent damping under ten earthquakes are presented in Figures 4.26-4.28. Based on the insight gained under harmonic loading, a power regression algorithm was used to best fit the original data. The regression analysis results in the following design equations:

$$\xi' = 0.0671 \cdot \left(\frac{\delta}{A_{\max}} \right)^{-1.52} \quad \text{for } \beta = 1.0 \quad (4.17)$$

$$\xi' = 0.0767 \cdot \left(\frac{\delta}{A_{\max}} \right)^{-1.71} \quad \text{for } \beta = 0.5 \quad (4.18)$$

$$\xi' = 0.0899 \cdot \left(\frac{\delta}{A_{\max}} \right)^{-1.71} \quad \text{for } \beta = 2.0 \quad (4.19)$$

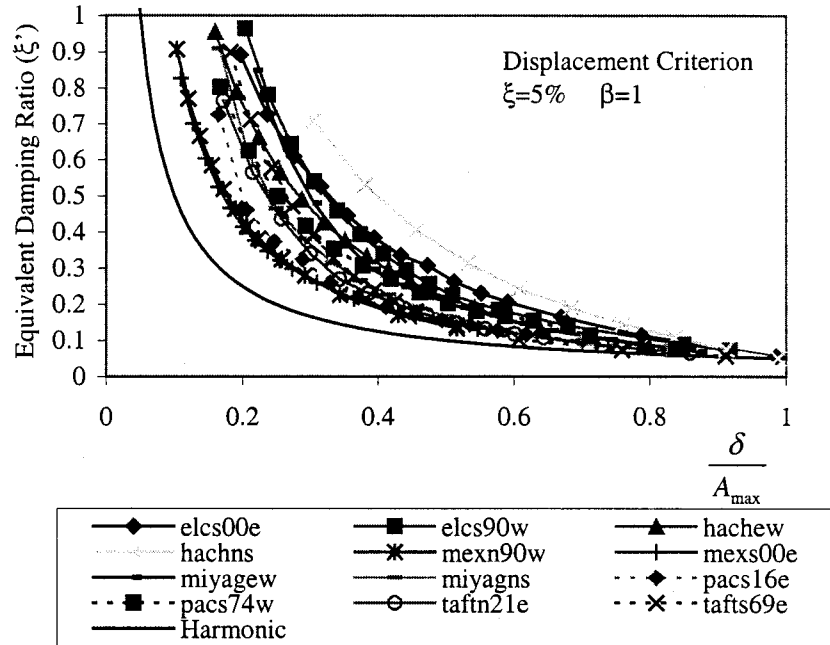


Figure 4.23. Displacement-Based Equivalent Damping Ratio for $\beta = 1$

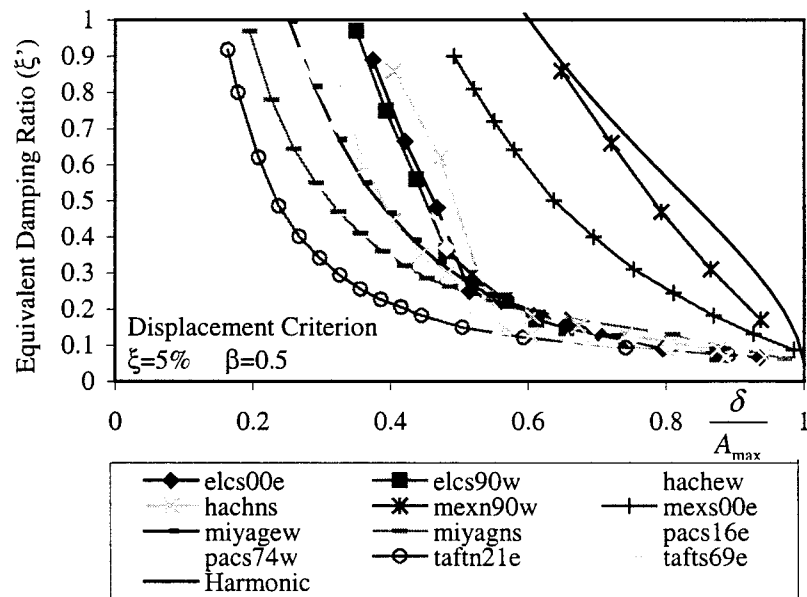


Figure 4.24. Displacement-Based Equivalent Damping Ratio for $\beta = 0.5$

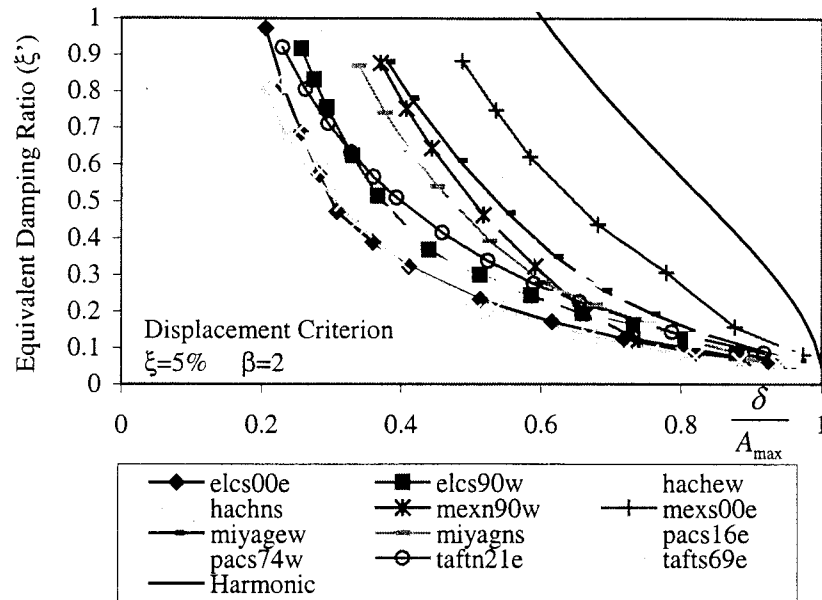


Figure 4.25. Displacement-Based Equivalent Damping Ratio for $\beta = 2$

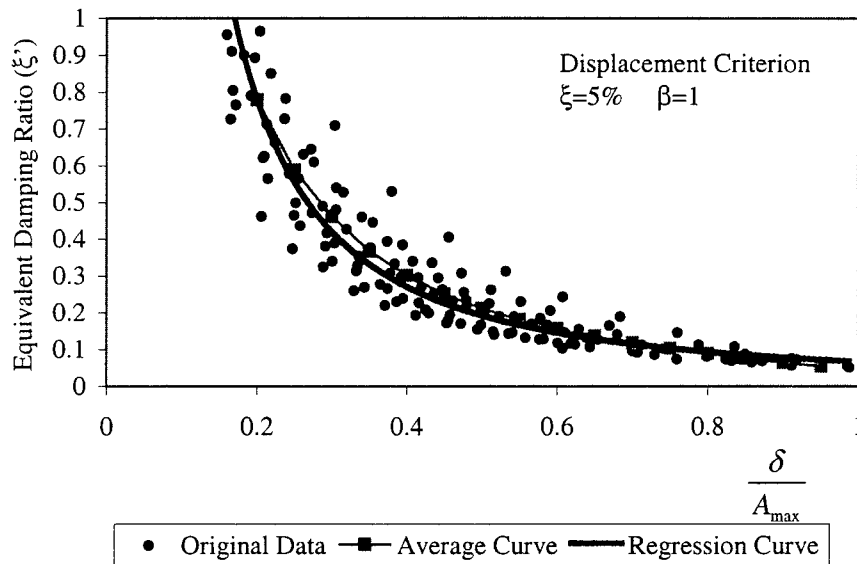


Figure 4.26. Displacement-Based Design Equation for $\beta = 1$

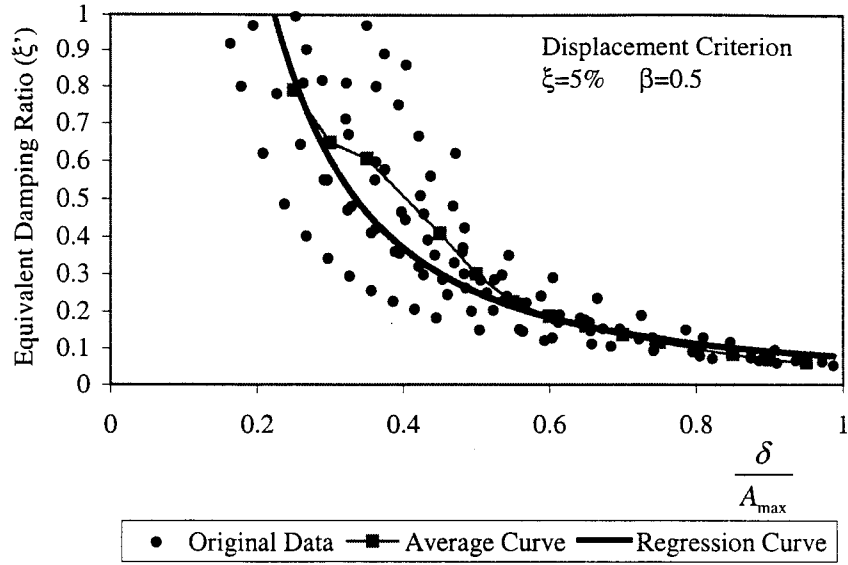


Figure 4.27. Displacement-Based Design Equation for $\beta = 0.5$

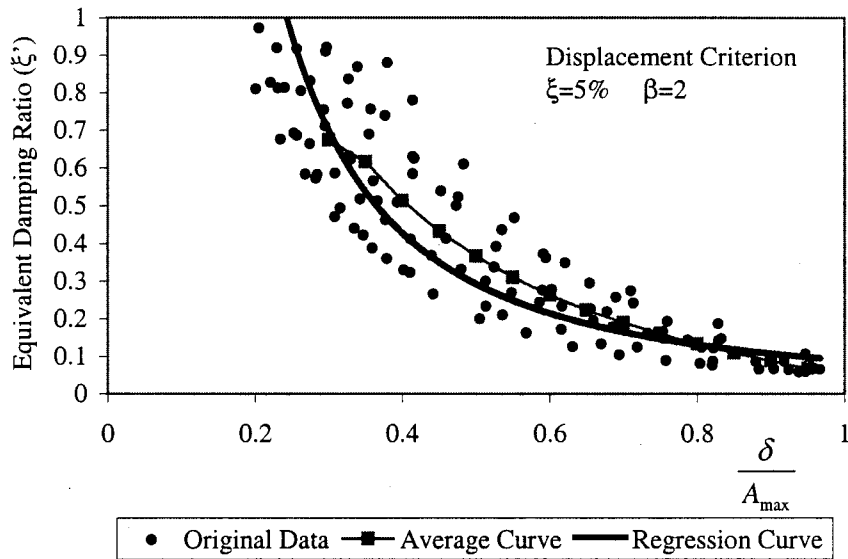


Figure 4.28. Displacement-Based Design Equation for $\beta = 2$

4.4.3 Energy Method

The Displacement Method is focused on the maximum displacement at one instant only. Structural behaviors may be better captured with a design parameter that represents the overall average of earthquake effects over the entire duration. The equivalence of mechanical energy in two systems with and without pounding effect was used as another criterion to develop the equivalent damping. Mechanical energy includes two parts: potential energy and kinetic energy. Together they may provide a good indication of the state of structural responses. The energy-based equivalent damping is

determined by minimizing the overall difference of the mechanical energy of two systems. That is,

$$\left. \begin{aligned} M &= \sqrt{\frac{1}{T} \cdot \int_0^T [E_{m_{pd}}(t) - E_{m_{nopd}}(t)]^2 dt} \\ M_{\min} &= \min(M) \end{aligned} \right\} \quad (4.20)$$

where $E_{m_{pd}}$ and $E_{m_{nopd}}$ denote the mechanical energy of the system with pounding and without pounding, respectively; T is the duration of the earthquake; and M_{\min} is the minimum value of the mechanical energy difference M . The mechanical energy difference above is a function of the damping ratio of the linear system without pounding effect. Figure 4.29 shows the function under the Miyagiken Oki Earthquake (Miyagew), and the equivalent damping ratio ξ' corresponding to M_{\min} . It can be observed that the mechanical energy difference changes slightly with the damping ratio when it is larger than the equivalent damping ratio. Figure 4.30 compares the mechanical energy of the two systems with and without pounding. The equivalent damping is included in the system without pounding. Clearly the behavior of the linear system is similar to that of the system with pounding effect during the strong motion.

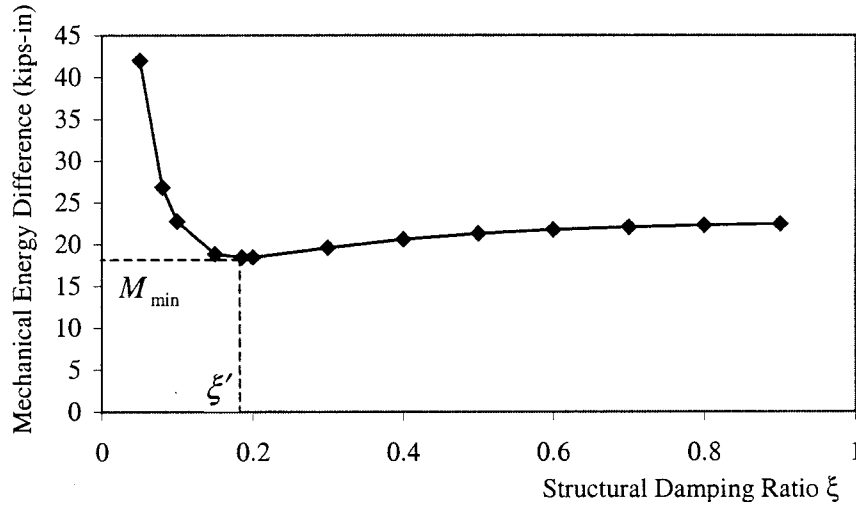


Figure 4.29. Mechanical Energy Difference vs. Damping Ratio of Linear System

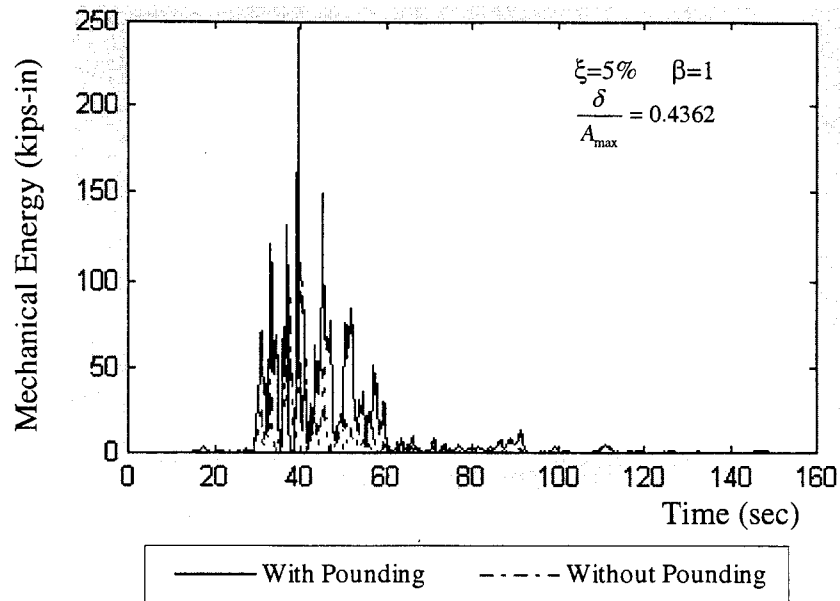


Figure 4.30. Mechanical Energy under the Miyagiken Earthquake

Since the Energy Method captures the gross feature of response histories, it is very complicated, if not impossible, to derive an equation for the equivalent damping ratio under harmonic loading as done in the Displacement Method. Due to the nonlinear behavior of pounding effect, a nonlinear time history analysis must be used to derive the mechanical energy time history of the system with pounding effect. Based on the energy criterion, the equivalent damping ratio for $\beta = 0.5$, 1.0 and 2.0 are plotted in Figures 4.31-4.33 under the harmonic and twelve earthquake excitations.

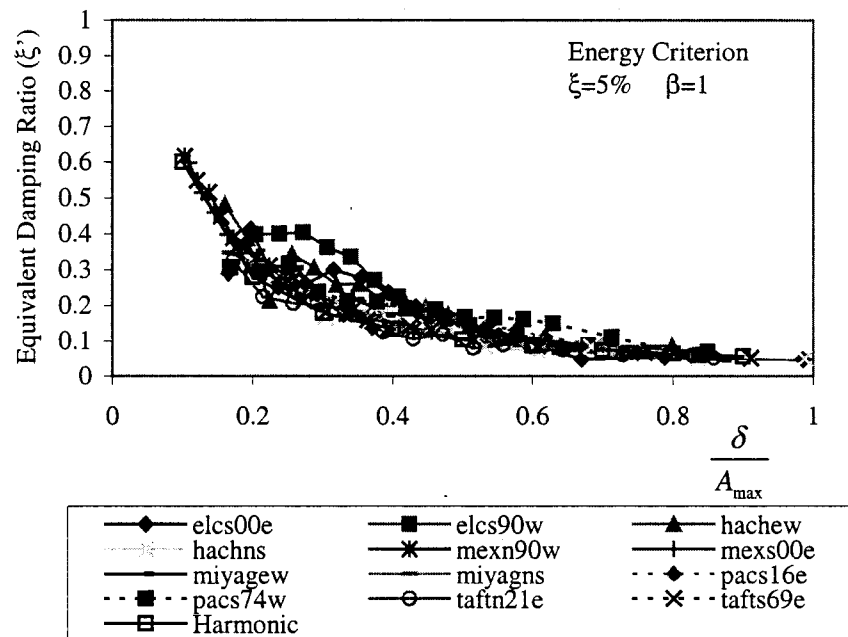


Figure 4.31. Energy-Based Equivalent Damping Ratio for $\beta = 1$

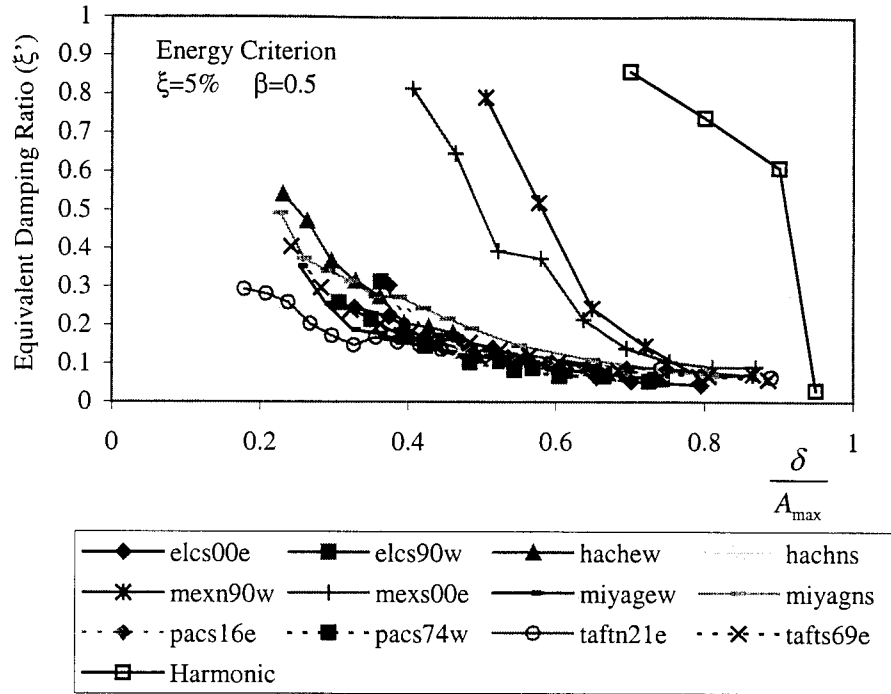


Figure 4.32. Energy-Based Equivalent Damping Ratio for $\beta = 0.5$

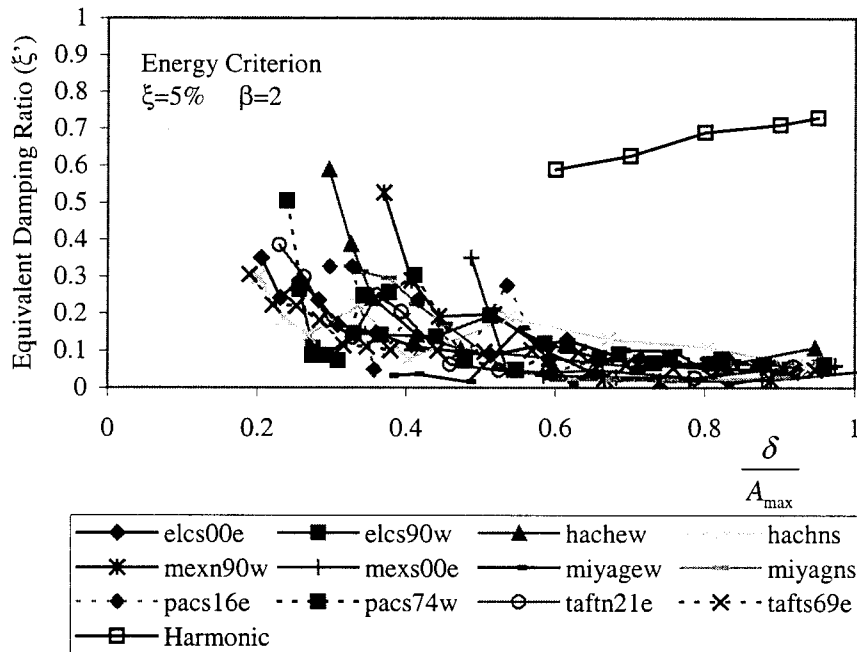


Figure 4.33. Energy-Based Equivalent Damping Ratio for $\beta = 2$

In comparison with Figures 4.23-4.25, the equivalent damping ratio curves based on the energy criterion are no longer as smooth as those based on the displacement criterion and their magnitudes are significantly smaller. The energy criterion is aimed at capturing the global variation of the energy history which is greatly influenced by several factors in a complicated way. The local rise and fall of the equivalent damping ratio

curves reflects the non-linear behavior of the pounding effect as well as the phase difference of the mechanical energy history for the system with and without pounding as indicated in Figure 4.34. The difference in phase makes the equivalent damping ratio possibly smaller than its neighbor points. As β increases, pounding occurs more frequently. As a result, Figure 4.33 corresponding to $\beta = 2$ shows more significant fluctuation of the equivalent damping ratio curves. Even under harmonic loads, the damping curve is exceptionally high for $\beta = 0.5$ and $\beta = 2$. This result is mainly due to splitting of the peaks of the harmonic responses as indicated in Figure 4.3. The equivalent damping ratio curves under the Mexico Earthquake (Mexn90w and Mexs00e) generally follow the results under the harmonic loads due to their narrow bandwidth.

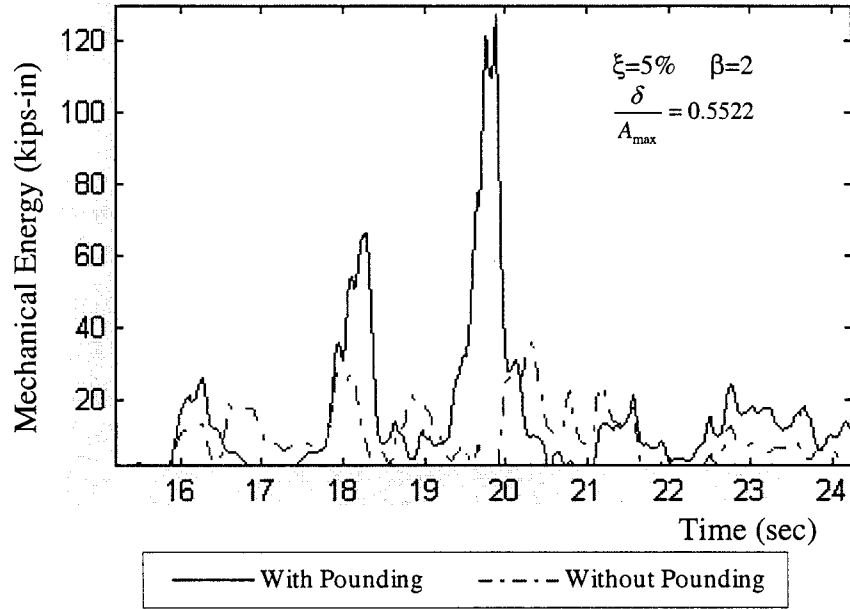


Figure 4.34. Mechanical Energy under Miyagew Earthquake

Similar to the Displacement Method, the Mexico Earthquake records were excluded in the statistical analysis. The average curves and regression curves are shown in Figures 4.35-4.37 based on the remaining ten earthquake records. These curves are very similar and both represent the original data very well. The regression curves can be expressed as:

$$\xi' = 0.0537 \cdot \left(\frac{\delta}{A_{\max}} \right)^{-1.20} \quad \text{for } \beta = 1.0 \quad (4.21)$$

$$\xi' = 0.0468 \cdot \left(\frac{\delta}{A_{\max}} \right)^{-1.44} \quad \text{for } \beta = 0.5 \quad (4.22)$$

$$\xi' = 0.0406 \cdot \left(\frac{\delta}{A_{\max}} \right)^{-1.27} \quad \text{for } \beta = 2.0 \quad (4.23)$$

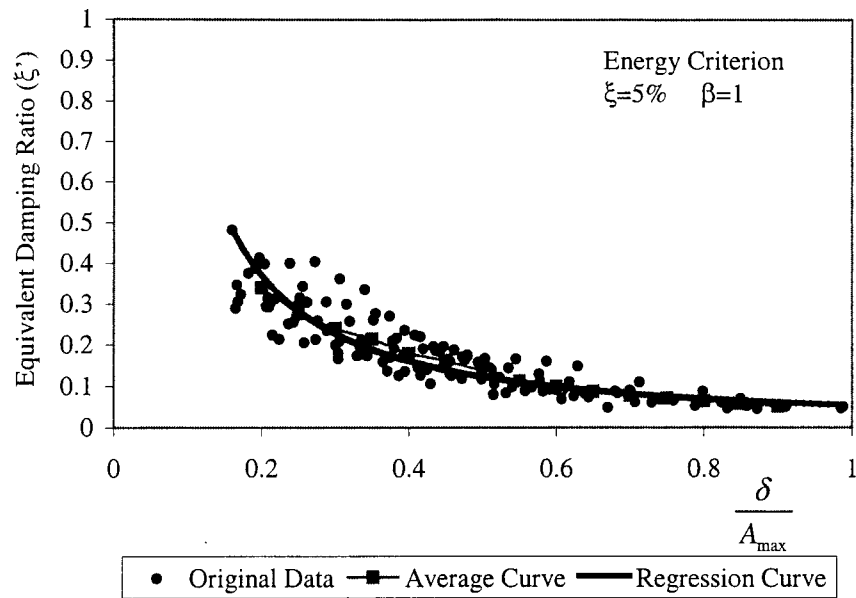


Figure 4.35. Energy-Based Design Equation for $\beta = 1$

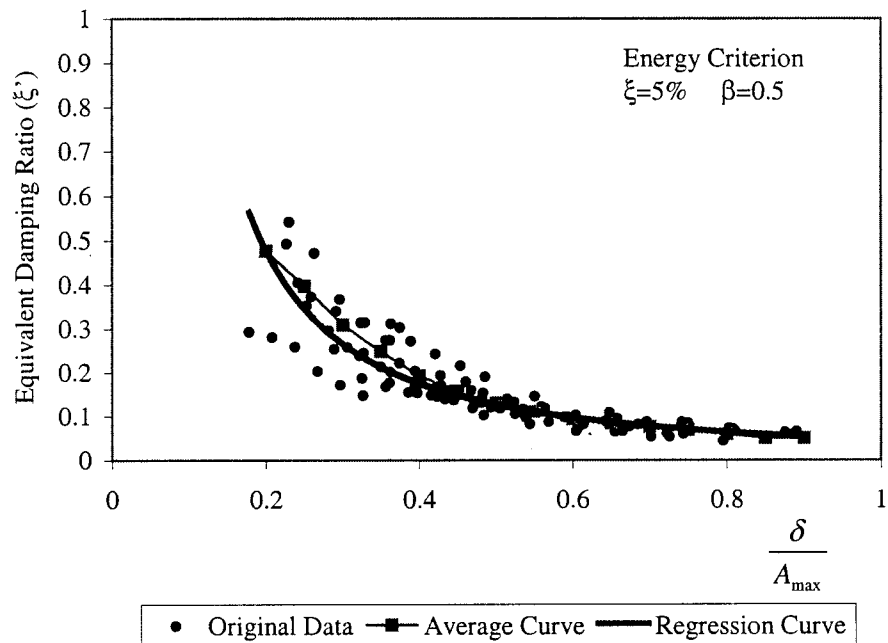


Figure 4.36. Energy-Based Design Equation for $\beta = 0.5$

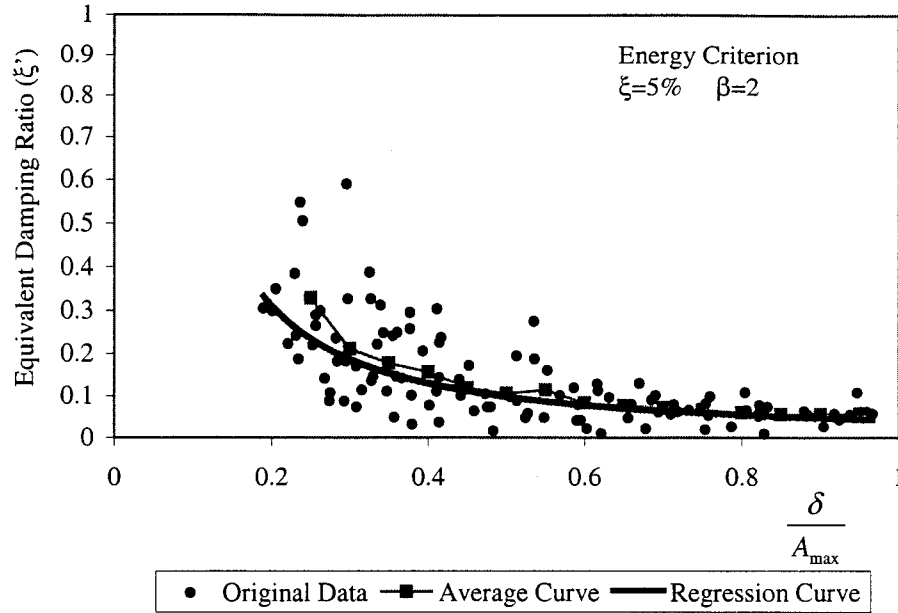


Figure 4.37. Energy-Based Design Equation for $\beta = 2$

4.5. Summary

An equivalent damping concept was proposed to take into account pounding effect on the seismic responses of highway bridges in linear analyses. Both the Displacement Method and Energy Method were developed to determine the equivalent damping as a function of the gap width of expansion joints, structural dynamics and earthquake characteristics. Based on the extensive numerical simulations under harmonic loading and twelve earthquake loads (ground accelerations) measured during six historical earthquakes, the following observations can be made:

1. Pounding reduces the maximum displacement of a structure and may amplify its acceleration due to impulsive pounding force. Reduction in displacement actually leads to the release of stress in columns and therefore, pounding effect is equivalent to the addition of damping.
2. The equivalent damping strongly depends upon the gap width of expansion joints and the dominant frequency of excitations. There is no conclusive interrelation between the equivalent damping and the frequency bandwidth.
3. The equivalent damping associated with harmonic loading is the lower bound at resonance and the upper bound under non-resonant situations of those corresponding to the earthquake excitations of various frequency spectra.
4. Two sets of design equations were developed based on the equivalence of the maximum displacement in the Displacement Method and the mechanical energy in the Energy Method. They were formulated from the regression analysis of the equivalent damping data under ten actual earthquake records.
5. The equivalent damping on the energy basis reflects the global feature of dynamic responses over the earthquake duration while the Displacement Method signifies the importance of the maximum responses at one instant. Consequently, the former is significantly smaller than the latter.

5. APPLICATION OF THE EQUIVALENT DAMPING PROCEDURE TO BRIDGE A-237R

Bridge A-237R on US Highway 60 is a three-span continuous, steel-girder bridge. It carries four-lane traffic. The general elevation of the bridge is illustrated in Figure 5.1. The bridge is supported on two seat type abutments and two RC piers. All substructures (abutments and piers) are supported by pile foundations. The two expansion joints are located at the ends of the bridge deck. Under a strong earthquake, pounding between the deck and the abutments may occur when the response of the superstructure exceeds the available gap width. To validate the equivalent damping procedure developed in Section 4 and understand the effect of soil non-linearity on bridge pounding, the bridge is being analyzed using three models. In the first model, the entire bridge system including foundation, substructure, superstructure and expansion joints are modeled using FEM. Both pounding and the nonlinear behavior of pile foundation are taken into account. This model represents the most sophisticated one and serves as a benchmark to show the efficiency of the proposed equivalent damping procedure. The second model is the same as the first one except that the expansion joints are not included and an equivalent damping ratio from Eqs. (4.17-4.19) and (4.21-4.23) was used as modal damping for the vibration mode in longitudinal direction. The last model is similar to the second model except for the linear modeling of foundation stiffness. Since the first two models account for the non-linearity of soil property, their response are determined using the time history analysis. The last model is linear. Its responses are calculated using three procedures: time history analysis (THA), response spectrum analysis (RSA), and the AASHTO single mode spectrum analysis (SMSA). The relation between model and analysis procedure is summarized in Table 5.1. The intent of using RSA and SMSA for the bridge responses is to provide a simple tool incorporating the equivalent damping concept for practical applications.

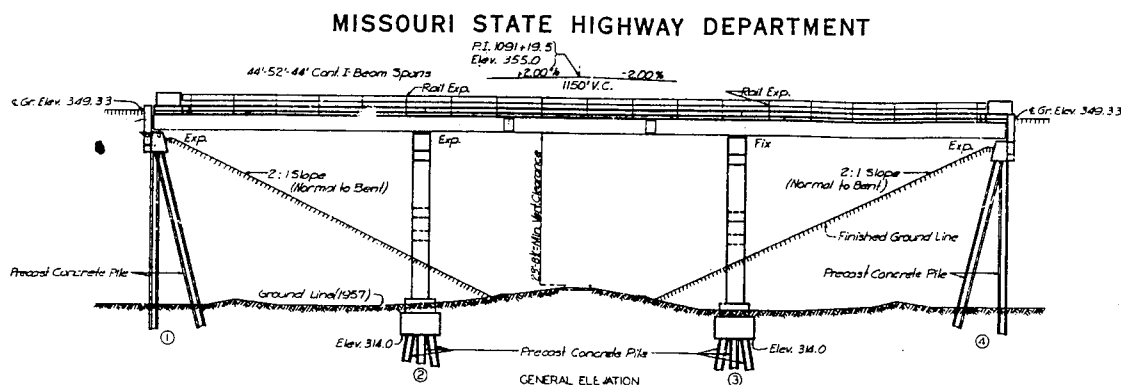


Figure 5.1. General Elevation of Bridge A-237R

Table 5.1. Computer Model and Analysis Procedure

Computer Model	Analysis Procedure		
	Time History Analysis	Response Spectrum Analysis	AASHTO Procedure
1	Case 1		
2	Case 2		
3	Case 3	Case 4	Case 5

5.1 FEM Modeling

Three models were developed using FEM for Bridge A-237R. The individual components of the superstructure, substructure and bearings are explicitly modeled. At the location of footing foundations, a set of springs was used to model the rigidity of piers and surrounding soil mass. The determination of foundation stiffness and the detailing of the superstructure and substructure components in the first model are discussed below.

5.1.1 Foundation

The bridge foundation system consists of pile groups and footings (or pile caps). To take into account the soil-structure interaction effect under earthquake loading, the foundation stiffness due to soil flexibility is determined below.

5.1.1.1 Soil Property Estimation

The subsurface exploration was made at one location of the bridge site during the construction. The soil profile determined from sampling during the Standard Penetration Test (SPT) is shown in Figure 5.2. As one can see, most soils at the site are cohesionless. The SPT blow counts shown in the figure have been corrected to account for the overburden pressure (Bowels, 1990). They are used to estimate the unit weight and internal friction angle based on the empirical relation in Bowels. These soil properties, the corrected SPT blow counts, and the thickness of each layer of soil deposit are presented in Table 5.2. To validate the estimation of soil properties, the load test results of a pile located near the bridge site are compared with those calculated based on the estimated parameters. The bearing capacity of the tested pile is shown in Figure 5.3. The corresponding theoretical values at various depths were computed using the SPILE program and they are compared in Table 5.3 with the test results. It can be seen that the theoretical and experimental results are in reasonably good agreement considering the limited test data used for calibration. The foundation stiffness to be determined varies with the soil shear modulus, which is in turn a nonlinear function of strain amplitude, confining stress and soil type. The upper and lower bounds of the normalized shear modulus are expressed in Figure 5.4 (FHWA, 1986) as a function of shear strain. The

maximum shear modulus at the low strain (less than 0.001 percent), G_{max} , can be determined from the SPT blow-counts (FHWA, 1986) and they are related by

$$G_{max} (kip / ft^2) = 245.4 * N^{0.8} \quad (5.1)$$

where N is the SPT value. In this study, a Poisson's ratio of 0.35 is considered for the cohesionless soil.

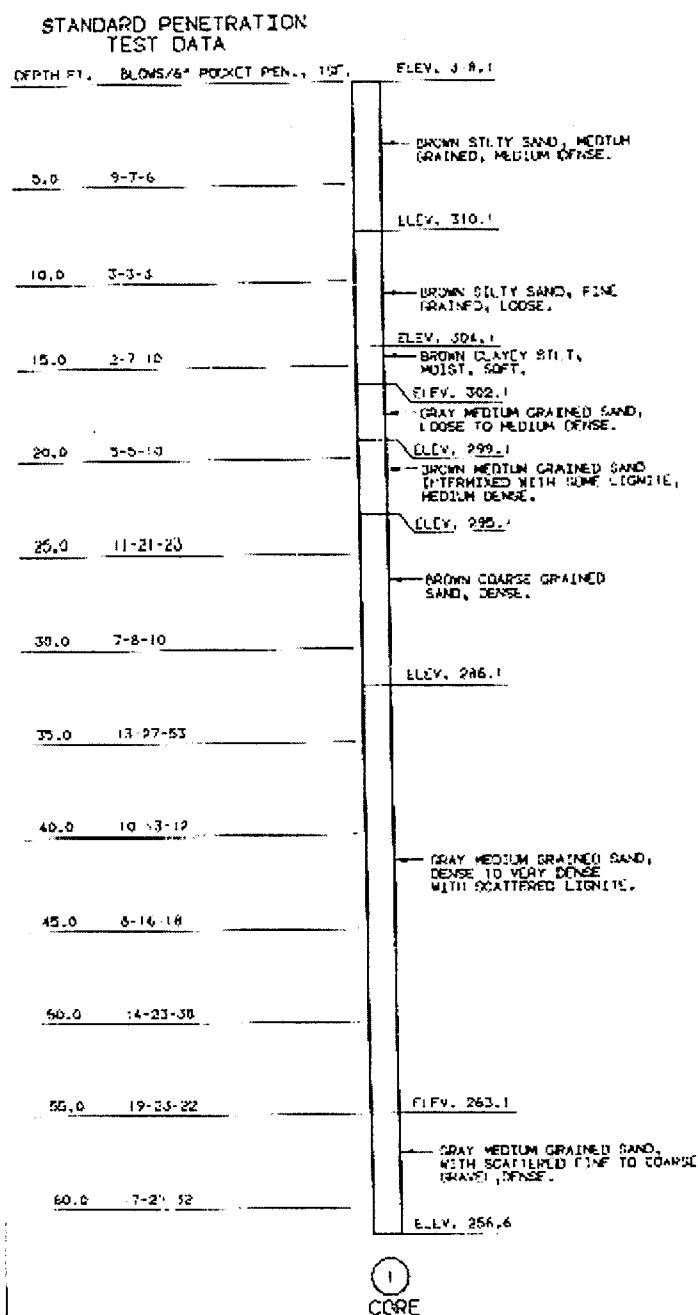


Figure 5.2. Standard Penetration Test (SPT) Blow-Count Values

Table 5.2. Estimated Soil Properties

Layer	Soil Type	Thickness (ft)	Unit weight (pcf)	Internal Friction Angle	Corrected SPT Blow Count
1	Brown silty sand	8	125	32	18
2	Brown silty sand	6	100	29	7
3	Brown clayey silt	2	135	32	18
4	Gray medium grained sand	3	120	31	14
5	Brown medium grained sand	4	125	31	14
6	Brown coarse grained sand	9	130	32	18
7	Gray medium grained sand	23	135	34	22
8	Gray medium grained sand	7	130	35	26

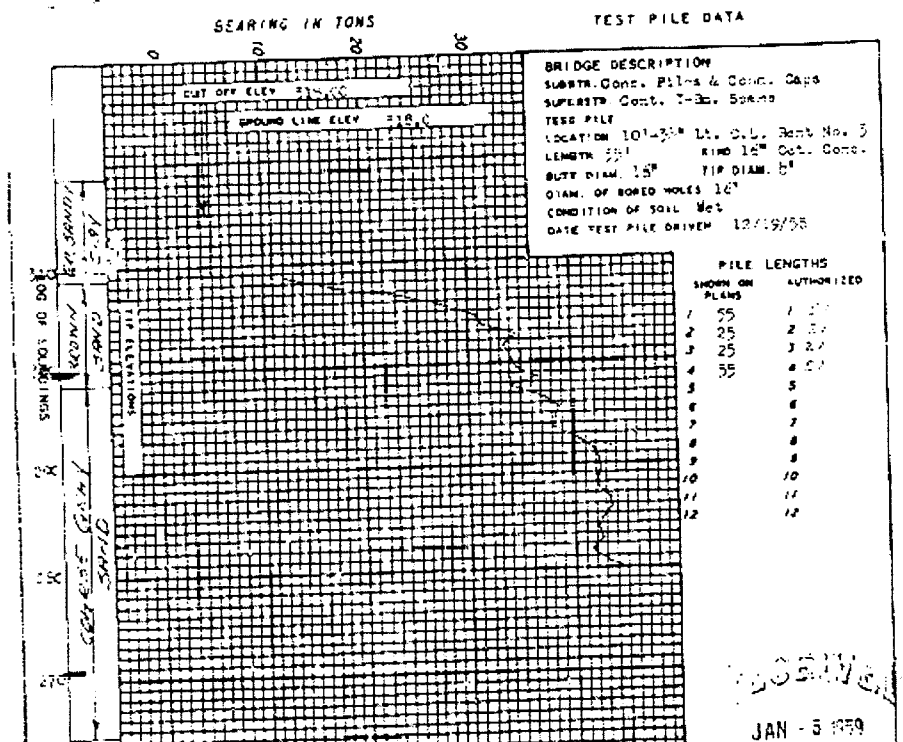


Figure 5.3. Pile Bearing Capacity From in-Situ Test

Table 5.3. Theoretical vs. Experimental Bearing Capacity

Depth	13 ft	18 ft	28 ft	38 ft
Theoretical Result	42 kips	43 kips	80 kips	131 kips
Test Result	56 kips	69 kips	85 kips	90 kips

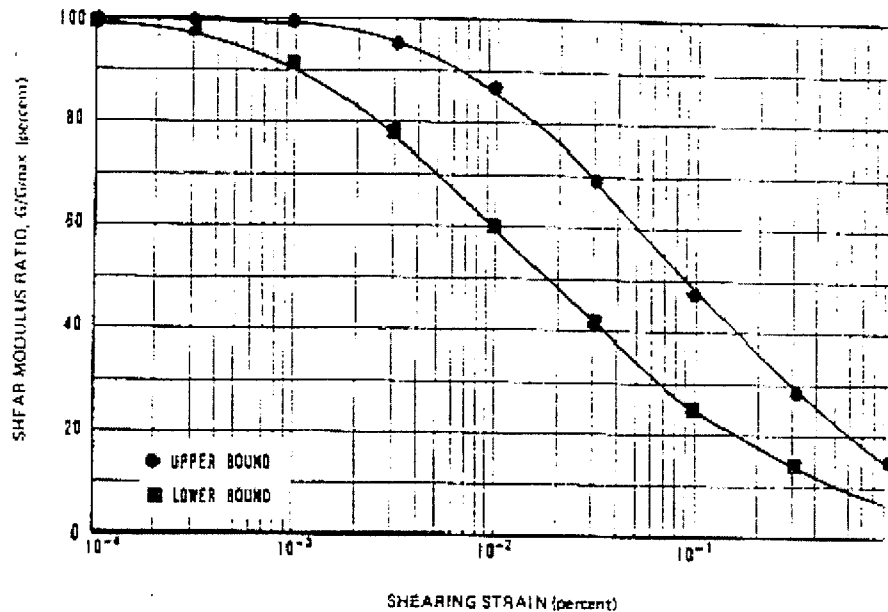


Figure 5.4. Variation of Shear Modulus With Shear Strain Amplitude

5.1.1.2 Foundation Stiffness

When a bridge interacts with soil and foundation during earthquakes, the stiffness of the foundation system may affect the overall response of the bridge. For Bridge A-237R, two piers at Bents 2 and 3 are supported by several groups of piles. The two abutments consist of the backwall, pile caps and piles. The stiffness of each individual component such as the backwall, pile cap and a single pile are analyzed as follows. In this study, the dynamic effect on the foundation stiffness is neglected since the natural frequency of the bridge is expected to be significantly smaller than 3 Hz (FHWA, 1986).

Footing Stiffness. Bridge A-237R uses the embedded footings for the pile foundations at Bents 2 and 3 as well as abutments. The embedment is effective to develop the side friction between a footing (pile cap) and its surrounding soil only when dense granular backfill is used. The lateral resistance of the footing is therefore neglected in most applications, though it may contribute to the lateral load capacity. In addition, the soil beneath the base of the footing may settle and separate from the footing. Therefore, the footing stiffness at the abutments and pile caps is neglected in this report.

Single Pile Stiffness. A single driven pile in soil may experience the axial and lateral displacements as well as rotating about three principal axes under earthquake loads. In general, the lateral soil reactions are developed within the top 5 to 10 pile diameters while the axial soil resistance is developed at greater depths. Therefore, the axial and lateral pile stiffness can be determined separately.

The seismic behavior of a vertical pile depends on its axial pile stiffness, and the shear-transfer characteristics along the side of the pile and at the pile tip. The elasticity of the pile member, or pile compliance, can be taken into account with a simple mechanical approach. The soil-related vertical pile stiffness consists of two parts: side-friction capacity over the pile length and ultimate resistance at the pile tip. They were determined using the SPILE program for soil profiles with nonlinear properties. A set of nonlinear curves to characterize the transferring of axial loads is referred to as q-z curve. The load transfer-displacement relationship can be simply expressed as (FHWA, 1986)

$$f = f_{\max} \times \left(2\sqrt{\frac{z}{z_{c1}}} - \frac{z}{z_{c1}}\right) \quad \text{for side friction force} \quad (5.2)$$

$$q = q_{\max} \times \left(\frac{z}{z_{c2}}\right)^{\frac{1}{3}} \quad \text{for end bearing capacity} \quad (5.3)$$

where f is the unit friction mobilized along a pile segment at displacement z ; f_{\max} is the maximum unit friction; z_{c1} is the critical movement of the pile segment at which f_{\max} is fully mobilized; q is the tip resistance mobilized at any value of $z < z_c$; q_{\max} is the maximum tip resistance; z_{c2} is the critical displacement corresponding to q_{\max} . In this study, $z_{c1}=0.2$ in. and $z_{c2}=0.05$ times the pile diameter are used (FHWA, 1986).

The procedure for the determination of the vertical pile stiffness is summarized as follows:

- Step 1. Determine the maximum unit friction and the maximum tip resistance using the SPILE program.
- Step 2. Construct the load transfer characteristic curves along the side of the pile and at the end of the pile according to Eqs. (5.2) and (5.3), respectively.
- Step 3. Construct the load-displacement curve by summing the load values of side-friction and tip-resistance curves at a given displacement value.
- Step 4. Add the pile compliance into the above load-displacement relation to formulate the total pile vertical load-displacement curve.

The pile vertical load-displacement curves for abutment pile and footing pile are illustrated in Figure 5.5. The initial pile vertical stiffness was estimated by the secant modulus of the stiffness which is the slope between the point at which the axial load is equal to zero and the point where the axial load is equal to $q_{\max}/2$.

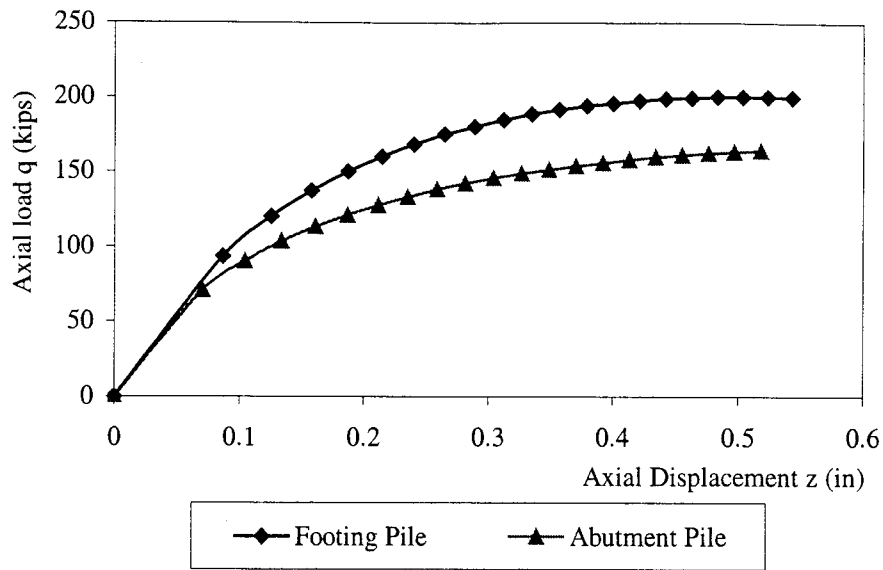


Figure 5.5. Vertical Load-Displacement Relation

The determination of lateral stiffness requires the calculation of a set of p-y curves that relate the lateral soil reaction to the lateral pile deflection. These curves were determined with the COM624P computer program. The nonlinear soil properties were considered in this investigation and an iterative procedure was used to determine the lateral deflection. The load at the pile caps is in equilibrium with the soil reaction and pile resistance. The load-displacement relation at the top of the piles for the abutments and footings are illustrated in Figure 5.6. The initial pile lateral stiffness was determined by using the secant modulus of elasticity of these p-y curves. The secant modulus is defined in the load-displacement curve as the slope between two points corresponding to zero and half the ultimate load capacity, respectively.

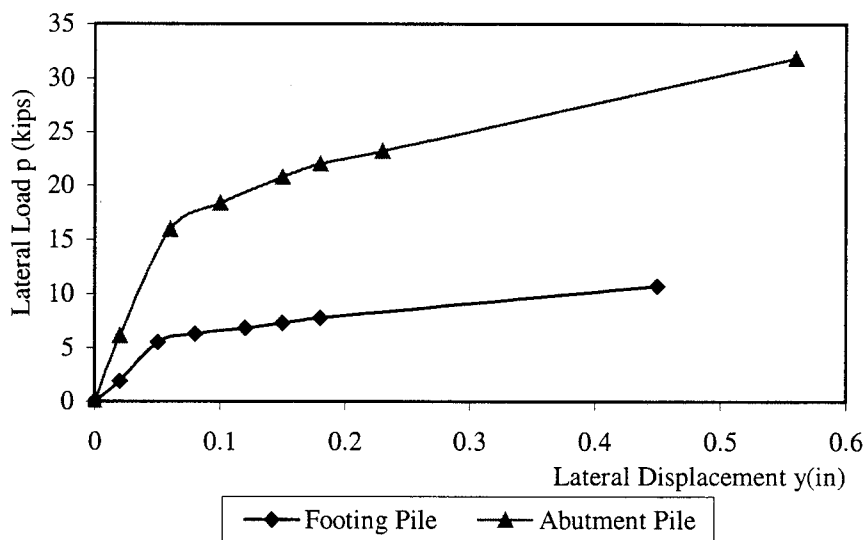


Figure 5.6. Lateral Load-Displacement Relation

Abutment Backwall Stiffness. The abutment stiffness differs before and after the backfill behind the abutment yields. At the low level of stress in backfill, the abutment wall and backfill are both elastic and a linear pressure-displacement relation is developed when the wall is displaced into the backfill. The translational and rotational stiffness of the abutment wall-backfill system can then be developed based on the pressure distribution along the height of the backwall. They can be determined by:

$$k_s = 0.425 \times E_s \times B_w \quad \text{for longitudinal stiffness} \quad (5.4)$$

$$k_r = 0.072 \times E_s \times B_w \times H_s^2 \quad \text{for rotational stiffness} \quad (5.5)$$

where H is the height of the abutment wall; E_s is the Young's modulus of the soil; and B_w is the width of the wall. The stiffness matrix for the abutment backwall can thus be formulated by considering the resultant force at the bottom of the wall.

When the deflection at the top of the wall is greater than approximately 0.5 percent of the height of the abutment, the backfill is considered to have mobilized along a failure surface. The reaction of the backfill becomes constant and it is referred to as passive earth pressure. The resultant of the earth pressure including the horizontal and vertical earthquake effects can be derived using the extended Coulomb sliding wedge theory and it is determined by

$$\left. \begin{aligned} E_{PE} &= \frac{1}{2} \gamma H_s^2 (1 - k_v) K_{PE} \\ K_{PE} &= \frac{\cos^2(\phi - \theta + \beta)}{\cos \theta \cos^2 \beta \cos(\phi - \beta + \theta) \left[1 - \sqrt{\frac{\sin(\phi - \delta) \sin(\phi - \theta + i)}{\cos(\phi - \beta + \theta) \cos(i - \beta)}} \right]^2} \end{aligned} \right\} \quad (5.6)$$

where γ is the unit weight of backfill soil; H_s is the height of soil face; ϕ and φ are the angle of friction among soil particles and between soil and abutment; $\theta = \arctan[k_h/(1 - k_v)]$; k_h and k_v are respectively the horizontal and vertical acceleration coefficient; i is the backfill slope angle; β is the slope of soil face; E_{PE} is the passive force; and K_{PE} is the passive pressure coefficient.

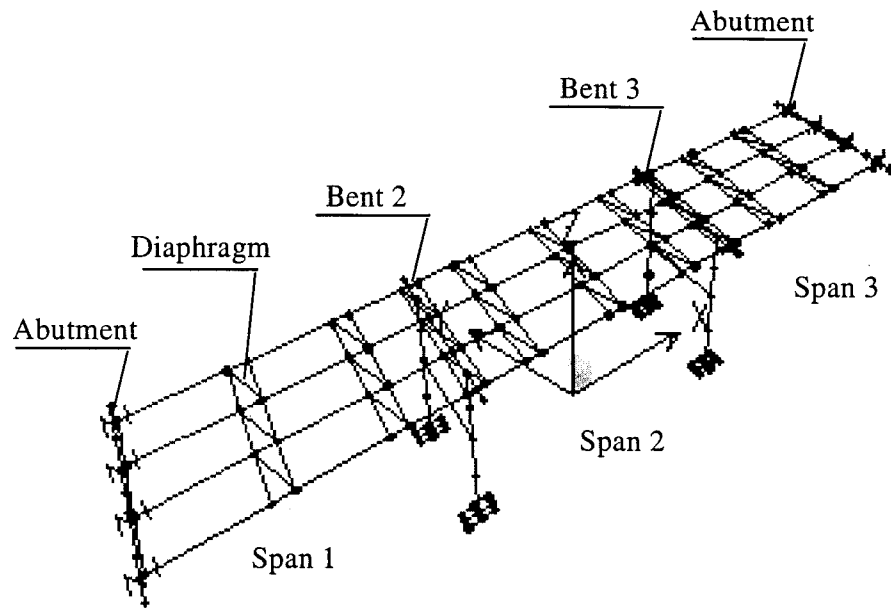
Integrated Stiffness of Foundation System. The stiffness of a group of piles depends upon the rigidity of individual pile and their configuration. In the computer model, a rigid shell element was employed to integrate the stiffness of individual pile and transfer the reaction force and displacement from superstructure to each pile. Rocking of a pile group is mainly resisted by the single pile's vertical stiffness and it is insensitive to the individual pile's rocking stiffness. The deflection of pile groups is significantly affected by the fixity condition of the pile cap. Pile head is fixed in this analysis for conservative consideration. Abutment stiffness can be determined similar to the pile group, considering the piles and abutment backwall contribution.

5.1.1.3 Foundation Damping

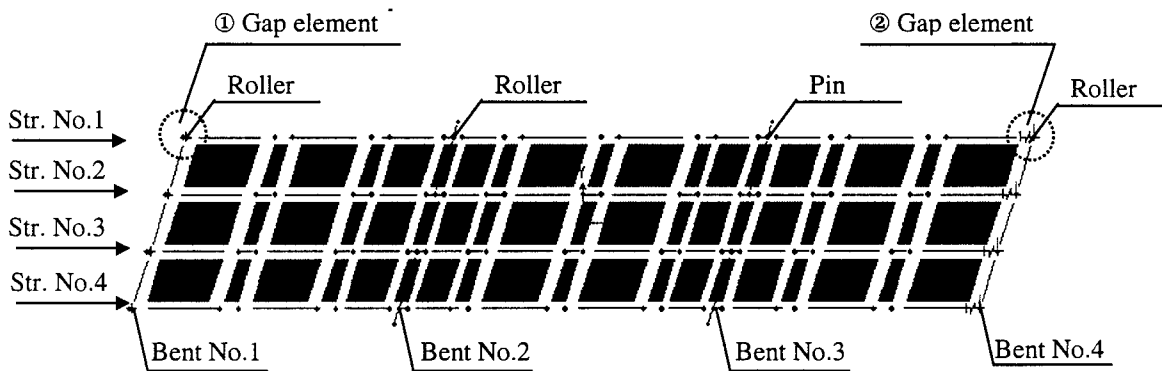
The soil material and radiation damping are important factors in bridge analysis. However, it is very difficult to quantify them with reasonable accuracy. Furthermore, the implementation of the damping as dashpots at the location of pile caps makes the bridge model have a non-classical damping matrix and thus the modal analysis procedure does not apply in a strict sense. This significantly complicates the bridge analysis. Therefore, a model damping of 5% is used in the analysis of Bridge A-237R supported on cohesionless soils as suggested by FHWA (1986).

5.1.2 Superstructure and Substructure

A three-dimensional FEM model was set up for the three span continuous bridge A-237R using the SAP2000 program as shown in Figure 5.7. The concrete bridge deck is modeled using shell elements while the remaining structure components (girders, diaphragms and piers) are modeled using frame elements. Nonlinear link gap elements are used at the two ends of the bridge to represent the expansion joints between the bridge deck and abutment as shown in Figure 5.8. The abutment consists of backwall and pile cap that are supported on the pile foundation. Considering the geometry of the abutment, a rigid beam was used at the abutment to integrate the component stiffness from the backfills behind the concrete wall and pile cap as well as from the pile foundation. To simulate the behavior of expansion bearings, roller supports with restraints in vertical and transverse directions were introduced at two abutments and Bent 2. They are connected to the steel girder elements. For the fixed bearings, pin supports were added between every girder and the cap beam at Bent 3, which prevents relative translational movement in any direction.

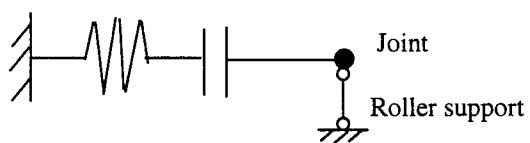


(a) Complete Model

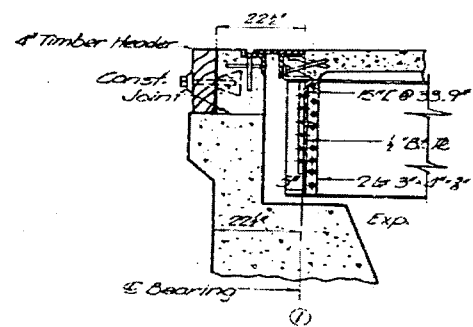


(b) Top View

Figure 5.7. 3-D FEM Model of Bridge A-237R



(a) Modeling



(b) Physical Connection

Figure 5.8. Gap Element

5.2 Dynamic Responses

The fundamental period of the bridge is 1.155 sec. It corresponds to the dominant vibration of the entire bridge in the longitudinal direction (traffic direction). The second vibration mode of period equal to 0.391 sec. represents the local vibration of substructure at Bent 2 due to the presence of expansion joints on the top of the capbeam. The third mode corresponds to the transverse vibration of the entire bridge at the period of 0.148 sec. The fourth vibration mode of period equal to 0.072 sec. corresponds to the longitudinal movement of all substructures without engaging significant motion in the bridge deck. The fifth vibration mode represents the tension and compression motion of the bridge deck only. Its natural period is 0.017 sec.

Due to the nonlinear behavior of soil materials and pounding between bridge deck and abutment, the bridge model discussed in Section 5.1 must be analyzed in theory with a nonlinear analysis procedure. However, the non-linearity of the model is concentrated only in a few components. In this study, an iterative linear analysis procedure is employed by numerically treating the pounding force as part of the load on the bridge model and using the secant stiffness of pile foundations. After the bridge model is analyzed and its responses become available, the secant stiffness is updated. This process continues several times until the secant stiffness is compatible with the load-displacement relation of pile foundations. Every step in the process involves the linear analysis of the same structure but different external loads. The Ritz vectors were selected to accelerate the calculation of the natural frequency, mode shape and response.

5.2.1 Ground Motion

Two synthetic acceleration histories at bedrock with 10% probability of exceedance in 50 years are used in this study. They were generated by a seismologist for another project at the location of the St. Francis River Bridge on U.S Highway 60. This site is near the bridge under investigation. One represents the near-field acceleration (called SF100103) resulting from an earthquake of magnitude 6.2 on the Richter Scale and the other (called SF100203) is a far-field acceleration from a magnitude 7.2 earthquake. The rock motions were propagated through the local soil profile shown in Figure 5.2 to the ground surface at the elevation of footings (pile caps) of pile and abutment foundations using the SHAKE program. These ground acceleration time histories and their corresponding response spectra are illustrated in Figures 5.9-5.12. Their Fourier spectra are presented in Figures 5.13 and 5.14 with the dominant frequencies and bandwidths shown in the legends. The characteristics of the ground motions are listed in Table 5.4.

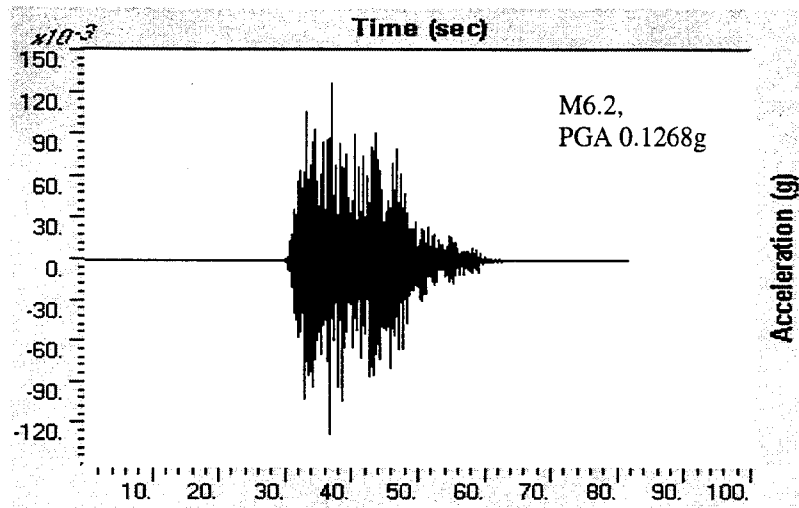


Figure 5.9. Synthetic Ground Motion (SF100103) at Pile Cap Base

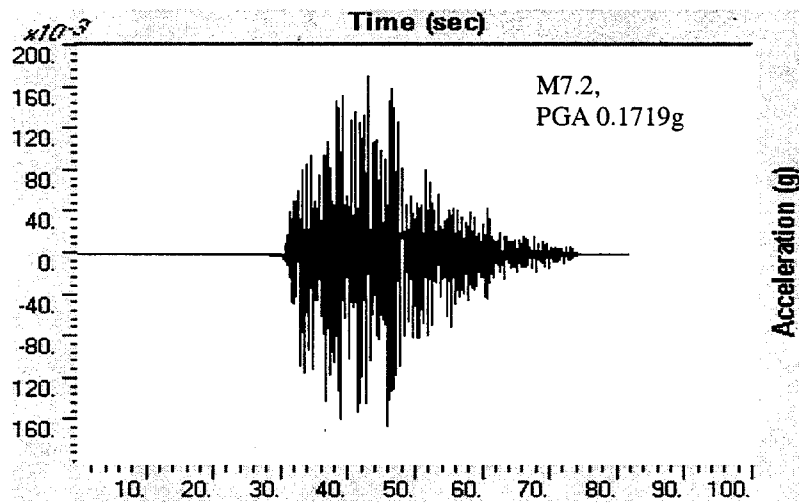
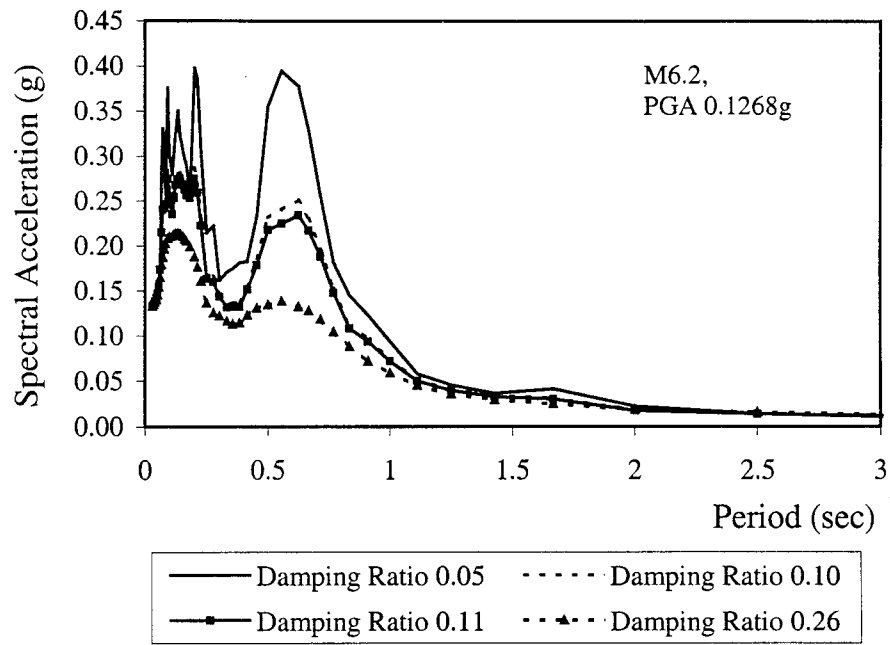
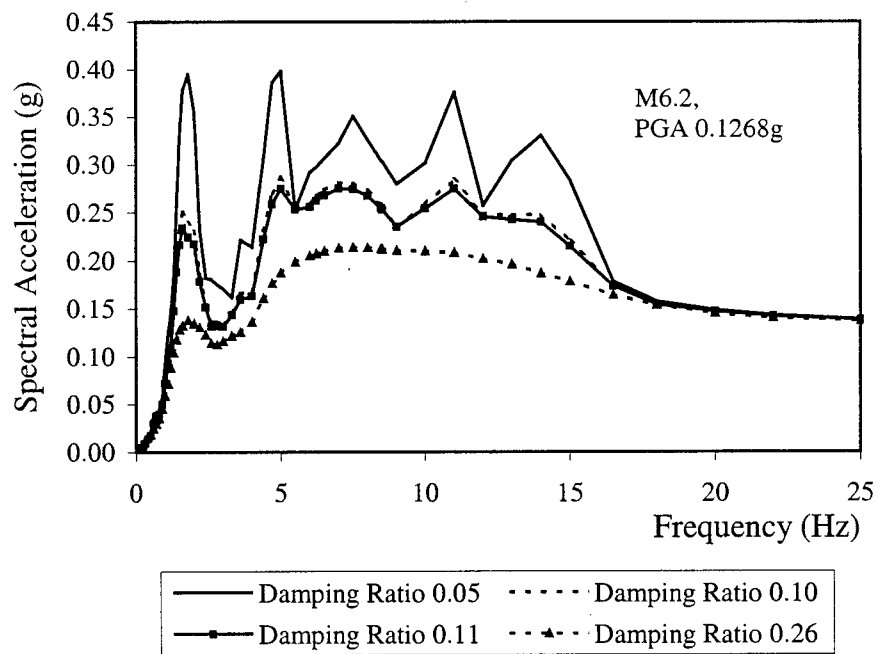


Figure 5.10. Synthetic Ground Motion (SF100203) at Pile Cap Base

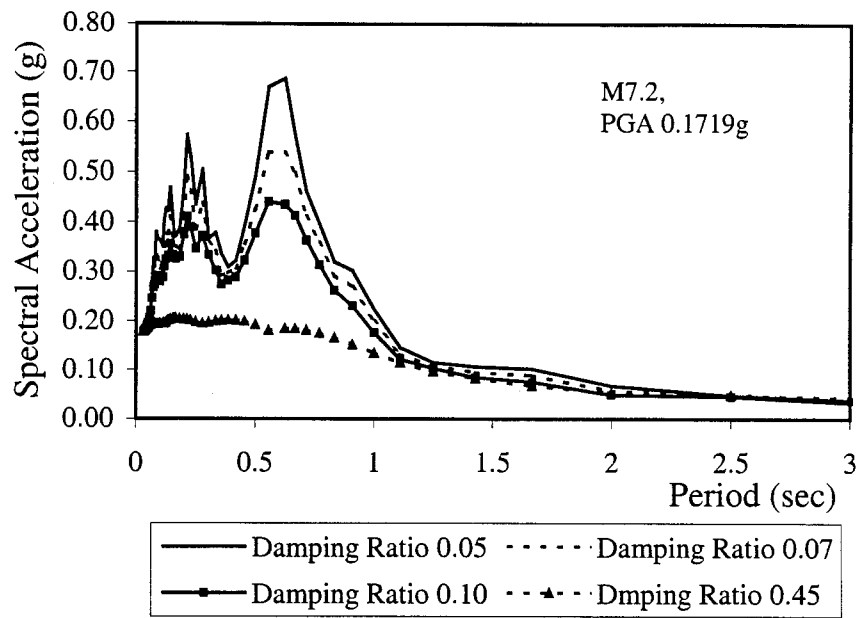


(a) Acceleration Response Spectra vs. Period

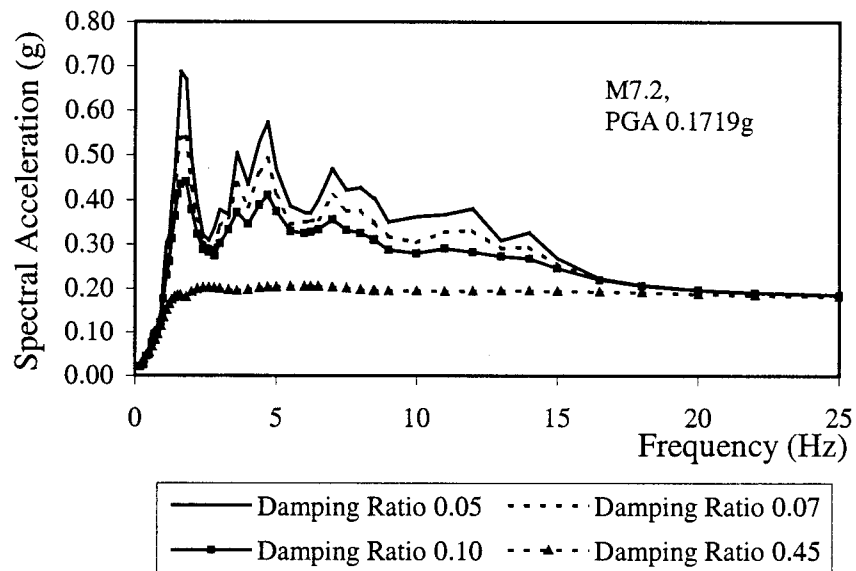


(b) Acceleration Response Spectra vs. Frequency

Figure 5.11. Acceleration Response Spectra for SF100103



(a) Acceleration Response Spectra vs. Period



(b) Acceleration Response Spectra vs. Frequency

Figure 5.12. Acceleration Response Spectra for SF100203

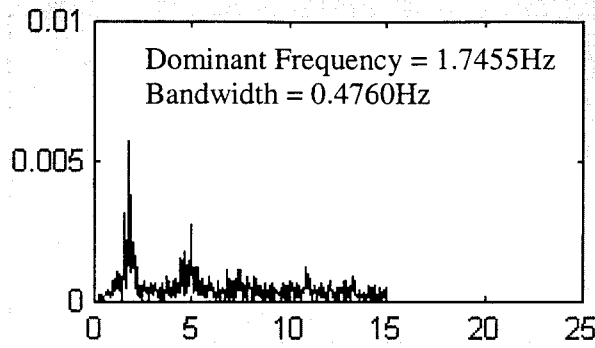


Figure 5.13. FFT for SF100103 Ground Motion

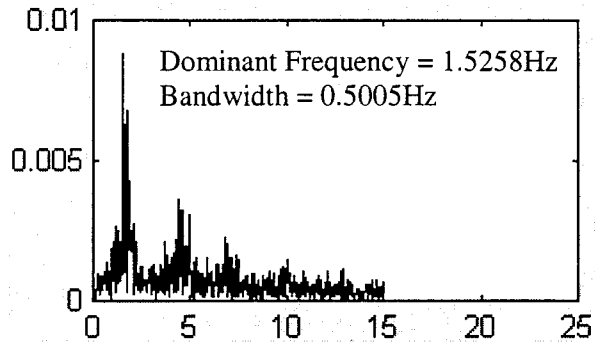


Figure 5.14. FFT for SF100203 Ground Motion

Table 5.4. Characteristics of Input Ground Motions

Earthquake Name	Maximum Acceleration (g)	Dominant Frequency (Hz)	Bandwidth (Hz)
SF100103	0.1268	1.7455	0.4760
SF100203	0.1719	1.5258	0.5005

5.2.2 Bridge Analysis Procedures in Five Cases

The model discussed in great detail in Section 5.1 and its simplified versions (2 models) were analyzed using three procedures as summarized in Table 5.1. A total of five cases were considered and they are discussed below.

Case 1. Nonlinear time history analysis with explicit modeling of pounding and pile foundation behavior

The first model as described in Table 5.1 was used for this case. The analysis procedure is detailed below:

Step 1. Estimate the spring stiffness of pile foundations supporting the abutments and piers.

Step 2. Compute the seismic responses of the bridge model with the time history analysis method including nonlinear gap elements.

Step 3. Find the maximum displacement and its corresponding force of each spring from Step 2 and check these responses for compatibility with the spring's force-

displacement relation at the foundation of abutments and piers. If they are not compatible, update the spring stiffness based on the displacement and repeat Steps 2 and 3.

Step 4. Check the maximum displacement at the top of the abutment. If it exceeds 0.5% of the abutment wall height, revise the backwall stiffness and repeat Steps 2-4 until the backwall stiffness is compatible with the strength of backfill behind the abutments.

The structural responses were calculated under two horizontal ground motions (SF100103 and SF100203) according to the above steps. The maximum displacement occurs at the end of the bridge deck, joint 13 as shown in Figure 5.15. It is equal to 0.72 in. under the SF100103 motion and 1.82 in. under the SF100203 ground motion. Both numbers are less than the 3-inch gap at the end of the bridge deck. Therefore, pounding will not happen under these excitations. To validate the equivalent damping procedure for pounding effect, the ground motions are scaled up to five (SF100103a) and seven (SF100103b) times for the SF100103 ground motion and to two (SF100203a) and four (SF100203b) times for the SF100203 ground motion.

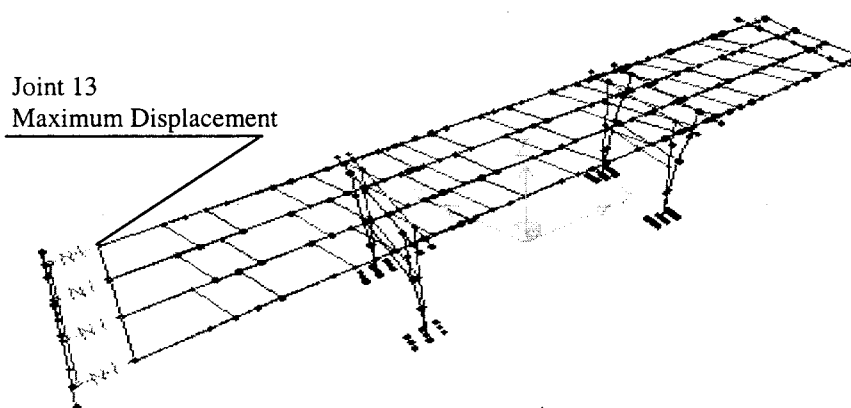


Figure 5.15. Deformed Shape under Horizontal Earthquake

Case 2. Nonlinear time history analysis with explicit modeling of pile foundation behavior and equivalent damping ratio for pounding effect

The second model as described in Table 5.1 was used for this case. The pounding effect is taken into account by using the equivalent damping ratio, which is determined from Eqs. (4.17-4.19) and (4.21-4.23). The same procedure as summarized for Case 1 was followed to compute the bridge responses under various earthquake excitations. The comparison between Cases 1 and 2 will show the accuracy of using the equivalent damping ratio to represent the pounding effect.

Case 3. Linear time history analysis with equivalent linear modeling of both pounding and pile foundation behavior

In this case, the third model was used and the equivalent damping ratio is determined from Eqs. (4.17-4.19) and (4.21-4.23) to account for pounding effect. The equivalent foundation stiffness was determined as the secant stiffness corresponding to 50% of the pile capacity. The comparison between Cases 2 and 3 will shed light on the effect of soil non-linearity on the bridge responses.

Case 4. Multi-mode response spectrum analysis with equivalent linear modeling of both pounding and pile foundation behavior

The multi-mode response spectrum analysis was also exercised for the third model as used in Case 3. Since the equivalent damping ratio including the pounding effect on the bridge responses is significantly larger than the structural damping, coupling between various vibration modes becomes stronger. The Complete Quadratic Combination (CQC) rule was used to combine the contribution of various modes. The intent of this exercise is to understand the response difference between time history analysis and response spectrum analysis.

Case 5. Single-mode response spectrum analysis with equivalent linear modeling of pounding and pile foundation behavior

For practical applications, most highway bridges are analyzed with the single-mode response spectrum analysis as recommended in AASHTO (1996). Model 3 is once again employed to illustrate how the equivalent damping ratio can be used to simulate the pounding effect on the bridge responses. The comparison between Cases 4 and 5 also gives one more insights about the accuracy of the simplified AASHTO procedure.

The single-mode spectrum analysis procedure is described in Division I-A (Seismic Design) of the AASHTO Specifications. This procedure is also illustrated step-by-step in Appendix D for the calculation of the Bridge A-237R responses. To make a fair comparison with the time history analysis in Case 3, the elastic seismic coefficient in AASHTO is replaced with the response spectra of 5% damping corresponding to the time histories used in Case 3, which are proportional to the spectra shown in Figures 5.11 and 5.12. The upper limit on the seismic coefficient is also lifted up. In addition, to account for the effect of different damping on the response spectra, a damping modification factor A_ξ is introduced. According to Newmark and Hall (1982), the factor A_ξ normalized by the 5% spectrum can be computed by

$$A_\xi = \frac{4.38 - 1.04 \cdot \ln(100\xi')}{4.38 - 1.04 \cdot \ln 5} \quad (5.7)$$

5.3.3 Bridge Responses

It is straightforward to compare the maximum displacements in various cases using the Displacement Method. Four scaled ground motions, designated as SF100103a, SF100103b, SF100203a, and SF100203b, were selected as earthquake excitations to Bridge A-237R. The key parameters of the ground motions and the maximum displacement of the bridge without presence of the expansion joints, calculated using Model 1, are listed in Table 5.5. The natural frequency of the bridge was determined based on the secant stiffness of pile foundation at the level of 50% ultimate capacity. It can be seen from the table that the maximum displacement of the bridge deck, without presence of the expansion joints, exceeds the gap width of the joints. Therefore, pounding will occur when the expansion joints are included in the computer model.

Tables 5.6-5.9 compare the maximum displacements at the bridge deck in five cases when Bridge A-237R is subjected to each of the four ground motions listed in Table 5.5. These tables also include the equivalent damping ratio determined based on the displacement criterion. It is observed from Tables 5.6-5.9 that the maximum displacements computed in Cases 1-3 are in good agreement, indicating that the design

equations of the equivalent damping ratio, (4.17-4.19), are accurate and the secant stiffness of pile foundation is a good approximation to the nonlinear behavior of pile foundation for Bridge A-237R. When the response spectrum analysis, especially with the single mode procedure, is conducted, the maximum displacement at the deck significantly deviates from the gap width. Part of this result is due to the difference between the spectrum analysis and the time history analysis. But more importantly, it reflects the difference in structural model for damping due to static soil-structure interaction. The structural damping of all vibration modes of Bridge A-237R is considered as 5% when the bridge is fixed at all supports. Due to the introduction of foundation stiffness, the natural frequencies of the bridge will be slightly reduced and the damping matrix of the bridge plus foundation (augmented system with increased degrees of freedom) is no longer proportional in a strict sense. If the augmented system is approximately considered to have a classical damping matrix, the modal damping of the system will deviate from the original value (5%). For the fundamental mode, damping ratio increases as the fundamental frequency decreases, resulting in a smaller displacement in the time history analysis. On the other hand, the response spectrum corresponding to 5% damping ratio is always used in the response spectrum analysis, which can not reflect the change of modal damping ratio. Consequently, the introduction of foundation stiffness or static soil-structure interaction tends to increase the difference in maximum response computed following two different analysis procedures.

Table 5.5. Input Earthquake and Structure Characteristics

Ground Motion	Scale Factor (Amplitude)	Peak Ground Acceleration (g)	Dominant Frequency ω (Hz)	Band width (Hz)	Maximum Displacement A_{\max} (in)	Natural Frequency ω_0 (Hz)	Gap Width δ (in)
SF100103a	5	0.6340	1.7455	0.4760	3.566	0.8900	3
SF100103b	7	0.8876	1.7455	0.4760	4.992	0.8900	3
SF100203a	2	0.3438	1.5258	0.5005	3.629	0.8900	3
SF100203b	4	0.6876	1.5258	0.5005	7.258	0.8900	3

Table 5.6. Bridge Responses under the SF100103a Earthquake (Displacement Method)

Case	Maximum Displacement (in)	Equivalent Damping Ratio (ξ')	Presence of Expansion Joints	$\frac{\delta}{A_{\max}} = 0.84$ $\beta = \frac{\omega}{\omega_0} = 1.96$
1	3	0.05 (Structural damping)	Yes	
2	3.2	0.11	No	
3	2.9	0.11	No	
4	3.1	0.11	No	
5	3.4	0.11	No	

Table 5.7. Bridge Responses under the SF100103b Earthquake (Displacement Method)

Case	Maximum Displacement (in)	Equivalent Damping Ratio (ξ')	Presence of Expansion Joints	$\frac{\delta}{A_{\max}} = 0.60$ $\beta = \frac{\omega}{\omega_0} = 1.96$
1	3	0.05 (Structural damping)	Yes	
2	3.1	0.26	No	
3	3	0.26	No	
4	3.9	0.26	No	
5	2.5	0.26	No	

Table 5.8. Bridge Responses under the SF100203a Earthquake (Displacement Method)

Case	Maximum Displacement (in)	Equivalent Damping Ratio (ξ')	Presence of Expansion Joints	$\frac{\delta}{A_{\max}} = 0.83$ $\beta = \frac{\omega}{\omega_0} = 1.71$
1	3	0.05 (Structural damping)	Yes	
2	3.2	0.10	No	
3	3.1	0.10	No	
4	3.1	0.10	No	
5	3.1	0.10	No	

Table 5.9. Bridge Responses under the SF100203b Earthquake (Displacement Method)

Case	Maximum Displacement (in)	Equivalent Damping Ratio (ξ')	Presence of Expansion Joints	$\frac{\delta}{A_{\max}} = 0.41$ $\beta = \frac{\omega}{\omega_0} = 1.71$
1	3	0.05 (Structural damping)	Yes	
2	3.5	0.45	No	
3	3.4	0.45	No	
4	5.7	0.45	No	
5	1.3	0.45	No	

It is also seen from Tables (5.6-5.9) that the accuracy using the equivalent damping concept decreases as δ/A_{\max} decreases or pounding occurs more often. Based on the analysis results, the equivalent damping ratio from the Displacement Method can be used to accurately represent the pounding effect when the normalized gap width is larger than 0.6. In fact, Eq. (5.7) is invalid when $\xi' > 0.26$.

In the Energy Method, the design parameter of interest is the mechanical energy. It is impossible to determine the energy time history using the response spectrum method. Therefore, the equivalent damping ratios for the bridge system under the specified ground motions in Table 5.5 and from Eqs. (4.21-4.23) are determined for Case 3. They are compared in Table 5.10. To understand the relative accuracy of the proposed

Displacement and Energy Methods, the equivalent damping ratios on the displacement basis are also compared with those from Eqs. (4.17-4.19) in Table 5.11.

Table 5.10. Equivalent Damping Ratios under Various Earthquake Excitations: Case 3
(Energy Method)

Ground Motion	ξ' from Time History Analysis	ξ' from Design Equations	δ/A_{\max}	$\beta = \omega/\omega_0$
SF100103a	0.03	0.06	0.84	1.96
SF100103b	0.04	0.08	0.60	1.96
SF100203a	0.05	0.06	0.83	1.71
SF100203b	0.09	0.15	0.41	1.71

Table 5.11. Equivalent Damping Ratios under Various Earthquake Excitations: Case 3
(Displacement Method)

Ground Motion	ξ' from Time History Analysis	ξ' from Design Equations	δ/A_{\max}	$\beta = \omega/\omega_0$
SF100103a	0.11	0.11	0.84	1.96
SF100103b	0.26	0.26	0.60	1.96
SF100203a	0.10	0.10	0.83	1.71
SF100203b	0.47	0.45	0.41	1.71

Table 5.10 indicates that the equivalent damping ratios from the design equations with necessary interpolation are slightly greater than the structural damping when pounding does not occur frequently under the ground motions SF100103a, SF100103b and SF100203a. The damping ratios calculated with the time history analysis are even smaller than the structural damping corresponding to the first two ground motions. These results reflect the local fluctuation of the equivalent damping as seen in Figures 4.31-4.33. Since pounding occurs more frequently under the ground motion SF100203b, the equivalent damping ratio increases appreciably. In comparison with Table 5.11, the energy-based damping ratios are significantly smaller than their respective ones determined with the Displacement Method since mechanical energy is not as sensitive to damping as the maximum displacement. Considering that the energy-based equivalent damping fluctuates and is significantly less than that from the Displacement Method, the Energy Method may have limited applications in practice. Additionally, the difference in energy-based damping from the time history analysis and design equations is considerably larger than that on the displacement basis.

5.3 Summary

Both sets of design equations derived from the Displacement and Energy Methods have been applied in the linear analysis of Bridge A-237R to account for pounding effect. Based on the five case studies, the following observations can be made:

1. The displacement-based equations formulated for a simple model were validated by comparing the maximum displacement of an actual bridge analyzed using the nonlinear time history procedure with explicit modeling of pounding effect and using the linear procedure with the equivalent damping. These comparisons indicated that the equations based on the Displacement Method are sufficiently accurate to represent the pounding effect in actual structures. These equations become less accurate as the normalized gap width decreases from 0.6 or pounding occurs more frequently.
2. The bridge responses using the response spectrum analysis with the equivalent damping ratio on the displacement basis are in good agreement with those determined by nonlinear analyses in which pounding effect is explicitly modeled. Therefore, the design equations from the Displacement Method are recommended for practical applications.
3. The energy-based equations focus on the average behavior of bridges in the duration of earthquakes and, therefore, substantially underestimate the equivalent damping for the purpose of realistically estimating the peak responses of bridges.
4. The bridge responses seem insensitive to the change in foundation stiffness. Therefore, the secant stiffness based on the 50% ultimate strength can be used to simulate the rigidity of the foundation.

6. CONCLUSIONS AND RECOMMENDATIONS

The purpose of this study was to develop a practical bearing arrangement scheme for continuous steel-girder highway bridges in infrequent seismic zones such as the Central and Eastern United States. The bearing scheme includes two critical components: high rocker bearings and metallic dampers. The rocker bearings support the gravity loads and the metallic dampers are introduced to carry longitudinal forces in the traffic direction. In addition, steel-girder bridges are typically built with expansion joints at both ends of the bridge decks and therefore pounding may occur during a strong earthquake event.

Conclusions. Experiments were conducted and analyzed to evaluate how a metallic damper acts as an isolator and an energy dissipater in bridge applications. An equivalent damping concept was developed from a simple structure for practical application. It was applied to a three-span steel-girder bridge, A-237R on US Highway 60, to account for pounding effect on the bridge responses in a linear analysis. Based on the extensive tests on physical models and numerical simulations, the following conclusions can be drawn:

1. No stiffness degradation was observed from the cyclic tests of four full-scale metallic dampers. The hysteresis loop of the metallic dampers can be steadily developed. A reasonable energy dissipation capability of the dampers has been achieved even at a small loading level. Test results have indicated that for straight rods a 10 percent damping with respect to the damper stiffness can be used for pinned-fixed steel rods in bridge design.
2. The performance of the dampers tested is consistent with respect to load and displacement. The tapered steel rods can dissipate more energy than the straight rods.
3. The dampers are effective as isolation units in bridge systems. In the event of a destructive earthquake, damage will be localized to the dampers while the columns retain their structural integrity.
4. It was observed from the shake table tests of a 1/10-scale bridge model that rocker bearings remain stable even when the bridge is subjected to an excitation of 0.54g at resonance.
5. Pounding reduces the maximum displacement of a structure and may amplify its acceleration due to impulsive pounding force. Reduction in displacement actually leads to the release of stress in columns and therefore, pounding effect can be considered as addition of damping to the structure.
6. The equivalent damping strongly depends upon the gap width of expansion joints and the dominant frequency of earthquake excitations. There is no conclusive interrelation between the equivalent damping and the frequency bandwidth of the excitations.
7. The equivalent damping associated with harmonic loading is the lower bound at resonance and the upper bound under non-resonant situations of those corresponding to the earthquake excitations of various frequency spectra.
8. Two sets of equivalent damping equations were developed based on the equivalence of the maximum displacement in the Displacement Method and the mechanical energy in the Energy Method, respectively. They were derived from a simple

structure under ten actual earthquake records. The design equations on the displacement basis are more accurate.

9. The displacement-based equations were applied into the linear time-history analysis of Bridge A-237R that is geometrically nonlinear due to presence of the expansion joints. They are sufficiently accurate to represent pounding effect on the bridge responses provided the gap width of the joints exceeds 60% of the deck displacement when pounding is ignored.
10. Response spectrum analysis with the displacement-based equivalent damping can predict the bridge responses that are in good agreement with those determined by a nonlinear analysis with pounding effect modeled explicitly.
11. The energy-based equations focus on the average behavior of bridges in the duration of earthquakes and, therefore, substantially underestimate the equivalent damping for the purpose of realistically estimating the peak responses of bridges.
12. The bridge responses seem insensitive to the change in foundation stiffness. Therefore, the secant stiffness based on the 50% ultimate strength can be used to simulate the rigidity of the foundation in bridge analysis.

Recommendations. Based on the above study, several recommendations can be made for the practical design and retrofit of highway bridges. A number of issues are also identified for future investigations. They are summarized below.

1. For metallic dampers with pinned-fixed straight rods, a 10% viscous damping ratio can be used in the design of highway bridges. For dampers assembled with tapered rods, the damping ratio increases with the applied load as observed from one test. More tests on tapered rods are needed at higher loading levels to develop a design equation for the viscous damping ratio.
2. Metallic dampers tested in this study consisted of steel rods and base plates that were assembled with a reusable semi-rigid connection. The connection flexibility absorbed part of the deformation of the steel rods and caused reduction in energy dissipation capability. To improve their performance, a weld connection or rigid connection is required but then fatigue may become a critical issue due to high stress in the steel rods. Further tests of dampers are therefore imperative to address these implementation issues.
3. An ultimate strength method is recommended for the design of metallic dampers. As sacrificing elements during earthquakes, dampers are sized such that they yield before the formation of plastic hinges at the bottom of bridge columns. To better understand the performance of the bridges, the ductility demand on the dampers must not exceed their capacity. Therefore, it is critical to establish the ductility capacity for performance-based designs through tests of steel rods and plastic analyses of bridge columns.
4. For a bridge system with metallic dampers and rocker bearings, friction between pin and web of the rocker bearings significantly affects the bridge responses under dynamic loads. In order to understand how the system responds to earthquakes, it is necessary to characterize the friction feature such as the coefficient of friction in various circumstances.
5. Displacement-based equivalent damping can accurately account for pounding effect on the seismic responses of steel-girder bridges with seat-type abutments. Therefore, the equivalent damping equations developed from the Displacement Method are

recommended for the seismic analysis and design of highway bridges in the framework of response spectrum analysis. This approach substantially simplifies the dynamic analysis of a geometrically nonlinear bridge system into that of an associated linear system without pounding. Its implementation into the routine design and retrofit of highway bridges will save tremendous time and effort in practice.

7. BIBLIOGRAPHY

1. American Association of State Highway and Transportation Officials (AASHTO), (1996). *Standard Specifications for Highway Bridges*. 16th Edition.
2. Bowles, J. E. (1990). *Foundation Analysis and Design*, 4th Edition, McGraw-Hill Companies.
3. Buckle, Ian (1995). "Report from the Hanshin-Awaji Earthquake: Overview of Performance of Highway Bridge," *NCEER Bulletin*, National Center for Earthquake Engineering Research, State University of New York at Buffalo, NY, 9(2), 1-6.
4. Buckle, I. G. and King, P. G. (1980). "Mechanical Properties of Cantilever Mild Steel Energy Dissipators," *Proc. 33rd Annual Conference of the Australasian Institute of Metals, Metals and Energy*, University of Auckland, Auckland, New Zealand, May, 156-164.
5. Ciampi V. (1991). "Use of Energy Dissipating Devices, Based on Yielding of Steel, for Earthquake Protection of Structure," *Int. Meeting on Earthquake Protection of Buildings*, Ancona, Italy, June, 41/D-58/D.
6. Dargush, C. F. and Soong, T. T. (1995). "Behavior of Metallic Plate Dampers in Seismic Passive Energy Dissipation Systems," *Earthquake Spectra*, Earthquake Engineering Research Institute, 11(4), 545-568.
7. Fiero, E., Perry, C., Sedarat, H. and Scholl, R. (1993). "Seismic Retrofit in San Francisco Using Energy Dissipation Devices," *Earthquake Spectra*, , Earthquake Engineering Research Institute, 9(3).
8. Hanson, R. D., Aiken, I., Nims, D. K., Richer, P. I. and Bachman, R (1993). "State-of-the-Art and State-of-Practice in Seismic Energy Dissipation," *Proc. of Seminar on Seismic Isolation, Passive Energy Dissipation, and Active Control*, San Francisco, 2, 449-471.
9. International Conference Building Officials (ICBO). (1994). *Uniform Building Code*.
10. Mander, J.B., Kim, D-K, Chen, S. S., and Premus, G.J. (1996). "Response of Steel Bridge Bearings to Reversed Cyclic Loading," *Technical Report NCEER-96-0014*, National Center for Earthquake Engineering Research, State University of New York at Buffalo, NY.
11. Newmark, N. M. and Hall, W. J. (1982). "Earthquake Spectra and Design", *Monograph*, Earthquake Engineering Research Institute, Berkeley, California.
12. Tsai, K. C., Chen, H. W., Hong, C. P. and Su, Y. F. (1993). "Design of Steel Triangular Plate Energy Absorbers for Seismic-Resistant Construction," *Earthquake Spectra*, 9(3), 505-528.
13. U.S. Department of Transportation (1986). "Seismic Design of Highway Bridge Foundations", *Report No. FHWA/RD-86*, Federal Highway Administration.
14. Whittaker, A. S., Bertero, V. V., Thompson, C. L. and Alons, L. J. (1991). "Seismic Testing of Steel Plate Energy Dissipation Devices," *Earthquake Spectra*, 7(4), 563-604.

8. APPENDIX

A. Additional Experimental Data of Full-Scale Dampers

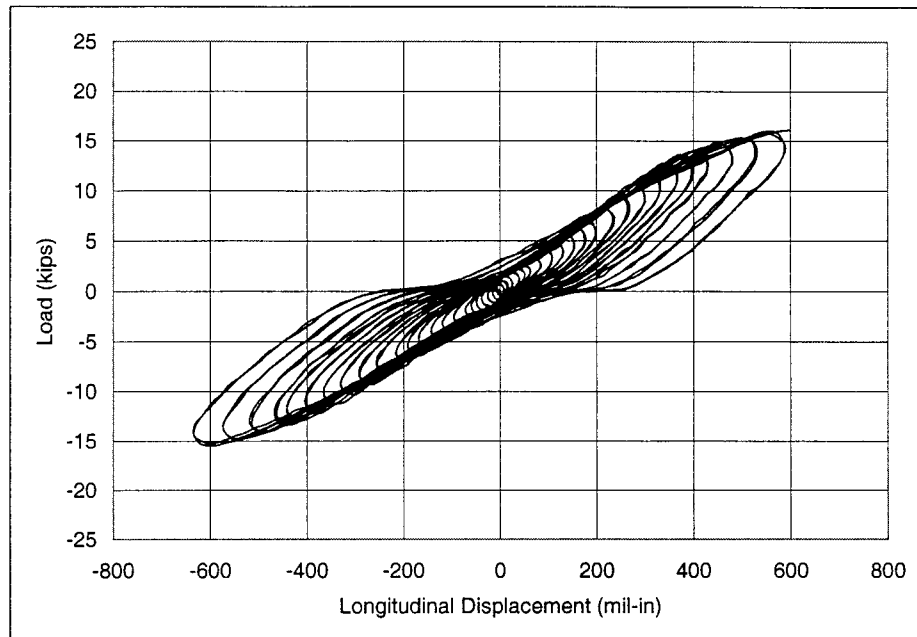


Figure A.1. Load vs. Longitudinal Displacement, LVDT 3, Damper 2

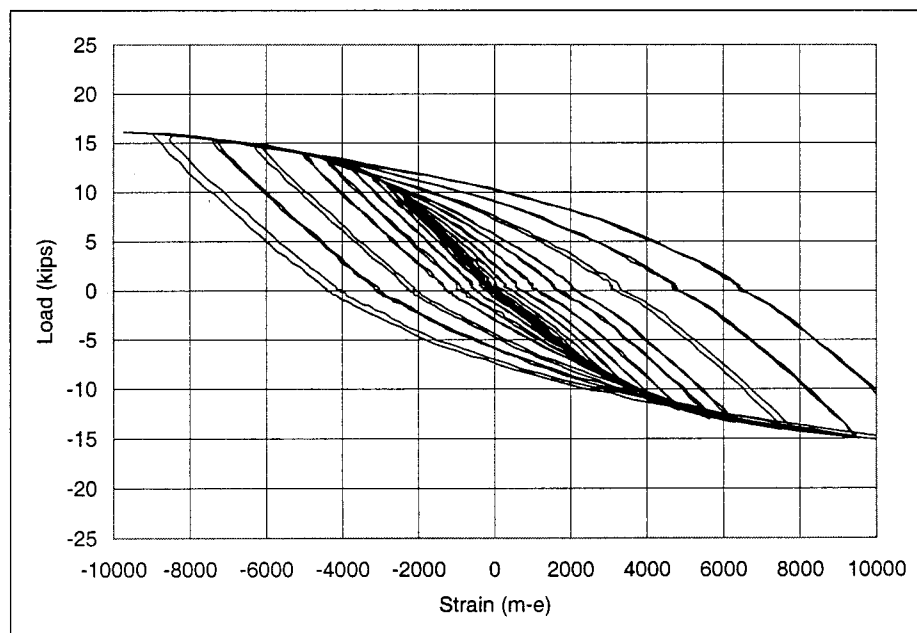


Figure A.2. Load vs. Longitudinal Displacement, Lower Gauge of Bar 2, Damper 2

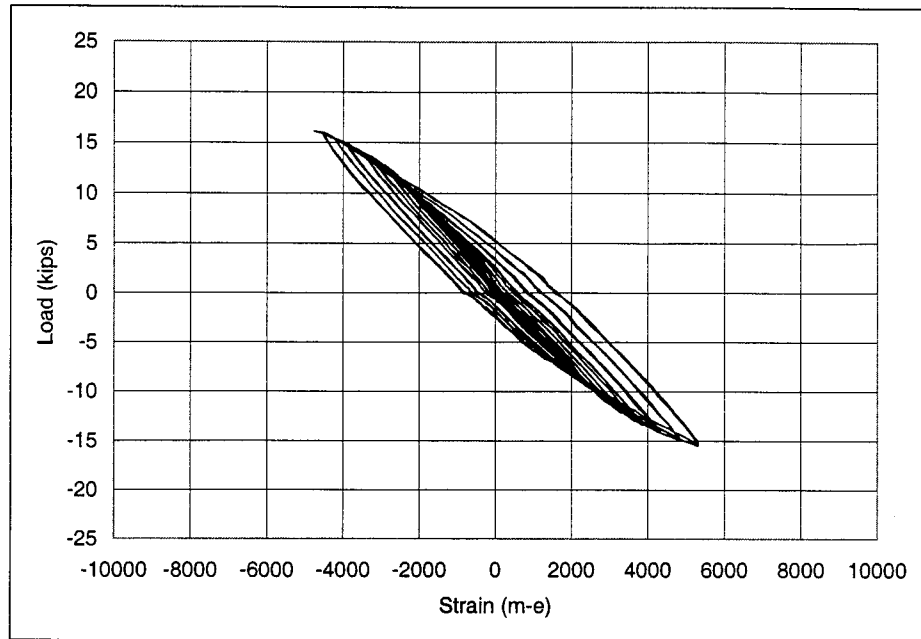


Figure A.3. Load vs. Strain, Middle Gauge of Bar 1, Damper 2

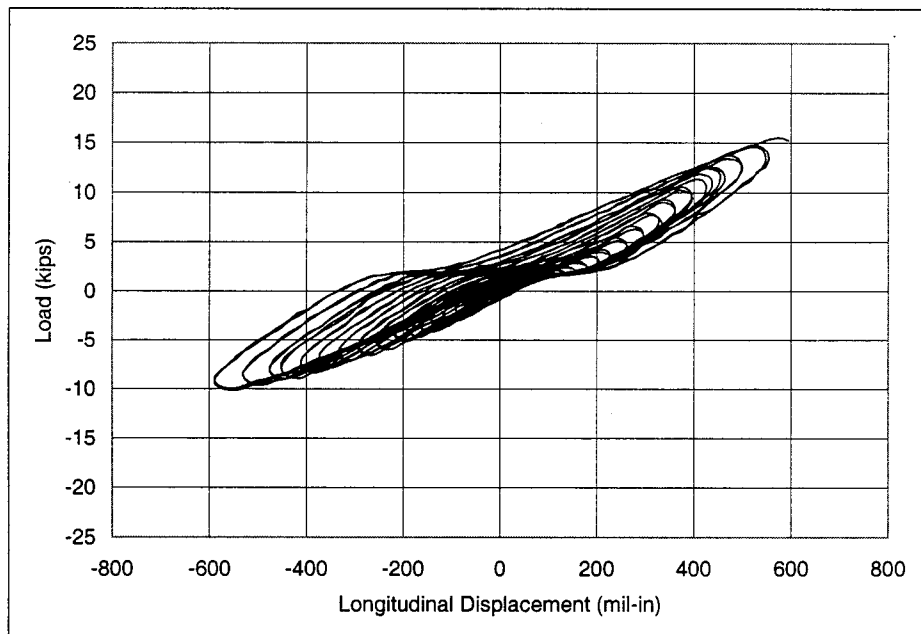


Figure A.4. Load vs. Longitudinal Displacement, LVDT 3, Damper 3

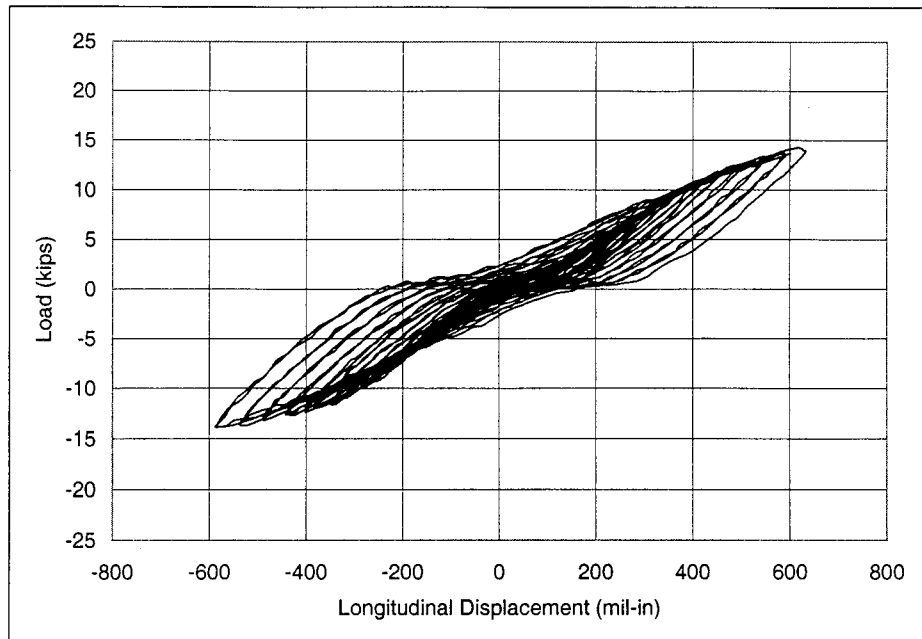


Figure A.5. Load vs. Longitudinal Displacement, LVDT 2, Damper 4

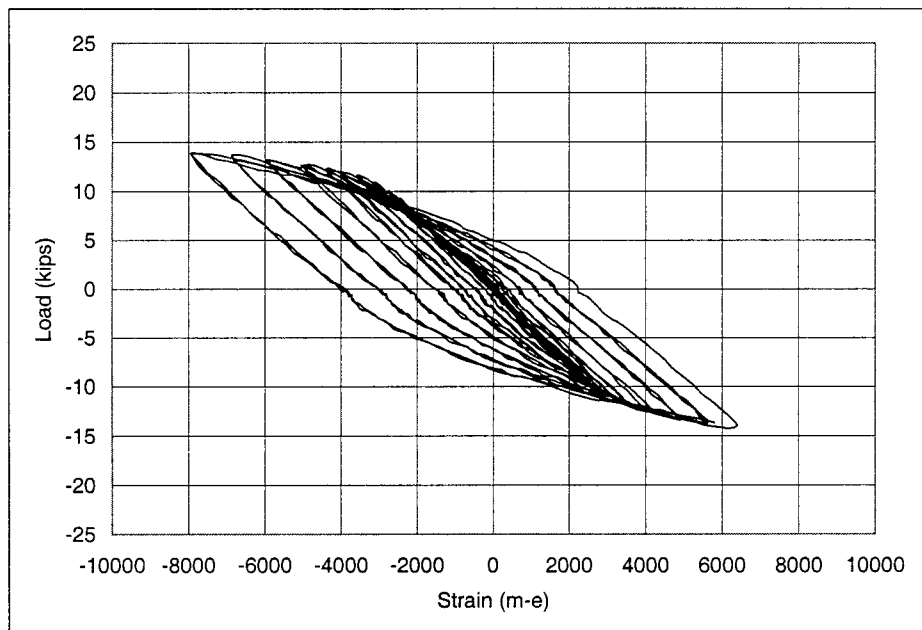


Figure A.6. Load vs. Strain, Lower Gauge of Bar 2, Damper 4

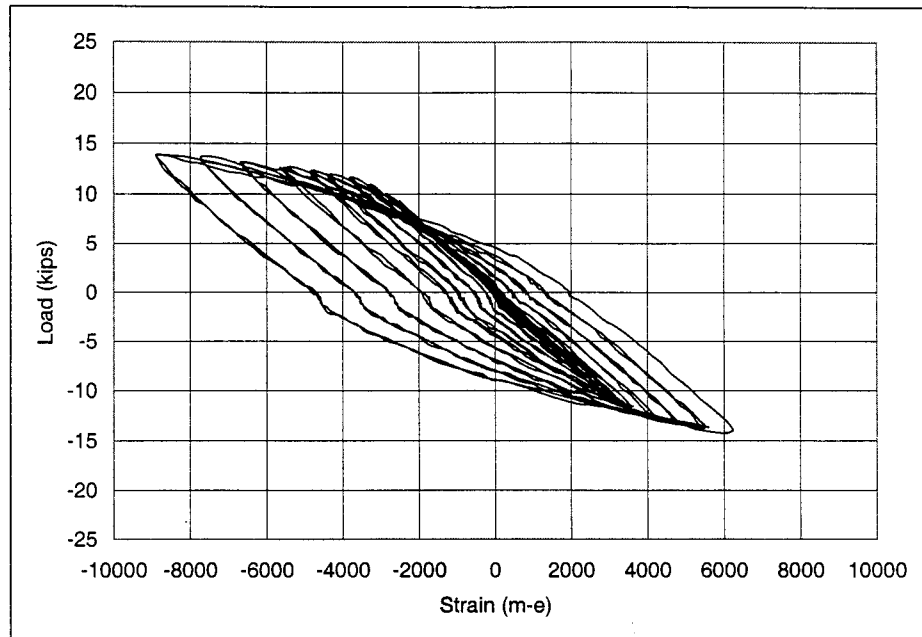


Figure A.7. Load vs. Strain, Middle Gauge of Bar 1, Damper 4

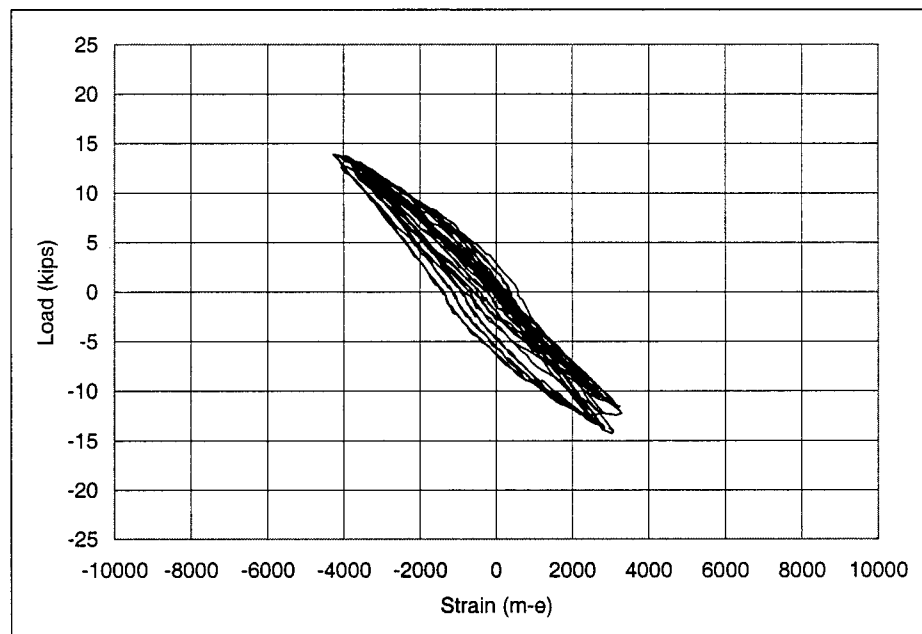


Figure A.8. Load vs. Strain, Upper Gauge of Bar 2, Damper 4

B. Additional Experimental Data of Small-Scale Bridge

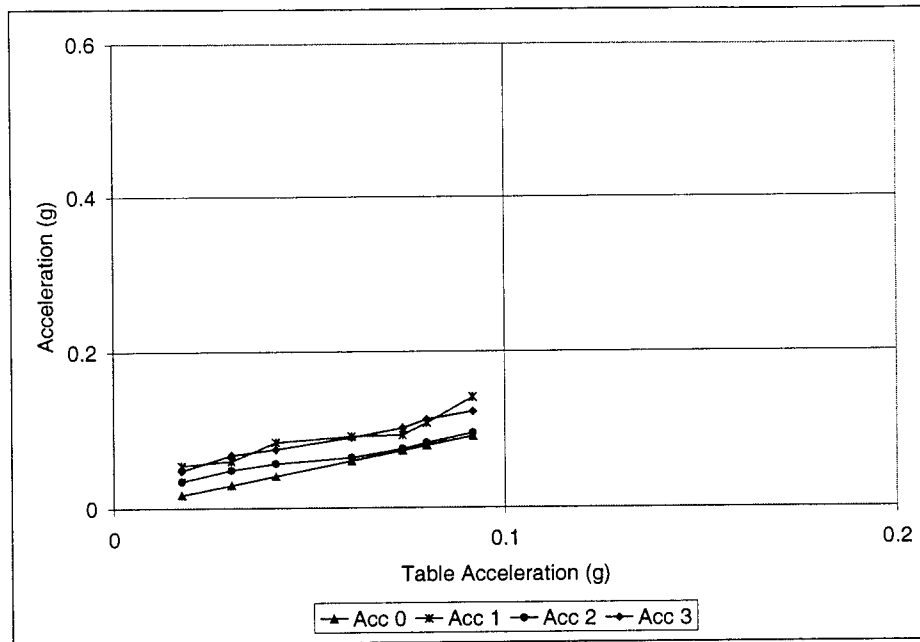


Figure B.1. Acceleration vs. Input, Taft Earthquake, Without Damper

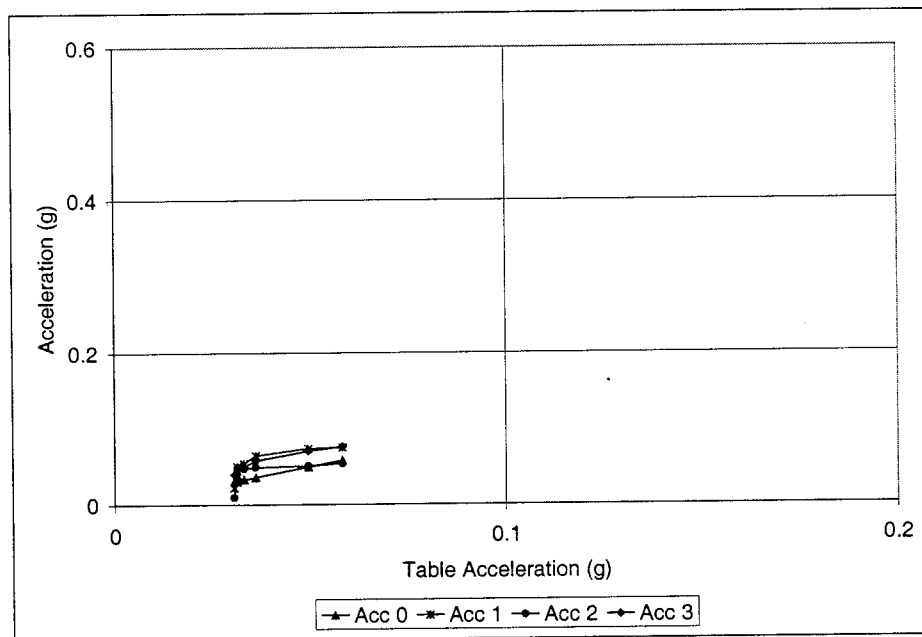


Figure B.2. Acceleration vs. Input, El Centro Earthquake, Without Damper

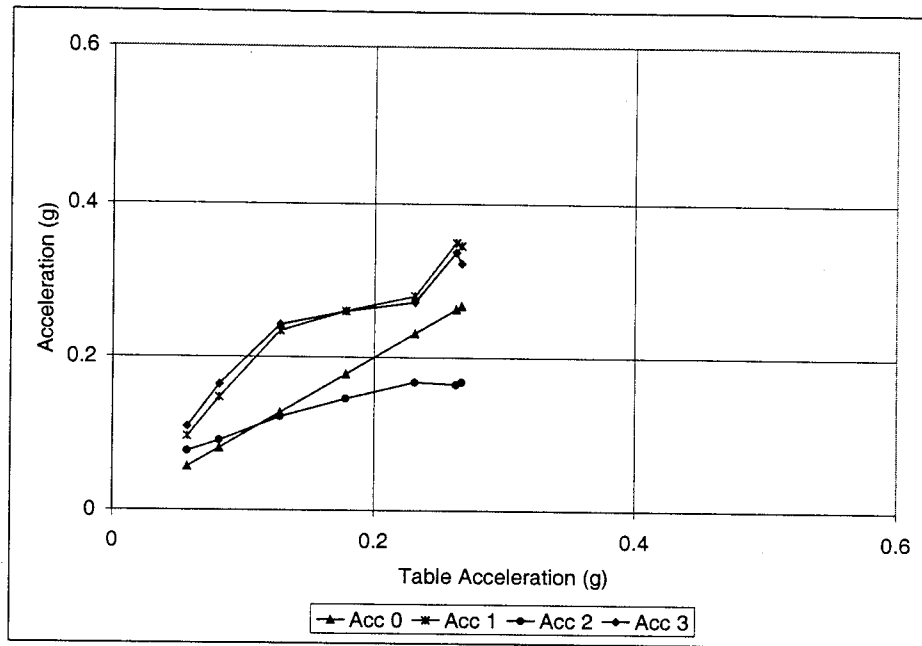


Figure B.3. Acceleration vs. Input, Harmonic Input, Without Damper

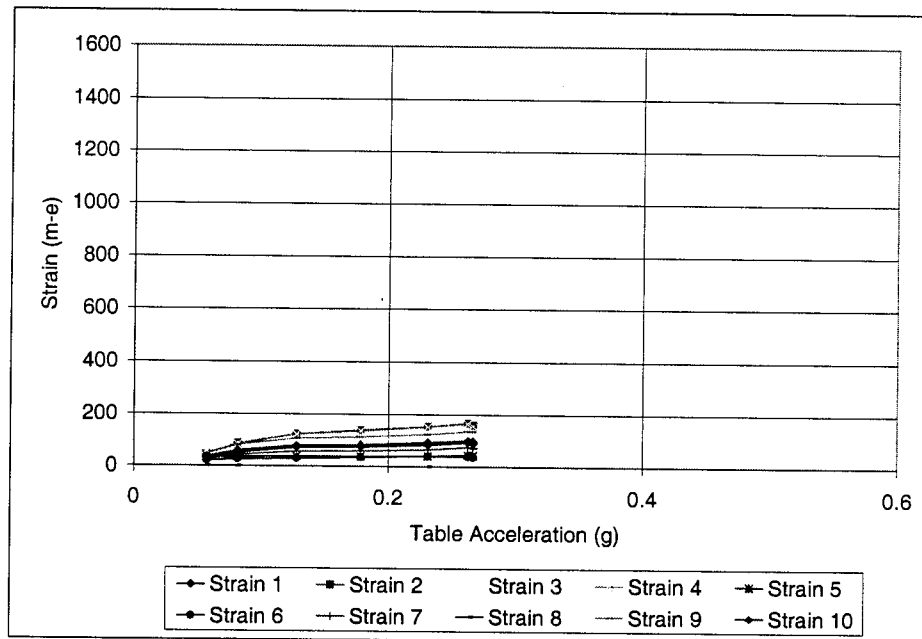


Figure B.4. Strain vs. Input, Harmonic Input, Without Damper

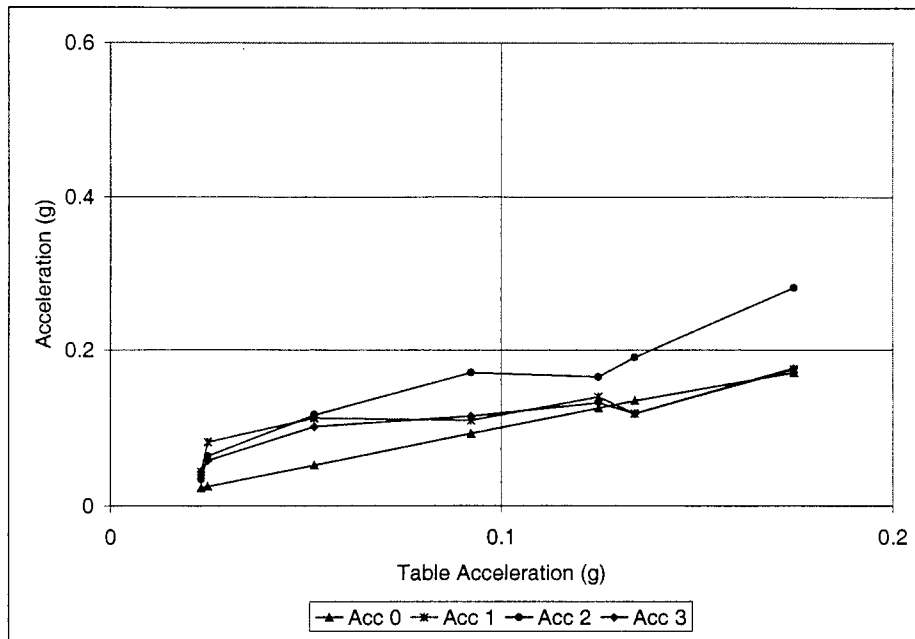


Figure B.5. Acceleration vs. Input, Taft Earthquake, Damper 1

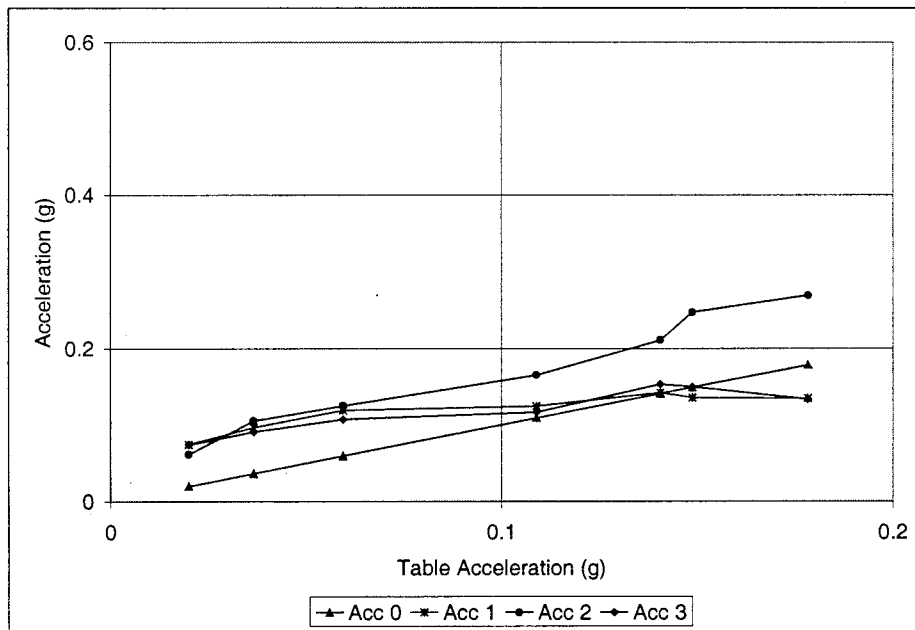


Figure B.6. Displacement vs. Input, Taft Earthquake, Damper 1

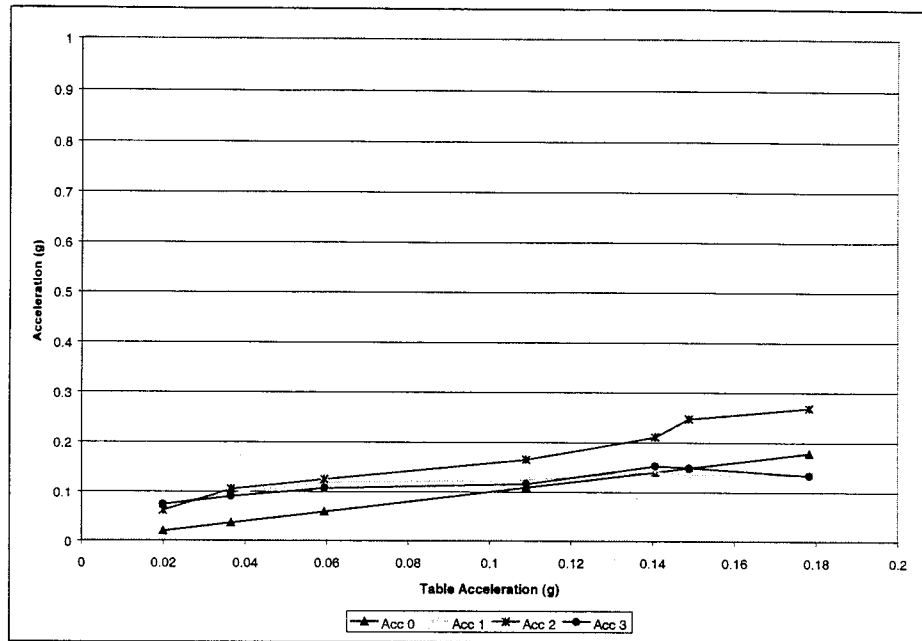


Figure B.7. Acceleration vs. Input, El Centro Earthquake, Damper 1

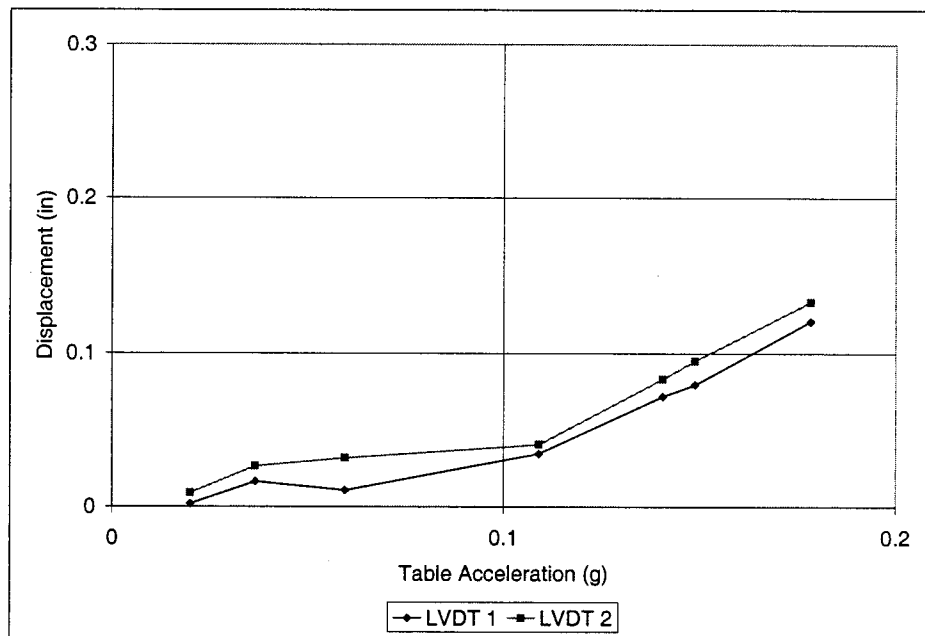


Figure B.8. Displacement vs. Input, El Centro Earthquake, Damper 1

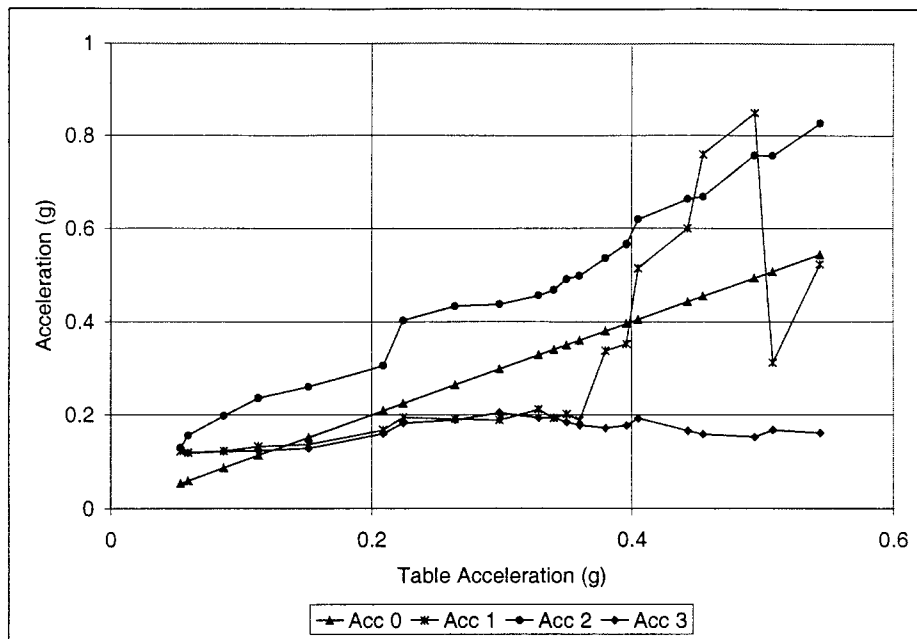


Figure B.9. Acceleration vs. Input, Harmonic Input, Damper 1

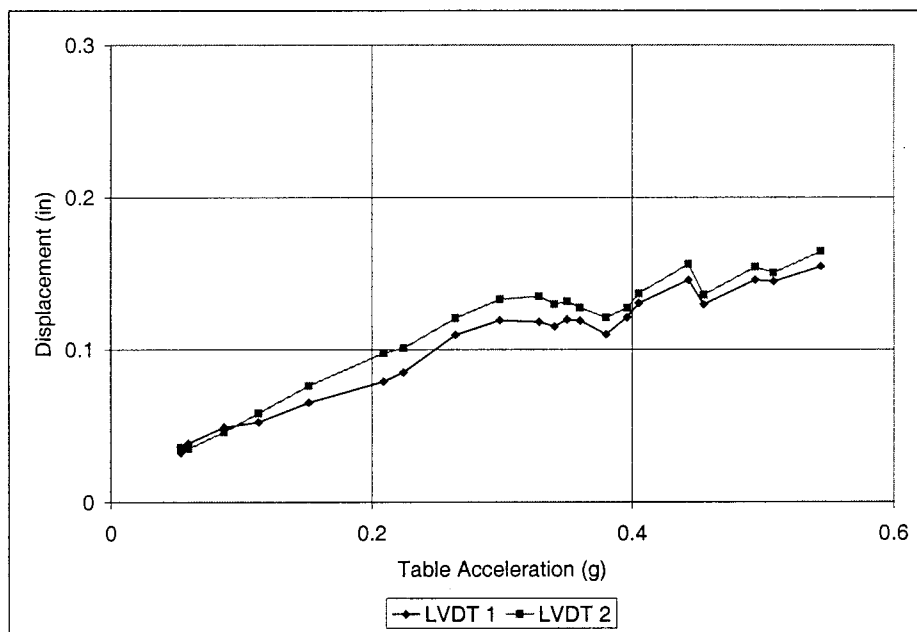


Figure B.10. Displacement vs. Input, Harmonic Input, Damper 1

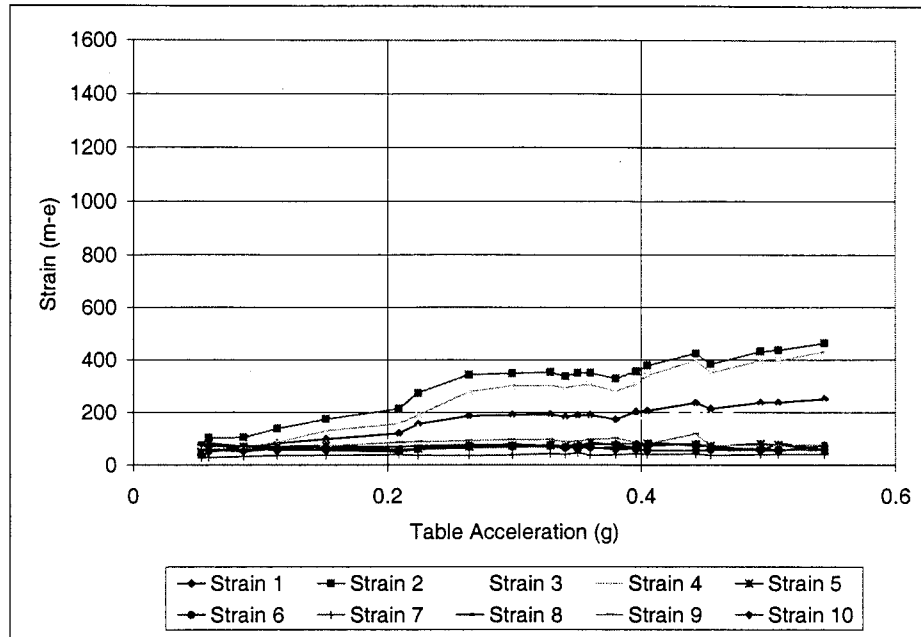


Figure B.11. Strain vs. Input, Harmonic Input, Damper 1

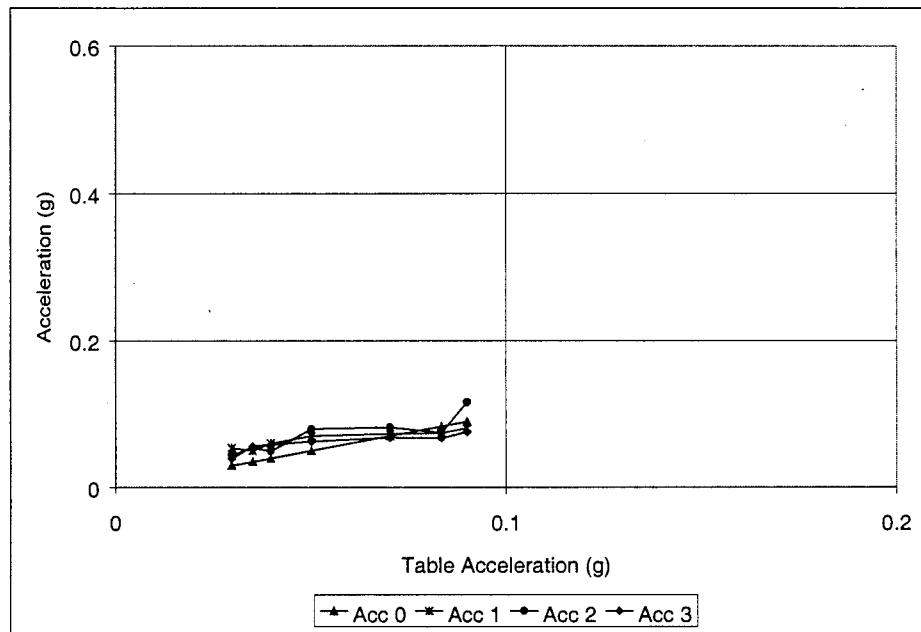


Figure B.12. Acceleration vs. Input, Taft Earthquake, Damper 2

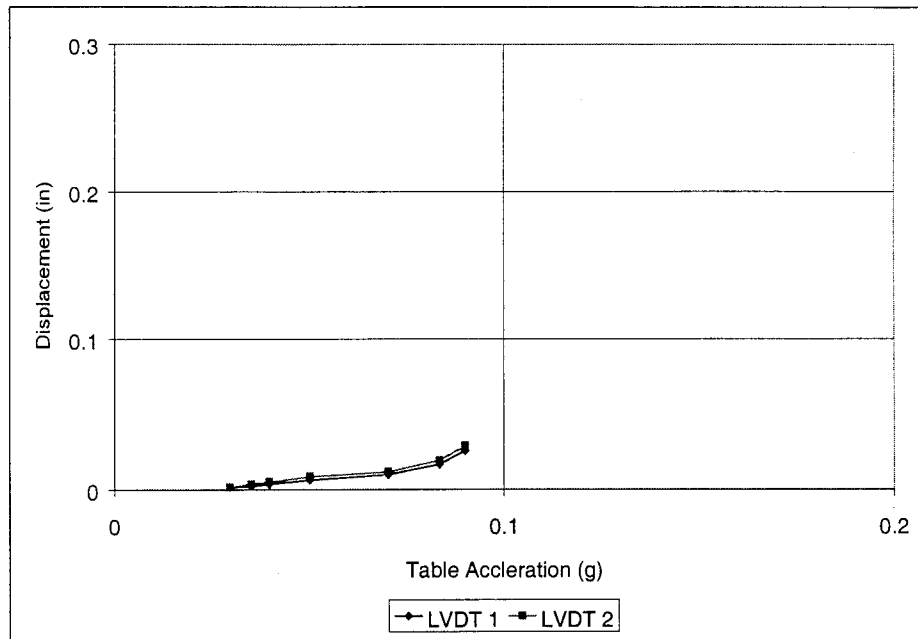


Figure B.13. Displacement vs. Input, Taft Earthquake, Damper 2

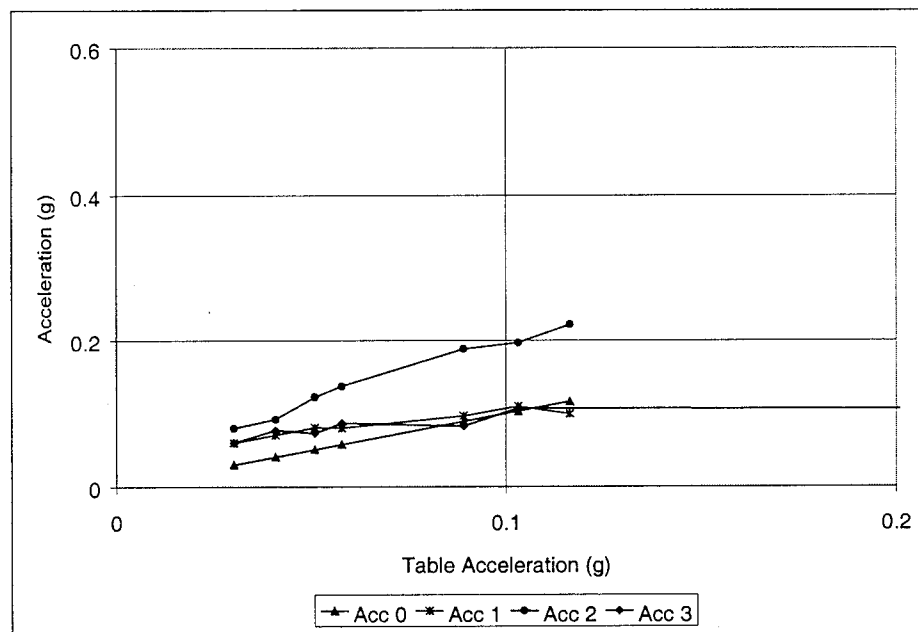


Figure B.14. Acceleration vs. Input, El Centro Earthquake, Damper 2

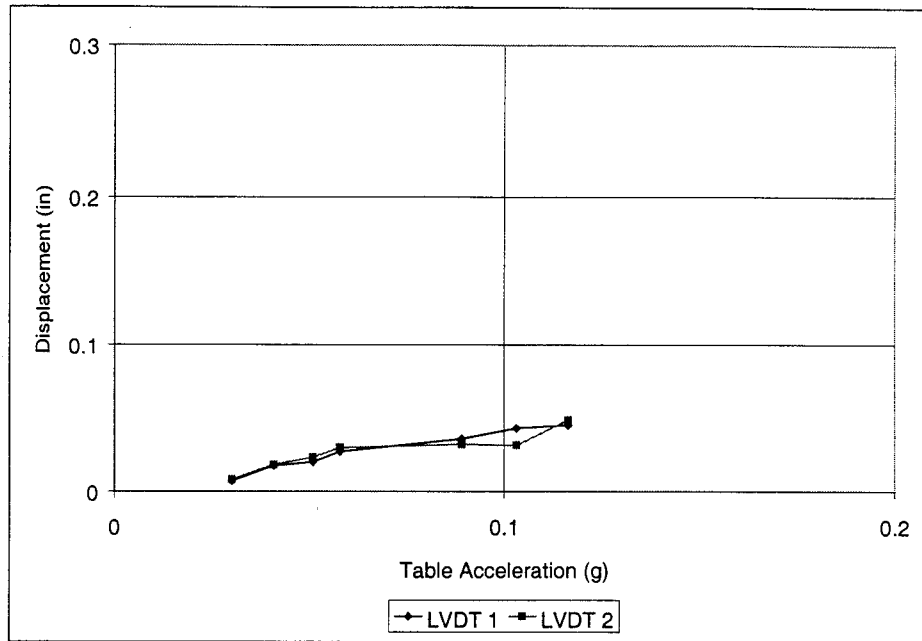


Figure B.15. Displacement vs. Input, El Centro Earthquake, Damper 2

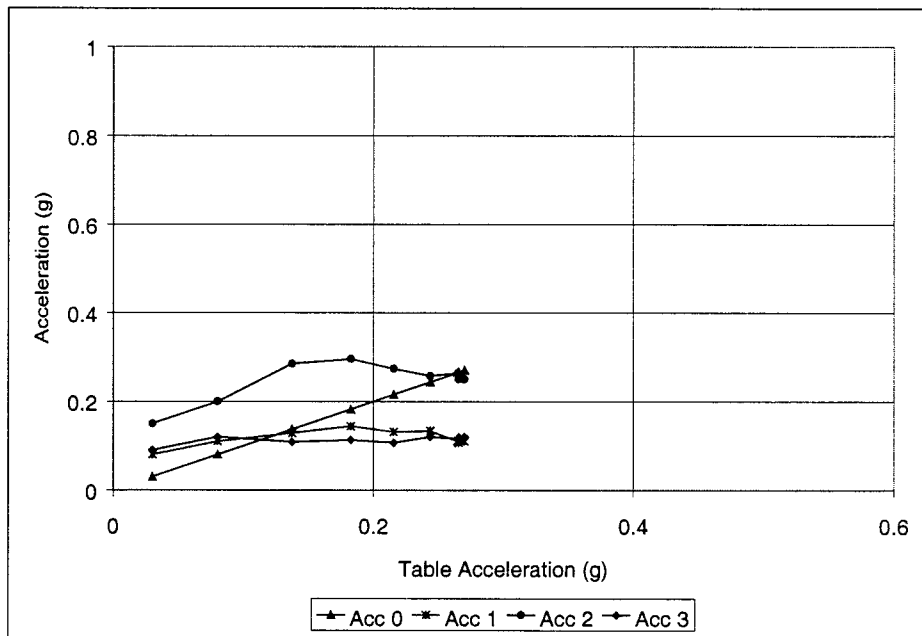


Figure B.16. Acceleration vs. Input, Harmonic Input, Damper 2

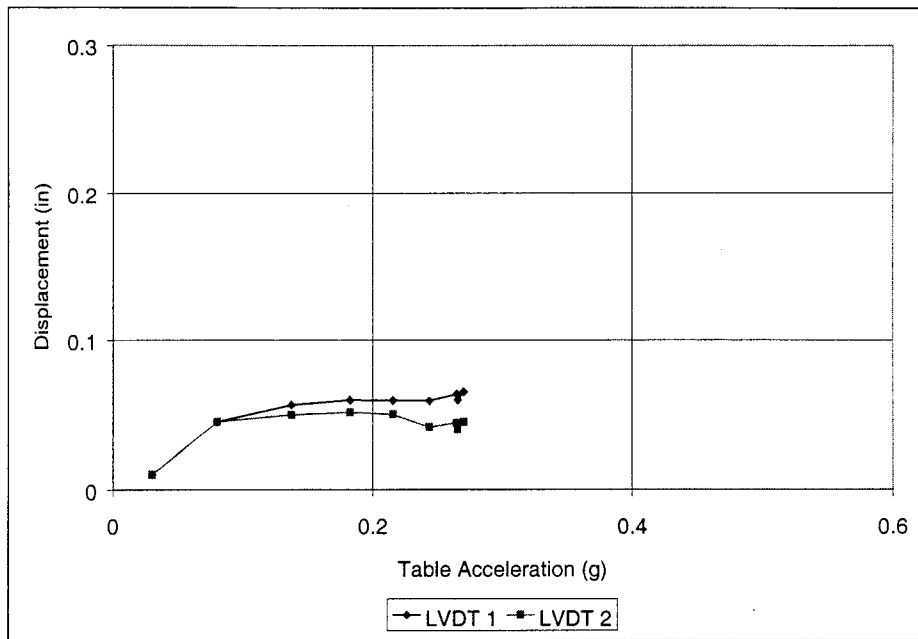


Figure B.17. Displacement vs. Input, Harmonic Input, Damper 2

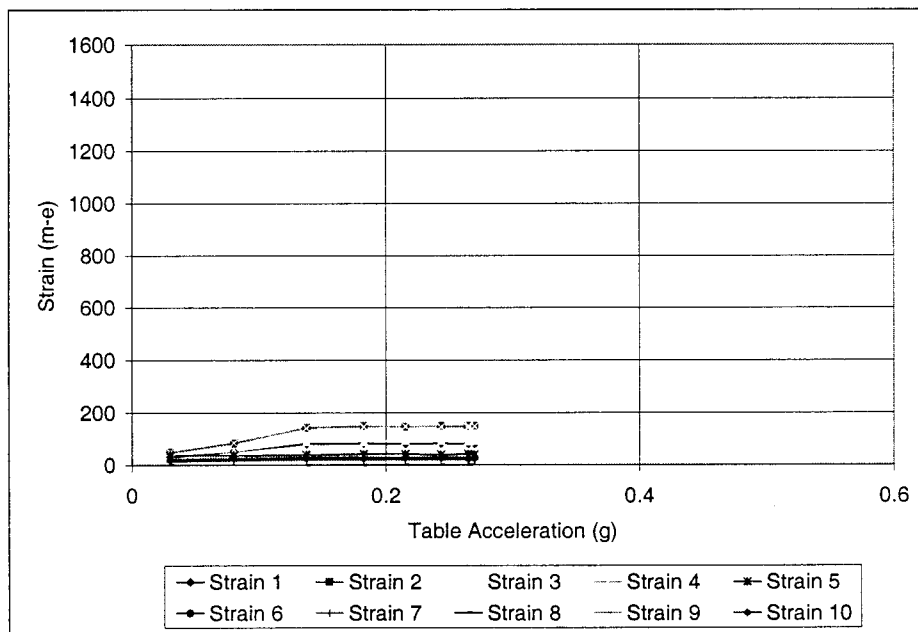


Figure B.18. Strain vs. Input, Harmonic Input, Damper 2

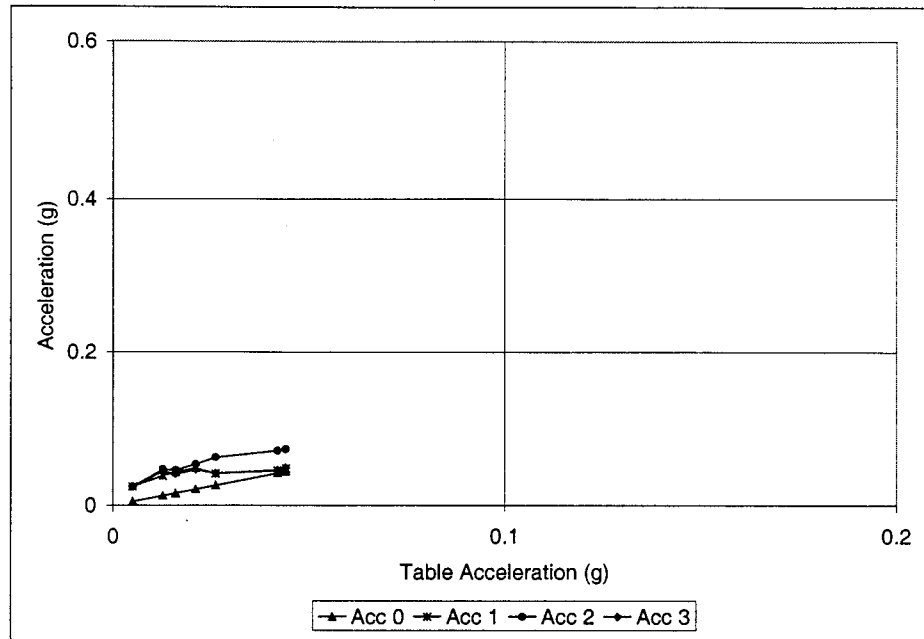


Figure B.19. Acceleration vs. Input, Taft Earthquake, Damper 4

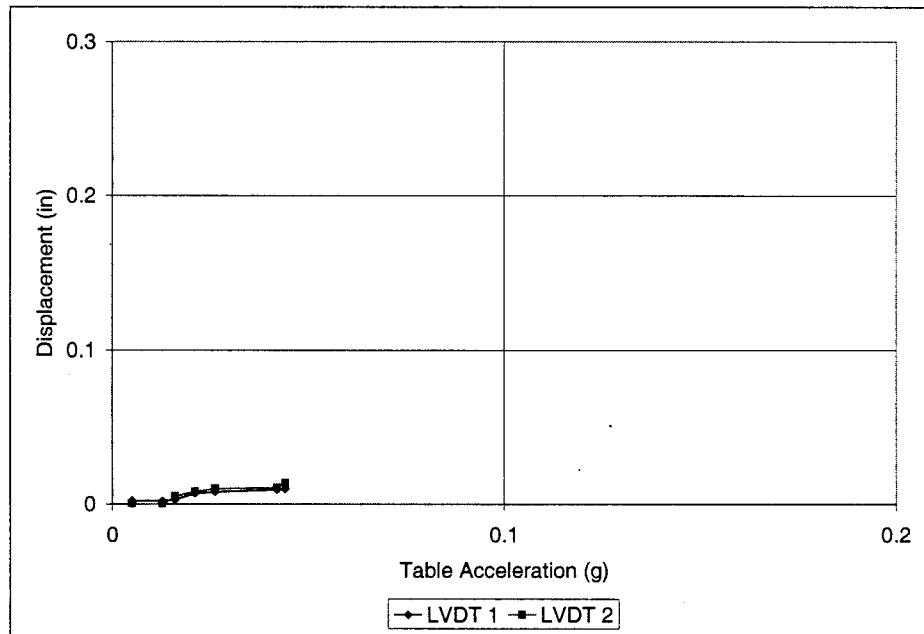


Figure B.20. Displacement vs. Input, Taft Earthquake, Damper 4

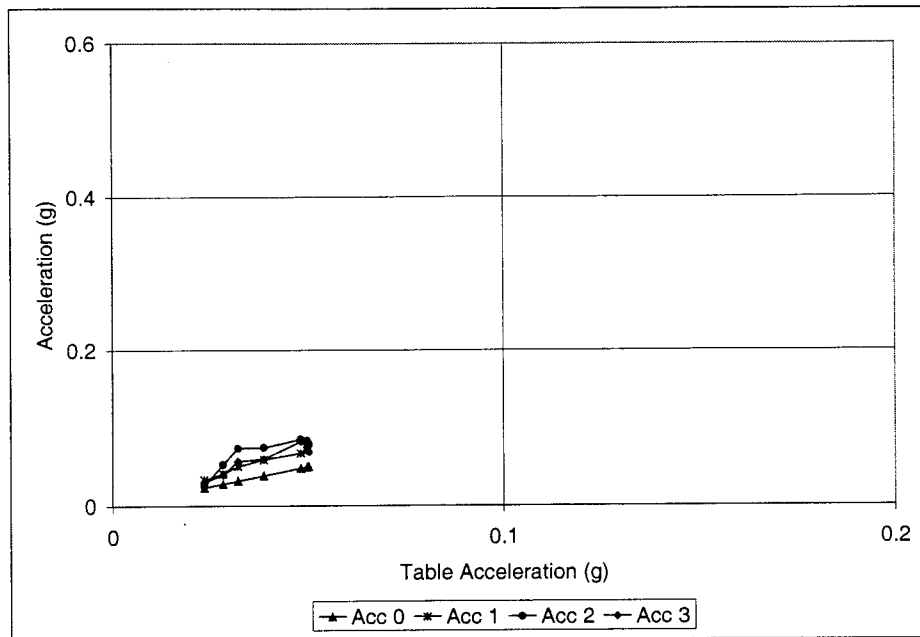


Figure B.21. Acceleration vs. Input, El Centro Earthquake, Damper 4

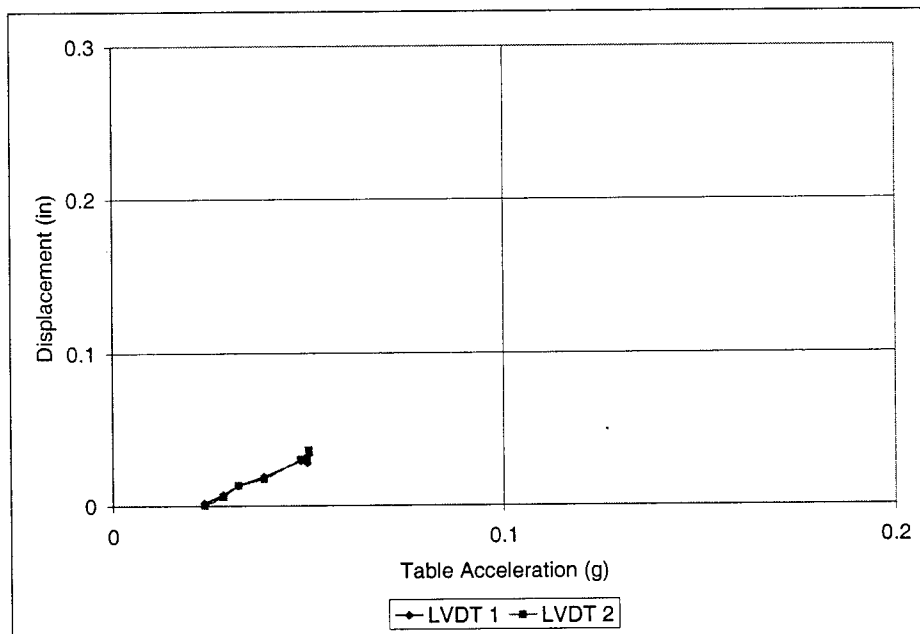


Figure B.22. Displacement vs. Input, El Centro Earthquake, Damper 4

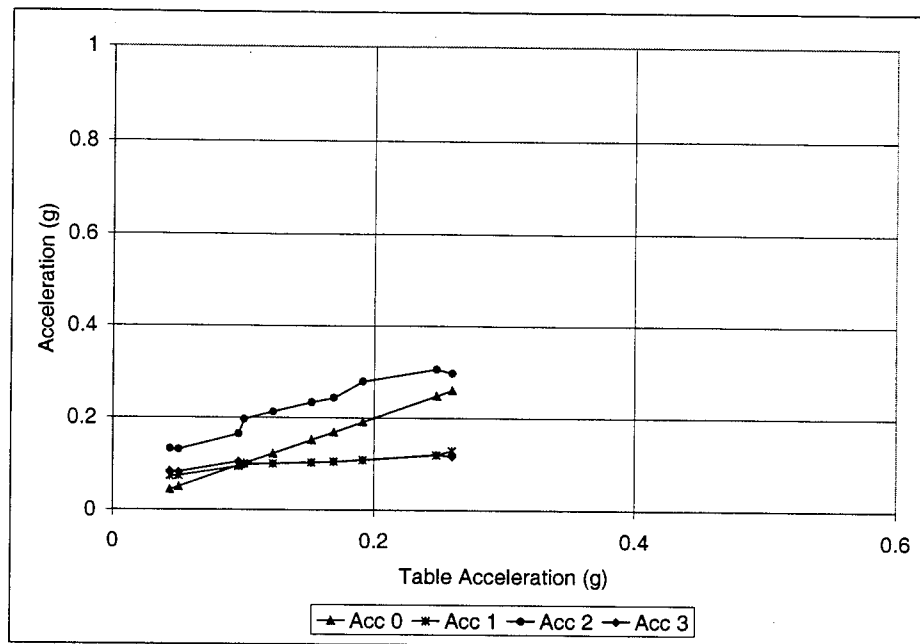


Figure B.23. Acceleration vs. Input, Harmonic Input, Damper 4

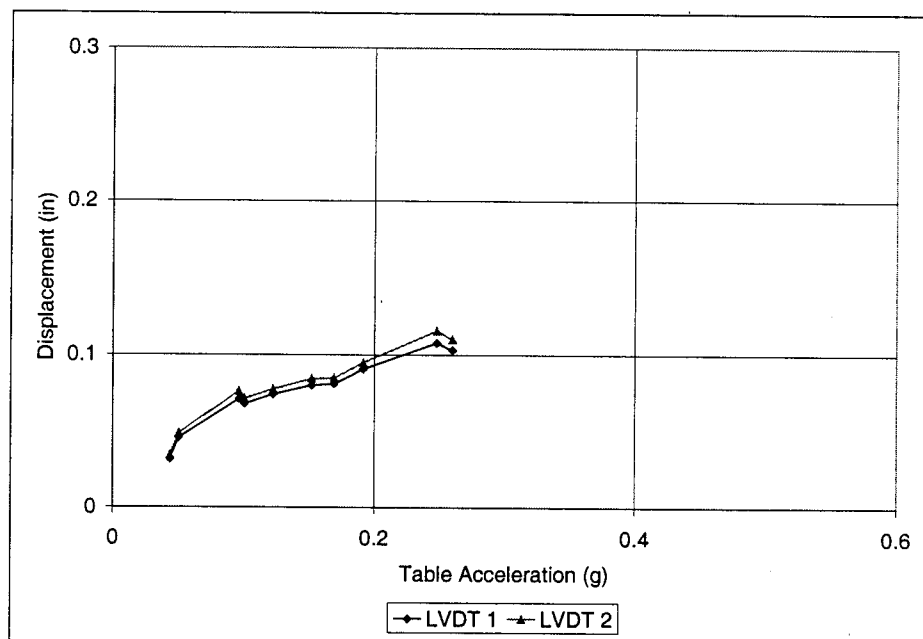


Figure B.24. Displacement vs. Input, Harmonic Input, Damper 4

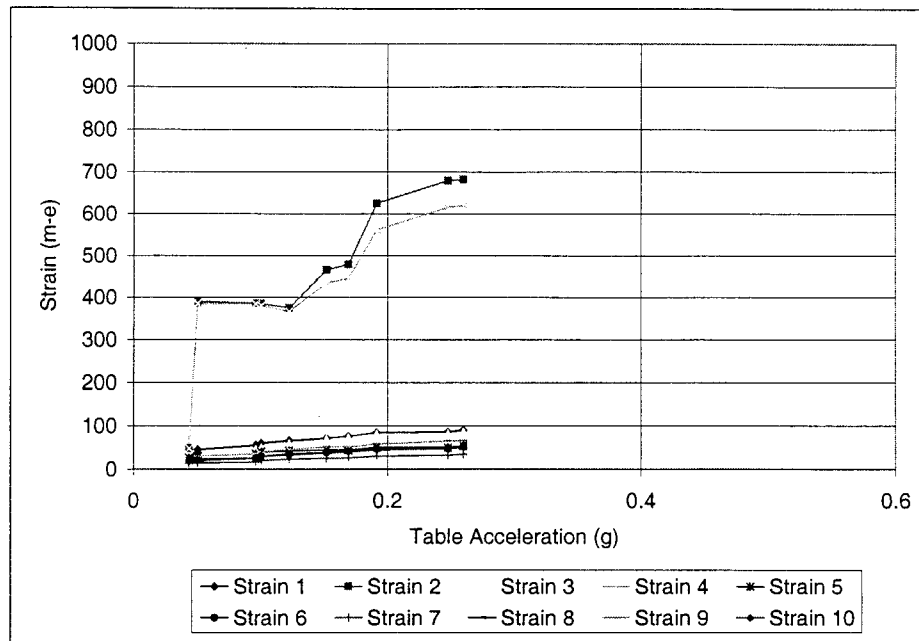


Figure B.25. Strain vs. Input, Harmonic Input, Damper 4

C. Tensile Test Data

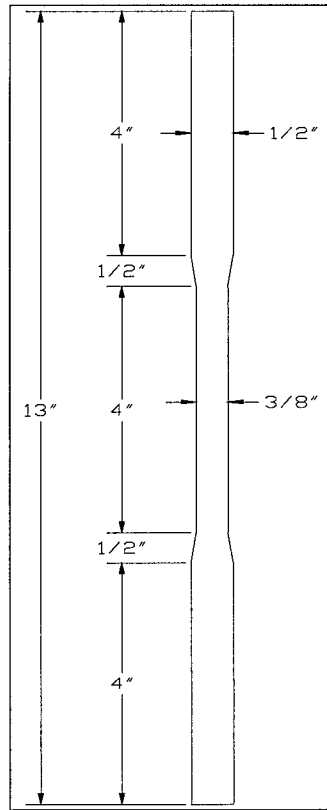


Figure C.1. Tensile Rod Detail

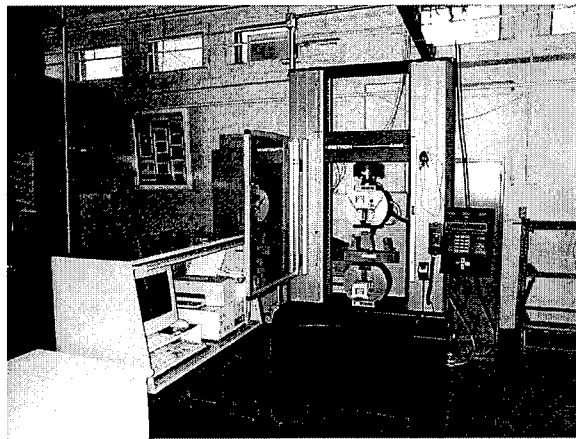


Figure C.2. Tensile Rod Setup and Data Acquisition

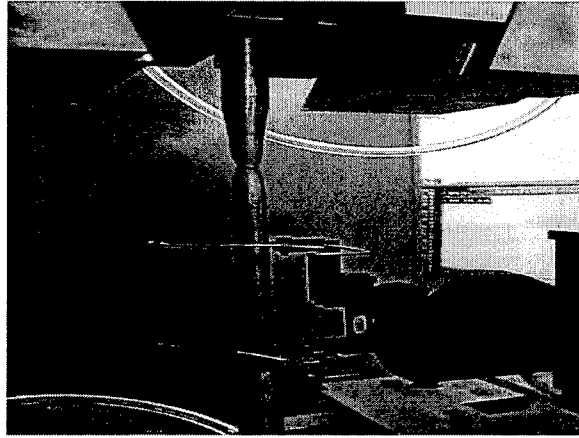


Figure C.3. Rod after Failure

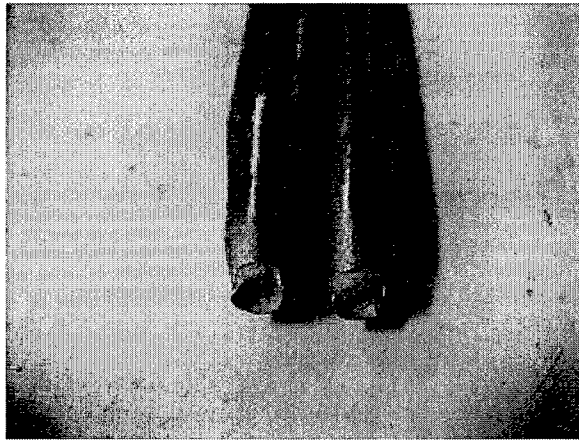


Figure C.4. Fracture Surface, Test 1

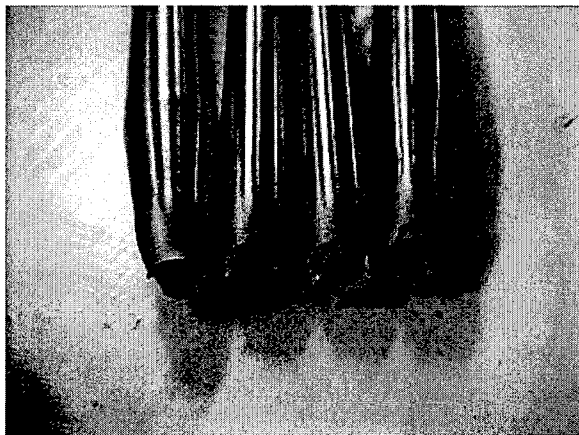


Figure C.5. Fracture Surface, Tests 2 and 3

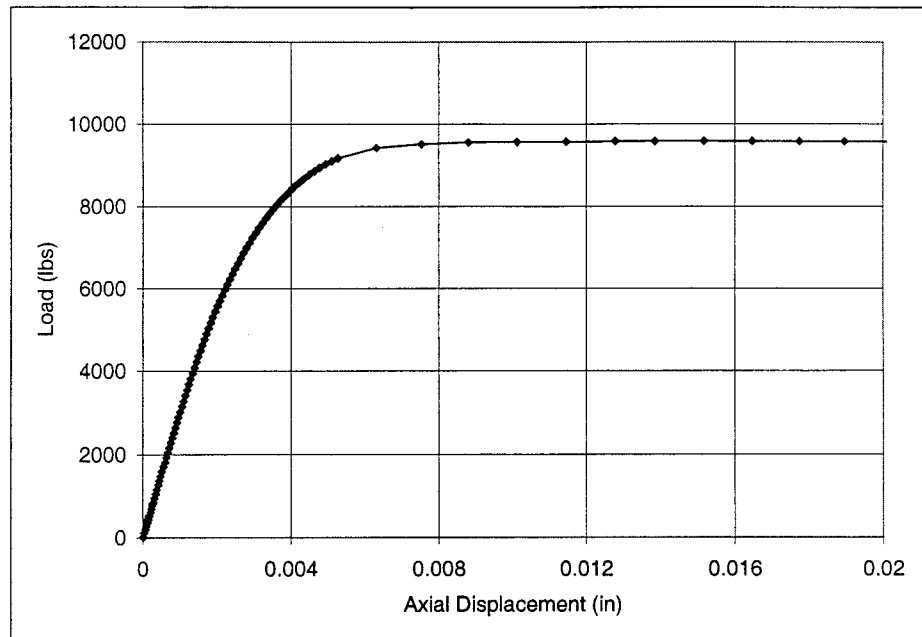


Figure C.6. Load vs. Axial Displacement, Test 1

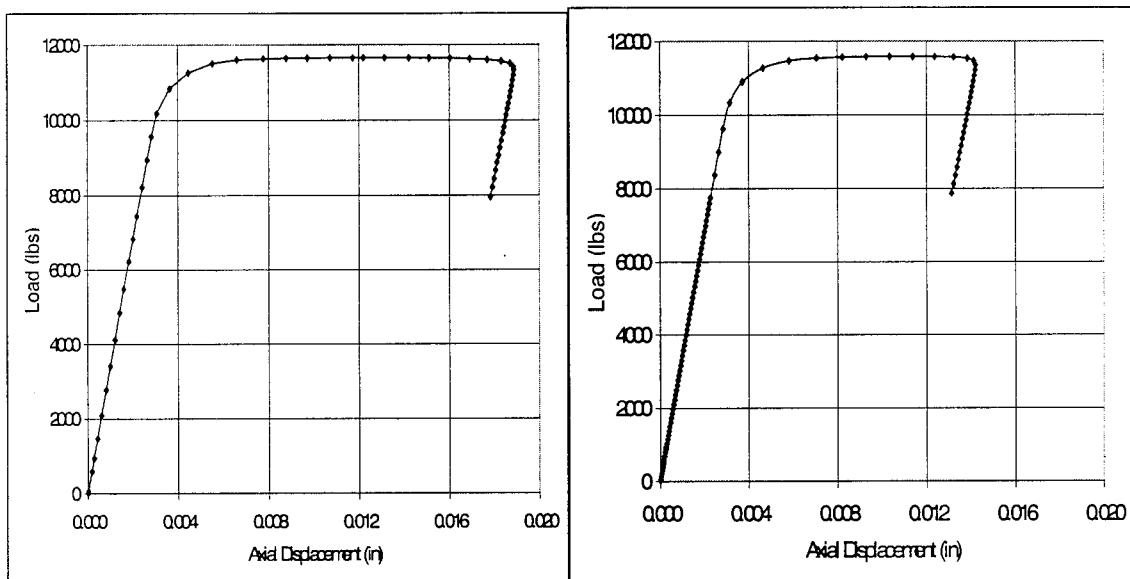


Figure C.7. Load vs. Axial Displacement, Tests 2 and 3, Respectively

Table C.1. Summary of Tensile Test Results

Test	Yield Stress (ksi)	Ultimate Stress (ksi)	Ultimate Load (kips)
1*	86	88.2	9.6
2**	105	106.1	11.6
3**	104.2	105.6	11.7

* Full-Scale Damper Material

** Small-Scale Damper Material

D. Single Mode Response Spectrum Analysis Procedure

The single-mode response spectrum analysis procedure in Case 5 is elaborated in greater detail in this appendix. The procedure is illustrated with Bridge A-237R subjected to the site-specific ground motion (SF100203a).

Step 1. Calculate the static displacements $V_s(x)$ of the structure due to the assumed uniform loading p_0 as shown in Figure D.1. The uniform loading p_0 is applied over the length of the bridge; it has units of force per linear length and is arbitrarily set equal to 1. The static displacement $V_s(x)$ has units of length.

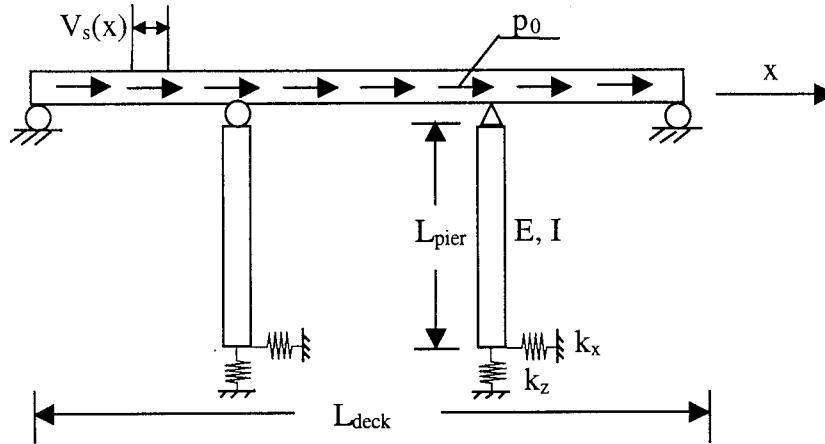


Figure D.1. Bridge A-237R Subjected to an Assumed Longitudinal Loading

For Bridge A-237R, $E = 3600$ kips/in², $I = 135000$ in⁴, $L_{deck} = 1680$ in., $L_{pier} = 308$ in., $k_x = 1000$ kips/in. The longitudinal displacements $V_s(x)$ under the uniform loading p_0 is equal to 35.5 in.

Step 2. Calculate the factors α , β and γ .

$$\left. \begin{aligned} \alpha &= \int V_s(x) dx \\ \beta &= \int W(x) V_s(x) dx \\ \gamma &= \int W(x) V_s(x)^2 dx \end{aligned} \right\} \quad (D.1)$$

where $W(x)$ is the weight of the dead load of the bridge superstructure and tributary substructure (force/length). For Bridge A-237R, $W(x) = 0.19$ kips/in.; the above factors can be computed as $\alpha = 59383$ in², $\beta = 11257$ kips-in, $\gamma = 397911$ kips-in².

Step 3. Calculate the period of the bridge, T .

$$T = 2\pi \cdot \sqrt{\frac{\gamma}{p_0 g \alpha}} \quad (D.2)$$

where g is the gravitational acceleration (length/time²). Based on the above values, $T = 0.83$ sec. Note that the calculated period is significantly shorter than that from the computer model due to the restraint on the longitudinal movement of a skewed deck.

Step 4. Calculate the elastic seismic coefficient C_s .

$$C_s = \frac{S_a(T)}{g} \cdot A_\xi \quad (D.3)$$

where $S_a(T)$ is the site-specific spectral acceleration and A_ξ is the damping modification factor defined in Eq. (5.7). The spectral acceleration of the SF100203a ground motion, $S_a(T)$, is equal to $0.6294g$ at the period of 0.83 sec, and $A_\xi = 0.7336$ corresponding to $\xi' = 0.10$. Therefore, $C_s = 0.462$. If C_s were determined according to the AASHTO Specifications, C_s would be

$$C_s = \frac{1.2 \cdot A \cdot S}{T^{2/3}} * A_\xi \quad (D.4)$$

in which A is the acceleration coefficient and S is site coefficient. At the bridge site, $A = 0.3438$ and the soil profile falls into Type III with $S=1.5$. As a result, $C_s = 0.515$, which is less than the upper limit $2.0AA_\xi$.

Step 5. Calculate the equivalent static earthquake loading $p_e(x)$, which is the intensity of the equivalent static seismic loading applied to represent the primary mode of vibration (force/length),

$$p_e(x) = \frac{\beta C_s}{\gamma} W(x) V_s(x). \quad (D.5)$$

Here $p_e(x)$ was determined to be 0.0875 kips/in based on C_s from the site-specific spectral acceleration. If C_s were determined according to the AASHTO Specifications, $p_e(x) = 0.0976$ kips/in.

Step 6. Apply loading $p_e(x)$ to the structure as shown in Figure D.2 and determine the resulting member forces and displacements.

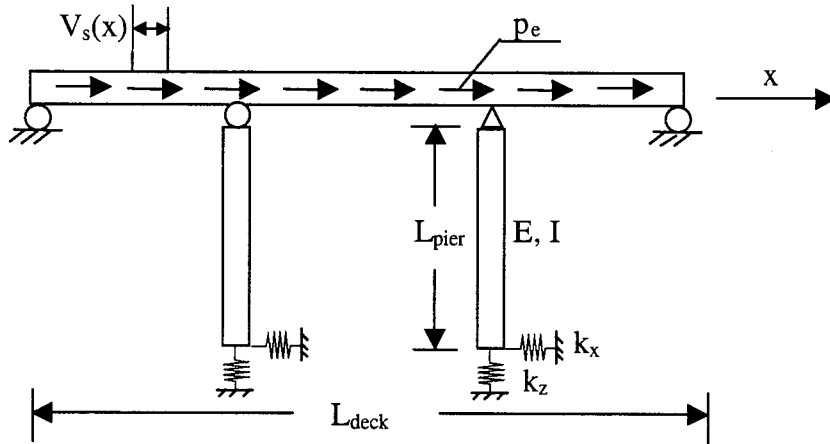


Figure D.2. Bridge Deck Subjected to Equivalent Longitudinal Seismic Loading

The maximum displacement of the deck under the equivalent seismic loading is 3.09 in. in the traffic direction or 3.45 in. when C_s were determined from the AASHTO Specifications.